CRANFIELD UNIVERSITY

Tamas Nagy

Investigation of Thermal Techniques to Mitigate Buckling Distortion in Welded Panels

SCHOOL OF APPLIED SCIENCES

PhD
Academic Year: 2011 - 2012

Supervisor: Professor Stewart Williams
May 2012

CRANFIELD UNIVERSITY

SCHOOL OF APPLIED SCIENCES

PhD

Academic Year 2011 - 2012

Tamas Nagy

Investigation of Thermal Techniques to Mitigate Buckling Distortion in Welded Panels

Supervisor: Professor Stewart Williams

May 2012

ABSTRACT

This thesis describes the advancements of the application of thermal tensioning techniques to different weld geometries in order to eliminate buckling distortion. The main goal of this work is to better understand these techniques through experimental and numerical investigation and increase their technological maturity to aid industrial implementation. The thermal tensioning techniques investigated in this work are Thermal Tensioning by Cooling and Thermal Tensioning by Heating. The investigation for both techniques encompasses thermal source characterisation, application to different weld geometries and residual stress measurements and analysis of both butt and fillet welded samples.

A detailed technology transfer study of Thermal Tensioning by Cooling was carried out in which different aspects of the application of TTC to arc welding (Gas Metal Arc Welding and Gas Tungsten Arc Welding) was examined. This study focused on the influence of both the liquid CO_2 delivery system installation and welding tooling and jigging on the effectiveness of Thermal Tensioning by Cooling in reducing buckling distortion. Experimental and numerical cooling source characterisation was also carried out in the Thermal Tensioning by Cooling work to investigate the characteristics of the cooling source under different cooling conditions. The Thermal Tensioning by Cooling work was then concluded with welding trials and residual stress measurement and analysis.

The results of the Thermal Tensioning by Cooling study show that the installation of the liquid CO_2 delivery system as well as the welding tooling and jigging has a major influence on the effectiveness of Thermal Tensioning by Cooling in reducing buckling distortion. The cooling source characterisation work reveals that the most important parameter of the cryogenic nozzle delivery system used in this work is the Air Entrainment Gap. A description of a control system of Thermal Tensioning by Cooling is suggested based on controlling the Air Entrainment Gap. The residual stress analysis shows a reduction in the

Applied Weld Load and minor changes in the tensile peak of the residual stress distribution of both butt and fillet welded panels.

The Thermal Tensioning by Heating investigation includes heat source characterisation, application of Thermal Tensioning by Heating on butt and fillet welds, utilisation of alternative heat sources and residual stress analysis. The results of these investigation show that Thermal Tensioning by Heating is also highly effective in eliminating buckling distortion in butt, fillet and overlapped panels. The applied heating temperature in this work is typically in the range of 160-250 °C but not greater than 330 °C. The residual stress measurements reveal that the additional heating of Thermal Tensioning by Heating generates a positive stress gradient at the location of heating.

ACKNOWLEDGEMENTS

The research presented in this thesis is part of the Stress Engineering Applied to Large Structures (SEALS) project funded by BAE Systems, Airbus, Bombardier, TSB (Technology Strategy Board), EPSRC (Engineering and Physical Sciences Research Council), Corus (now TATA Steel), BOC (now Linde), MoD (Ministry of Defence). I would like to express my gratitude to the project partners in making this PhD possible by providing funding and valuable comments and discussions throughout the project.

I am most thankful to Professor Stewart Williams for his never ceasing support, encouragement and inexhaustible patience throughout this work. Thank you for the countless discussions, the invaluable input and advice and also for taking me on as a PhD student in the Welding Engineering and Laser Processing Centre (WELPC).

I also would like to express my thanks to Dr Paul Colegrove for the support in the modelling work and Dr Supriyo Ganguly for the help in the residual stress measurements and analysis. Your input is also an integral part of this work.

Special thanks are also due to Brian Brooks and Flemming Nielsen, the technical staff of WELPC for all the technical support, ideas, patience and perseverance while I carried out my experiments.

My fellow PhD students – thanks for the discussions, support and companionship throughout.

I would like to also thank my entire family: my parents, my brothers and my in-laws for the encouragement, moral support and for being there during my studies. To my grandmother, RIP.

Nathan and Eli, thank you for being such wonderful and delightful children and for bringing me joy and laughter every day.

My deepest gratitude belongs to my beloved wife, Marge for completing me and persevering with me throughout this work. Without your love and support I couldn’t have finished this thesis. Thank you.

I dedicate this PhD thesis to Jesus Christ who gave up all He had so that we do not receive the one thing that we all deserve –living a life without purpose.

TABLE OF CONTENTS

List of Figures

List of Tables

Nomenclature

μ - dynamic viscosity

A - area

a - length of plate (in buckling

AEG - air entrainment gap

AWL - applied weld load

b - width of plate

BS - burners' separation

BWTD - burner-welding torch distance

C - coefficient of discharge

c - width of tensile stress region

CA - clamping arrangement

CBL - critical buckling load

CMT - cold metal transfer

c_p - specific heat capacity at constant pressure

d - lattice parameter

d_0 - unstrained lattice parameter

D_1 - inlet pressure

D1, D2 - CO2 spray diameter at the substrate surface

D_2 - outlet pressure

DC-LSND - dynamically controloled - low stress no distortion

DI - distortion index

D_i - distortion value at a point

D_n - cryogenic nozzle internal diametre

E - Young's modulus

EB - electron beam

E_m - surface emissivity coefficient

FEA - finite element analysis

FEM - finite element modelling

FSW - friction stir welding

g - gravitational constant

GMAW - gas metal arc welding

GMT - global mechanical tensiniong

GTAW - gas tungsten arc welding

h - convective heat transfer coefficient

h - thickness of plate

H1, H2 - Amal jet height

HAZ - heat affected zone

h_b - base heat transfer coefficient

h_b - burner height

h_c - convective heat transfer coeffient of co2 spray

h_p - peak heat transfer coefficient of co2 spray

ISRT - in-situ roller tensioning

ITY - induced tensile yielding

k - thermal conductivity

L - characteristic length of flow

L - latent heat of phase change

l_1 - initial length

l_2 - expanded length

LAr - liquid argon

LCO_2 - liquid co2

LMT - local mechanical tensioning

LN - liquid nitrogen

l_{subco2} - specific latent heat of sublimation of co2

LVDT - linear variable differential transformer

m - mass

$\dot{m}$ - mass flow rate

MCP - manifold cylinder pack

m_{inCO2} - mass flow rate of liquid co2

m_{inENT} - mass flow of air entrainment

m_{out} - mass flow rate in exhaust

Nu - Nusselt number

Nu_L - Nusselt number for a characeristic L length

p_1 - inlet pressure

p_2 - outlet pressure

PAPS - portable autimated plate straightener

p_{atm} - atmospheric pressure

p_{CO2} - liquid co2 pressure in delivery pipe

p_e - differential pressure in exhaust pipe

p_n - pressure in cryogenic nozzle

$p_{nbottom}$ - pressure at the bottom of cryogenic nozzle

p_{ntop} - pressure at the top of the cryogenic nozzle

Pr - Prandtl number

p_s - co2 supply pressure

PWRT - post weld roller tensioning

q - cooling flux

Q - scattering vector

Q - volumetric flow rate

Q_A - acetylene volumetric flow rate

Q_O - oxygen volumetric flow rate

Q_{phc} - cooling power of phase change

R_a - apperture radius

RCY - reduced compressive yielding

Re - reynolds number

RPEB - reduced pressure electron beam

RS - residual stress

$R_{s/g}$ - solid to gas ratio of co2 spray

R_{sgn} - solid to gas ratio of co2 spray at nozzle exit

R_{sgs} - solid to gas ratio of co2 spray at substrate surface

SCAT

SCO_2 - solid co2

SE - stress engineering

SEALS - stress engineering applied to large structures

S_{nt} - separation of cooling nozzle and welding torch

SRDW - synchronous rolling during welding

T_0 - cooling medium temperature

T_c - cooling medium temperature

TCP - total cooling power

T_g - cooling gas temperature

T_l - liquid spray temperature

T_{max} - maximum temperature

TMT - thermal mechanical tensioning

T_p - peak temperature

T_{pre}- substrate pre-heat temperature

T_s - substrate surface temperature

TS - travel speed

TTC - thermal tensioning by cooling

TTH - thermal tensioning by heating

TTHC - thermal tensioning by heating and cooling

TTT - transient thermal tensioning

UTS - ultimate tensile strength

v - velocity of CO2 spray

v_g - cooling gas veocity

WFS - wire feed speed

YS - yield strength

YS - yield stress

z - geodetic height

z_A - Amal jet height relative to the substrate surface

β - expansion coefficient

Δl - thermal expansion

ε - strain

θ - half diffraction angle

λ - incident neutron beam wavelength

ν - knematic viscosity of gas

ν - Poisson ratio

ρ - density

ρ_{LCO2} - density of liquid co2

σ_{cr} - critical buckling stress

σ_{tmt} - tensile stress applied by thermal mechanical tensioning

Φ_i - design variable

1 Introduction

Welding is the primary fabrication process in shipbuilding and railway carriage production. The material thickness used in these industries has reduced significantly in recent years. It is now common to use plates for hull and body applications as thin as 4-5 mm in shipbuilding and 2 mm in railway carriage fabrication, providing that the structure has sufficient strength. Although weight and manufacturing costs can be saved by reducing material thickness, buckling distortion caused by welding Residual Stresses (RS) becomes a major problem in fabrication (see Figure 1.1).

Figure 1.1 Distortion caused by welding is a major problem in shipbuilding (HMS Daring, launched in 2007 [1]

Corrective measures that introduce more, but counterbalancing stresses are used at present in both shipbuilding and railway car body production. These rectifying techniques, such as flame straightening, are difficult to apply and are very expensive and labour intensive. Blackburn [2] estimates that distortion costs $3.4 million per vessel (mid-size destroyer) including all the additional man-hours, materials, delays, etc. due to buckling distortion. In addition to these extra

costs, buckling distortion reduces the hydrodynamic performance of a vessel which results in lower speed and higher fuel consumption. Higher radar signal is also an unwanted result of buckling distortion which is important for navy vessels.

1.1 Welding Residual Stresses

Residual Stresses can arise due to a variety of reasons in a component or structure. Welding is only one of the many causes engineers need to consider while designing or manufacturing a structure.

1.1.1 Introduction to Residual Stresses

Residual stresses are stresses that would exist in a structure even if all external loads were removed. Residual stresses also develop if a structure is subjected to a non-uniform temperature change [3].

Residual stresses develop in metal structures during manufacturing for various reasons:

- In bars, plates and other metal products due to rolling, casting, forging, etc.
- Due to forming and shaping of metal parts, for instance shearing, bending, machining, etc.
- Due to fabrication processes such as welding
- Due to heat treatments (e.g. quenching)

1.1.2 Welding Residual Stress Formation

The thermal cycle of welding results in a longitudinal residual stress profile which is illustrated in Figure 1.2. There is a large tensile peak in the centreline of the weld which can reach the magnitude of the yield strength of the material. This tensile peak is balanced by compressive stresses further away from the weld line. If the load induced by the compressive stresses exceeds a critical value, called the critical buckling load, buckling occurs.

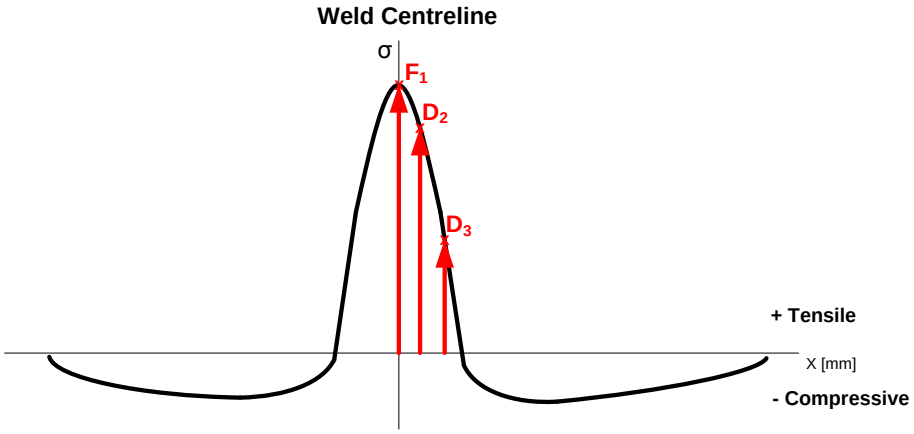

Figure 1.2 Typical residual stress profile of a bead on plate weld

It is critical to understand how residual stresses are formed during welding. Understanding this phenomenon gives the opportunity to tackle the problem of welding residual stresses and their resulting/induced distortion.

In order to understand how the longitudinal residual stresses are formed during welding let us first look at the material behaviour focusing on the Yield Strength (YS) at different temperatures. Looking at the stress-strain curves of a material at different temperatures (see Figure 1.3) it can generally be said that the YS decreases as the temperature increases ($YS_4<YS_3<YS_2<YS_1$).

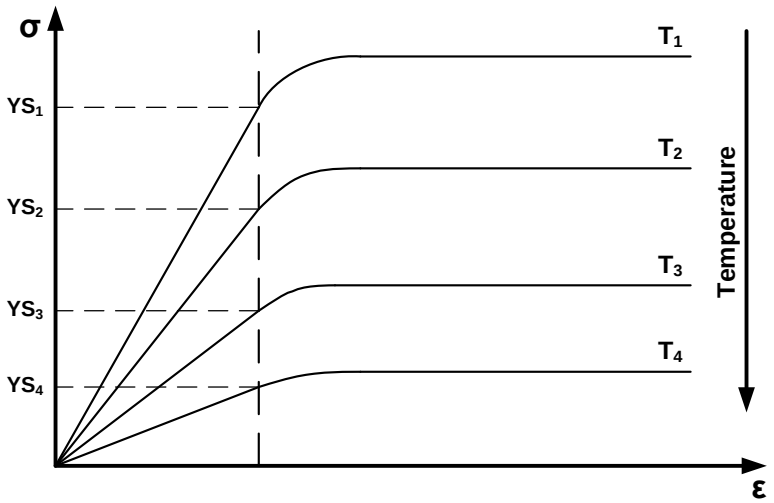

Figure 1.3 Schematics of the variation in Yield Strength (YS) on the stress-strain curves at different temperatures

If we plot these different YS values from the stress-strain curves we get temperature dependent YS (see Figure 1.4 solid line). The relationship between

the temperature and YS can be quite different depending on the material properties as illustrated in Figure 1.4 (solid and dashed lines).

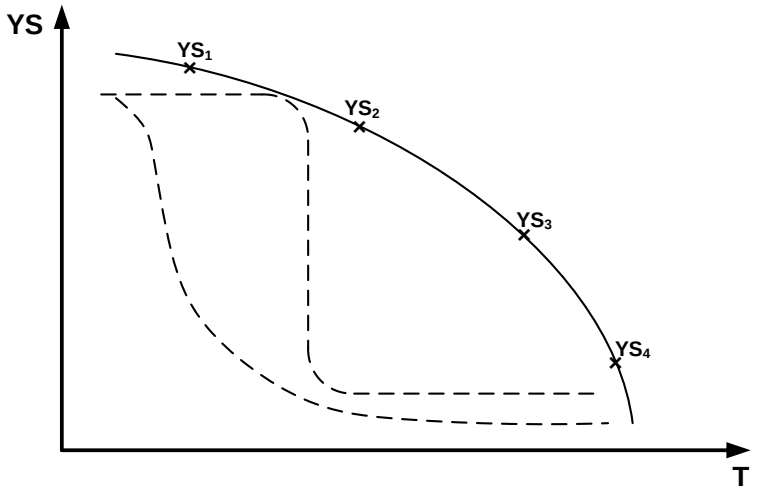

Figure 1.4 Temperature dependant Yield Strength (YS) curves of different materials

Radaj [4] represented the areas where plastic yielding occurs around a moving heat source as shown in Figure 1.5. The local maximum temperature is designated by T_{max}, ahead of this line the temperature of the material is increasing. Due to the increasing temperature thermal expansion occurs, which generates compressive stresses as the expansion is constrained by the surrounding cold material. Behind the T_{max} isotherm the temperature is decreasing, hence tensile stresses are generated due to the restricted contraction of the hot material. These tensile stresses remain even at ambient temperatures and form the tensile peak of the longitudinal welding residual stress profile shown in Figure 1.2.

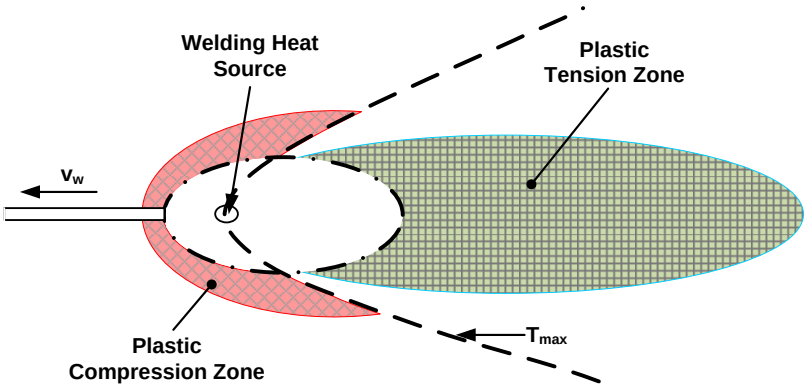

Figure 1.5 Plastic tension and compression zones represented by Radaj [4]

There is an isotherm (dash dot line in Figure 1.5) around the heat source where the temperature is so high that the yield strength of the material is close to zero or zero where the material is molten. Therefore inside this isotherm the stresses are zero or close to zero.

We can follow how the longitudinal tensile residual stresses arise around the weld centreline by following the temperature-stress history of a point traversing through the weld thermal field at different distances from the weld centreline. In this scenario only the longitudinal stresses are considered. The reason for this consideration is that the buckling distortion examined in the present work is caused by the longitudinal components of the welding residual stresses alone.

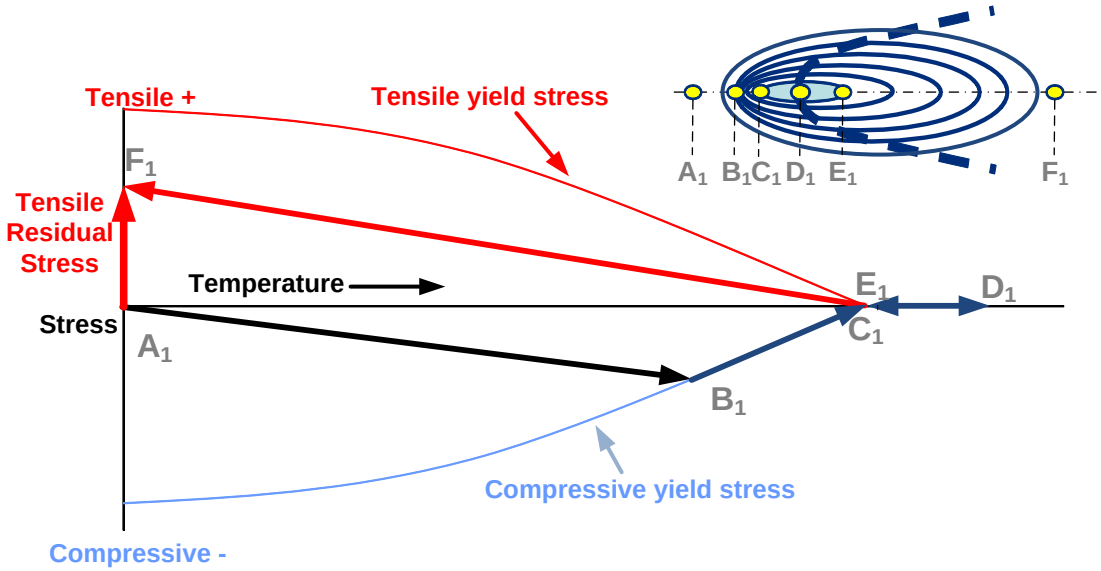

Figure 1.6 Residual stress formation following a point traversing through the welding thermal field at the weld centreline.

First, let us consider a point traversing through the thermal field of welding at the weld centreline as represented in Figure 1.5, and follow the temperature and stress changes as shown in Figure 1.6 after Williams [5]. At position A_1 – away from the weld zone - the material is at ambient temperature. As the traversing point approaches position B_1 the temperature increases and compressive stress is generated as explained previously. At position B_1 the temperature is so high that the induced compressive stress reaches the compressive yield stress of the

material at that elevated temperature. As the point traverses towards the molten pool, plastic yielding occurs as the B_1C_1 line illustrates in Figure 1.6.

Position C_1 is the front edge of the molten pool therefore the stresses are zero and remain zero until position E_1 where the point reaches the end of the molten pool. From position E_1 to F_1 the temperature is decreasing and tensile residual stresses arise as explained above. At position F_1 the material is at ambient temperature again and there is a tensile residual stress at this point (F_1 in magnitude).

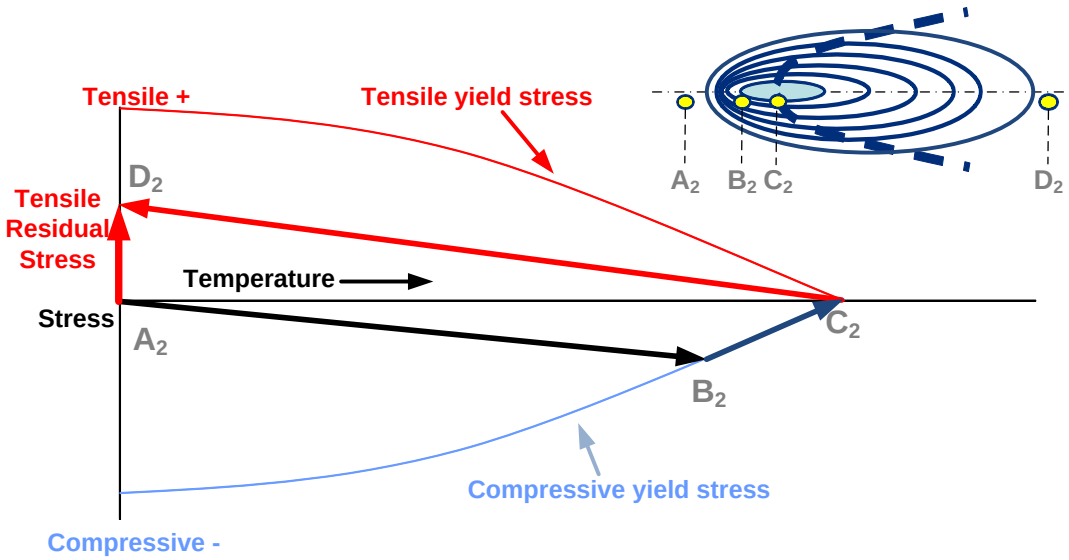

Figure 1.7 Residual stress formation following a point traversing though the welding thermal field at the edge of the molten pool

Now let us consider a similar description for a point traversing right at the edge of the molten pool as shown in Figure 1.7. In this case the compressive stress, induced ahead of the weld or the T_{max} isotherm reaches the yield stress level at higher temperature as the lower temperature gradient along A_2B_2 line results in lower stress gradient. This means the induced compressive yielding (B_2C_2 line) is less than that induced at the weld centreline (B_1C_1 line).

Finally, let us follow the temperature-stress changes of a point traversing through the thermal field of welding further away from the weld pool, as illustrated in Figure 1.8. In this case the induced compressive yielding (B_3C_3 line) is even less than (B_2C_2 line) that of the previous case. This is because the induced

compressive stress only reaches the yield strength at an even higher (T_3) temperature due to the lower stress gradient generated by the lower temperature gradient along A3B3 line. Less compressive yielding also means lower tensile residual stress at position D_3 where the temperature returns to ambient.

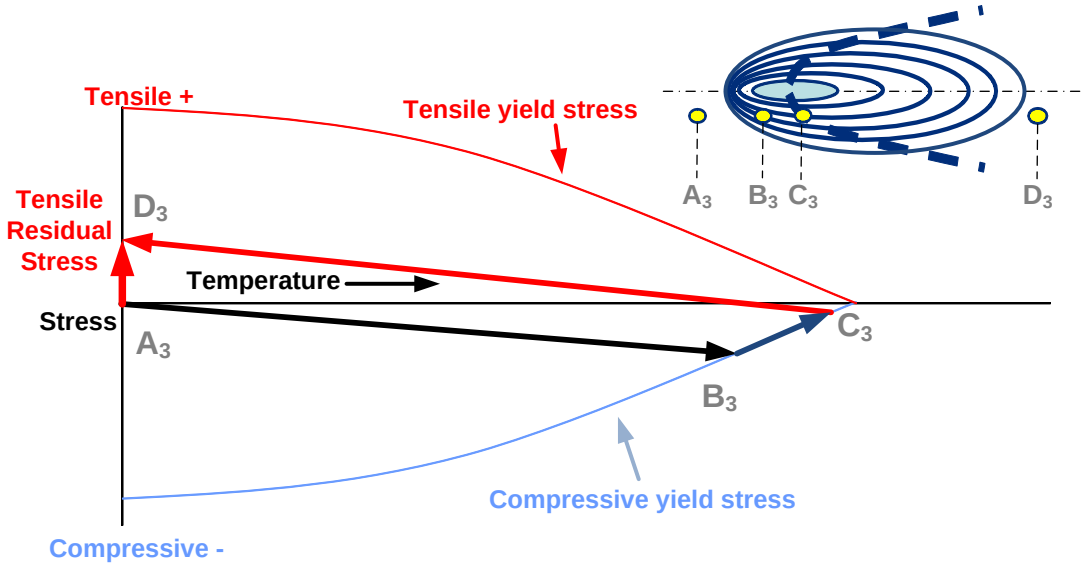

Figure 1.8 Residual stress formation following a point traversing though the welding thermal field further away from the edge of the molten pool

Following the temperature-stress changes as described above makes it clear that the longitudinal tensile residual stresses arise due to compressive yielding during welding. It is also clear that the further away from the weld centreline the point is traversing through the thermal field of welding the less compressive yielding occurs. Less compressive yielding results in lower tensile residual stresses (see the magnitudes of residual stresses from Figure 1.6-1.8 shown in Figure 1.2) and if the distance from the weld centreline is big enough – or the temperatures low enough - there will be no plastic yielding and no tensile residual stresses.

The tensile stresses generated by compressive yielding during welding as explained above are balanced by compressive stresses as Figure 1.2 illustrates. It is important to note that these compressive stresses are balancing stresses. This means that the tensile residual stresses need to be reduced to eliminate buckling

distortion even though buckling is caused by the compressive components of the welding residual stress profile.

1.2 Consequences of welding residual stresses

Residual stresses induced by welding affects the performance of the component or assembly significantly. Measuring residual stresses has become more reliable, accurate and cheaper in recent years. This development in measurement provides the tools for studying the influence of residual stresses in more details.

The most well known and described consequence of welding residual stresses is distortion, as it is visible and easy to measure. But welding residual stresses also influence stress corrosion and fatigue behaviour of materials significantly as these are all stress related properties.

1.2.1 Distortion

One of the most obvious and well known consequences of welding residual stresses is distortion. Most often it is this consequence that causes the most problems in different industries (e.g. shipbuilding and railway vehicle body fabrication).

Distortion in a welded structure is a permanent change of the shape and/or the dimensions of the structure. Six different types of distortion are distinguished in welded structures, as listed and illustrated in Figure 1.9 [3]: longitudinal and transverse shrinkage, rotational distortion, angular distortion, longitudinal bending and buckling distortion.

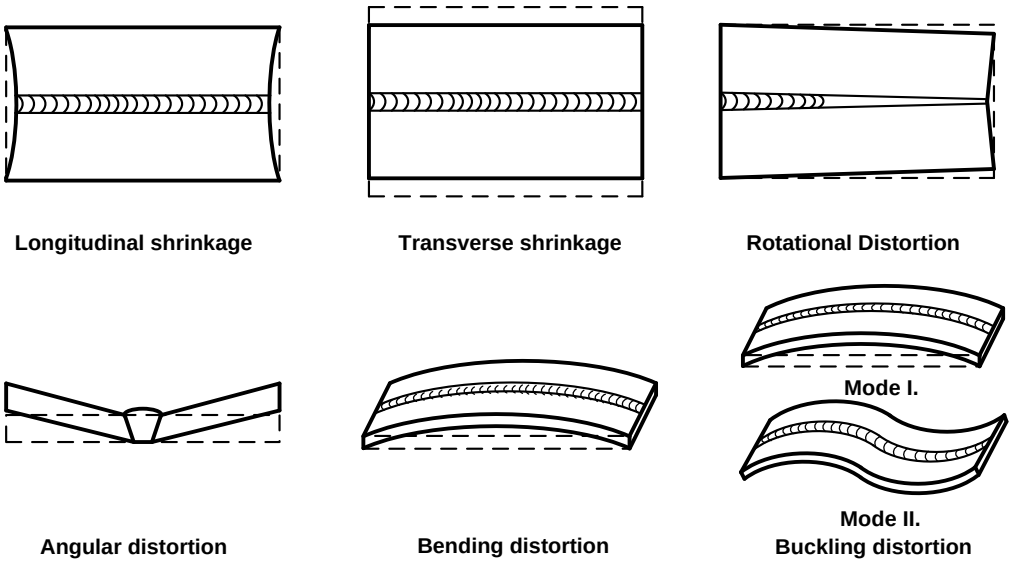

Figure 1.9 Common types of distortion caused by welding after [3]

Transverse shrinkage, longitudinal shrinkage and rotational distortion are caused by material movement towards the weld zone [5], if this material movement is different at the beginning and the end of the weld we get rotational distortion.

Angular and bending distortions are caused by non-uniform movement of material and non-uniform thermal field of welding in the through thickness direction. Angular distortion is generally caused by uneven shrinkage of the weld, i.e. the elastic contraction on the top is larger than at the bottom and this causes distortion in the transverse direction (see Figure 1.9). Longitudinal bending is caused by an uneven thermal field in the through thickness direction that results in a non-uniform residual stress distribution. The difference in the residual stresses generates a bending moment in the welding direction. This bending moment then changes the shape of the welded structure in the welding direction.

Buckling is caused directly by the welding residual stresses. The compressive components of the residual stresses produced by welding generate a load, known as the Applied Weld Load (AWL) [6]:

$$AWL = \overline{\sigma_t} \bullet w_t \tag{1.1}$$

where:

- $\overline{\sigma_t}$: average tensile residual stress
- w_t : width of the tensile residual stress peak (see Figure 1.2)

If the AWL exceeds a critical value, called the Critical Buckling Load (CBL) the part becomes unstable and buckling occurs.

Buckling distortion of welded structures can be described as column buckling and the critical buckling load can be determined using the Euler's formula for column buckling [7]. The critical buckling load is a characteristic of the welded structure and generally depends on the material type (strength) and geometry (thickness, width, length, etc.). Buckling distortion often has more than one stable form which makes it relatively easy to identify, though first mode buckling is very similar in appearance to longitudinal bending. This similarity calls for caution when identifying the type of distortion and hence the cause.

1.3 Distortion mitigating techniques

Complete elimination of distortion is difficult, expensive and very often is not achievable even with today's technological advancements. Therefore the different distortion mitigating techniques are now an integral part of the entire design and fabrication process.

Based on what happens to the welding residual stresses and distortion, distortion mitigating techniques can be classified as follows:

- Residual stress management
- Distortion rectification
- Stress Engineering (SE)

Each of these techniques represents a different approach towards controlling welding residual stresses and distortion.

1.3.1 Residual stress management

Management of welding residual stresses does not aim at reducing them, but to prepare for their unwanted effects on the structure right from the design and all through the fabrication process of a structure. Residual stress management generally aims to avoid or accommodate the undesired effects of welding residual stresses. All of these techniques are now an integral part of shipbuilding and railway carriage fabrication.

The main factors affecting welding distortion are as follows (after Lucas [8]):

- Parent material properties
- Position and amount of restraint
- Welded joint design
- Part fit-up
- Welding procedure

Considering these factors the following preventative techniques and measures have been developed over the years to manage residual stresses:

- Design techniques
- Assembly techniques
- Application of restraints
- Choice of welding process and technique

The design aspect of residual stress management generally aims to minimise the amount of weld. One way of achieving this is to use metal forming and extruded products to eliminate welding where possible (see Figure 1.10 a) or use intermittent welding instead of continuous seam if the structure allows. If welding is necessary the welds should always be positioned along or as close as possible to the neutral axis of the structure as shown in Figure 1.10 b.

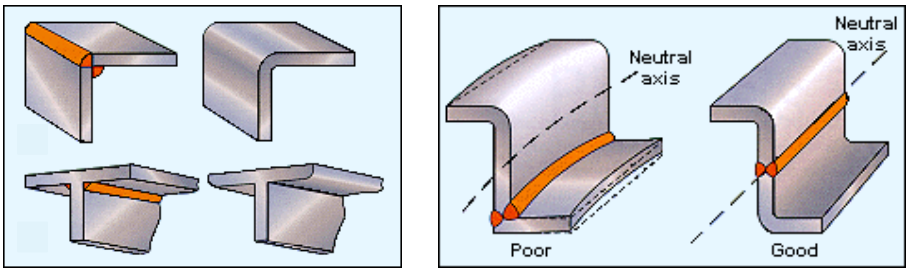

Figure 1.10 Residual stress management by design a) elimination of welds b) positioning welds along the neutral axis [8]

Assembly techniques usually aim to accommodate the distortion caused by welding. Typical examples of these techniques such as pre-bending, pre-setting and the application of tack welds are illustrated in Figure 1.11. Another common assembly technique is the back to back welding where the shrinkage of a weld (e.g. on part A) is restricted by the shrinkage of another weld (on part B) that is clamped to the first part and vice versa.

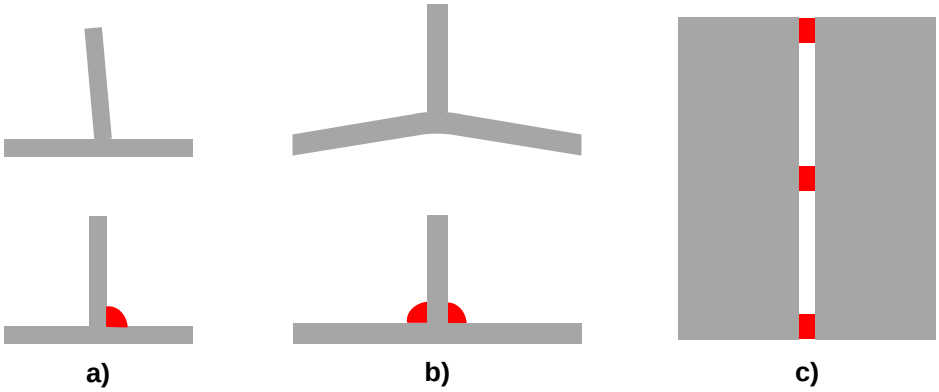

Figure 1.11 Assembly techniques to manage welding residual stresses: a) pre-setting b) pre-bending c) tacking

Restraints during assembly are also commonly used to reduce distortion. Investigation of the clamping parameters such as clamp distance from weld, release time after welding, clamp pre-heat temperature by Schenk et al. [9-11] revealed that both welding residual stresses and (angular and bending) distortion can be reduced by a well designed clamping setup and sequence. Typical restraints used for welding are welding jigs and strong-backs, both illustrated in Figure 1.12

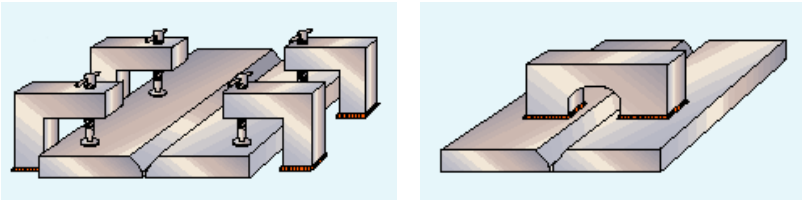

a) b)

Figure 1.12 Restraints applied in assembly to prevent distortion: a) welding jig and b) strong-back [8]

Finally, the choice of welding process is also critical in managing residual stresses. It is possible to significantly reduce welding residual stresses and distortion just by changing the welding process. Colgrove et al. [6] showed (see Figure 1.13) that only by using a different welding process on the same joint configuration (4mm butt weld), buckling distortion can be eliminated (Figure 1.13,a). This is due to the significant drop in the AWL achieved by low heat input processes (autogenous laser, hybrid laser, CMT) as Figure 1.13,b shows.

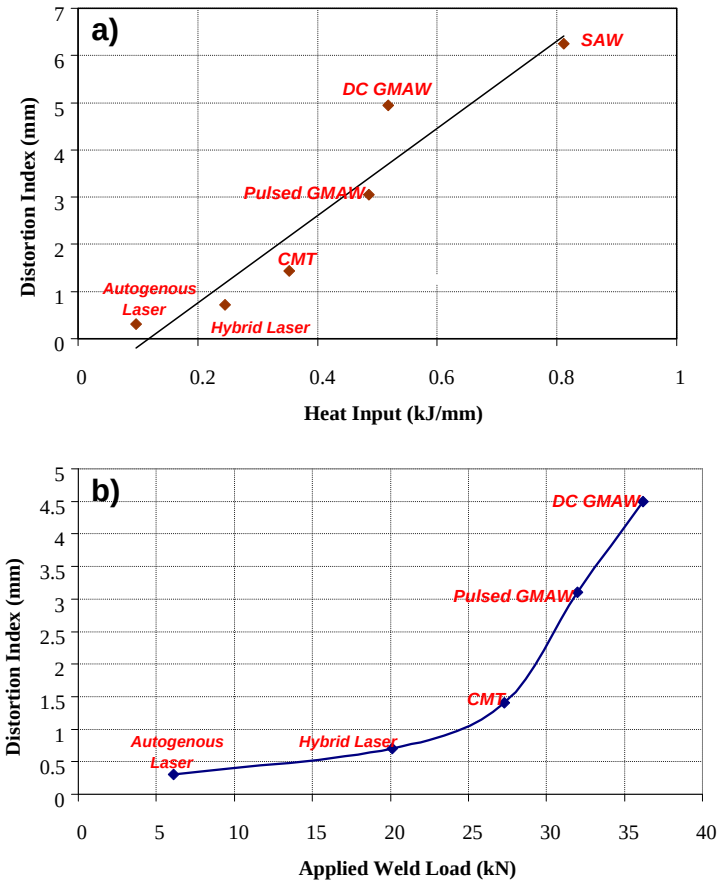

Figure 1.13 Influence of the selection of welding process on welding residual stresses and distortion of 4 mm thick DH36 plates [6]

Distortion can also be greatly reduced by using appropriate welding techniques that keep the weld size to an adequate minimum and by balancing the welds around the neutral axes of the joint (see Figure 1.14, a). Weld sequencing is a commonly used technique as well to minimise the heat build up in welded. In weld sequencing a complete weld is split into sub-sections and the order of these sections to be welded is often changed in order to avoid overheating any part of the assembly. Two examples of weld sequencing are illustrated in Figure 1.14, b.

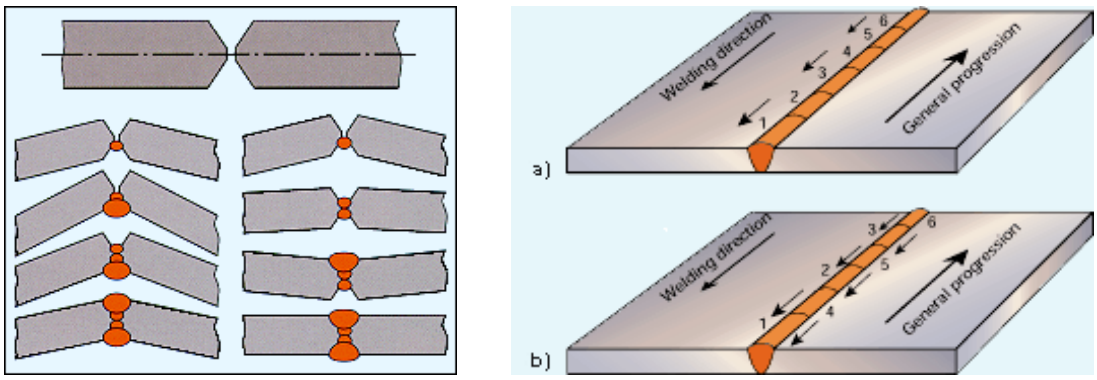

a) **b)**

Figure 1.14 Weld sequencing to a) balance welding around the neutral axis of the joint and b) to minimise heat input [8]

1.3.2 Distortion rectification

Distortion rectification aims to eliminate the consequences (i.e. distortion) of welding residual stresses rather than changing the residual stresses themselves. This is usually done by adding more stresses into the structure in order to increase the CBL. In this way, the AWL eventually falls below the increased CBL and buckling distortion is reduced. These stresses increasing the CBL are usually introduced into the structure by mechanical or thermal means.

Common mechanical straightening techniques are hammering and pressing. Hammering can cause surface damage and work hardening, therefore it is less and less used. Pressing is often difficult due to the size and shape of the structure, although it is still used on smaller components.

The most common straightening technique in shipbuilding is flame or induction straightening. Flame straightening is primarily done manually and requires a high level of skill from workers, which makes it a slow and expensive process. Flame straightening is usually an additional step or stage in the fabrication process, therefore it increases production time significantly. Some of the flame straightening techniques are illustrated in Figure 1.15.

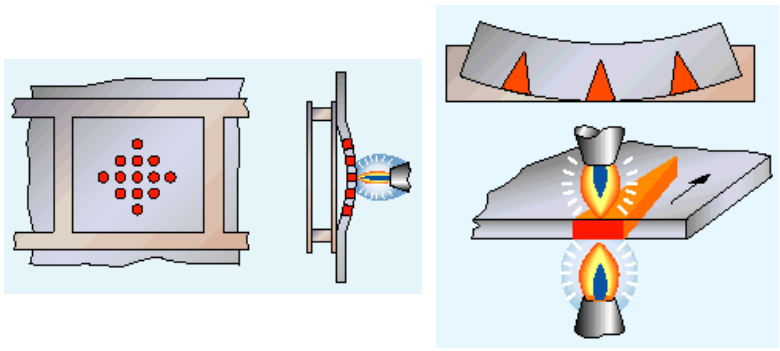

Figure 1.15 Flame straightening techniques to mitigate distortion a) spot heating and b) wedge shape heating techniques [8]

Although the principles of flame straightening have not changed much over the years, significant effort was spent on making it faster and more reliable. One of these efforts is a Portable Automated Plate Straightener (PAPS) by Turner et al. [12, 13].

1.3.3 Residual Stress engineering

Stress Engineering (SE) techniques aim to decrease distortion by reducing the compressive components of the welding residual stresses in the far field of the weld (see Figure 1.2). To achieve this, the tensile residual stress peak in the weld centreline needs to be decreased as the compressive stress components are balancing components of the tensile peak. Using Radaj's representation of plastic compression and tension zones during welding (see Figure 1.5), two main methods of reducing the tensile peak in the residual stress profile were identified [14]:

- Reduced Compressive Yielding (RCY): this method reduces the size and/or the magnitude of the plastic compression zone. This can be done by either cooling the plastic compression zone or by tensile stretching it. These methods can only be applied during welding.
- Induced Tensile Yielding (ITY): in this method an external longitudinal tensile stress is applied along the weld line behind the weld. In this way the stress levels in the plastic tension zone are increased above the yield limit of the material. By doing this some of the stresses will be relieved due to plastic tensile yielding. As a result the tensile peak in the residual stress pattern will be reduced. This method can be applied during welding or after welding as a post-weld straightening.

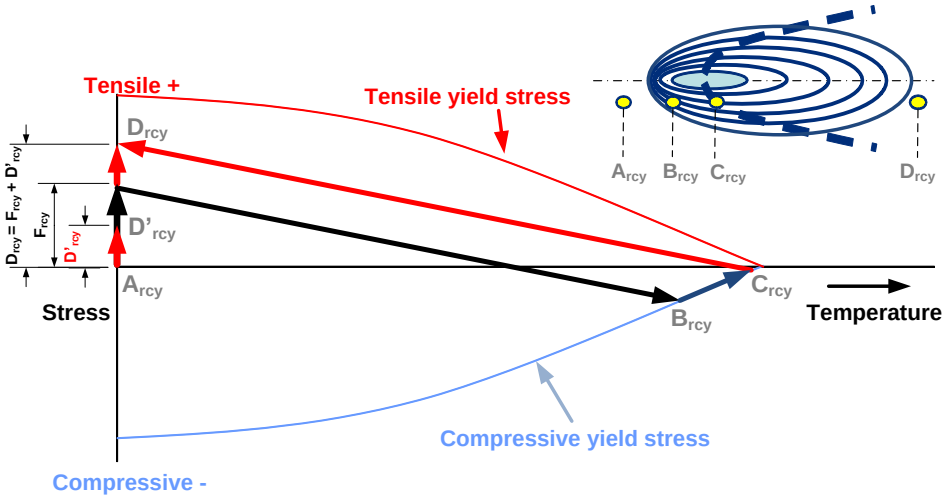

Figure 1.16 Welding residual stress formation when Reduced Compressive Yielding is implemented by applying tensile stresses along the weld centreline

One way of implementing the RCY method is to apply tensile stress along the weld centreline. If we look at the temperature-stress transients (explained before in Figure 1.6 through Figure 1.8) of a point travelling through the welding thermal field (similarly to Figure 1.8) the effect of the applied tensile stress on the formation of the tensile residual stress peak can be observed as demonstrated in Figure 1.16.

At point A_{rcy}, where the temperature is still at ambient F_{rcy} tensile load is applied, hence compressive yielding occurs at a higher temperature on $A_{rcy}B_{rcy}$

line. This also means that the amount of compressive yielding ($B_{rcy}C_{rcy}$ line) is less. As the temperature returns to ambient at point D_{rcy} there is still a large tensile stress, similarly to conventional welding. When the initially applied F_{rcy} tensile load is removed the remaining, final tensile residual stress (D'_{rcy}) becomes smaller, therefore the tensile peak at the weld centreline is reduced.

The method of ITY is employed by applying a tensile load (F_{ity} in Figure 1.17,b and c) at the weld centreline, where the tensile RS is already formed or being formed as shown in Figure 1.17,a. By applying this load the tensile peak in the residual stress profile is elevated, exceeding the tensile yield strength of the material (see Figure 1.17, b hashed area). Therefore some of the tensile stress will be relieved by the yielding induced and a new RS profile (RS_{ity}' in Figure 1.17,c) is formed. After releasing F_{ity} load, the final RS distribution has smaller tensile peak at the centreline compared to the original RS profile (see Figure 1.17,d), which also results in lower balancing compressive stresses.

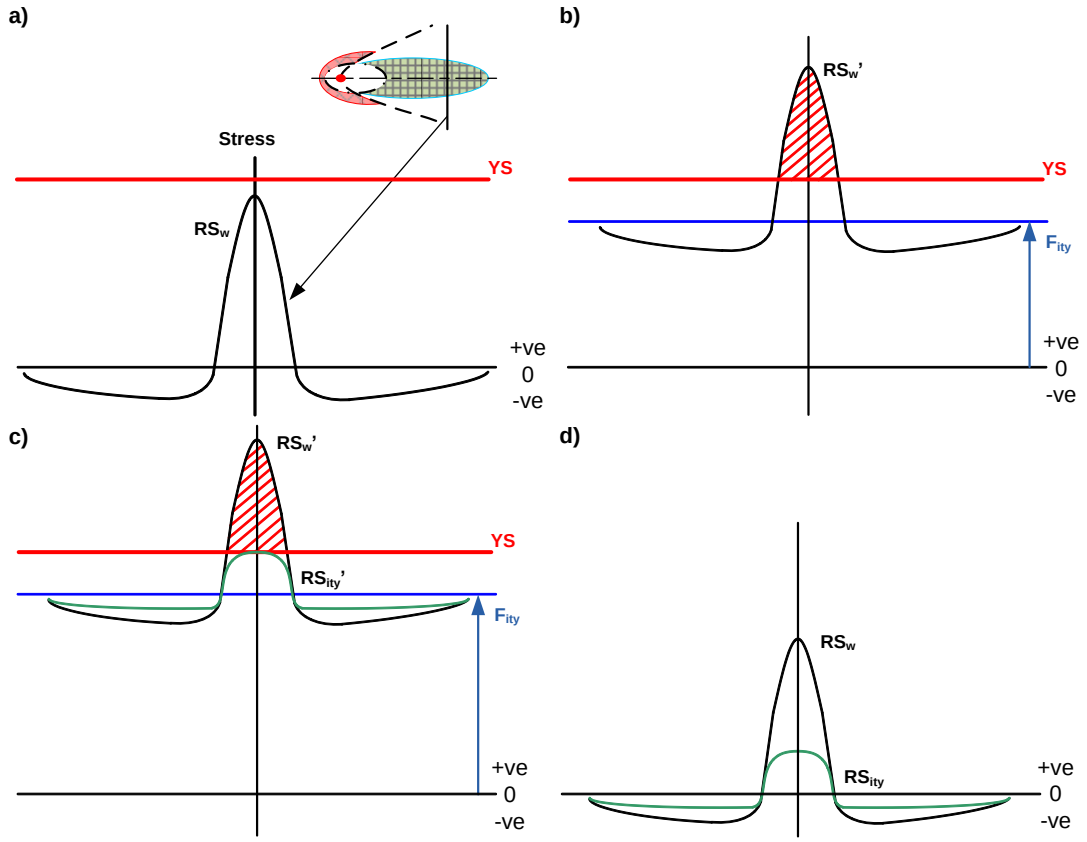

Figure 1.17. Residual stress reduction by Induced Tensile Yielding

As the ITY method affects the tensile peak directly, it can be applied both in-situ and after welding as post processing. The loads required to induce yielding will largely differ in the in-situ and post weld application due to the different yield limit at elevated and ambient temperatures. This creates an advantage for the in-situ application.

Both these methods use the application of longitudinal tensile stresses and six techniques have been considered for generating the load[14]:

- Thermal Tensioning
    - Thermal Tensioning by Heating (TTH)
    - Thermal Tensioning by Cooling (TTC)
    - Thermal Tensioning by Heating and Cooling (TTHC)
- Mechanical Tensioning
    - Global Mechanical Tensioning (GMT)
    - Local Mechanical Tensioning (LMT)
    - Thermal Mechanical Tensioning (TMT)

Developing different mechanical and thermal techniques to eliminate distortion is not a new idea. Several researchers have tried and failed or only partly succeeded in developing these techniques since the early 1940s [15, 16]. The issues have always been repeatability and inconsistency of these stressing techniques and their results as well as the repeatability of the welding processes itself. The main reasons behind this is on the one hand a lack of understanding of how the welding residual stresses are formed and also the dynamic stress field around the weld zone. On the other hand highly repeatable and well controlled stressing techniques and welding processes have not always been available although they are a necessity for a repeatable process.

1.3.3.1 Mechanical Tensioning

As the name suggests mechanical techniques use mechanical means to produce the tensile load around the weld to reduce the welding residual stresses.

1.3.3.1.1 Global Mechanical tensioning

This technique is realised by applying a preset tensile stress along the whole length of the plate as shown in Figure 1.18, hence the name global. Since the whole length of the plate is in tension both the plastic compression and tension zones are affected. This means this technique implements both RCY and ITY methods of SE.

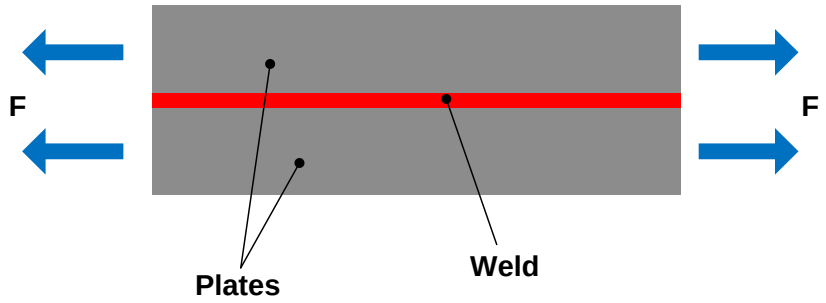

Figure 1.18 Schematic of Global Mechanical Tensioning technique on butt welded plates

Nikolaev, Prokhorov and Shiganov [16] carried out extensive research in the 1940s on different ways of pre-stressing the specimen: constant force, constant elongation and variable force. They suggest that the best method of applying the tensile load on the specimen is the constant force method applied through the neutral axis of each specimen. Their work was then extended by other researchers in the USSR to apply mechanical tensioning on fillet welds and also in aluminium welds [16].

Munsi et al. [13] incorrectly applied the tensile stress perpendicular to the weld line by pre-bending the specimen. This unfortunately results in a non-uniform stress field in the cross section (tension on top and compression at the bottom). Due to their implementation of pre-stressing their conclusion is not to use this technique in production because of the elevated residual stress levels at the welding toe.

Contrary to Munsi's results in the practical investigation of the GMT technique by Price et al. in the WAFS and SCAT collaborative projects [14, 17] concluded that it is a very reliable and highly repeatable technique. In these

projects GMT was applied on both Friction Stir Welding (FSW) and arc welding processes during and after welding as well. In the SCAT project significant effort was put into the clamp design of the tensioning rig as it was recognised that the design of the clamps is an important factor in achieving uniform stresses along the weld line.

Price et al. [14] in the SCAT project found that the relationship between the required load and the out-of-plane distortion is linear as shown in Figure 1.19. This is true for both in-process and post welding GMT, although it was found that post weld GMT does not reverse the distortion. This indicates that while with the in-situ GMT the RS peak at the weld centreline can be reversed into a compressive one, with the post weld GMT, this cannot be achieved. It is also clear in Figure 1.19 that in-situ GMT requires significantly lower loads for the same distortion reduction (e.g. 20% YS in-situ tensioning versus 70% YS post weld tensioning to reduce distortion down to 5 mm).

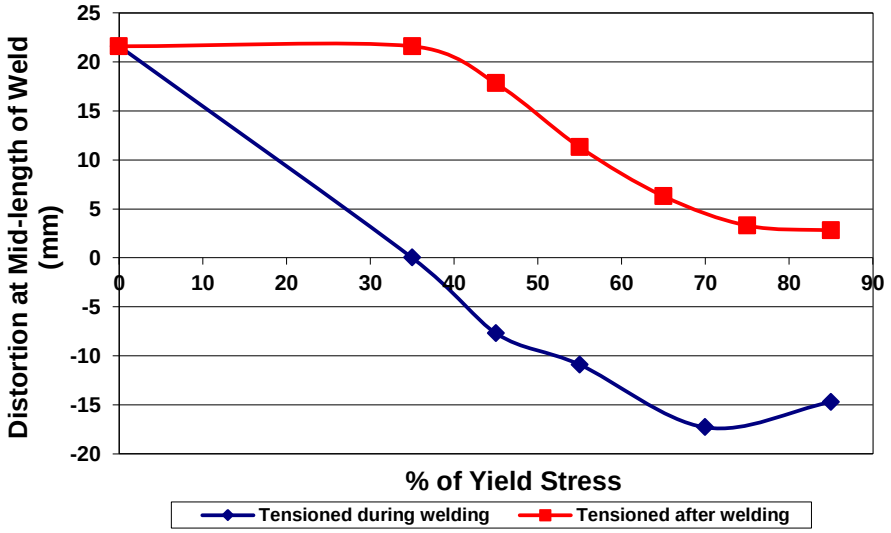

Figure 1.19 Relationship between the applied tensioning load (as percentage of Yield Stress) and out-of-plane distortion (measured at mid-length of weld) of Al 2024-T3 FSW butt joints [14]

This work was then carried on by Richards et al. to further understand the process [18]. In their work they confirmed a linear dependency of peak residual stress upon the applied tensioning (see Figure 1.20,b). They also investigated post weld mechanical tensioning, but realised it requires larger loads due to the

higher yield strength of the material at ambient temperature. Another limitation of the post weld application of GMT is that the stresses at the weld centreline cannot be converted to compressive stresses as Figure 1.20,a and b demonstrates.

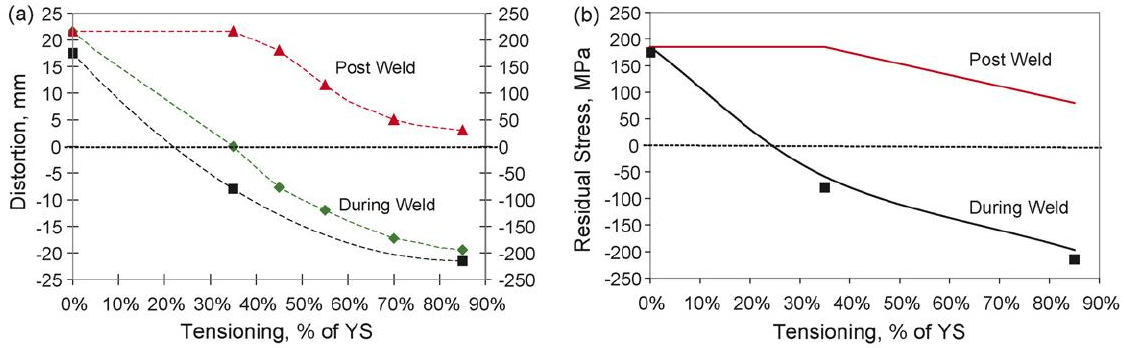

Figure 1.20 Effect of Global Mechanical Tensioning (GMT) (applied on 3 mm A2024-T3 FSW joints) on a) Distortion and b) Peak Residual Stress versus applied tensioning as percentage of Yield Strength (YS) [18]

Disadvantages of the GMT technique are the difficulty of generating a uniform tensile stress along a weld line that is a complex, perhaps a 3D curve. Also the equipment cost increases rapidly with increasing material thickness and yield strength and there is a practical limitation in the size of the panel to be welded as well.

Advantages of GMT are simple theory, improved fit-up and flatness during welding due to tensioning (improving weld quality in general), high level of control and the technique does not interfere with the welding process, hence it is applicable to any welding process.

1.3.3.1.2 Local Mechanical Tensioning

The Local Mechanical Tensioning (LMT) technique also applies a tensile stretch on the weld, but locally through rollers traversing with the welding heat source (if done online). Liu et al. used Synchronous Rolling during Welding (SRDW) to eliminate hot cracking in 2024 Al alloy [19]. The SRDW applies two rollers on either side of the weld behind the welding heat source to generate compressive transverse stresses in the hot weld material. These compressive

transverse stresses compensate for the tensile transverse stresses arising from the shrinking hot weld metal and hot cracking is eliminated.

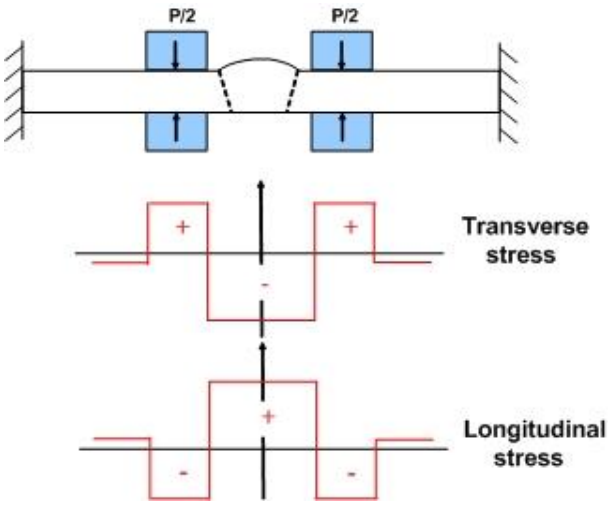

Figure 1.21 Distribution of longitudinal strains produced by rollers [14]

Applying rollers in a similar way can be useful for reducing residual stresses in welds. Figure 1.21 shows the longitudinal stresses that are generated when rollers are applied as Liu et al. suggested. Where the rollers are applied the material beneath them is stretched in the longitudinal direction. This stretching is restricted by the surrounding material, hence the material directly underneath the rollers experiences compressive stresses in the longitudinal direction. This also means that the material in between the compressed regions is in tension in the longitudinal direction so that the material is in equilibrium. The possible application of rollers to generate tensile stresses on the weld line was recognised by Price and her co-workers in the SCAT project [14] and then was realised in the SEALS project for further investigation. Williams et al. [20] and Altenkirch et al. [21] further investigated this technique on FSW using two different roller configurations: in-situ roller tensioning (ISRT)with two rollers and post weld roller tensioning (PWRT) with one roller as shown in Figure 1.22.

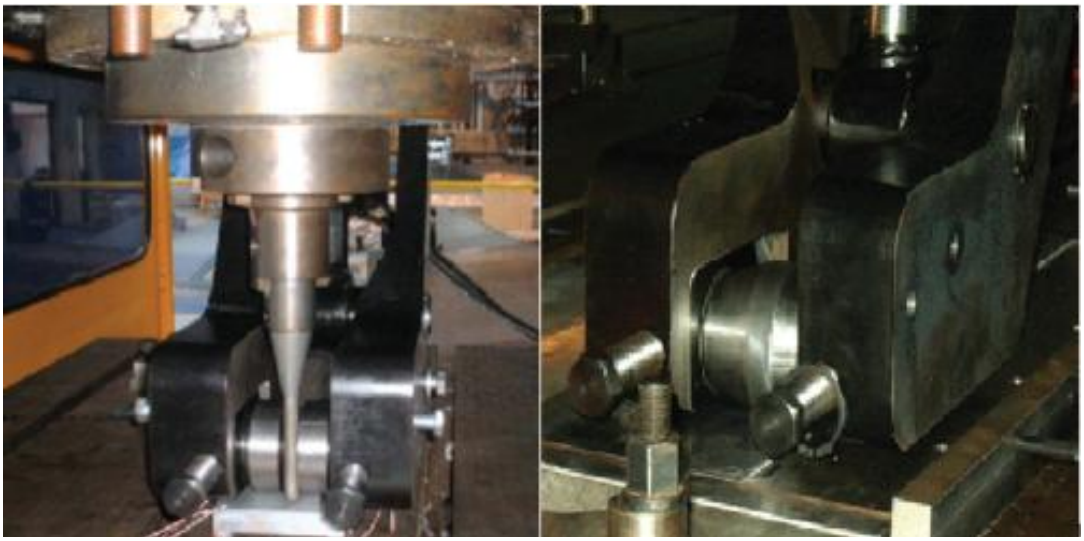

a) b)

Figure 1.22 Local Mechanical Tensioning equipment with a) ISRT and b) PWRT rollers arrangement [21]

They found that ISRT has only a small effect on the residual stresses and distortion due to the limitation in the minimum distance between the FSW tool and the rollers. Conversely PWRT was successfully applied to reduce residual stresses and to eliminate distortion. In PWRT the relationship between the applied roller tensioning load and longitudinal residual stress was found to be linear as illustrated in Figure 1.23.

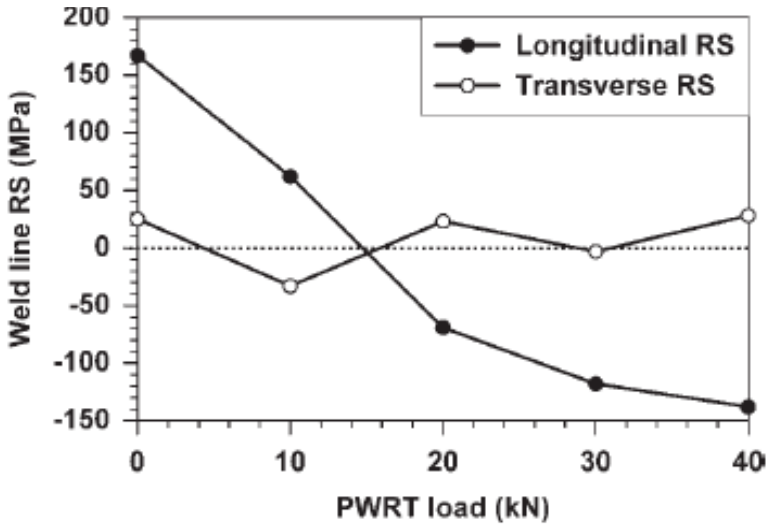

Figure 1.23 Applied roller tensioning load versus weld line residual stresses achieved in FS welds [21]

1.3.3.1.3 Thermal Mechanical Tensioning

Thermal Mechanical Tensioning is a similar SE technique to GMT: the tensile stress is applied along the entire length of the weld centreline, but the main difference is that the tensile stress is generated via thermal expansion and restricted contraction rather than a mechanical force.

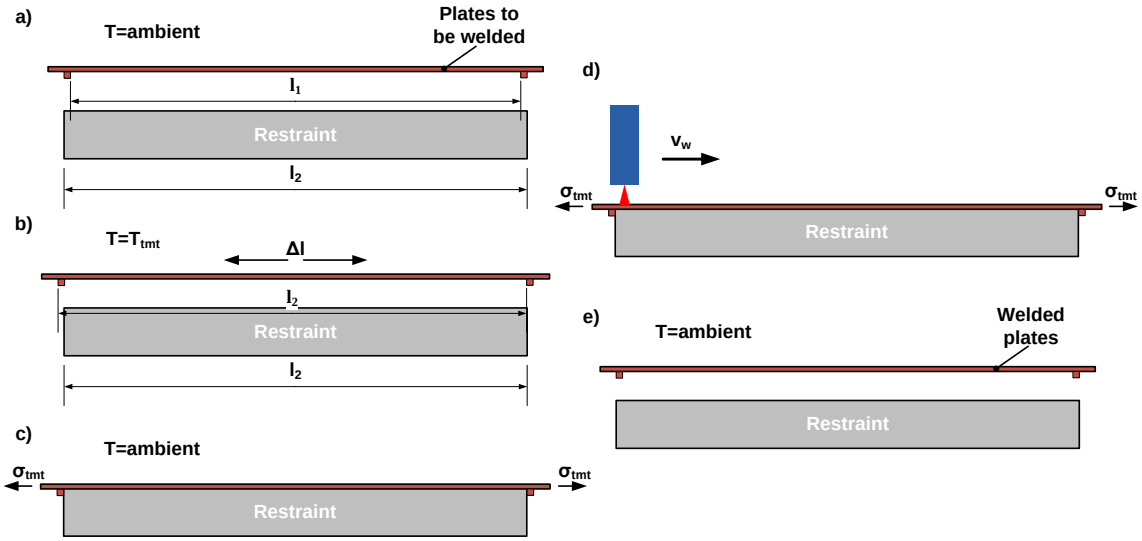

Figure 1.24 Schematic of the Thermal Mechanical Tensioning process [22]

A schematic of how this technique is carried out is shown in Figure 1.24. The plates to be welded have an initial length l_1, while the base plate that will act as a restraint has a length l_2 (see Figure 1.24,a). Prior to welding the plates to be welded are heated so they expand, Figure 1.24,b. When the adequate thermal expansion ($\Delta l=l_2-l_1$) is achieved the plates are restrained on the base plate (Figure 1.24,c). While the plate cools down to ambient temperature a σ_{tmt} tensile stress is being generated, because the thermal contraction is restricted due the length of the base plate (Figure 1.24,c). After the plates reach ambient temperature welding takes place as shown in Figure 1.24,d. After welding the plates are removed from the based plate, either by re-heating and expanding the plate or by mechanical means.

This technique was investigated in the SEALS project in detail by Colegrove et al. [22]. Their conclusion was that this technique gives inconsistent results (see Figure 1.25) and is generally difficult to implement. The sources of this

inconsistency are the difficulty of uniform and rigid clamping and uniform heating of the plates.

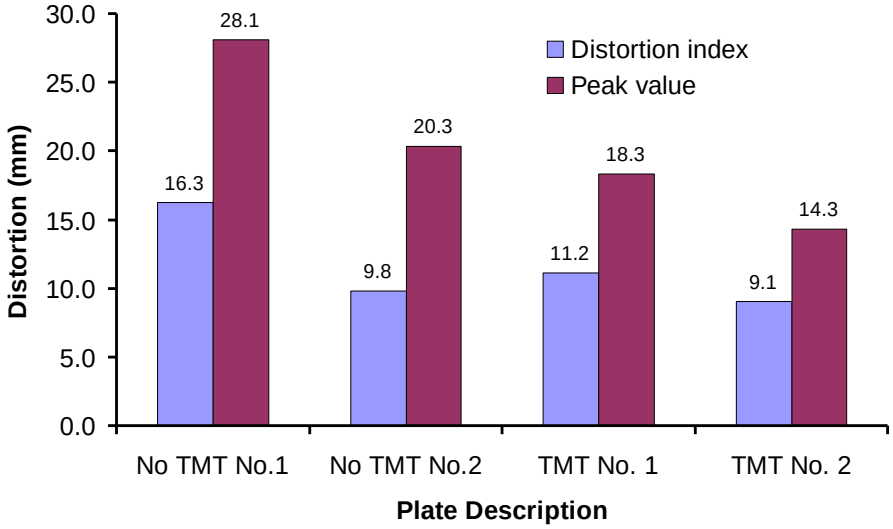

Figure 1.25 Distortion response of 1000x500x4 mm mild steel welded panels with the application of Thermal Mechanical Tensioning.

1.3.3.2 Thermal Tensioning

Thermal tensioning techniques rely on the application of hot or cold-spots (or regions) to create tensile stresses around the weld. The positions of these thermal spots are crucial in order to have the required stretching effect on the weld zone. Understanding the dynamic stress effect of these thermal spots around the weld is very important in order to position them to achieve the required thermal and therefore the resultant strain and stress patterns.

The effect of these hot and cold spots depends mainly on the position, achieved thermal gradient and size of them. In recent years FE modelling helped to understand how these thermal spots work; i.e. what the generated stress pattern and magnitude are.

The stress field generated around a hot-spot in the longitudinal direction is illustrated in Figure 1.26 [23]. It is clear in this figure that a hot spot generates longitudinal tensile stresses adjacent to it and compressive stresses in front and behind it.

Figure 1.27 illustrates the longitudinal stress patterns formed around hot and cold spots [14]. It is essential to know these patterns in order to impose the required stress on the weld.

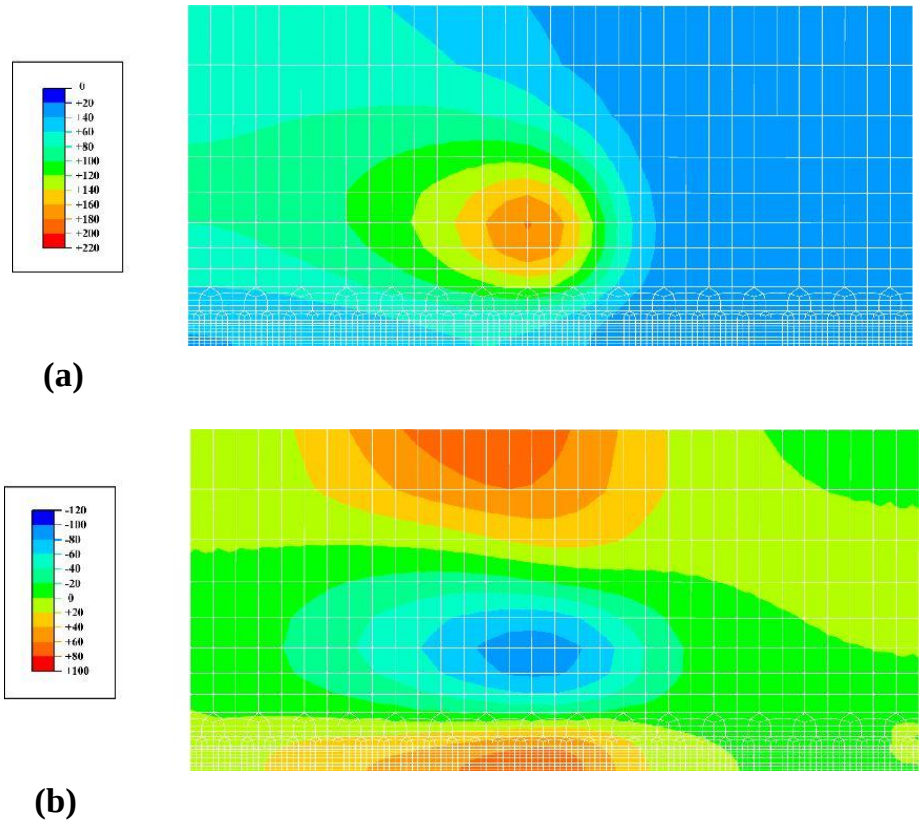

Figure 1.26 FE simulation results showing how a hot spot adjacent to the weld line (at 200°C) creates a transient thermal tensile stress of 100 MPa along the weld centreline [2]. a) Thermal profiles created by a 'hot spot', b) longitudinal stresses produced by these thermal profiles [23].

Knowing these patterns allows us to design the thermal field around the weld according to the stress field requirements of the SE technique to be used. Although positioning thermal spots very close to the weld pool can often be impractical or even impossible.

Disadvantages of the thermal tensioning processes are that the stresses generated by the cold or hot spots always depend upon their position in the thermal field of the welding process. This also means that the thermal tensioning techniques are greatly affected by the welding conditions (e.g. welding parameters, backing bar, clamping, etc.). Also the thermal spots are created by

surface heat transfer and therefore are affected by the material properties and the state of the surface.

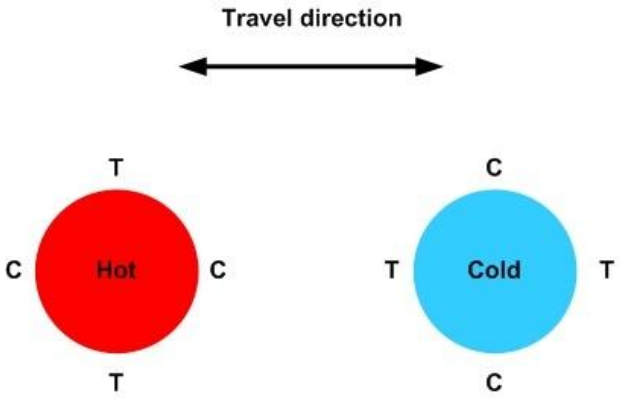

Figure 1.27 Longitudinal stress distribution around cold and hot spots

1.3.3.2.1 Thermal Tensioning by Heating

This technique applies hot spots on either side of the welds, hence the name tensioning by heating. The appropriate positions for the hot spots are shown in Figure 1.28,a and b as two alternatives.

The hot spots in Figure 1.28,a are applied ahead of the weld, creating tensile stresses in the immediate vicinity of the plastic compression zone. The tensile stresses generated on the weld centreline by the hot spots, therefore counteract the compressive stresses in the plastic compression zone as shown in Figure 1.16. As the hot spot positioned this way reduce the compressive yielding in front of the weld, TTH with leading hot spots is an RCY method.

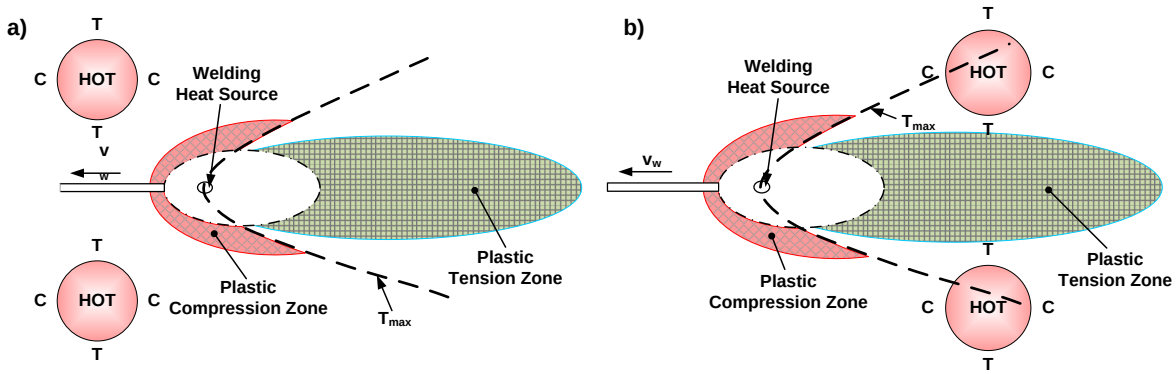

Figure 1.28 Positioning of hot spots in the plastic tension and compression zones of welding to implement TTH

Hot spots can also be positioned behind the weld pool and in this way affect the plastic tension zone. In this scenario the tensile stresses generated by the hot spot are exerted on the plastic tension zone inducing plastic yielding as detailed in Figure 1.17. Applying the hot spots this way then is a ITY SE technique.

Although rarely used in industry, significant research effort has been put into developing this technique. These efforts are further detailed in the literature survey,chapter 3.

1.3.3.2.2 Thermal Tensioning by Cooling

The TTC technique applies so called cold spots to create tensile stress along the weld line. Cold spots are usually positioned behind the weld in the plastic tension zone (ITY) as shown in Figure 1.29.

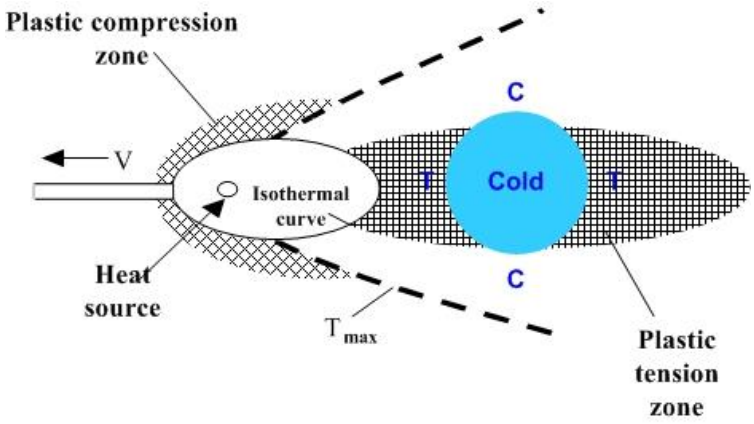

Figure 1.29 Position of cold spot in TTC technique in ITY method

When a cold spot is located behind the weld it induces tensile yielding in the plastic tension zone relieving some of the stresses as demonstrated in Figure 1.17. The advancement and development of this technique is also further detailed below in the literature survey chapter.

1.4 Research Aims and Objectives

Although significant effort has been put into researching thermal tensioning techniques they are still not fully understood and are at a relatively low maturity level. The low maturity level is shown by the fact that these techniques are not

yet implemented in production and distortion correction is still based on old rectifying techniques.

Therefore the aims of this project are the following, to:

- Characterise and understand thermal tensioning techniques (i.e. TTC and TTH)
- Investigate the applicability of these techniques on different weld geometries (butt and fillet welds)
- Increase the maturity of these techniques

2 Overview of Dynamic Thermal Tensioning Concepts

The effectiveness and applicability or even the success of thermal tensioning techniques highly depends on the cooling or heating medium selected for use. This is because the medium in question has to be stored and delivered from the storage container to the point of use with a high level of control and accuracy in order to ensure successful and repeatable tensioning effect. This distance between the storage container and point of use is in manufacturing environment such as a shipyard can often be tens of meters due to practical as well as health and safety reasons (e.g. oxy-fuel supply). Hence the selection of medium for thermal tensioning is critical for the successful application.

The aim of this chapter is to provide an overview of the practical concepts for thermal tensioning by both cooling and heating to help the selection of the adequate medium.

2.1 Concepts of Thermal Tensioning by Cooling

The cooling media in this thermal tensioning technique is very important as the cooling source has to produce a large thermal gradient behind the weld in order to generate sufficient tensioning effect. Therefore the cooling source is desired to have high cooling power or cooling capacity. In the current application the cooling mechanism is convective heat transfer, hence Newton's law of cooling can be used to estimate the cooling power (cooling flux) of the cooling media applied:

$$q = h \times A \times (T_s - T_c) \tag{2.1}$$

In Equation (2.1) h is the convective heat transfer coefficient, A is the cooled area, T_s is the surface temperature of the cooled surface and T_c is the temperature of the cooling media. It is clear from this cooling model that a high heat transfer coefficient (h) is desired as the cooled area is relatively small (as it is local cooling) and the temperature difference is often limited (by the welding process,

material properties, etc.). The different media are discussed further in order of phase at the point of use below.

2.1.1 Cooling by Gaseous Media

Using gases is a relatively simple and well known way of cooling in engineering applications. The gas used for cooling is usually stored at high pressure and delivered to the point of use through a simple delivery system (i.e. pipes, valves, flow rate or pressure measurement instruments, etc). As the cooling source for thermal tensioning needs to be a localised source with high heat transfer coefficient, the gas delivered to the point of use needs to be compressed (to ensure high flow velocity) and possibly cooled.

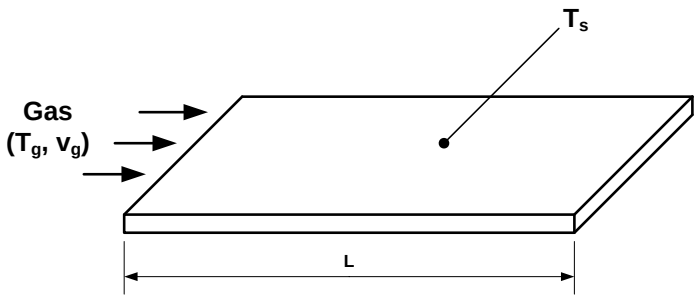

Figure 2.1 Schematics of the forced convection model used to describe gas cooling [24]

To estimate the heat transfer coefficient for gases used in TTC, a forced convective heat transfer model can be used. This model (see schematic in Figure 2.1) is described with the following equations [24]:

$$Nu_L = 0.644 \times \mathrm{Pr}^{1/3} \times \mathrm{Re}^{0.5} \tag{2.2}$$

$$Nu = \frac{h \times L}{k} \tag{2.3}$$

$$\mathrm{Re} = \frac{L \times v_g}{\nu} = \frac{L \times v_g \times \rho}{\mu} \tag{2.4}$$

$$\mathrm{Pr} = \mu \times \frac{c_p}{k} \tag{2.5}$$

where:

- Nu: Nusselt number
- Pr: Prandtl number
- R_e: Reynolds number
- h: heat transfer coefficient [W/m^2K]
- L: characteristic length of flow [m]
- k: thermal conductivity of gas [W/mK]
- v_{gas}: flow velocity of gas [m/s]
- ν: kinematic viscosity of gas [m^2/s]
- μ: dynamic viscosity [kg/ms]
- c_p: specific heat capacity at constant pressure [J/kgK]
- ρ: density [kg/m^3]

Substituting Equations (2.3)-(2.5) into Equation (2.2) we get Equation(2.6) for h.

$$h = 0.664 \times \frac{\sqrt{v_g \times \rho} \times \sqrt[3]{c_p \times k^2}}{\sqrt[6]{\mu} \times \sqrt{L^3}} \tag{2.6}$$

To increase the heat transfer coefficient in Equation (2.6) c_p, v_g and ρ can be increased or μ and L decreased. Increasing the heat transfer coefficient by increasing the velocity (v_g) of the gas is only practical at relatively low velocities as protecting the welding heat source and weld pool becomes increasingly challenging with high velocity gas flows near the weld pool. L is also limited as the cooling is expected to be local cooling.

The heat transfer coefficient can also be increased by selecting the appropriate gas with the most advantageous properties (c_p, ρ, k and μ). The biggest influence on the heat transfer coefficient in Equation (2.6) belongs to the thermal conductivity (k), while the density, specific heat and kinematic viscosity show less significance.

The most commonly available gases in welding are air, argon and CO_2. All of these gases are relatively cheap, available in large quantities and easy to store.

Air is available free of charge in nature, although a delivery system (pressurised air supply) has to be built in order to use this gas as cooling medium. As 20 % of the air is oxygen the weld pool and welding heat source have to be fully protected

from any air contamination. Air has been used as a cooling medium as it is relatively easy to apply in TTC.

Argon is also available in nature but not in pure form, hence it is more expensive than air. The advantage of argon is that it is an inert gas, widely used as a shielding gas in welding. This also means that contamination from this coolant will not have a pronounced effect on the weld quality as most of the shielding gas is argon anyway. Argon is known for its low thermal conductivity (see Table 2.1) which is a disadvantage compared to air. An advantage is that the welding gas supply (assuming that it is argon) can be used for supplying argon for the cooling which means lower capital cost of implementation.

Carbon dioxide is also widely available as a by product of burning fossil fuel (e.g. coal), hence it is cheap. It is also used as shielding gas in the welding industry, although not as widely as argon. CO_2 has even lower thermal conductivity than argon which makes it less effective in cooling. As CO_2 is not as widely used as argon in the welding industry there is high possibility that the coolant gas would contaminate the shielding gas during welding. A significant change of shielding gas (due to CO_2 contamination) composition could result in major changes in weld quality and performance.

Table 2.1 Properties of common gases available for TTC (at 1 bar, 20 °C).

Gas	ρ [kg/m^3]	c_p [J/gK]	k [mW/mK]	viscosity [kg/ms]
Air	1.161	1.163	26.2	18.6
Argon	1.633	0.52	17.9	22.9
CO_2	1.799	0.846	16.8	15
He	0.164	5.193	156.7	20
N_2	1.145	1.04	26	17.9

A major drawback of applying gases as a cooling medium for TTC is that the cooling mechanism is convection, which relies entirely on the gas flow rate, temperature difference between cooling media and cooled surface and thermal conductivity of the gas. This means the cooling power achievable by gas cooling is always relatively low regardless of which gas is selected for use.

2.1.2 Cooling by Liquids

Cooling with liquids, especially with the introduction of cryogenic liquids generally provides higher cooling power compared to gases. The increment in cooling power comes from the latent heat of vaporisation when the liquid is sprayed onto the hot surface.

Selecting the liquid to be used for TTC, one has to consider the fact that there is a heat source (arc, laser, etc.) and high surface temperatures present in the vicinity of the cooling source. These circumstances eliminate any flammable liquid due to health and safety reasons. Therefore the most viable and practical liquids to be considered are water, Liquid Argon (LAr), Liquid Nitrogen (LN) and Liquid CO_2 (LCO_2). These are all commercially available products mostly used in the pharmaceutical and food industry.

In case of liquids the cooling process can be divided into three stages: cooling via convective heat transfer (heating of liquid by substrate), cooling via phase change and cooling via jet impingement of gas. The cooling power of the first stage (convection between liquid spray and substrate) is:

$$Q_h = c_p \times \dot{m} \times (T_s - T_l) \tag{2.7}$$

where:

- c_p – specific heat of liquid [J/kgK]
- $\dot{m}$ - mass flow rate of liquid [kg/s]
- T_l – temperature of liquid spray [K]

When the liquid reaches the vaporisation temperature, the cooling becomes more effective due to the much higher value of latent heat of phase change compared to specific heat (see values in Table 2.2). This increased cooling power can be calculated as:

$$Q_{phc} = \dot{m} \times L \tag{2.8}$$

where:

- $\dot{m}$ – mass flow rate of cooling media [kg/s]

- L – latent heat of phase change [J/kg]

The last, third stage of cooling is no more liquid cooling as the phase change has already taken place and the cooling spray is now in the gas phase. This also means the cooling mechanism changed to forced convective cooling of impinging jet spray, which is described in the previous section (Equations (2.1) and (2.2)). The significant difference between c_p and L values in Table 2.2 suggests that the cooling power due to phase transformation is much higher than that of convection.

Table 2.2 Thermal properties of liquids suitable as TTC cooling source.

Liquid	Specific heat of liquid, c_p [J/kg]	Phase change temperature [°C]	Latent heat of phase change, L [kJ/kg]	Phase change at 1 atm
Water	4187	100	2270	vaporisation
LAr	1070	-185.9	160.78	vaporisation
LN	2042	-195.9	199.7	vaporisation
SCO_2		-78.5	573	sublimation

The advantage of the cryogenic liquids over water is that under ambient conditions (pressure and temperature) they all vaporise, whereas water first needs to reach its boiling point (100 °C at atmospheric pressure). In a cooling spray application this can be a significant limitation as the heating period forms a delay in utilising the latent heat of vaporisation. Also, the risk of weld contamination from water is very high, hence the application of water as a cooling source is impractical.

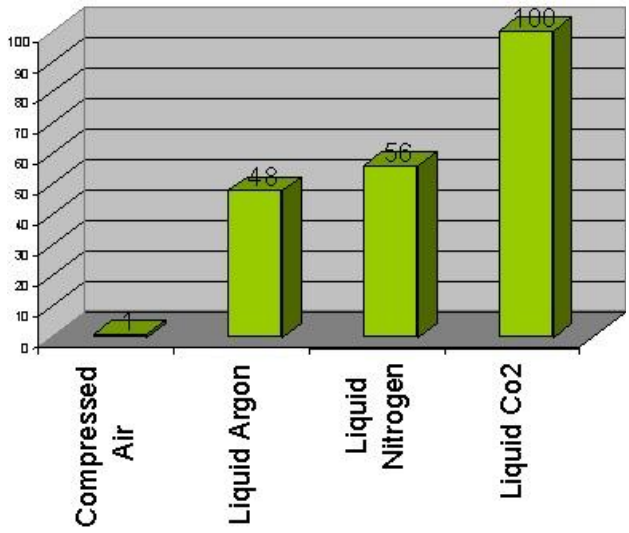

Figure 2.2 Comparison of the relative energy inputs required to take different cooling media from storage to ambient conditions (temperature and pressure) [14]

Cryogenic CO_2 stands out among the cryogens with its high latent heat of phase change, which was also realised by Price et al. [14] as Figure 2.2 shows. This increase in cooling power of the cryogenic spray is due to the phase change taking place at ambient pressure. Although cryogenic CO_2 is stored as a liquid at 18 bar pressure and -18 °C temperature, it changes into solid upon entry to the atmosphere as Figure 2.3 shows. This means that the CO_2 spray is in solid state when reaching the surface to be cooled. This solid then sublimes at -78.5 °C at the hot surface, hence the much higher latent heat.

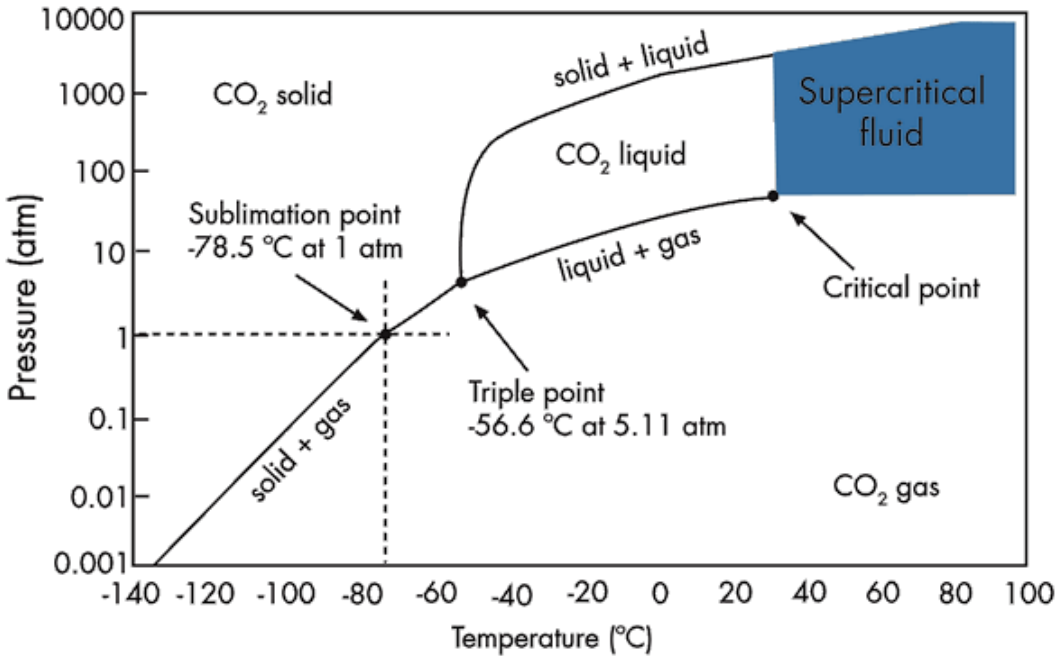

Figure 2.3 Phase diagram of CO_2 showing the sublimation point at ambient pressure [25]

The high achievable cooling power of the cryogenic CO_2 makes it the best candidate to be the cooling media of TTC. It should be pointed out though that the delivery systems of this product is optimised for the food industry, where only a low level of control is required and the operating conditions are significantly different.

2.1.3 Delivery concepts for cryogenic liquids

It is very clear from the previous section that the highest cooling power can be expected from cryogenic liquids, especially LCO_2. Hence the delivery options discussed below are mostly designed for LCO_2 cooling.

The simplest way of spraying the liquid carbon dioxide onto the surface is to use a small diameter tube. This is a cheap option but it does not provide control over the flow rates or the spot size of the cooling.

Using nozzles at the end of the delivery line gives much better control over both the flow rates and cooling spot size/shape and can even improve the solid to gas ratio of the cryogenic spray. These nozzles are detailed below.

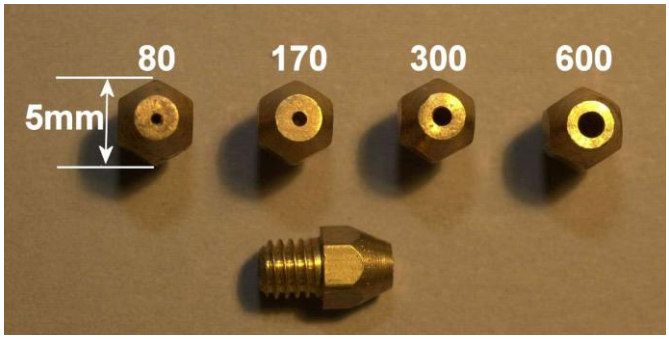

Figure 2.4 Amal jets nozzles with different orifice sizes [14]

The simplest nozzle is called an Amal jet which is a machined brass nozzle suitable to spray cryogenic liquids. These nozzles give circular sprays with different flow rates of liquid depending on the size of their orifice (see Figure 2.5). They have numbers stamped on their side to indicate the orifice size.

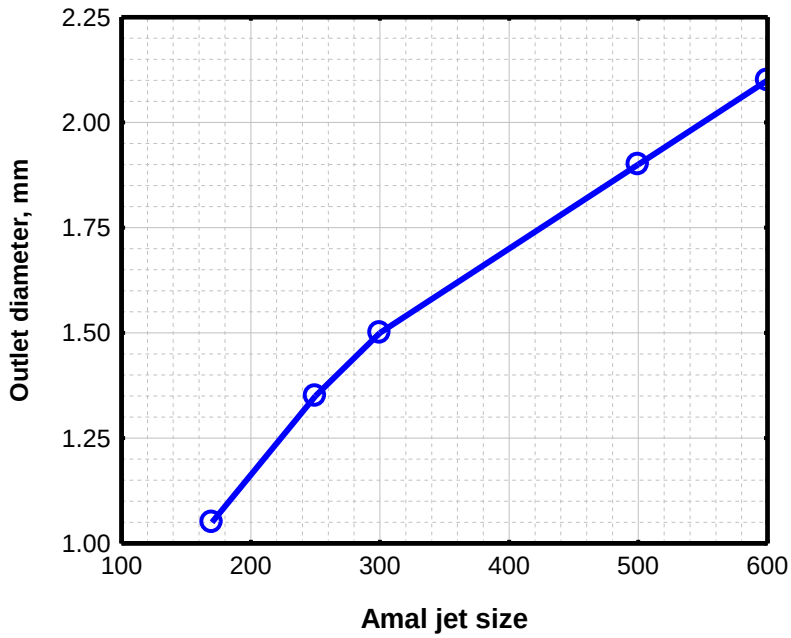

Figure 2.5 Outlet diameters of various Amal jet sizes

The CO_2 exiting the Amal jet forms a cone shaped spray of solid and gaseous carbon dioxide. This cone shape feature gives an opportunity to control the size of

the cooling spot (within a range) by varying the height of the nozzle relative to the surface to be cooled as shown in Figure 2.6.

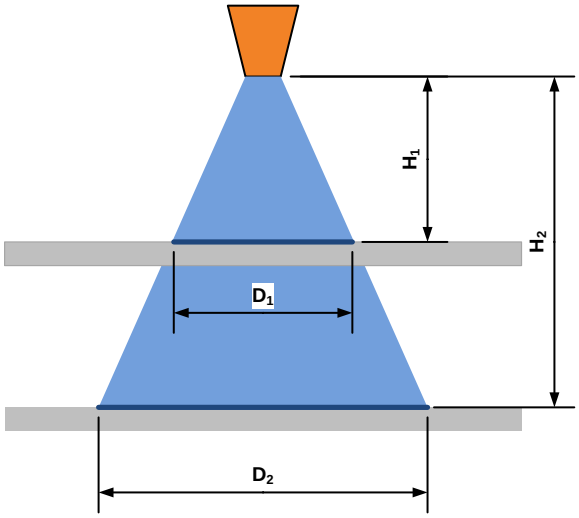

Figure 2.6 Schematic of how the cooling spot changes with the height of the nozzle from the surface to be cooled

Line nozzles operate very similarly to Amal jets by controlling the flow rate of the cryogenic sprays with the orifice size. The main difference is that line nozzles have a slot machined across the diameter of the nozzle (which forces the cryogenic spray into an oval shape instead of a circular one.

Figure 2.7 Line nozzle designs showing a) different orifice sizes and b) slit machined across the diameter [14]

Another device used for LCO_2 delivery is a snow horn shown in Figure 2.8. This device is also based on the Amal jet, but it is modified to attach a tube in order to constrict the expansion of the CO_2 liquid and have a more focused and better

controlled solid CO_2 spray. This constriction increases the solid to gas ratio of the CO_2 spray up to 40 wt% [14].

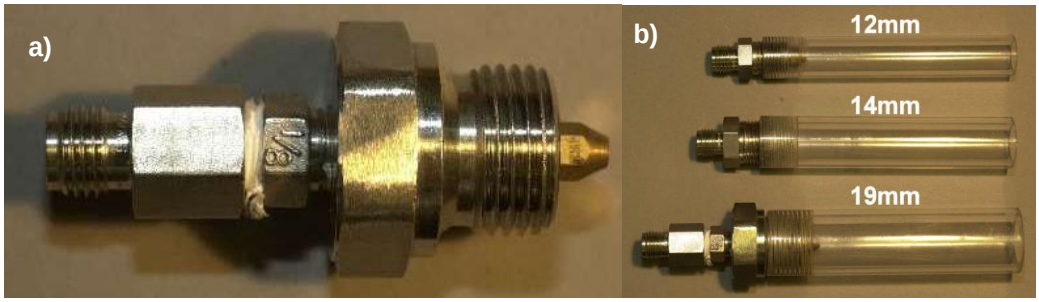

Figure 2.8 Snow horn designs showing a) the Amal jet assembly that is enclosed by a tube and b) snow horns with different size tubes [14]

All of the above delivery equipment controls the flow rate of cryogen the same way (through the orifice) and are based on the Amal jet. This means that different flow rates can only be achieved by different size nozzles at constant supply pressure. This also means that if different flow rates are required for different jobs they need to be changed to the required orifice size.

A CO_2 delivery nozzle has been developed recently [26], which takes a different approach in controlling the flow rate of a cryogen. This nozzle has an axially displaceable valve (see Figure 2.9) which enables the variation of flow rate without changing the nozzle itself. To increase the flow rate the valve is retracted along the vertical axis which increases the size of the orifice (gap between the valve and duct). The divergent duct section at the exit of the nozzle controls the shape of the jet stream of cryogen.

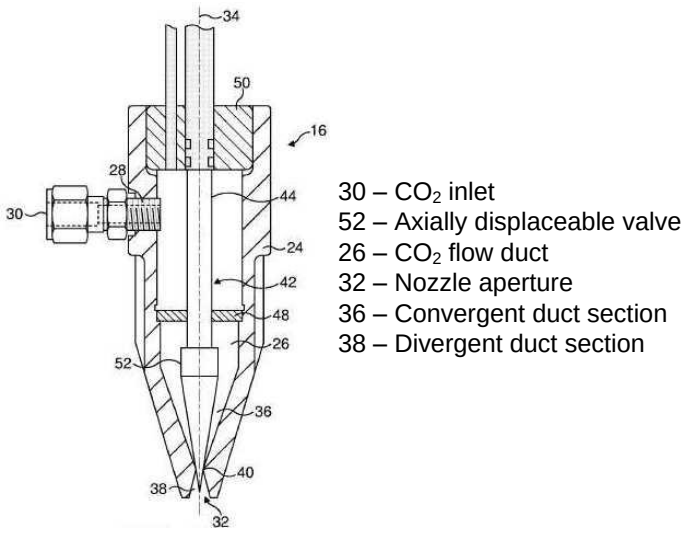

Figure 2.9 Variable flow rate cryogenic nozzle patented by Johnson [26]

This nozzle gives the opportunity to automate the flow rate control of the cooling source of TTC by simply moving the valve with e.g. a stepper motor. This also makes it possible to develop a more sophisticated system that uses temperature measurement and possibly adjust the flow rate during operation using the thermal measurement data.

2.2 Concepts of Thermal Tensioning by Heating

Some of the most common heat sources that can be applied for Thermal Tensioning by Heating are reviewed in this section.

2.2.1 Heating by oxy-fuel gases

Oxy-fuel heaters or burners are widely used equipment in several industries. They are generally used in welding (mostly for preheating large parts), cutting, thermal spraying (coating), surface heat treatments and many more applications. Straightening of large parts (e.g. ship panels) are most commonly done using flame straightening which means the gas supply for such heaters are readily available. This also means that thermal tensioning by heating using oxy-fuel heaters only needs small capital investment.

There are a number of gases (e.g. propane, methane, ethane acetylene, etc.) commercially available for heating purposes. Which one of these is the most suitable depends on a number of factors: required peak temperature and heat pattern, cost, safety, etc.

Comparing these fuel gases in terms of flame peak temperature and flame propagation rate, shown in Figure 2.10,a and b [27]it is clearly seen that acetylene exceeds the rest of the gases by far in both properties. The high flame temperature means that the achievable temperatures are higher and the high flame propagation rate means that the heat is transferred from the flame to the metal quicker. These qualities translate into localised heating with small temperature gradients in the through thickness direction. An advantage of the acetylene flame is that it is easy to control and is easily adjustable by eye due to the very visible flame cone.

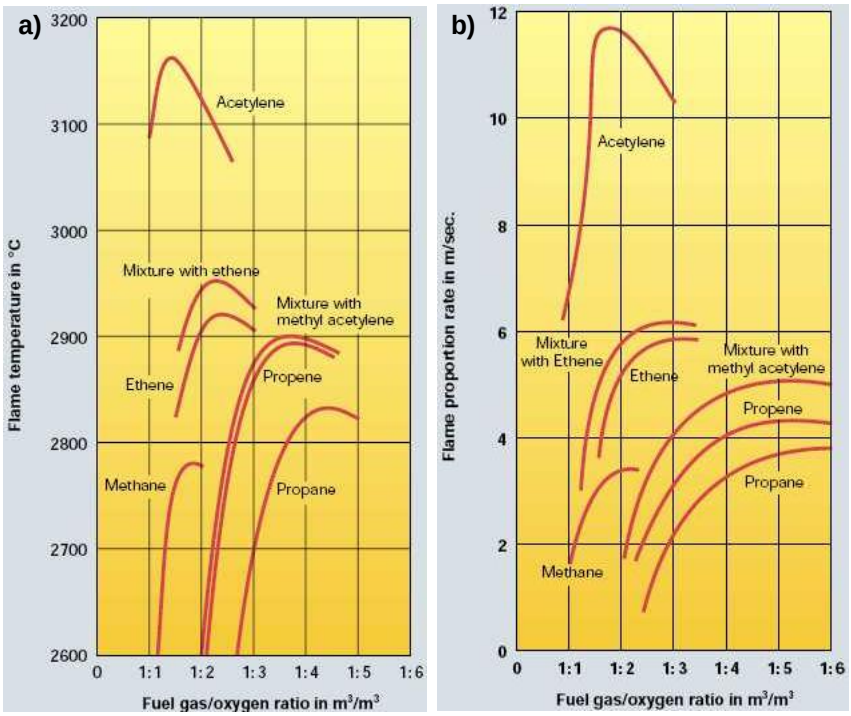

Figure 2.10 Comparison of fuel gases according to a) flame temperature and b) flame propagation rate [27]

It is possible to replace the oxygen with air for the oxy-acetylene heaters which results in lower intensity and lower velocity flame with lower flame temperature (~2300 °C) and much lower flame propagation rate (~1.5 m/s). These properties give the air-acetylene heater better flame stability with lower flame intensity that makes is ideal for relatively low temperature heating applications.

A great advantage of oxy-acetylene and air-acetylene heating is that the heating head can be in various shapes and sizes (seeFigure 2.11) and they are relatively cheap to fabricate.

Figure 2.11 Different oxy-acetylene heating and air-acetylene torches [27, 28]

A drawback of oxy-fuel heating is the relatively low accuracy and the high sensitivity of the heating process to any air movement. Heating of high thermal conductivity materials

such as aluminium alloys can be a problem due to the relatively low intensity of the flame compared to other heat sources (arc, laser, etc.).

2.2.2 Heating by induction heaters

Induction heating uses coils, based on the principle of transformers to induce Eddy currents in a workpiece that generate heat. High frequency alternating current is supplied to a copper coil, which acts as a primary of a transformer. This alternating current generates an alternating magnetic field around the coil as shown in Figure 2.12. The workpiece is placed into this magnetic field and acts as a short circuit secondary of the transformer. This magnetic field induces eddy currents in the workpiece placed inside or near the coil. The eddy currents generated within the part flow against the electrical resistivity of the metal, generating localised heat referred to as Joule heat. This heat is generated in electrically conductive materials - both magnetic and non-magnetic materials.

Additional heat is generated in magnetic materials through hysteresis – an internal friction created when magnetic parts pass through the induction coil due to the electrical resistance of the material. This heating stops being generated above the Curie point, a temperature above which the material is no longer magnetic.

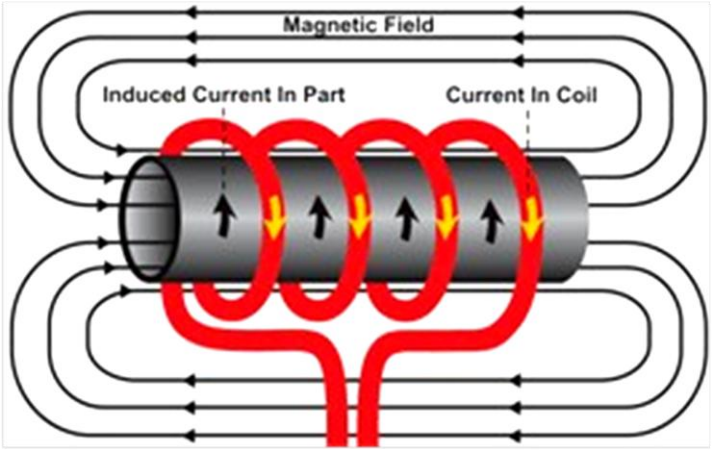

Figure 2.12 Schematic of induction heating principles

A major drawback of induction heating is the higher capital cost of the equipment relative to flame heating, although this is compensated by low consumable costs due to the high efficiency of the process. Induction heating relies largely, although not solely on magnetism, which means induction heating applied

on non-magnetic materials, such as aluminium and its alloys, non-magnetic steels, etc. is limited.

2.2.3 Heating by laser

Laser technology has developed tremendously in the past decades. Nowadays it is used in several industries such as metal fabrication (welding, cutting, peening, etc.), instruments, textile industry and health care. The development and wider application of lasers has made them cheaper and more efficient. Because of these reasons considering lasers to be the heat source of TTH is a reality.

Industrial lasers generally have very high energy density and are very directional beams which make it possible to apply laser heating remotely, without installing the laser equipment in the immediate vicinity of the welding equipment (bed, jig, welding torch, etc.). Lasers are also highly controllable and easy to manipulate (direction, shape).

The advantages of lasers mentioned above are clouded by the few disadvantages that mostly discourage industries from using them. One of these drawbacks of lasers is the difficulty/poor optical coupling of the laser beam and the surface to be heated. Coupling of laser to a surface means the transfer of energy from the laser onto the surface.

Issues with laser coupling lie in the electromagnetic nature of the laser beam. As an electromagnetic radiation, the laser beam reflects from the surface of materials that has high electrical conductivity. This can mean that only a fraction of the laser power is transferred into the workpiece. Although coupling can be greatly improved by coating the surface to be heated with a black material (i.e. graphite) that also has good thermal conductivity properties.

Other major problems of lasers are the still relatively high capital cost of equipment (power source, head and robot or manipulator) and health and safety management.

3 Literature Survey

Mitigating buckling distortion by manipulating welding residual stresses using thermal methods has been researched before by several groups. These efforts, successes and failures are detailed in this chapter, focusing on the development of cooling and heating techniques.

3.1 Technology Review of Thermal Tensioning by Cooling

The earliest recorded work on TTC was carried out by Cole [15] at NASA in 1968. He carried out extensive work on modifying the dynamic thermal field of welding to control distortion and residual stresses. He used liquid CO_2 jet manifolds with and without auxiliary heating in different shapes to manipulate the thermal field.

He investigated a V-shape manifold leading the welding as well as line and circular manifolds trailing behind the welding heat source. Some of these manifolds are shown in Figure 3.1.

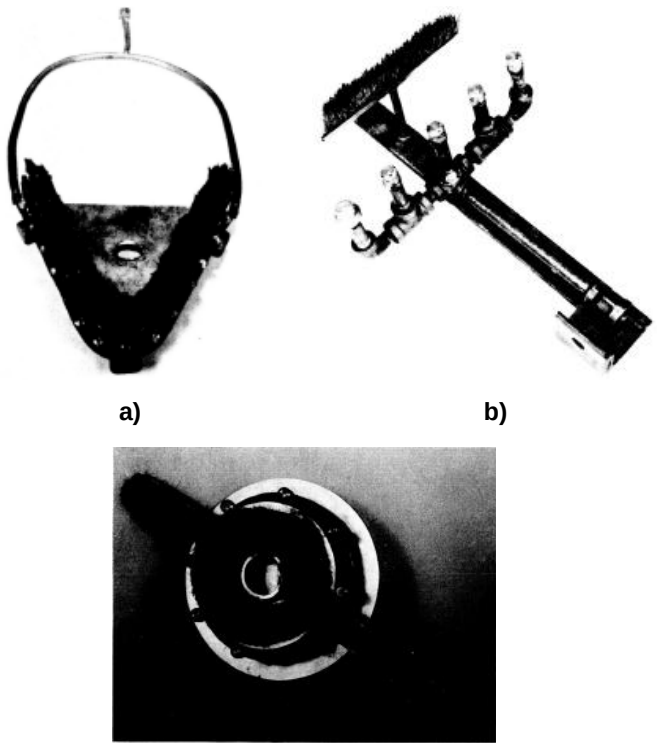

Figure 3.1 Liquid CO_2 jet manifolds used by Cole a) leading V-shape b) trailing line and c) trailing circular arrangements [15]

Cole applied cooling to GMA welds on 10 mm thick Al 2014 T651 alloys. Amongst all the jet arrangements the most significant reduction was achieved by combining the CO_2 cooling (V-shape leading manifold) with auxiliary heating. With the thermal pattern produced (see Figure 3.2) by the combination of cooling and heating they achieved an 80% peak distortion and 40% longitudinal residual stress reduction.

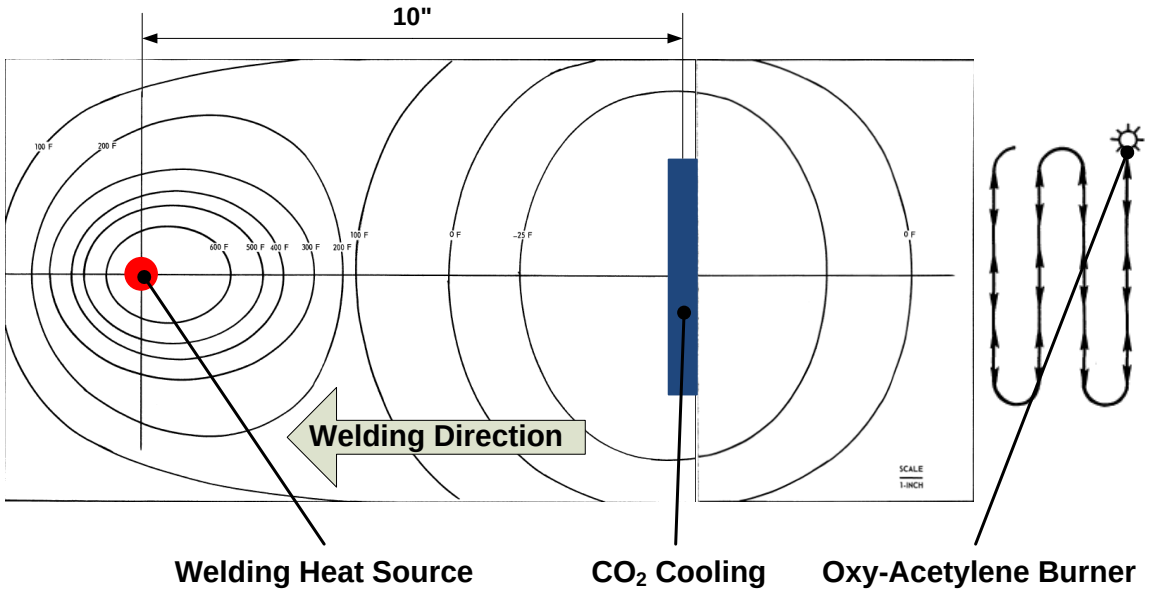

Figure 3.2 Heating and cooling sources arrangement with the measured thermal field that produced 80% reduction in distortion [15]

Cole achieved good results and proved the feasibility of modifying the thermal field of welding to reducing buckling distortion. But he failed to give an explanation of why this process was successful as his work was only an empirical study. He also faced difficulties with controlling the CO_2 flow and even with the auxiliary oxy-acetylene heater, which resulted in having to manually move the heater during his experiments.

Cole's selection of Al alloy combined with the thickness of his samples also made his work more difficult. Since Al alloys have relatively high conductivity it is difficult to achieve high temperature gradients with cooling as the heat conducts away from the weld rapidly. The thickness of the panels only improves the heat conduction making it even harder to generate thermal gradients.

Several researchers in Russia [16] have worked on reducing distortion and residual stresses by using different cooling substrates. In the 1960s research was

carried out in using water as cooling media but it was soon realised that it is difficult to protect the weld from the effect of hydrogen and also the excessively high cooling rates.

From the 1970s [16] research was focused on developing a heat absorbing paste that was deposited on the surface to act as a cooling substance. The deposition is done either before welding next to the weld or during welding behind the weld and then collected. The most advanced pastes relied on water vaporisation on the surface but were ductile enough to ease the accurate deposition and collection. These pastes were then further developed into crystalline heat absorbers to improve on the cooling rate and were used successfully.

Later in the mid 1980s liquid CO_2 jets and compressed air jets were also investigated by Russian researchers [16] and they reported the ability to effectively use it on up to 4 mm thick components.

Guan et al. [29-32] has been working on and patented a process called Dynamically Controlled Low Stress No Distortion (DC-LSND) technique to mitigate buckling distortion in thin walled aerospace structures. This process was developed as the active, in-process variant of the Low Stress No Distortion technique, also patented by Guan [33].

The DC-LSND equipment consists of a trailing heat sink that is generated by an atomized cooling jet nozzle (1) and a co-axial tube (2) to extract the vaporized coolant as shown in Figure 3.3. The welding setup also contains a backing bar and finger clamps to prevent out of plane distortion of the parent metal during welding [31].

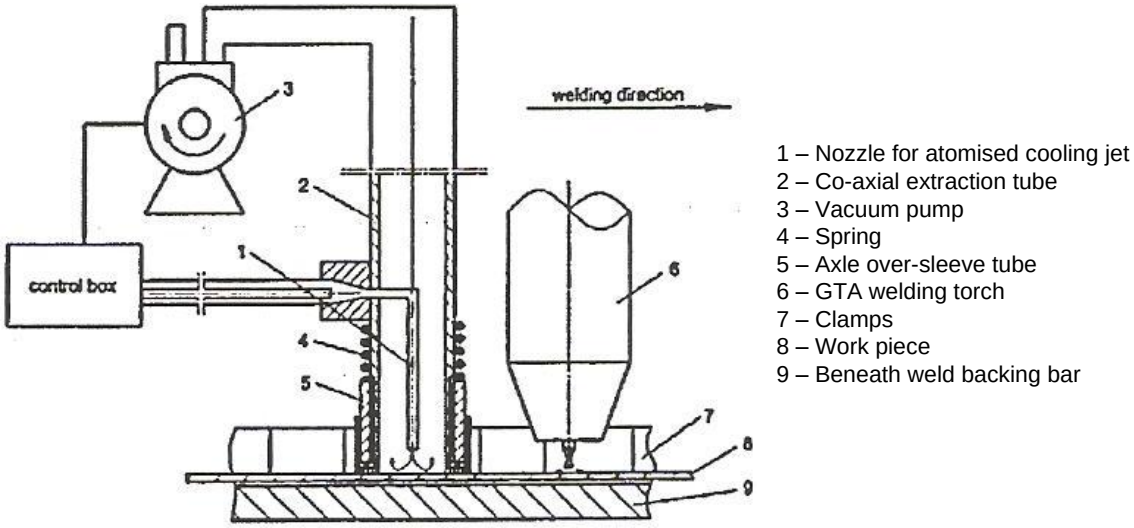

Figure 3.3 Apparatus of DC-LSND process as patented by Guan et al. [31]

The DC-LSND process was successfully applied on thin (1-2.5 mm thick) mild steel, stainless steel, aluminium alloy as well as titanium alloy weldments by Guan and Li et al. [30, 31, 34, 35]. During these experiments Guan identified two main parameters to control the magnitude of the weld centreline residual stresses: distance between the heat sink and the welding heat source and the intensity of the heat sink. Guan not only produced lower residual stresses at the weld centreline but even reversed them from tensile stresses to compressive stresses when the distance between the heat sink and the welding torch was short enough [31].

In Guan's reasoning the thermal field generated by the trailing heat sink gives a high temperature gradient zone immediately after the welding heat source as shown in Figure 3.4. This steep temperature gradient generates a tensile stress behind the weld pool, where the material is still soft. This tensile stress (strain) behind the weld compensates for the compressive plastic strain normally formed after the weld in the cooling weld metal and as a result the residual stresses are reduced.

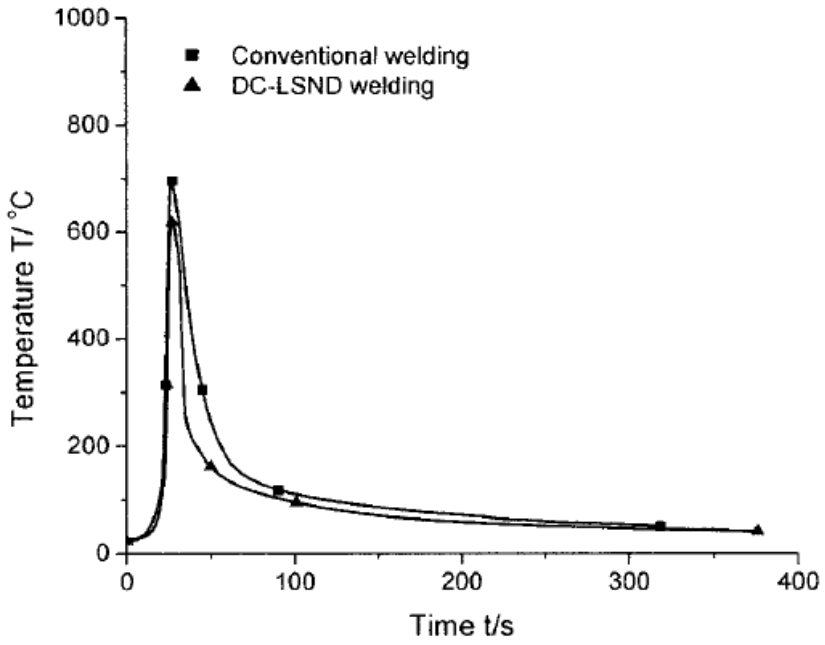

Figure 3.4 Comparison of the temperature histories of DC-LSND and conventional welding of Ti-6Al-4V [35]

Li et al. [32, 34-36] have done extensive FEA of the DC-LSND technique. In their FEA they used an impinging jet heat transfer model for the cooling source. Using this model they calculated an average *h* heat transfer coefficient and applied it as a boundary condition on the top surface of the specimen. They reported good correlation between the measured and calculated thermal histories using the impinging jet model.

Guan and his colleagues have proved the feasibility and applicability of the DC-LSND technique to reduce the welding residual stresses and buckling distortion. The advantage of the DC-LSND technique is that it is a localised process, hence applicable to curved, non-linear welds. Although they have done extensive thermal and mechanical analysis of this technique, they did not provide a detailed explanation of the process. Also their experiments were limited to 1-2 mm thick sheets, therefore they did not explore the limitation of the process in material thickness.

Yang et al. have used a trailing heat sink to mitigate hot cracking in 2.5 mm thick Al 2024 TIG welded sheets [37]. They used liquid N_2 as a cooling source in a top-side delivery system illustrated in Figure 3.7.

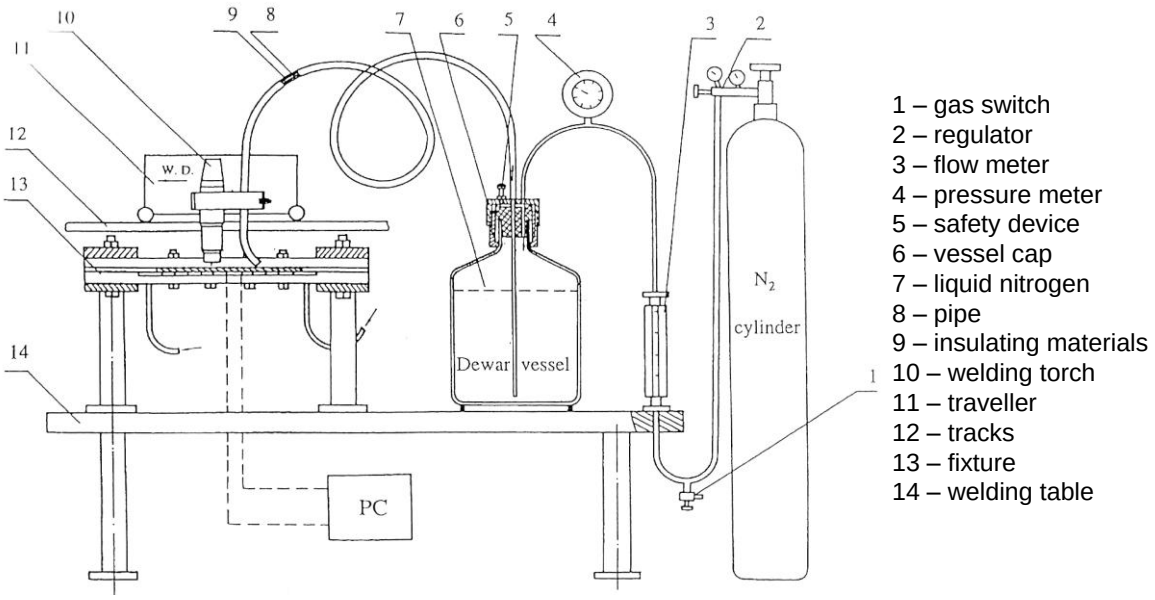

Figure 3.5 Top-side N_2 delivery system used by Yang to mitigate hot cracking [37]

Yang also recognised the importance of the distance between the welding torch and cooling source and carried out a series of trials changing this parameter (D). In their experiments they successfully eliminated hot cracking when D was 18 mm or less.

As Yang et al.'s work focused on the transverse stresses that contribute to the hot cracking phenomena they did not discuss the effect of cooling on the longitudinal residual stresses or distortion. Meanwhile their work was an important contribution as they used a different cooling medium and demonstrated the applicability of TTC to eliminate hot cracking, which is also a consequence of welding residual stresses similarly to distortion.

Luan et al. applied the DC-LSND technique patented by Guan to FSW of two different Al alloys: 6068-T2 and 5AO6 [38]. They improved on Guan's original design of cooling source and implemented a trailing impinging jet array with additional air cooling in front of the weld tool as shown in Figure 3.6.

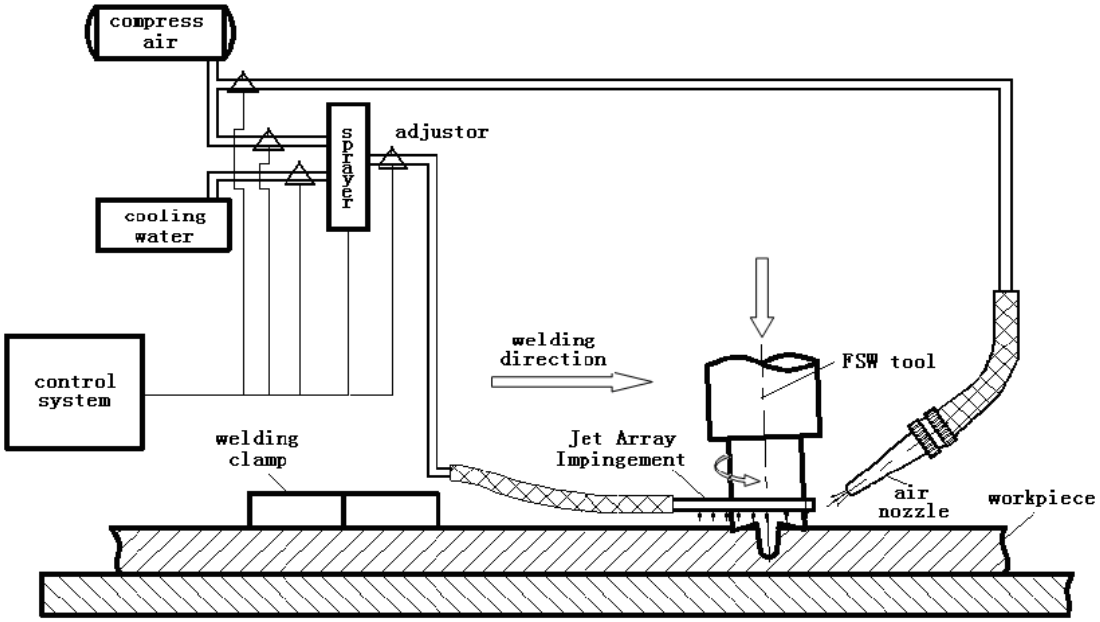

Figure 3.6 DC-LSND FSW assembly with trailing jet array and leading air cooling [38]

Using this setup they eliminated distortion in 3 mm thick FS welds and achieved 60% reduction in the magnitude of the residual stresses. They also observed a significant (about 50%) reduction in the width of the tensile region of the residual stress profile measured. The magnitude and width reduction together produces a lot less Applied Welding Load (AWL, load generated by the tensile peak of the weld residual stress profile), hence the elimination of buckling distortion.

Luan et al. showed that the DC-LSND process patented by Guan can be applied to solid state welding successfully. They eliminated buckling distortion and significantly reduced the AWL as well with the cooling device shown in Figure 3.6. Their jet impingement array used water as a cooling medium, although there is no detail about the shape and size of the array or the cooling power applied by the water jets. Also they did not study the effect of different shapes of the array or different cooling power distribution in the array.

Staron and Gabzdyl et al. [39-42] also implemented topside cooling sources for DC-LSND of autogenous laser and friction stir welds. Both cooling sources used cryogenic CO_2 as the cooling medium, but were slightly different in design due to the difference in the welding processes (see Figure 3.7).

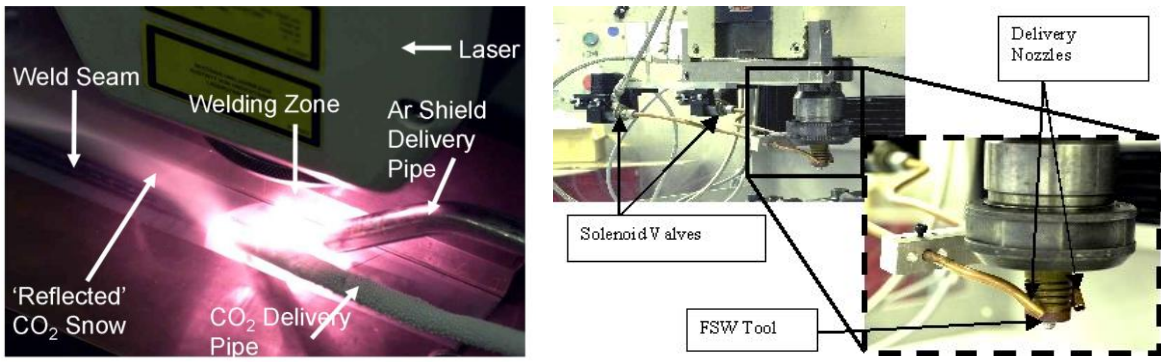

Figure 3.7 Topside CO_2 delivery devices developed for a) laser and b) Friction Stir Welding [14, 43]

In both cooling systems the CO_2 was delivered onto the top surface of the weld close to the welding heat source. The only weld pool protecting measure in these delivery systems is that the cryogenic spray is directed away from the welding heat source.

The laser welding was carried out on 1.6 mm 304 stainless steel in conduction mode. Gabzdyl [39]carried out experiments with a varying cooling source and laser beam distance and his results confirm Guan's finding that the smaller the distance the lower the distortion.

Staron [42]performed FSW on 6.35 Al2024 plates using the CO_2 delivery system shown in Figure 3.7,b spraying the weld surface 15 mm from the welding tool. The measured residual stress distribution of the FSW with cooling shows a large compressive peak at the centreline of the weld where the cryogenic spray was directed (see Figure 3.8,b).

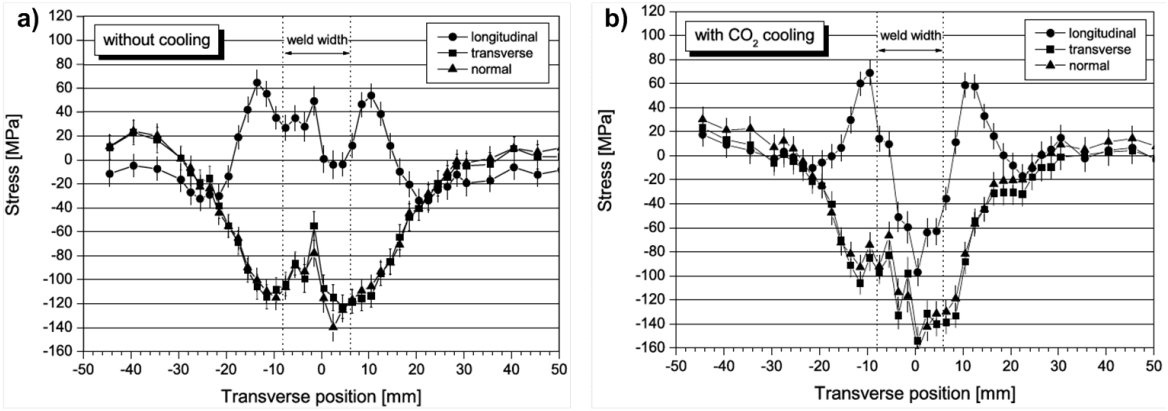

Figure 3.8 Comparison of longitudinal residual stress distribution of 6.35 mm thick Al2024 FS welds a) without and b) with cryogenic cooling

Gabzdyl and Staron et al. [39, 42] have shown the application of the TTC technique on two welding processes: laser conductivon and FS welds. None of these welding processes were used in conjunction with TTC before. Gabzdyl was the first to apply TTC on 6 mm thick sheets (FSW). Although the CO_2 delivery systems Gabzdyl used were primitive: there is no control over the flow rate of the liquid CO_2 and there is no enclosure or entrapment of the CO_2. Despite the crude delivery system the successful application of TTC on two new, modern welding processes and thicker material shows great promise for TTC with liquid CO_2.

Bertaso et al. [44] also used liquid CO_2 as a cooling source on 1.5-2.5 mm thick stainless steel and 2.3 mm IN718 TIG welds successfully. Bertaso applied the cooling at the bottom of the plate behind the weld pool. They faced a lot of issues initially with the cryogenic spray interrupting the weld when positioned too close to the weld pool. This problem was solved by directing the spray away from the weld pool with an angled delivery nozzle shown in Figure 3.9.

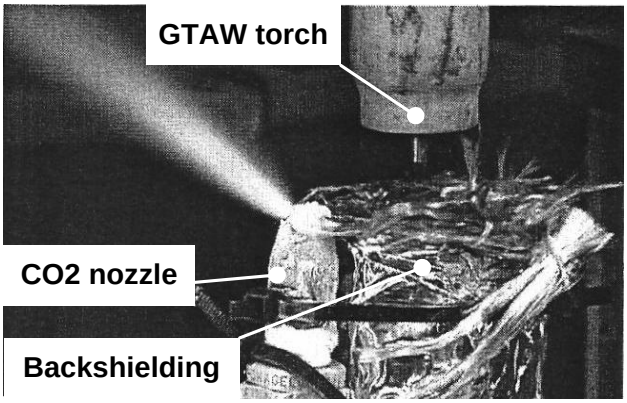

Figure 3.9 Cooling nozzle and back shielding device for bottom side cooling by Bertaso et al. [44]

Application of the cooling at the bottom caused problems with the back shielding being blown away by the high velocity cryogenic spray. A special back shielding device was designed (see Figure 3.9) to overcome this shielding issue. The final setup was then successfully used on both stainless steel and Inconel welds.

They tried to control the flow rate of the cryogenic CO_2 spray by a manual valve in the delivery line but realized it had very little affect on the spray at the end of the nozzle. It was pointed out that the orifice of the nozzle was the major parameter controlling the cryogenic spray. When using the same cooling parameters on

thinner sheets it was concluded that on thinner material a smaller cooling spray-welding heat source distance is necessary.

This is based on the assumption that the welding speed is increased on thinner sheets hence the thermal field is significantly smaller. Although Bertaso did not prove this in his work, this dilemma indicates how much the cooling source effectiveness depends upon the thermal field generated by the welding heat source.

Bertaso et al. again demonstrated the feasibility of using liquid CO_2 as cooling medium, although their equipment is too complicated: the backside of the weld needs to be accessible, which is often difficult or even impossible in production. Also the back shielding has to be improved significantly to produce good quality welds.

Van der Aa also applied CO_2 cooling successfully for the DC-LSND technique to eliminate buckling distortion of GTA welded thin (2 mm) sheets [45]. In her work she had three different approaches to the cooling source: roll-cooling, gas or water jet and CO_2 snow.

The roll-cooling concept comprises of a steel roll that is cooled internally with solid CO_2. The contact between the weld and the roll is improved by spring load as shown in Figure 3.10.

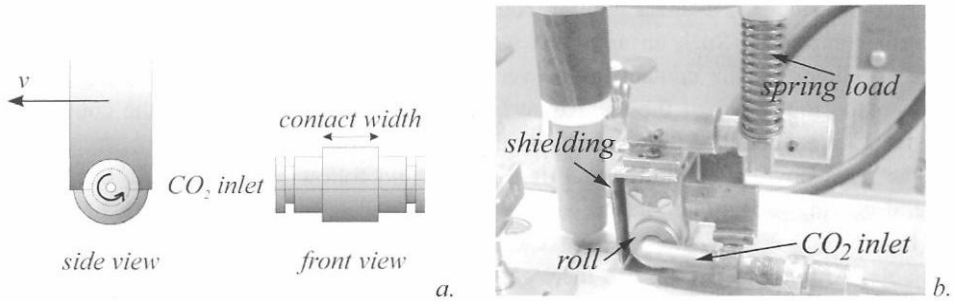

Figure 3.10 Roll cooling concept by Van der Aa a) schematic of the roll b) experimental setup[45]

The advantage of this concept is that the width of the cooled surface is well defined by the rollers and there is no interruption of the welding process. In spite of these advantages this cooling source does not have sufficient cooling power to reduce buckling distortion.

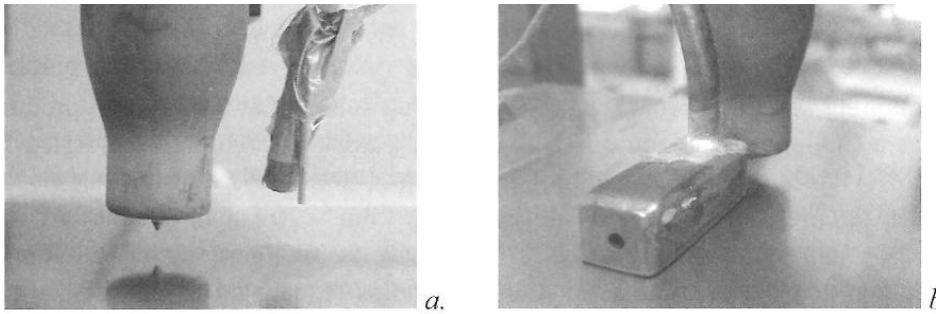

Figure 3.11 Gas and water jet cooling sources a) without and b) with shielding box [45]

Van der Aa's second approach was to use jets (ie: compressed air, water, helium) as the cooling source. Simple devices were built to implement these cooling sources as shown in Figure 3.11. Although these jets provided enough cooling to reduce buckling distortion, none of them were sufficient to completely eliminate it as Figure 3.12 illustrates.

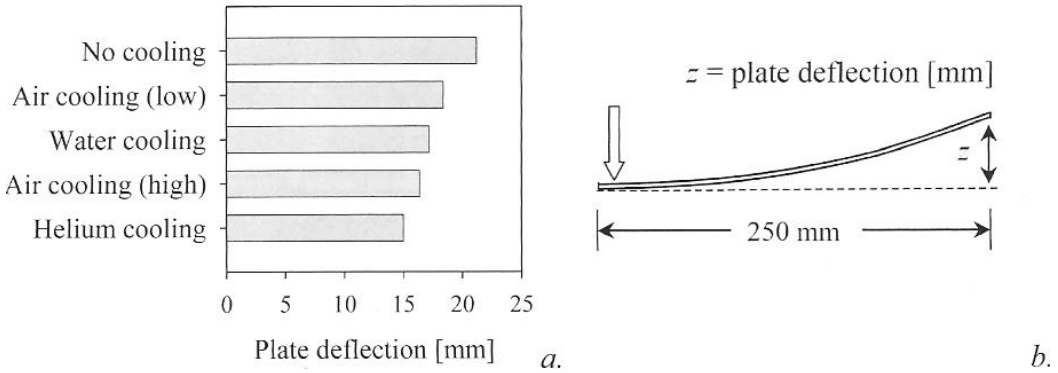

Figure 3.12 Measured buckling distortion for different jet cooling sources [45]

The final and successful cooling source applied by van der Aa was a liquid CO_2 snow jet. In this case the liquid CO_2 was delivered through a pipe with 0.8 mm diameter hole at the end. Van der Aa pointed out that the amount of CO_2 snow generated highly depended on the design of the nozzle. She recognised the importance of adequate shielding and implemented one in her final DC-LSND setup as shown in Figure 3.13. This cooling source is then used to eliminate buckling distortion in 1.5 and 2 mm steel and stainless steel plates.

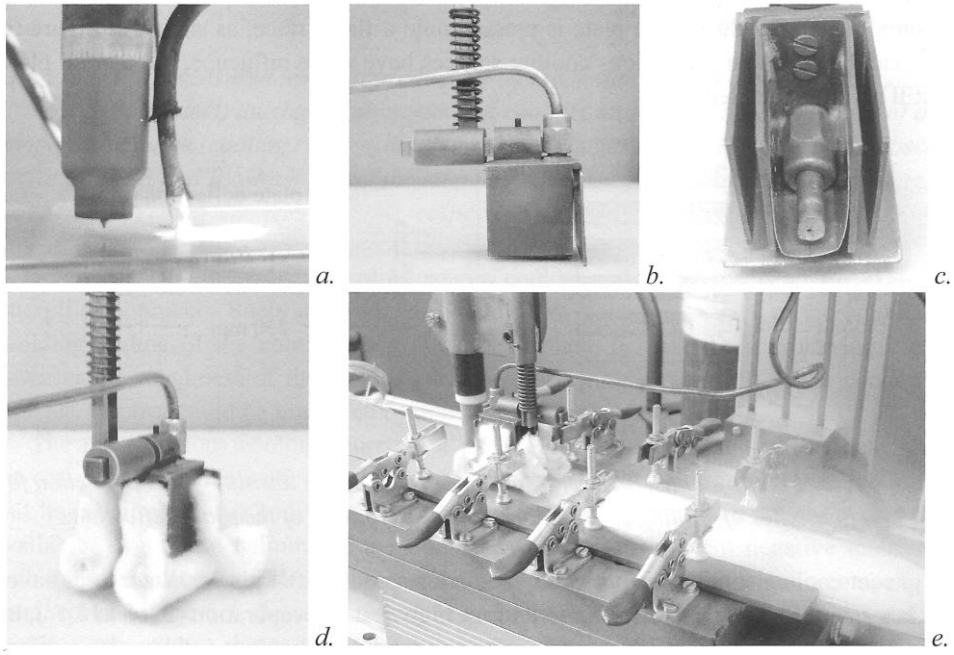

Figure 3.13 Cryogenic CO_2 cooling as implemented by Van der Aa a) delivery nozzle without shielding b) and c) delivery nozzle in a copper shielding box d) shielding box stuffed with glass wool and e) experimental setup with cooling source during DC-LSND welding [45]

Van der Aa showed that the most practical cooling source for DC-LSD welding is liquid CO_2. She developed a primitive delivery device with shielding and used it successfully to eliminate buckling distortion. The drawback of her setup was the lack of flow rate control of CO_2 and provision to extract or at least collect the CO_2 spray. Also the glass wool stuffing is an easy way of protect the arc from the CO_2 spray but it needs changing often and there is a high chance of misalignment of cooling and welding source as van der Aa reported herself [45].

Price, Williams and Morgan et al. [14, 46, 47]did extensive work on Thermal Tensioning by Cooling using different cooling media, delivery arrangements and welding processes since 1997. Their first successful experimental setup uses liquid CO_2 delivered at the underside of the GTAW welded stainless steel plate as shown in Figure 3.14 [14]. In this equipment assembly the CO_2 is sprayed onto a thin copper sheet rather than directly spraying it onto the weld surface. The liquid CO_2 was delivered through a ¼" tube fitted with an Amal jet to restrict the CO_2 flow.

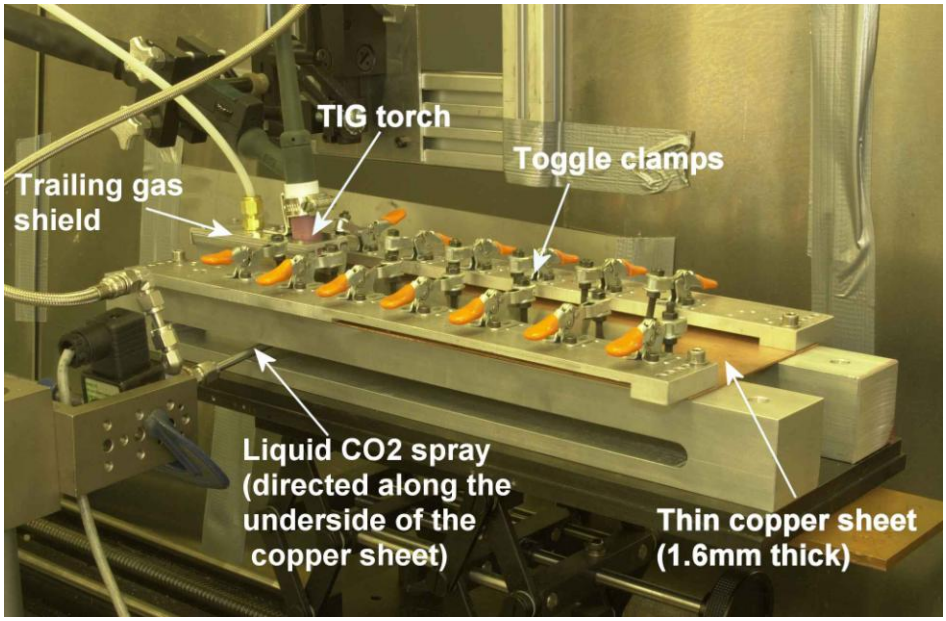

Figure 3.14 Experimental setup of TTC on GTAW with bottom side CO_2 delivery by Price [14]

Although 50% reduction in distortion was achieved with this setup, buckling was not completely eliminated. The copper sheet at the underside of the weld gave good protection against the cooling spray and made it possible to move the cooling spray close to the weld pool. However the same copper sheet de-concentrates the cooling effect of the cryogenic spray, hence the high intensity and high cooling power characteristics of the liquid CO_2 spray are reduced. As with all other underside cooling delivery solutions this setup also needs access to the bottom of the weld which makes it difficult to implement in production.

Although Price et al.'s underside delivery had its limitation, they demonstrated the TTC technique on 5 mm thick DH36 panels with a similar setup shown in Figure 3.15 [14]. This is the first successful application of TTC (or DC-LSND) on a thicker than 2-2.5 mm metal.

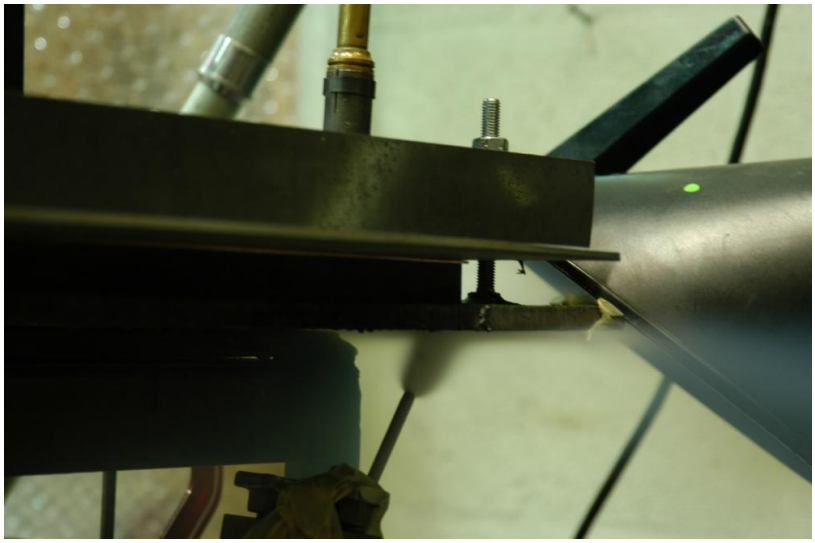

Figure 3.15 Experimental setup of GMAW of 5 mm thick DH36 panels showing the underside CO_2 delivery through a ¼" tube in operation

The bottom side delivery was later changed to top-side delivery and used successfully in conjunction with GTAW, laser and FSW [14]. The FSW and laser welding setups are detailed in Gabzdyl's work in Figure 3.7.The schematics of the GTAW setup with topside CO2 delivery is shown in Figure 3.16.

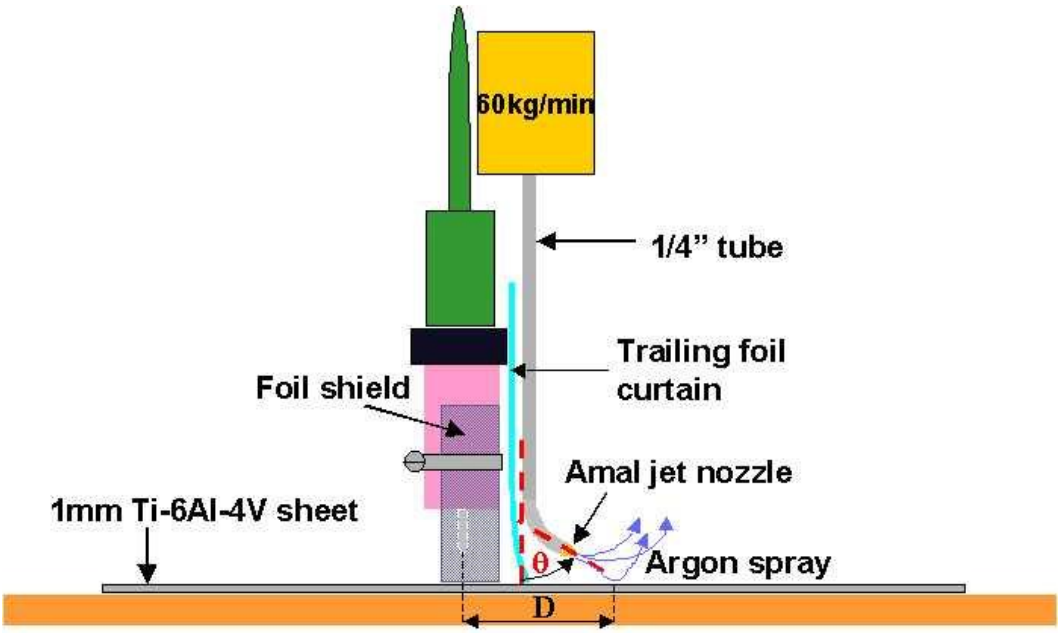

Figure 3.16 Schematics of topside CO_2 delivery system with gas Tungsten Arc Welding (GTAW) by Price et al. [14]

This setup unfortunately did not produce less distorted welds even though several parameters of this cooling arrangement were investigated (i.e. pipe angle, D, coolant mass flow). There were a lot of issues with the protection of the welding arc and proper shielding of the weld pool using this setup. While in laser welding and

FSW shielding is less problematic due to the low sensitivity of the heat sources to shielding gas, GTAW is highly sensitive to any excessive gas flow around the weld pool and even small contamination of the shielding gas.

Great effort was put into examining different cooling media and delivery options of these media (primarily liquid CO_2) [14]. The first step of this study was the comparison of different possible cooling media. Preice et al. compared compressed air, liquid argon, liquid nitrogen and liquid CO_2 as shown in Figure 3.17 [14].

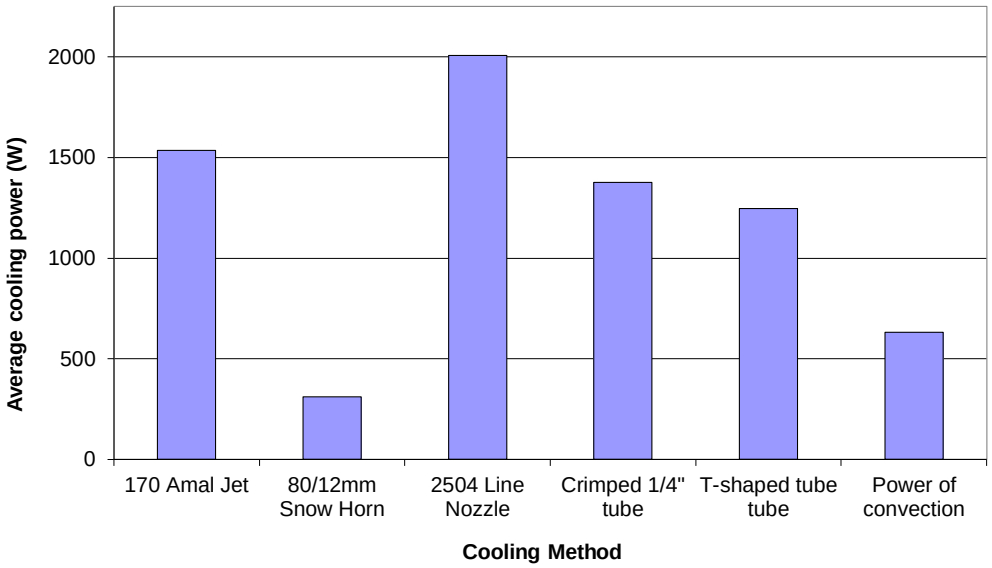

Figure 3.17 Comparison of the relative energy inputs required to take different cooling media from their storage pressure/temperature to ambient conditions

Their conclusion based on Figure 3.17 is that liquid CO_2 is the most practical cooling media for TTC. Based on this conclusion a detailed study was carried out to investigate and optimise the liquid CO_2 delivery for TTC. In this study ¼" tube, Amal jets, line nozzles and snow horns were compared. The conclusion of these trials is that the cooling power of a particular delivery system primarily depends on the mass flow rate and therefore the orifice size of the nozzle. The highest cooling powers are produced with Amal jets and line nozzles, although these delivery options produced unacceptable welds due to the high velocity of the spray.

The surprisingly low cooling power of the snow horns (illustrated in Figure 2.8) relative to the other nozzles in Figure 3.17 lies in the fact that the solid CO_2 reaches the hot surface at low speeds and easily builds up on the surface. This snow build-up then floats on the surface due to a layer of CO_2 vapour. This vapour acts as a

barrier stopping solid CO_2 spray reaching the hot surface. Hence the large latent heat of sublimation of solid CO_2 cannot be utilised resulting in a large drop in cooling power.

To overcome the interruption of the welding arc by the violent CO_2 spray (setup shown in Figure 3.16) a co-linear extraction nozzle was patented by Morgan et al. [47]. The schematic of this nozzle is shown in Figure 3.18. The main features of this nozzle is the double action co-axial extraction of the CO_2 spray, which protects the welding arc and weld pool from any interruption and contamination.

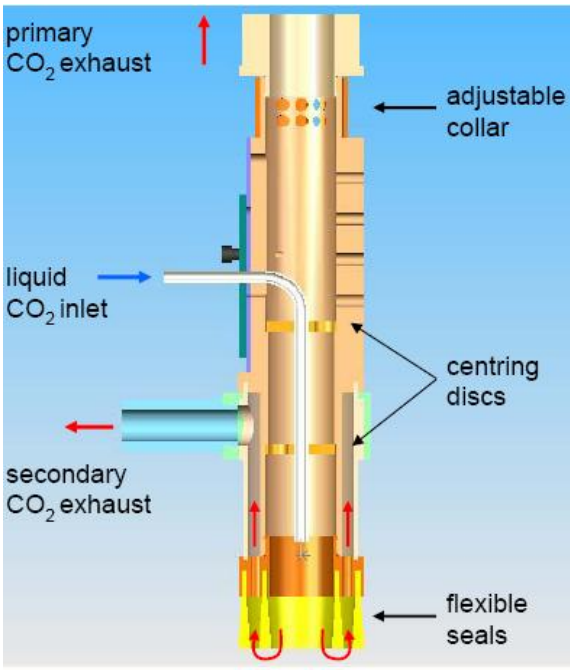

Figure 3.18 Schematics of the cryogenic nozzle patented by Morgan et al. [47]

This nozzle was then successfully applied on GMAW of 4 mm thick DH36 panels in a shipyard production environment, although the nozzle was modified to accommodate smaller D nozzle-welding torch separation [46]. The results of these shipyard trials (see Figure 3.19) clearly show that TTC using topside cooling via this cryogenic nozzle is not just feasible but relatively easily retrofittable in harsh production environments.

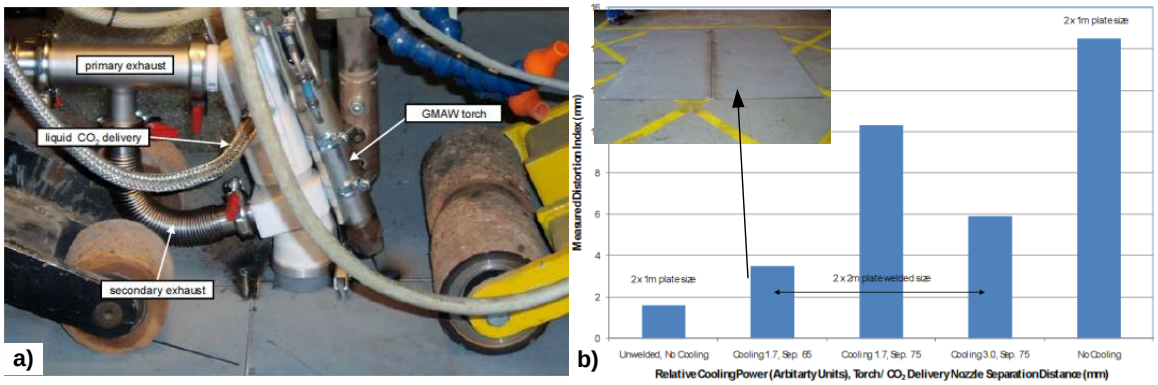

Figure 3.19 Measured distortion of DH36 panels GMA welded with TTC via the cryogenic nozzle patented by BAE [46]

3.2 Numerical Modelling of Thermal Tensioning by Cooling

The main goal of numerical modelling in welding and welding related processes is to help understanding the phenomena in question. The TTC technique is no exception: although many groups have implemented this technique successfully to eliminate buckling distortion, the experimental results alone gave little understanding of the process.

Li et al. have done numerical modelling of the DC-LSND technique patented by Guan [31, 34-36]. They used the FE method to carry out thermo-mechanical analyses of the application of TTC with GTA welding of Ti-6Al-4V 2.5 mm thick sheets. In Li et al.'s 3D numerical model the welding arc is modelled as a surface heat source with a Gaussian energy density distribution. The cooling source is modelled as forced convective heat transfer boundary condition represented by Equation (3.1).

$$q = h \times (T - T_0) \tag{3.1}$$

They used an average value for the h convective heat transfer coefficient calculated from:

$$\bar{h} = \lambda \times \frac{\overline{Nu}}{D} \tag{3.2}$$

where:

- λ is the thermal conductivity of the atomized water
- D is the diameter of the cooling nozzle
- Nu is the average Nusselt number calculated based on the impinging jet heat transfer model

Although this predicted thermal field (see Figure 3.20) seems correct, no comparisons to experimental measurements were made to find out the accuracy of the model.

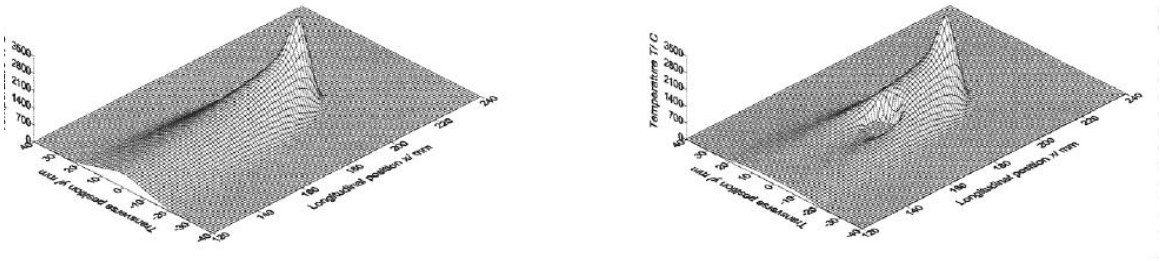

Figure 3.20 3D temperature fields of conventional (left) and DC-LSND (right) GTAW as predicted by Li et al.'s FE model [36]

Van der Aa introduced a new concept for the numerical modelling of DC-LSND [45, 48, 49]. She used a 3D thermal model for temperature predictions and a five bar model to predict residual stresses and strains. She identified five characteristic areas in the thermal field of DC-LSND welding (Figure 3.21,a) and assigned a discrete bar to each of them. The temperature history of the characteristic area were then applied to these bars as temperature loads (Figure 3.21,c) These bars were rigidly connected at both ends (see Figure 3.21,b), therefore as they went through different thermal cycles different stresses would be induced in them.

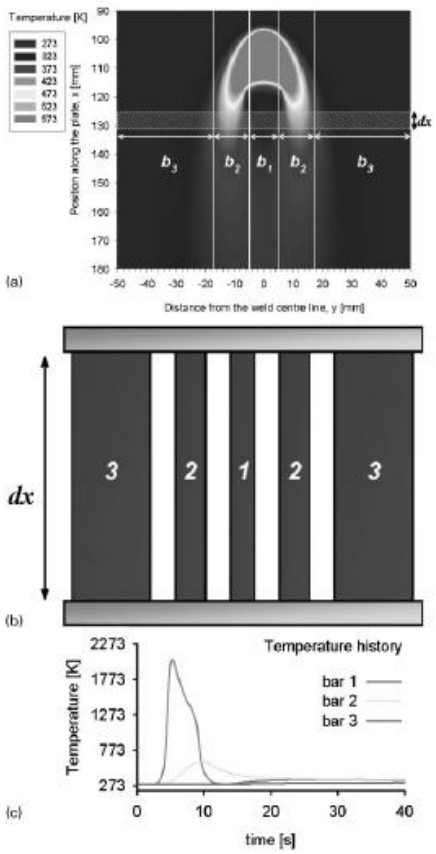

Figure 3.21 Van der Aa's five bar conceptual model: a) temperature distribution from 3D F model b) bar model and c) temperature loads applied to the bars

This five bar concept was then further developed to an *n* bar concept, in which the number of bars was the number of nodes in the transverse cross section of the 3D FE thermal model. Van der Aa achieved good agreement with experimental measurements of the welding residual stresses using this *n* bar model as shown in Figure 3.22.

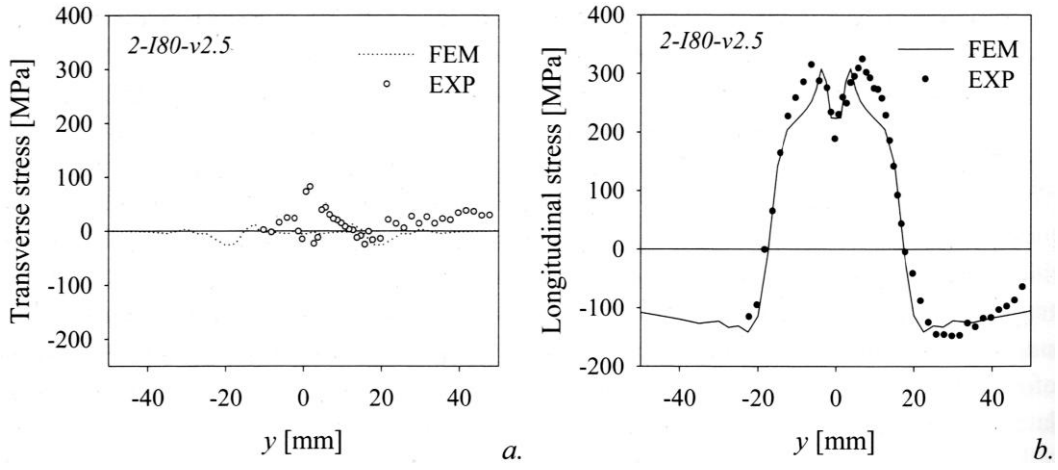

Figure 3.22 Comparison of FEM predictions and experimental measurements of a) transverse and b) longitudinal residual stresses by Van der Aa using the *n* bar model [45]

Van der Aa used a similar thermal model to Li et al., but extended the welding heat source into 3D using Goldak's double ellipsoid heat source model. The cooling source was modelled as a cooling flux defined byEquation (3.1). The area of the cooling source was an elliptically shaped surface and within this surface the heat transfer coefficient had a Gaussian distribution. The temperature of the cooling medium also varied in the cooling source model as Figure 3.23 shows.

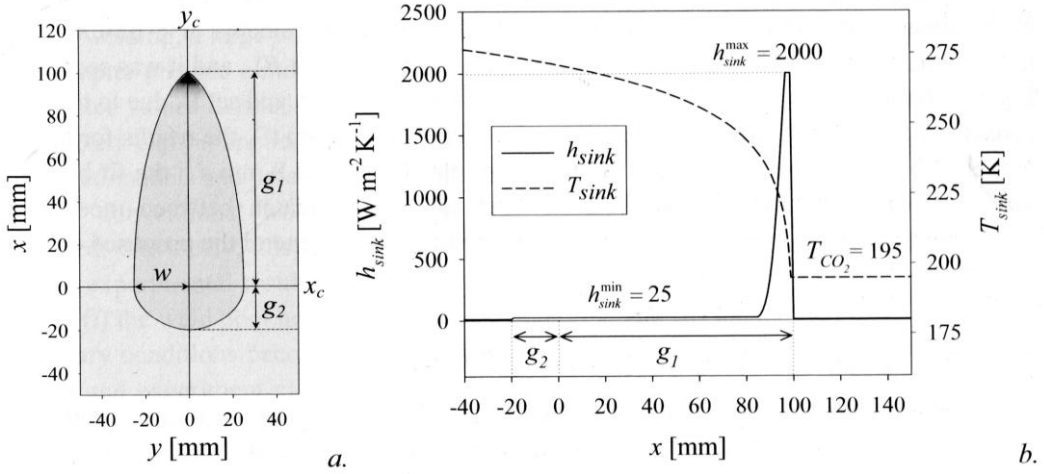

Figure 3.23 Van der Aa's cooling source model a) countour plot and b) heat transfer coefficient and cooling source temperature distribution [45]

Although the temperature measurements were highly variable due to the primitive design of the CO_2 delivery system, van der Aa achieved good temperature predictions with her 3D thermal model as shown in Figure 3.24

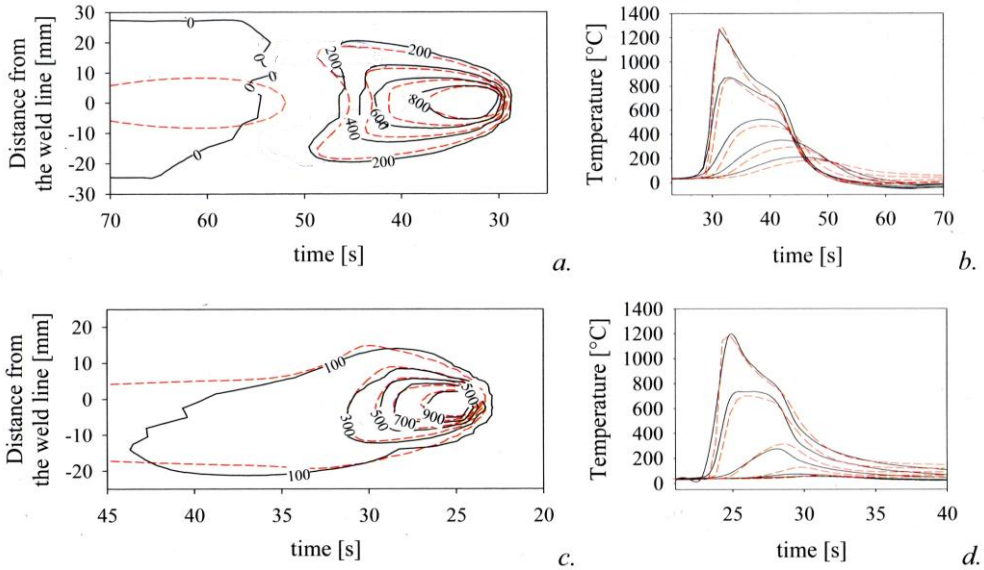

Figure 3.24 Comparison of measured and predicted thermal field of DC-LSND welding (experiments solid, FE model dashed line) by van der Aa at (a,b) 3mm/s^{-1} and (c,d) 8mm/s^{-1} travel speeds [45]

Camilleri et al. [50]performed a numerical investigation of DC-LSND welding using cryogenic CO_2 as the cooling medium. They investigated both butt (2 mm thick plates) and fillet (5 mm thick plates) welds. They implemented three models: thermo-elasto-plastic, hybrid and a computationally efficient model for both the butt and fillet weld geometries. In these models the cooling was represented as a heat loss (1.2 kW) 60 mm behind the welding arc. The cooling source has a normal radial distribution with a radius of 45 mm.

In case of butt welds the thermo-elasto-plastic model predicted 62 % reduction in distortion, which diminishes to 28 % for both hybrid and computationally efficient models. In case of fillet welds the cryogenic cooling did not show any effect on the distortion neither on the residual stresses for any of the models.

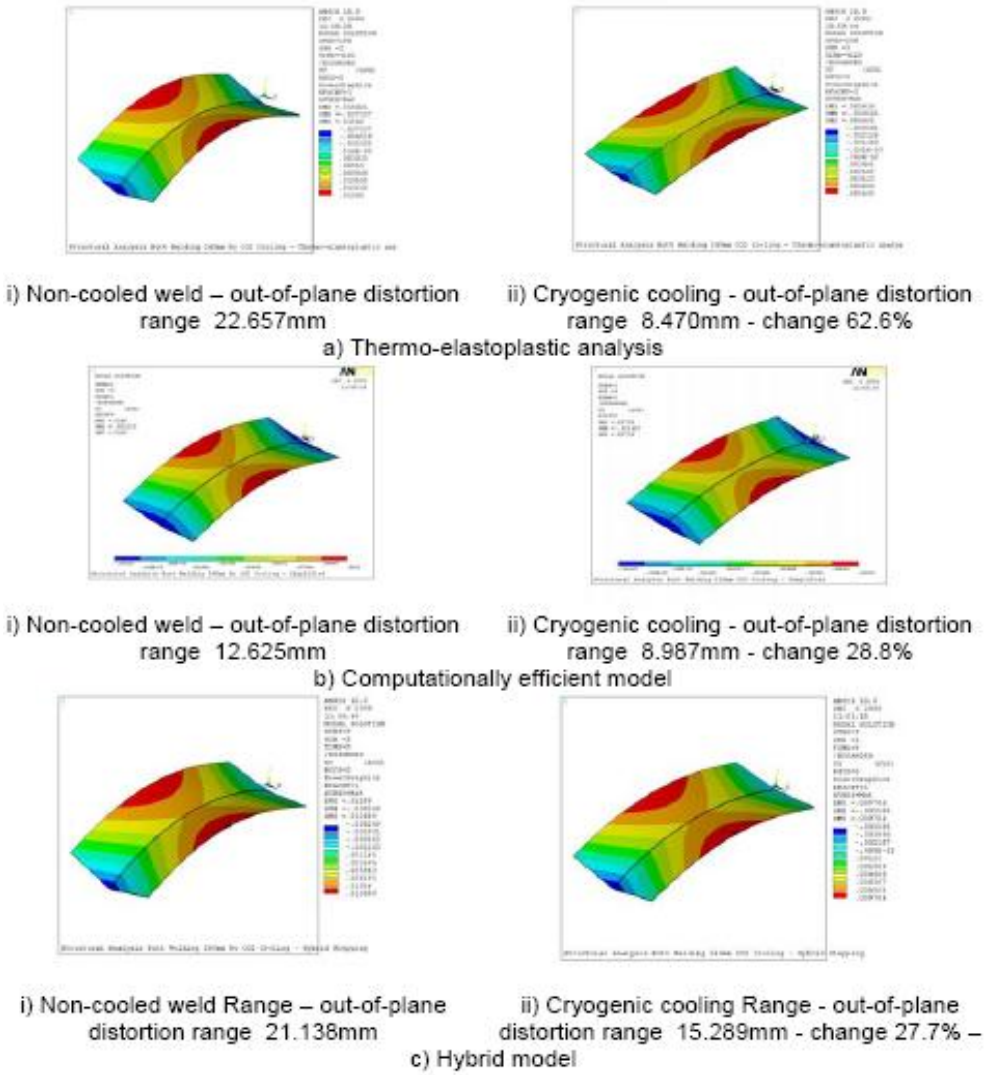

Figure 3.25 Comparison of the out-of-plane distortion predicted by three different models by Camilleri et al. [50]

Applying the same cooling source on fillet welds (5 mm+5 mm plate thickness) Camilleri et al. [50] predicted no change in distortion: 1.95 mm peak distortion without and 1.87 peak distortion with the application of cryogenic cooling. This lack of effect on the distortion reflects on the predicted residual stress profiles as

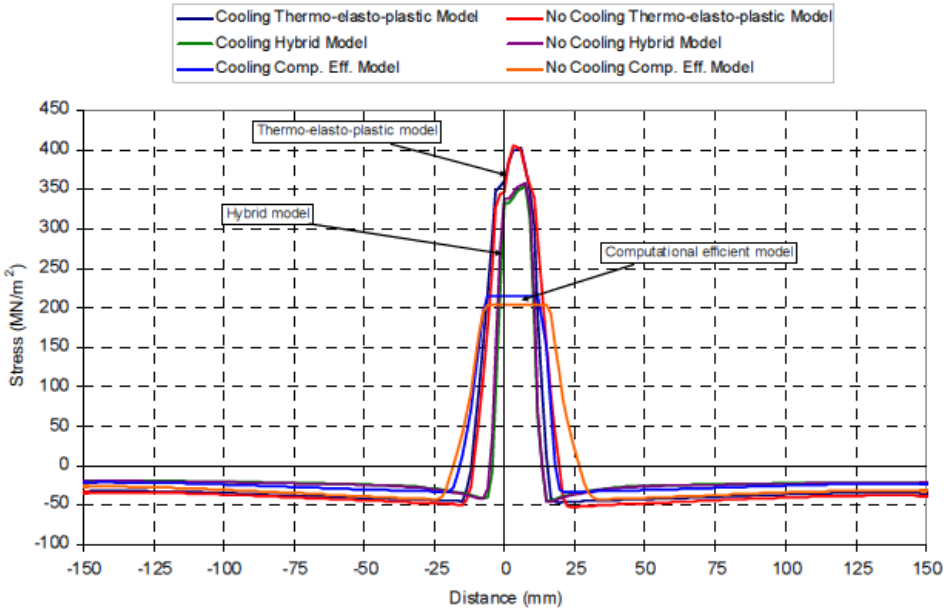

Figure 3.26 Residual stress distribution of fillet welded panels with and without the application of cryogenic cooling predicted by Camilleri et al. [50]

Camilleri et al. [50] put a lot of effort into the numerical modelling of DC-LSND welding on butt and fillet welds using complex models with high computational demands as well as simplified models that are quicker to solve. Unfortunately the simplified models give significantly different results in case of butt welds, which suggests that some aspects of the process were over simplified.

Some of the possible reasons for the low success of the numerical model simulatioins (especially the fillet welds) could be as follows: the travel speed for both butt and fillet welds were relatively high and the size of the cooling source is much larger than sizes implemented previously by others.

3.3 Thermal Tensioning by Heating

Thermal Tensioning by Heating, similar to TTC can be used to eliminate hot cracking as the cause of both hot cracking and buckling distortion are tied to the stress/strain cycle the material goes through during welding. It is not surprising then that thermal tensioning by heating was initially described as a process to eliminate

hot cracking primarily in welding of aluminium alloys by several researchers in the early 1970s [51].

Hernandez et al. carried out detailed experiments on GTA welding of aluminium alloys using external heat sources to eliminate hot cracking in 1984 building on the results and knowledge gathered by earlier research mentioned above [51]. Hernandez et al. used oxyacetylene heaters as heat sources to apply approximately 130 °C peak temperature on either side of the weld line behind the weld as shown in Figure 3.27.

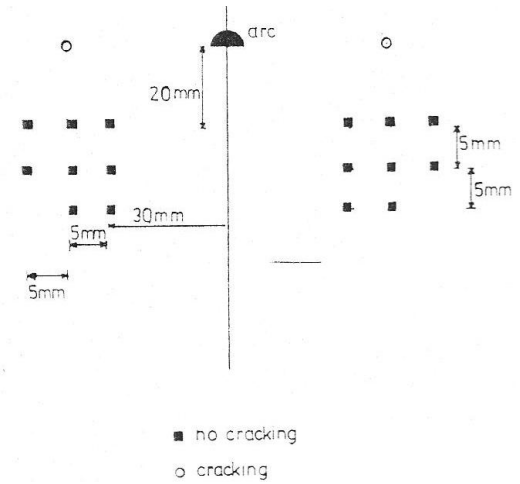

Figure 3.27 Heating torch positions and their effectiveness in eliminating hot cracking as applied by Hernandez et al. [51]

Hernandez et al. carried out detailed dynamic strain analysis in a region adjacent to the weld pool using the Moiré fringe technique. Their conclusion of this analysis is that the external heating makes the strain field around the weld more uniform with smaller gradients (producing lower shear strains) as illustrated in their measurement results in Figure 3.28.

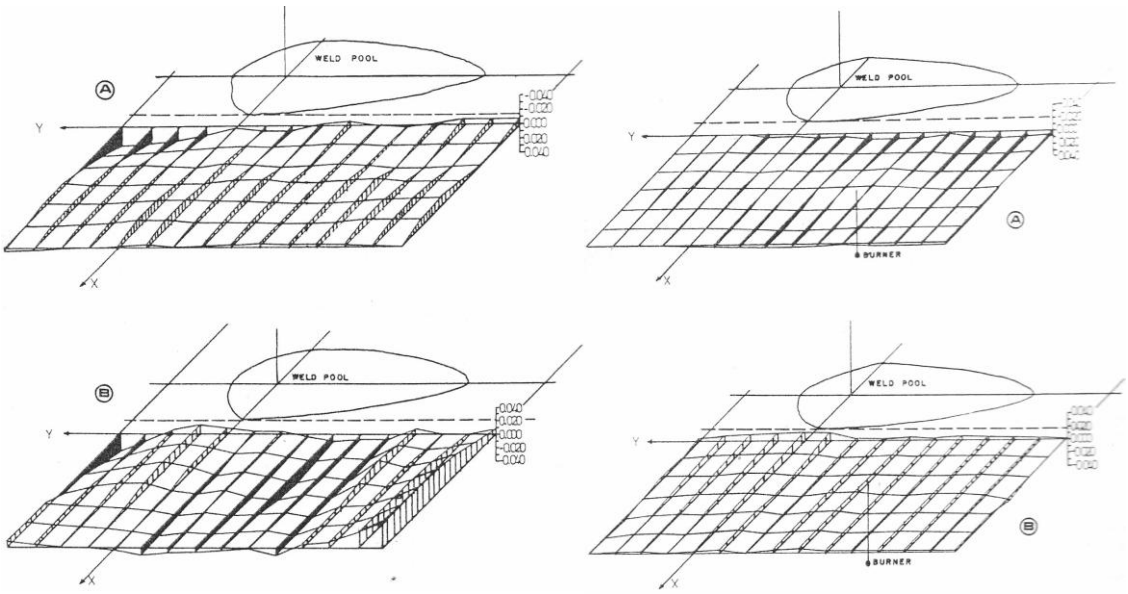

Figure 3.28 Dynamic strain fields adjacent to the weld pool measured using the Moiré fringe technique by Hernandez et al. [51]

Although the understanding of dynamic stress field and the mechanism of hot cracking was limited at the time, Hernandez et al. realised the significance and practicality of modifying the dynamic strain field using external heat sources. They pointed out the low sensitivity of the process to the position of the heaters, even though the aim of their work was eliminating hot cracking and not buckling distortion.

Masubuchi summarised the results of detailed studies carried out at MIT on in-process control of residual stress and distortion in the late 1980s [52]. Initially the research at MIT focused on reducing the rotational distortion of butt welded panels during welding to improve the weld quality of large panels. At the same time Masubuchi et al. realised that the most effective way of reducing distortion is to control the plastic strain development in the weld area.

The idea of using side heating to reduce the forces acting upon tack welds came from Chang [52]. His aim was to produce additional stresses by heating to counteract the welding stresses. The experimental setup used by Chang is shown in Figure 3.29. In this setup strain gauges were installed on rings attached on each end of the weld to measure the forces acting at the ends of the weld.

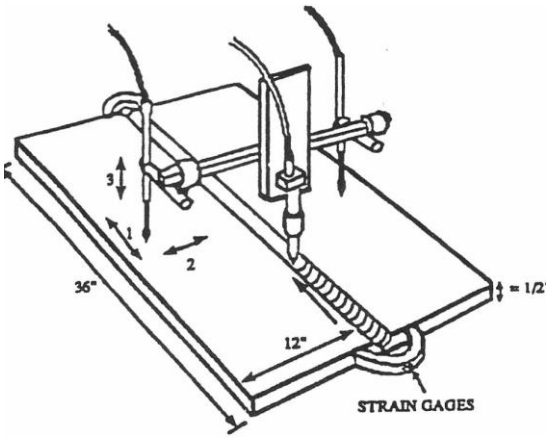

Figure 3.29 Welding setup with side heaters used by Chang to study the effectiveness of side heating on reducing rotational distortion [52]

In Chang's study he found that the forces acting on the ring at the end of the weld can be reduced significantly (e.g. from 1125 pounds to 105 pounds) by optimised side heating.

Chang's side heating idea was then employed to reduce residual stresses and distortion of high strength steel weldments by Bass and Vitooraporn [52]. They observed 17-39 % reduction in residual stresses and distortion using side heating. In FEA they also indicated that the side heating reduced the width of the plastic deformation zone by 30 %.

Michaleris et al. also investigated thermal tensioning techniques using heaters [53-57] primarily on fillet welds. Their first step was a numerical investigation of a static thermal tensioning technique derived from Guan's LSND patent [33, 56]. This technique uses heating and cooling elements to create a pre-set thermal field before welding. The panels are heated by resistive heaters on either side of the weld line and cooled by water jet at the weld centreline as Figure 3.30 illustrates.

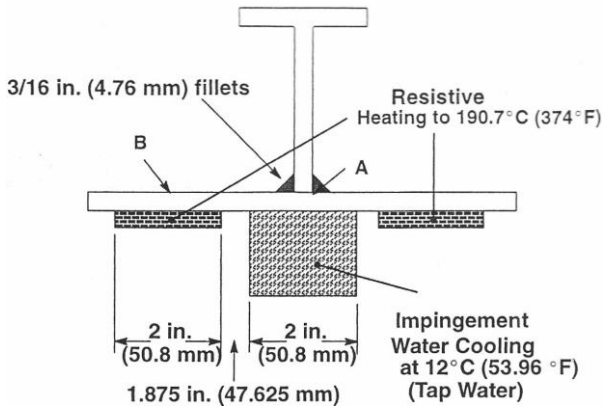

Figure 3.30 Static thermal tensioning apparatus by Michaleris et al. [56]

Michaleris et al. examined different applications of the static heating and cooling during welding of large panels. These experiments revealed that the application of water jet cooling during welding reduces the width of the tensile region of the welding residual stress distribution, but did not influence the magnitude. At the same time using the resistive heaters in conjunction of the water cooling proved to be successful in reducing both the magnitude and width of the tensile peak as shown in Figure 3.31.

Using 270 °C temperature difference not only reduced the tensile peak to zero but also created two tensile peaks at the positions of the heaters. These extra peaks are produced by the high enough temperature gradient of the pre-set thermal field. Michaleris et al. suggested to avoid these extra peaks and use only the elastic tensioning range of the equipment.

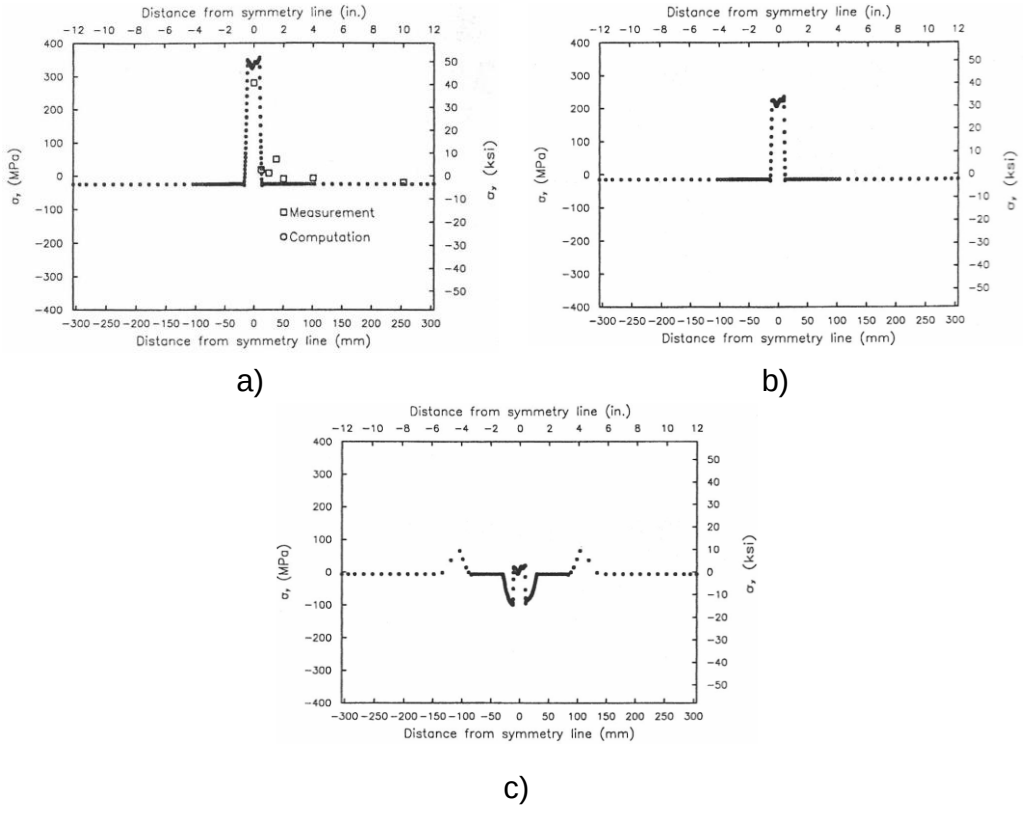

Figure 3.31 Comparison of predicted residual stresses applying static thermal tensioning using a) water jet cooling only and water cooling and resistive heating with b) 110 °C and c) 270 °C temperature differentials

This static thermal tensioning setup, although successful in reducing the welding residual stresses is not ideal for industrial application. The reasons for this are the following: it takes considerable time to set the desired temperature field, which

slows down the production; also installing static cooling and heating equipment on large welds such as ship panels is expensive.

To overcome the limitations of the static thermal tensioning, Michaleris et al. carried out numerical investigation (using FEA) of transient thermal tensioning using moving heat bands as shown in Figure 3.32 [54]. They optimised this process (shape and position of heaters) to minimise the welding residual stresses. They had two design cases in their optimisation: one to achieve minimum stress at the edge of the plate and one to achieve minimum sum of squares of stress.

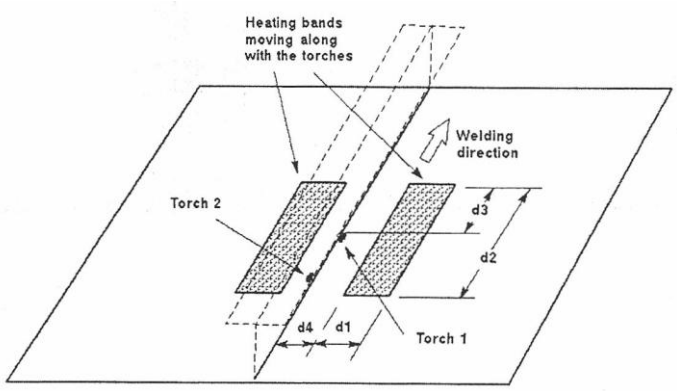

Figure 3.32 Transient thermal tensioning using moving heat bands by Michaleris et al. [54]

These two cases have significantly different optimum designs of the thermal tensioning process as is clearly seen in Figure 3.33. The heaters in the two cases are not the same shape: for minimum plate edge stress the heaters are close to a square shape and are positioned symmetrically in between the plate edge and the stiffener. At the same time the minimum sum of squares stress design has heaters stretching across the entire width of the base panel and the shape of these heating bands is rectangular, approximately twice as wide as long. A common feature of these designs is the position of the heaters; in both cases the welding torches are in between the heaters.

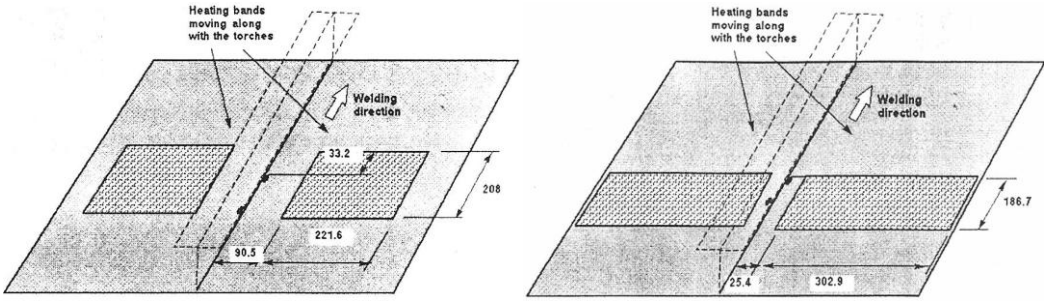

Figure 3.33 Comparison of optimum process design for two different objectives: a) minimum stress on plate edge and b) minimum sum of squares stress

After the numerical investigation Michaleris et al. performed experimental verification of the transient thermal tensioning [53]. In this work they used rectangular propane heaters on either side of the welding torches on a fillet joint that was welded on both sides simultaneously as shown in Figure 3.34. In their trials they used different temperatures and clamping arrangements.

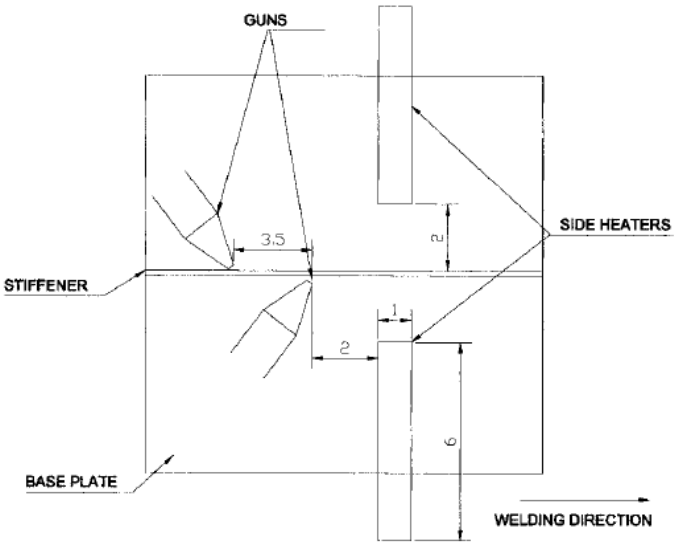

Figure 3.34 Experimental arrangement of transient thermal tensioning using propane side heaters by Michaleris et al. [53]

With the presented arrangement Michaleris et al. achieved significant reduction in welding residual stresses and complete elimination of buckling distortion (and angular distortion with the application of additional clamping at the free edge of the panel). They found that applying 250 °C preheat temperature further reduces the residual stresses (see Figure 3.35), even though 200 °C preheat temperature is sufficient to eliminate buckling.

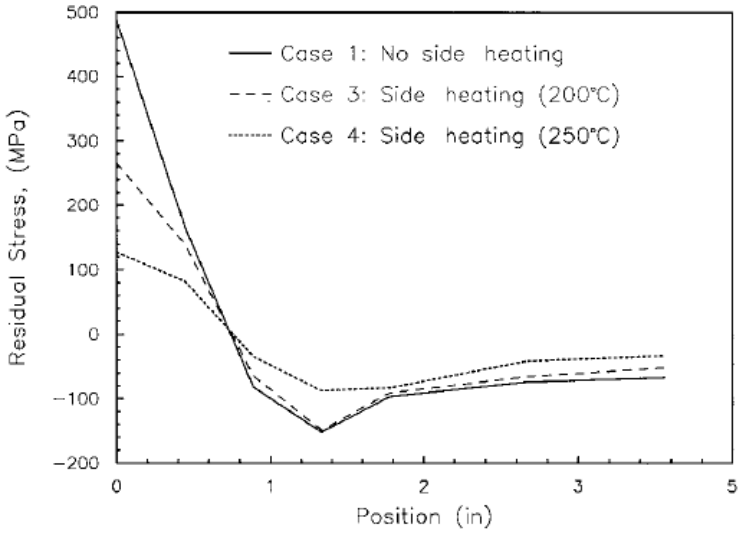

Figure 3.35 Comparison of residual stress distribution in as welded and transient thermal tensioned panels measured by Michaleris et al. [53]

Song, Shanhvi and Michaleris then carried on with more numerical modelling and optimisation of the transient thermal tensioning process [57]. They used the same arrangement in their FE model as shown in Figure 3.34 and optimised the positioning of the heaters (Φ_2 and Φ_3) and the heat input (Q_s) for minimum residual stresses in the objective region (see Figure 3.36).

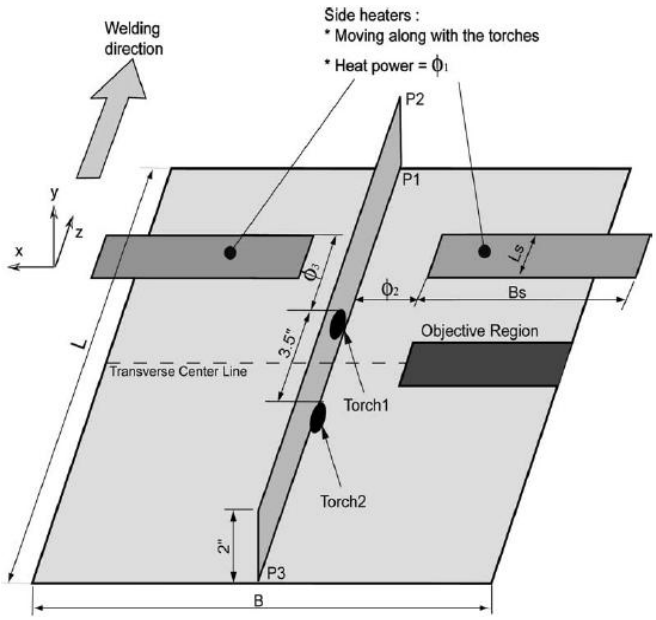

Figure 3.36 Transient thermal tensioning model showing the objective region and the optimisation parameters explained by Song et al. [57]

The results of this optimisation are summarised in Table 3.1. The longitudinal and horizontal positions did not change significantly, while the heat input nearly

doubled in the optimum parameters. This small change in the positioning of the heaters reinforces the low sensitivity of the process to these parameters.

Table 3.1 Results summary of the transient thermal tensioning optimisation by Song et al. **[57]**

Design variable Φ_i	**Initial value**	**Optimum value**
Φ_1: Heat input [W]	5000	9288.01
Φ_2: Side offset [mm]	50.80	54.24
Φ_3:Longitudinal offset [mm]	50.80	47.00

The effect of the heaters is clearly seen in the residual stress profile in Figure 3.37. When the side heaters are applied the compressive residual stress components are decreased and with the optimum side heater design (high heat input) the residual stresses become tensile or very close to zero. A consistent reduction in the magnitude of the tensile peak at the weld line is observed as well.

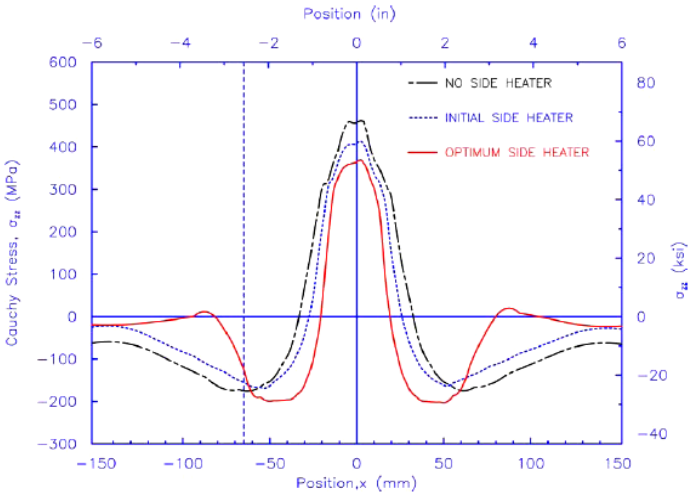

Figure 3.37 Residual stress comparison of the transient thermal tensioning process by Song et al. [57]

With the numerical modelling and optimisation of the transient thermal tensioning Song et al. gave a good insight into how this process works. They demonstrated the effect side heaters have on the residual stress profile and how this profile changes with different heater parameters even though they only considered two design variants and did not do any experimental verification.

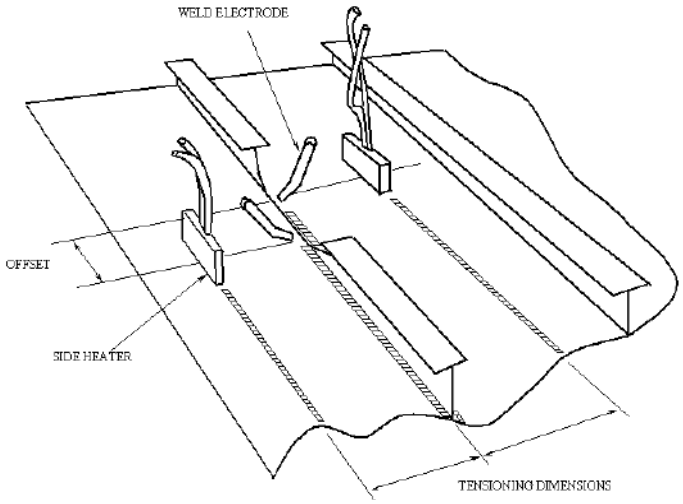

Figure 3.38 Experimental arrangement of transient thermal tensioning by Dull et al. [58]

Dull et al. also did a lot of work on transient thermal tensioning applied to welding of large ship panels [58-60]. Dull et al. started their work using Michaleris' suggestion of applying heat bands on either side of the weld moving simultaneously with the welding heat source (see Figure 3.33,b). They realised the impracticality of heating nearly the entire width of the panel on either side of the weld and used a different approach to the heating process as shown in Figure 3.38. The rectangular heaters travelling simultaneously with the welding torch are oriented parallel to the welding direction.

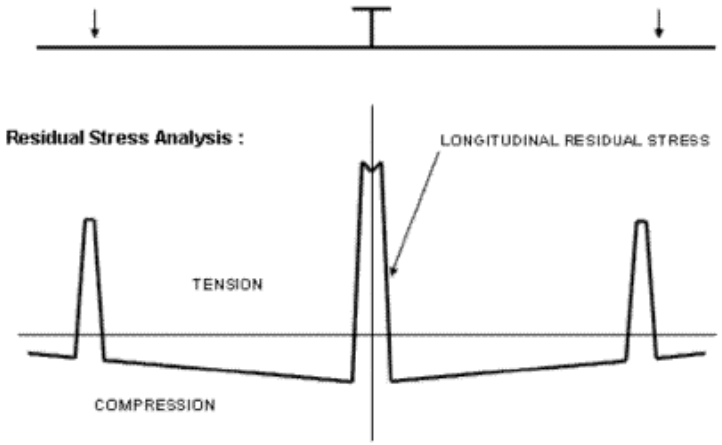

Figure 3.39 Residual stress profile of a weld with the addition of tensile regions generated by side heaters as proposed by Dull et al. [58]

The aim of the heaters aligned parallel to the weld line is to create additional tensile regions in the residual stress pattern of the welded panels at the position of the heaters as illustrated in Figure 3.39. With these extra tensile regions the critical buckling load increases significantly and most likely exceeds the applied welding

load generated by the compressive components of the modified residual stress profile.

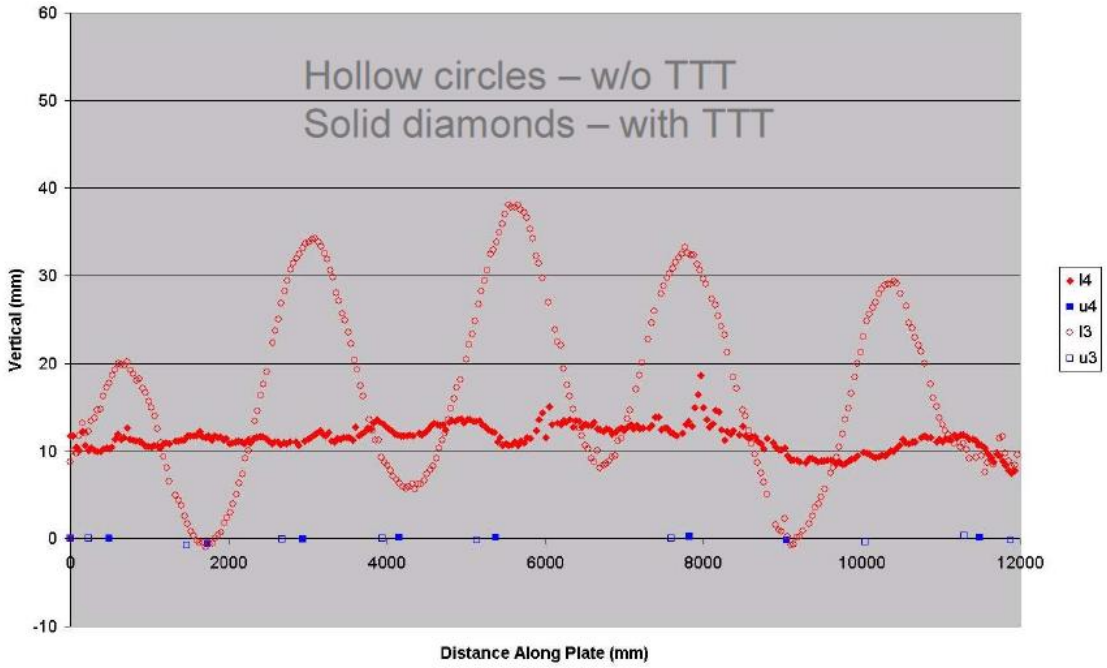

Figure 3.40 Distortion comparison at the edge of panels with three stiffeners welded with and without TTT [59]

Dull et al. carried out extensive laboratory and shipyard trials of this process and the results of these trials (see Figure 3.40) show great effectiveness in eliminating buckling distortion. Dull et al. [60] patented this process and in this patent they showed residual stress measurements of a large panel with three stiffeners welded onto it using TTT (see Figure 3.41). These measurements clearly show how the heaters alter the residual stress pattern generated by welding.

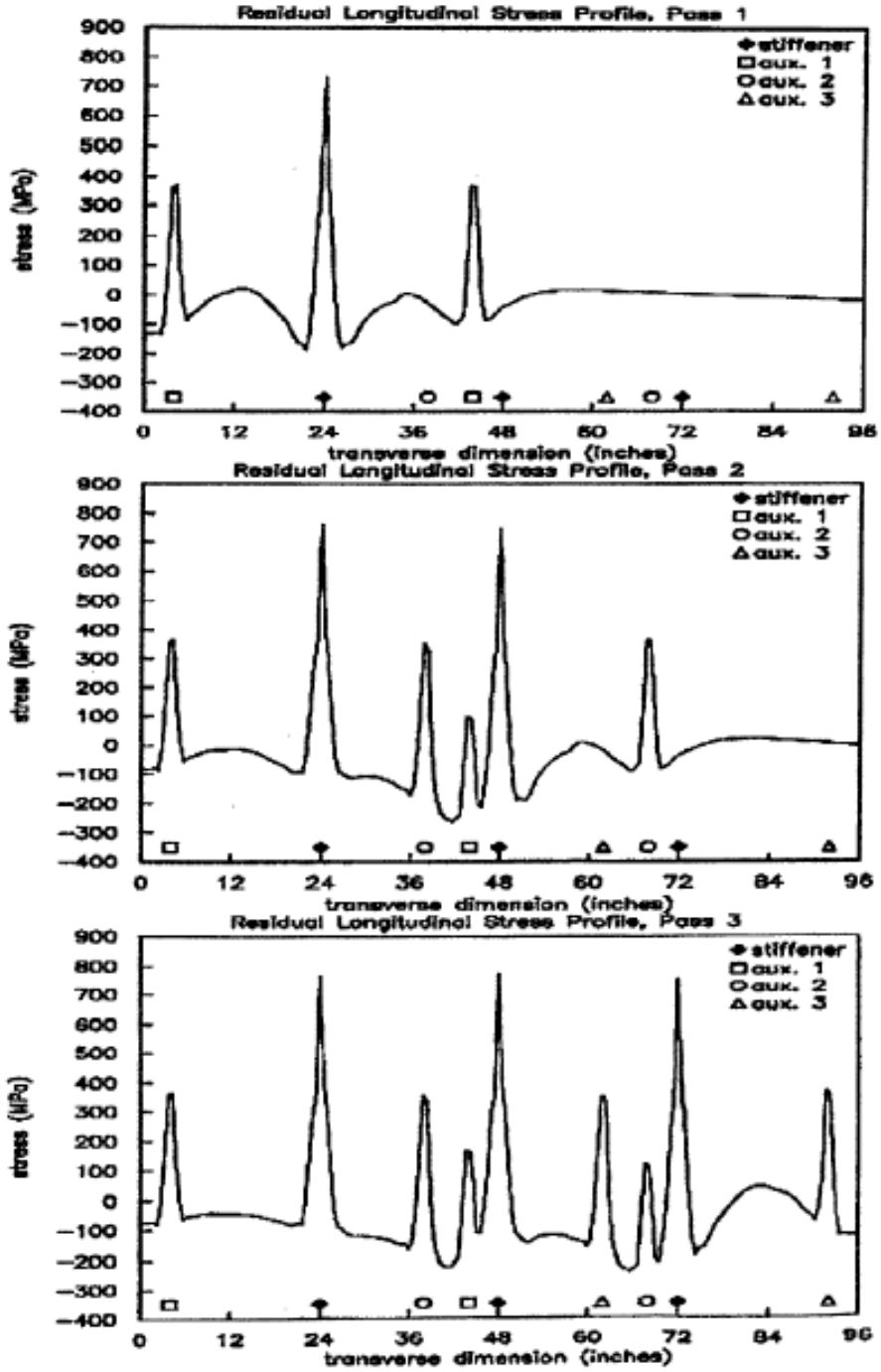

Figure 3.41 Stages of residual stress pattern development in welding three stiffeners onto a panel using Transient Thermal Tensioning by Dull [60]

This technique was later automated with a control unit and software to integrate it into the production process [59].

Dull et al. [58-60]used a new approach to TTT successfully on welding large panels and demonstrated how this process alters the residual stress pattern in order to eliminate buckling distortion. They did not mention though the temperatures they use to achieve additional tensile stress peaks. If these temperatures are too high they

can cause significant and undesired microstructural changes in the parent metal. Also the effect of these tensile peaks generated by the heaters(typically half the magnitude of that of the weld) on the material behaviour such as fatigue and damage tolerance, is not yet known.

Bagshaw et al. patented a thermal process to reduce the tensile residual stresses in primarily thick (~20 mm) welds [61]. This process comprises two or four induction heaters on either side of the weld (four if heated from top and bottom) positioned at the edge of the tensile stress region of the RS profile of the weld as shown in Figure 3.42. The induction coils traverse along the weld generating a peak temperature that is less than that required for any microstructural changes to occur. They suggest using this technique as both post- or during welding.

Bagshaw et al. extended the application to Electron Beam (EB) welding and replaced the induction coils with heating using the EB during welding. The peak temperature and heated area (position and width) were similar to that of the induction heating.

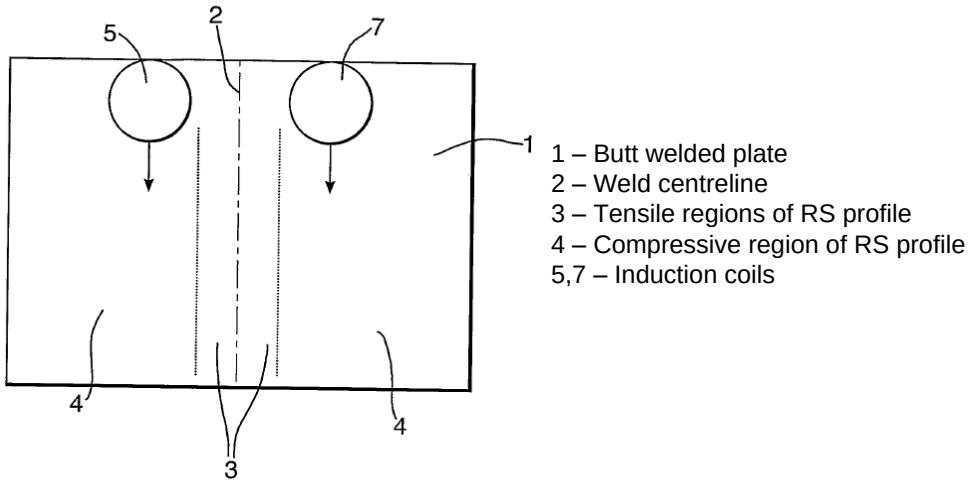

Figure 3.42 Experimental setup of transient thermal tensioning by heating using induction coils by Bagshaw et al. [61]

How this process works can be explained using the RS predictions of Bagshaw et al.'s FEA of the EB welding and heating process. It is clearly seen in Figure 3.43 that the induction coils generate an additional tensile zone in the RS profile of the weld adjacent to the welding tensile peak and at the same time the welding tensile peak is reduced significantly.

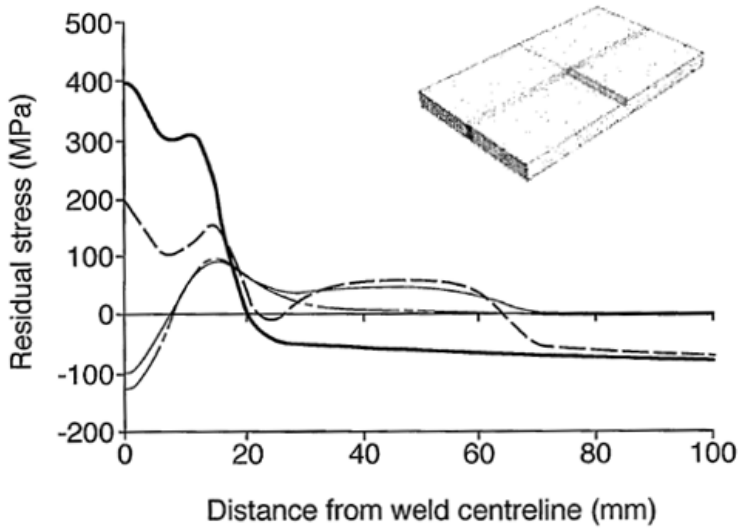

Figure 3.43 FE prediction of the induction heating process by Bagshaw et al. [61]

Bagshaw et al. demonstrated that residual stresses can be reduced by heating even in relatively thick (typically 25 mm and above) section welds, although they did not provide detailed explanation of how the residual stresses are altered/changed. The drawback of their process is the dependence on the exact location and width of the tensile peak in the weld region of the RS profile of the weld. Both measurements and numerical predictions are expensive and form an additional stage in adapting the process to production.

Although TTH seems to be a less researched area in the battle against mitigating buckling distortion, it is a more mature process than TTC. Having said that, it is not (widely) used in production, though some effort was put into industrialising it [59].

4 Investigation of Thermal Tensioning by Cooling

The Thermal Tensioning by Cooling SE technique is investigated in this chapter to reduce buckling distortion. This investigation covers technology transfer, cooling source characterisation (experimental and numerical characterisation) and weld applications. The study of TTC is detailed in this chapter.

4.1 Experimental Method

The TTC study started with an experimental investigation including: a technology transfer study, cooling source characterisation, welding trials and finally residual stress measurements. These experiments are detailed in this section further below.

4.1.1 Technology Transfer and Equipment Development

The technology transfer study was necessary as the patented BAE nozzle was only briefly tested previously on a different setup to that used in this work. In this technology transfer various aspects of the CO_2 delivery system and the welding process were also examined.

4.1.1.1 Installation of TTC Equipment on Seamer

The aims of the technology transfer study were to eliminate the issues experienced during the installation of the CO_2 delivery and extraction system and to improve the system based on the observations and the experience drawn from this study.

Figure 4.1 shows the seamer on which the technology transfer study was carried out as received from VT Shipbuilding.

Figure 4.1 Seamer before installation of TTC equipment

All the equipment, including the welding torch and the cryogenic nozzle had to be installed on the carriage (see Figure 4.2,a), since this provides the linear motion for the welding process. The installation of the cryogenic equipment and the extraction nozzle in particular were restricted by the confined space in the groove of the seamer as Figure 4.2,b shows.

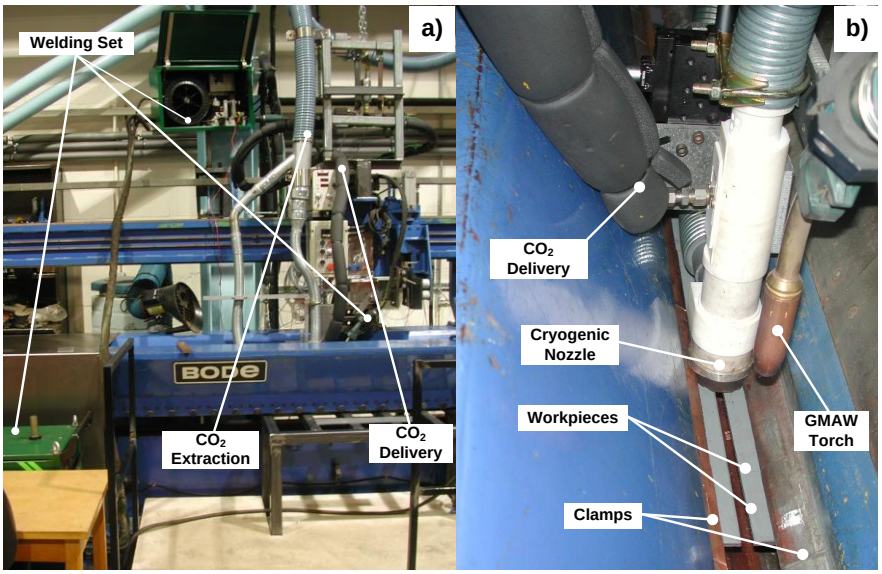

Figure 4.2 Setup1: first installation of TTC and welding equipment on seamer a) overall view b) limited access in the groove of seamer

It became clear during the first trials that visibility was a major issue and that it was very difficult to measure the height of the nozzle from the surface. The confined space around the nozzle also made access difficult, which hampered the operation of the equipment (e.g. adjust extraction flow rate).

Still, the primary issue with Setup1 was the catching of the silicon seal of the nozzle on the finger clamps of the seamer. The reason for this is that the distance in between the clamps was smaller than the diameter of the nozzle. There were also problems with the seal catching on the weld bead. This caused a side load on the end of the nozzle which resulted in the detachment of the nozzle end piece from the body. These catching issues were resolved by profiling the silicon seal, so that it fitted the groove made by the seamer clamps as well as the weld bead (see Figure 4.3,a).

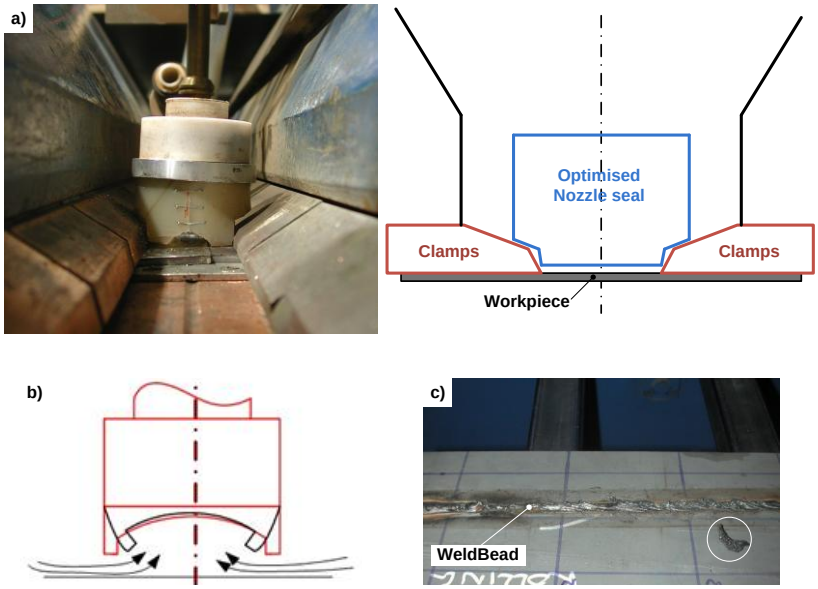

Figure 4.3 Issues with the silicon seal of the cryogenic nozzle. a) Arrangement of the profiled silicon seal in the seamer b) schematics of bending seal due to the low stiffness of the profiled shape c) a piece of weld pool that had been 'sucked-up' due to initial cut outs on seal

Although the profiling of the silicon seal eliminated the catching problems, it created another one. Having a larger extraction cross section caused the molten metal of the weld pool to be sucked up (Figure 4.3,c – solidified weld, previously pool, sucked into the nozzle during welding). To avoid this problem the seal was then further optimised to better fit the shape of the clamps. Another problem with the optimised seal design was reduced seal stiffness. As a consequence, the extraction bent the seal, which blocked the nozzle as illustrated in Figure 4.3,b. This bending stopped the extraction containing the CO_2 spray within the nozzle, which resulted in very poor quality of welds.

To overcome the issues with the seal and to improve visibility of the process and access to the setup the carriage track of the seamer was raised and the process performed on top of the seamer. The raised carriage track in Setup2 allowed the welding to be done with a jig on the seamer as illustrated in Figure 4.4.

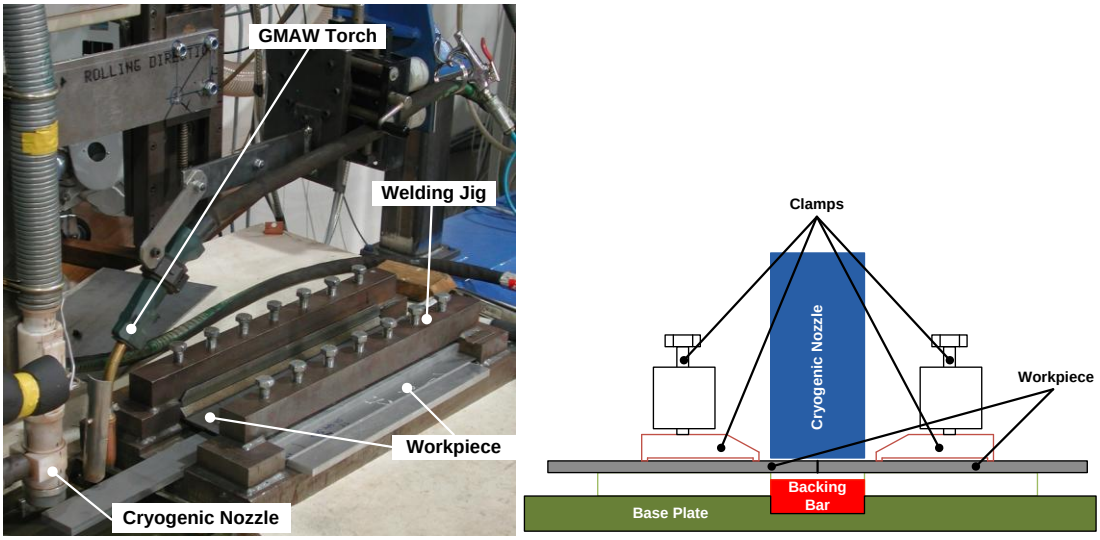

Figure 4.4 Setup2: Welding jig used on top of the seamer after raising the carriage beam.

This new setup meant that the seal could be installed without cutting it to the shape of the finger clamps. Using this setup 4 mm thick DH36 ship panels (500x250 mm in size) were butt welded with the MIG process. The welding parameters used for the trials are listed in Table 4.1. The area near the weld zone on the plates was ground prior to welding to avoid the contamination of welds.

Table 4.1 GMAW parameters of 4 mm DH36 butt welds

Current, A	Voltage, V	TS, m/min	WFS, m/min	CTWD, mm	Shielding Gas	Welding Wire Diameter, mm
256	31.5	0.65	12	18	Ar 78%, 20% CO_2, 2% 0_2	1

The results from these trials showed a high level of inconsistency and lower than expected levels of distortion reduction as Figure 4.5 illustrates. This inconsistency and the lack of distortion reduction suggested that the cooling was not working effectively.

The reasons for this inconsistency were identified as follows:

- The level of distortion when welding 4 mm plates of this size (500x250 mm) is already low; therefore it is not appropriate to use distortion for determining the effectiveness TTC.
- Distortion due to preparation (e.g. cutting, grinding, etc.) of the plates is similar in magnitude to that due to welding.
- Some vertical movement ('lifting') of the cryogenic nozzle was observed. This movement was compensated for by manually adjusting the height during welding.
- Problems with the CO_2 delivery which included pulsing and high gas to solid ratio. This resulted in ineffective cooling of the weld. The problem is discussed further in 4.1.1.5.

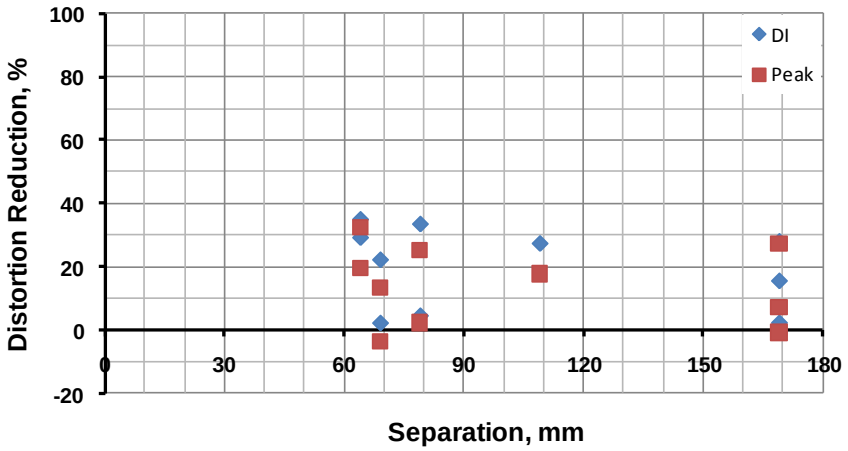

Figure 4.5 Distortion reduction versus separation between the welding torch and cooling nozzle for butt welds of 4 mm thick plates (Amal jet 170) reference weld Pead Distortion: 12.35 mm, DI: 6.31 mm

To increase the distortion level, the thickness of the plates was reduced to 2 mm. Welding parameters for these plates were developed which used the same travel speed. These welding parameters are listed in Table 4.2.

Table 4.2 GMAW parameters developed for 2 mm butt welds

Current, A	Voltage, V	TS, mm/min	WFS, m/min	CTWD, mm	Shielding Gas	Welding Wire Diameter, mm
178	25	0.65	7	16	Ar 78%, 20% CO_2, 2% 0_2	1

Applying TTC on the 2 mm thick plates using Setup2 showed the same ineffective cooling and therefore the lack of reduction in distortion (Figure 4.6). When using lower travel speeds (e.g. 0.18 m/min) another problem occurred. During welding, lifting of the nozzle by several mm was observed, which was exacerbated by the lower travel speeds.

This lifting increased the gap between the nozzle and the plate surface. The increased gap resulted in excessive extraction due to the increased air in-take, which decreased the cooling effect of the CO_2 spray. This movement of the nozzle was observed in previous experiments; however then the magnitude of the movement was not significant. When the travel speed was reduced to 0.18 m/min the vertical displacement increased to several mm when welding the 500 mm long plates.

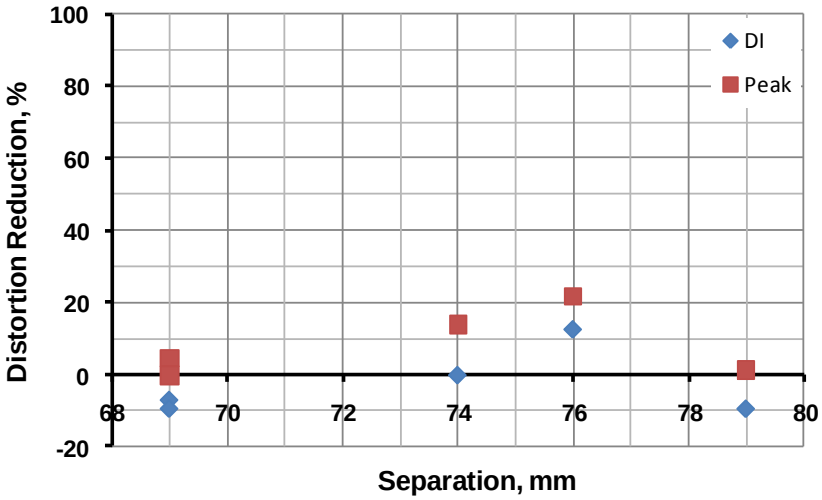

Figure 4.6 Distortion versus separation distance between the welding torch and the cooling nozzle for 2 mm butt welds (Amal jet 170) reference weld Pead Distortion: 14.44 mm, DI: 6.21 mm

The lifting problem was at first thought to be caused by the thermal contraction of the metallic extraction hose attached to the nozzle. To overcome this problem the metallic hose was replaced by a PTFE hose. Unfortunately this did not solve the problem. A further investigation showed that the lifting was caused by the general cooling of the mounting equipment for the nozzle. This cooling created thermal stresses, which resulted in rotation and displacement of the bracket holding the nozzle as shown in Figure 4.7. During these experiments the low temperature of the CO_2 spray caused problems with not only the mounting of the nozzle. The

extraction hose, connected to the extraction fan and the PTFE hose via a metallic reducer fractured due to the low temperature of the CO_2 spray, which made the hose brittle. The broken hose was then replaced by a thin walled hose with helical wire reinforcement. The new hose proved to be adequate for this cryogenic application.

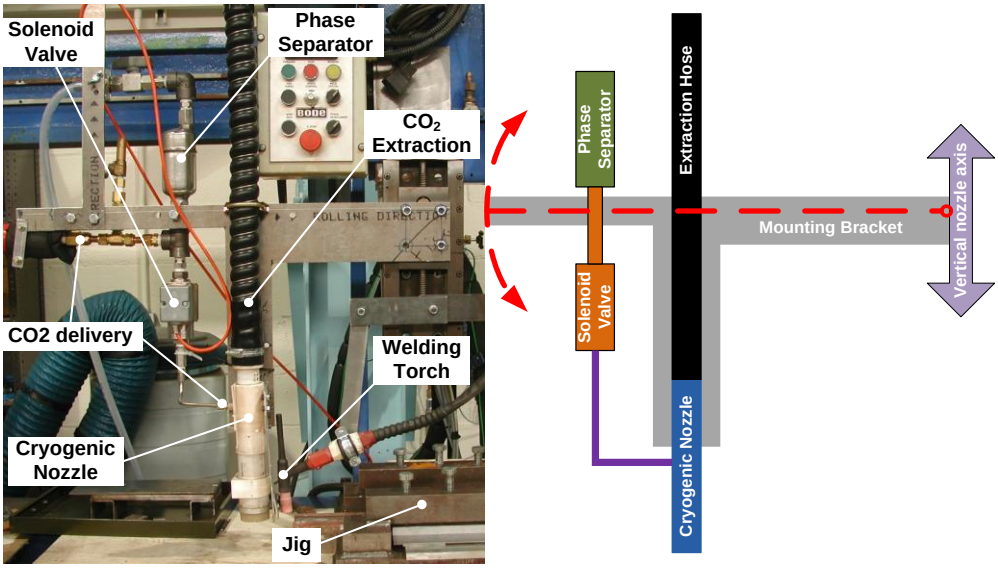

Figure 4.7 Picture and schematics of TTC Setup3 demonstrating the nozzle lifting due to rotation

To resolve the lifting issue, the mounting bracket of the nozzle was changed to Setup4. The phase separator and solenoid valve were mounted on a bracket separate to the nozzle as shown in Figure 4.8.

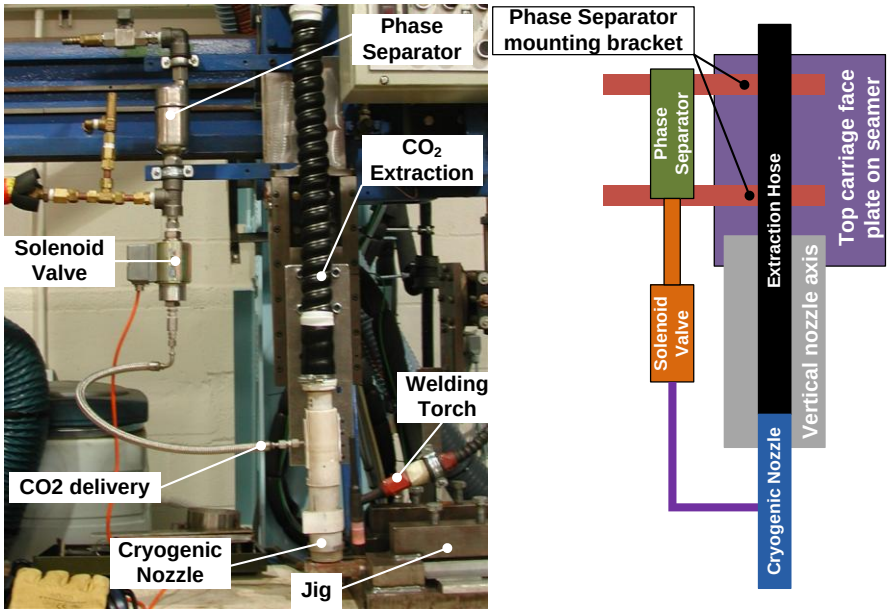

Figure 4.8 Picture and schematics of TTC Setup4 with changed nozzle and phase separator mounting arrangement to reduce nozzle lifting

The nozzle was mounted directly onto the vertical motion axis, hence the rotating arm was eliminated. Also, the solenoid valve with the phase separator was not moving with the nozzle and was connected by a flexible hose.

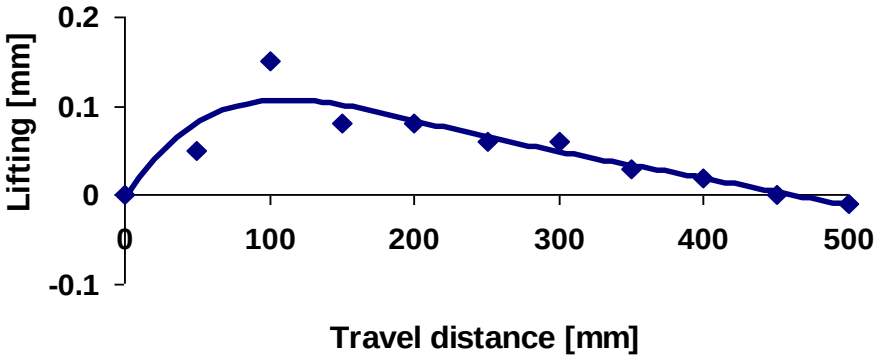

Figure 4.9 Measured nozzle lifting during TTC of a 500 mm long plate

With this arrangement the cooling of the solenoid valve and phase separator mount does not affect the cryogenic nozzle mount. Also the possibility of a rotating arm is eliminated by positioning the nozzle directly on the motion axis. Hence, the lifting of the nozzle with Setup4 was reduced to a minimum as shown in Figure 4.9.

4.1.1.2 Travel speed study on the effectiveness of TTC

Van der Aa in her study on TTC using cryogenic CO_2, showed that travel speed is a key parameter in reducing distortion The temperature contours for welding speeds of 3 and 8 mm/s are shown in Figure 4.10 and indicate that the horse shoe shaped temperature contour required for effective TTC is only produced with low welding speeds. As a consequence of these results a preliminary study on the effect of travel speed on TTC was carried out.

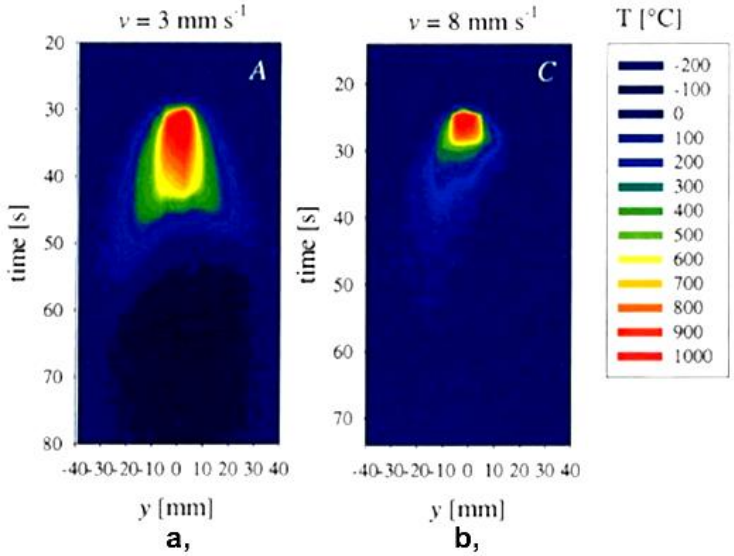

Figure 4.10 Cryogenic cooling from Van der Aa [45] a) Temperature contours at 3 mm/s travel speed b) Temperature contour at 8 mm/s travel speed

A MIG welding process was used for this study on 2 mm thick plates at different travel speeds. The welding parameters used are shown in Table 4.3. The same welding wire and shielding gas were used as previously (see Table 4.2).

Table 4.3 GMAW parameters of TTC travel speed study

Travel Speed [m/min]	Voltage [V]	Current [A]	Wirefeed Speed [m/min]
0.55	22.5	134	5.2
0.45	21	122	4.4
0.18	18	80	2.8

The following parameters were kept constant for all the travel speeds: 65 mm separation between the welding torch and cooling nozzle, Amal jet size 170. The TTC setup shown in Figure 4.7,a was used for this work.

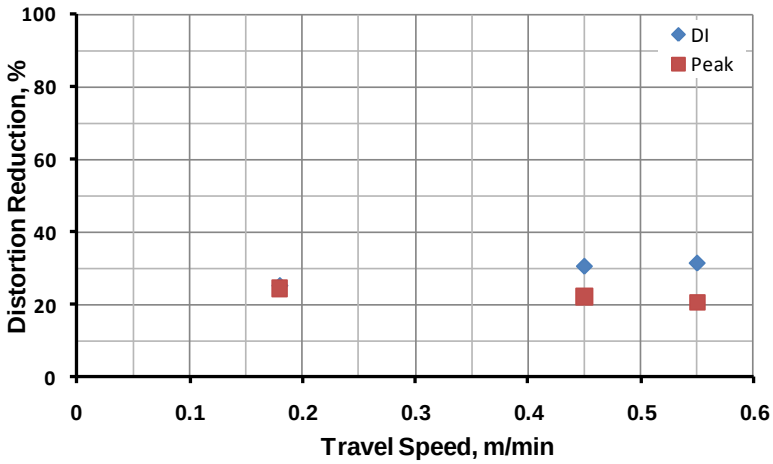

Figure 4.11 Distortion response of the butt welded plates in the TTC travel speed study

These results were the first ones in this work to show any significant improvement in distortion with TTC, which is shown by the results in Figure 4.11. However these results did not show any increasing effectiveness of TTC with reduced travel speed. As Figure 4.11 illustrates the reduction in distortion at the lowest travel speed (0.18 m/min) is only slightly bigger than at highest travel speed (0.55). This minor improvement is because the old TTC setup was used with the significant lifting problem, which is worse at lower travel speeds.

4.1.1.3 Study of the effect of clamping on TTC

- Different clamping arrangements were tested to determine their effect on TTC. The clamping arrangements had the following effects on the thermal profile:
- If the heat sink of the side clamps is too high, a significant amount of heat is extracted from the weld area and the side of the weld in particular. This makes it more difficult to create the horse-shoe shaped thermal profile. Therefore low thermal conductivity materials for the clamps are preferred and the contact area of the clamps with the work piece should be minimised.
- The in process stresses of welding with TTC are increased which caused the distortion near the end of the plate shown in Figure 4.12. To resolve this problem improved clamping is required necessitating the need for the clamps to be as close to the weld line as possible. Finally a backing bar is needed to provide firm support of the weld zone.

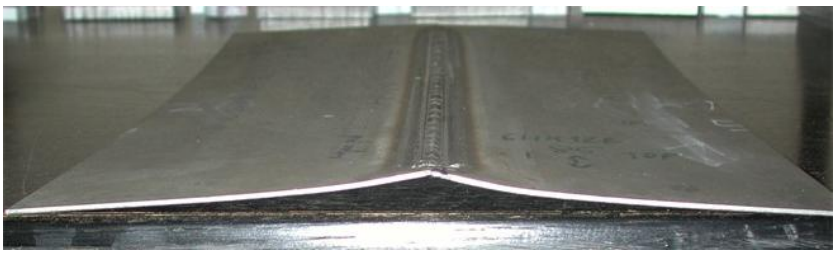

Figure 4.12 Enhanced dynamic stresses add local buckling to the overall distortion at the end of the weld

A welding speed of 0.18 m/min was used for these trials with the welding parameters shown in Table 4.3 (at this speed). Two different clamping arrangements were tested, which are illustrated in Figure 4.13. The same jig was

used for all three cases but the clamps were at different positions and had different contact areas with the plates being welded. In all cases insulating pads were placed between the plates and the jig to minimise heat loss from the plate to the jig.

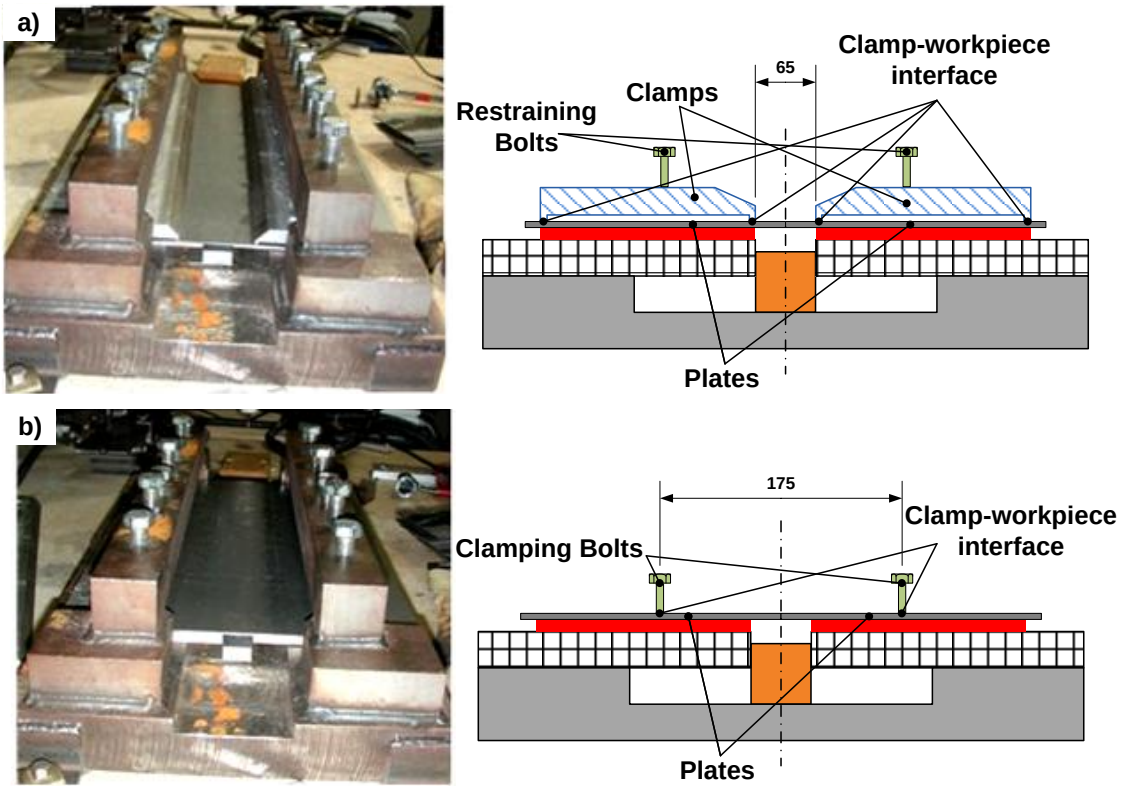

Figure 4.13 Clamping arrangements investigated with TTC a) clamping applied via Aluminium plates machined to minimise clamp heat sink b) clamping applied via restraining bolts directly

In Clamping Arrangement 1 the plates are clamped by aluminium plates that are placed close to the weld line, only to accommodate the nozzle without interfering with it. These Aluminium plates were machined at the bottom side (see Figure 4.13,a) to minimise their heat sink effect. This small contact area ensured a minimum effect on the thermal field. In CA 2 the plates are clamped by the restraining bolts on the top directly, which are further apart from each other than the aluminium clamps in CA1.

Although not proved it is believed that the heat loss is greater with CA1 than with CA 2. The results from these trials are shown in Figure 4.14 and indicate that CA1 with tacking provided the greatest reduction in distortion. It should also be noted that during these trials vertical movement of the nozzle was also observed as described previously. Therefore the results are only qualitative and more extensive

study is necessary to find the best arrangement for clamping and tooling in a particular production facility.

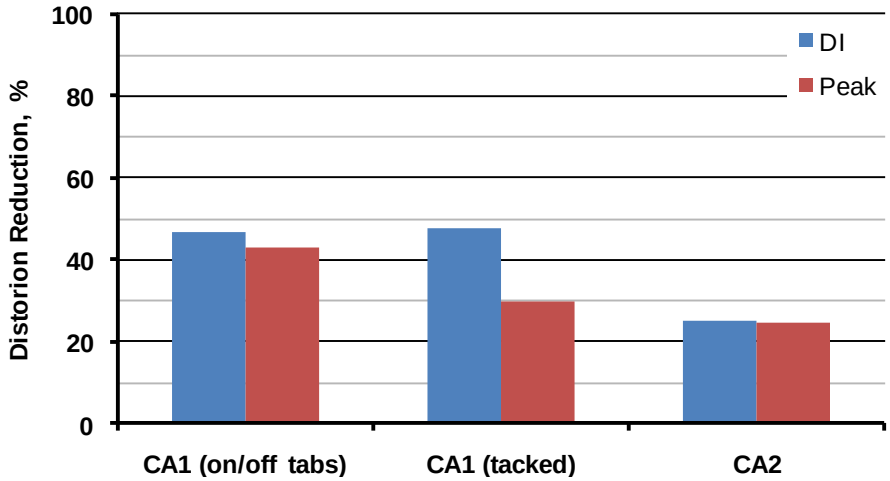

Figure 4.14 Distortion reduction of TTC GMAW plates with different clamping arrangements (see Figure 4.13 for clamping arrangements schematics)

4.1.1.4 TTC GTAW trials

GMAW usually produces a relatively large cap on the top of the weld, at the same time the root is usually much narrower than the cap as illustrated in Figure 4.15. This variation in the width of the weld bead through the thickness translates to proportional variation in the width of the tensile peak, and with it the AWL from top to bottom. This difference in AWL is increased by the extra material on the top of the weld (cap) and produces bending distortion, which is similar in appearance to 1st order buckling (see Figure 1.9 for illustration). Though similar looking, bending distortion is different in nature and needs to be addressed differently to buckling.

Hence, TTC experiments were carried out with autogenous TIG welding in order to reduce the through thickness variation (see Figure 4.15) of the residual stress profile and to eliminate the excess material on top, to minimise bending distortion.

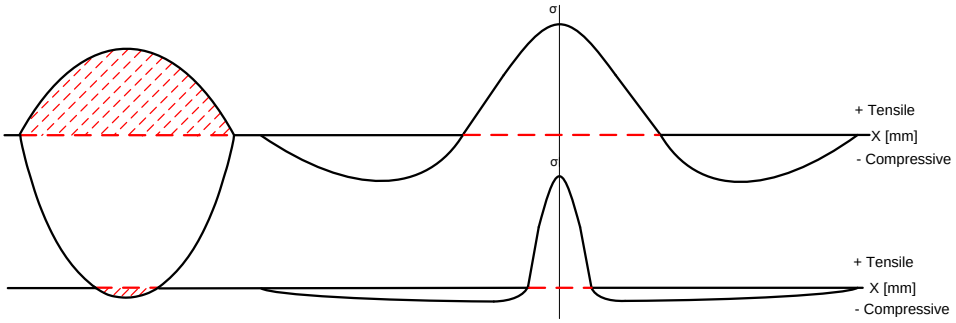

Figure 4.15 Through thickness variation of welding residual stresses

The material and geometry of the panels were the same as described in previous GMAW experiments. The experimental setup used was TTC Setup3 in Figure 4.7 with clamping arrangement CA1 in Figure 4.13. The welding parameters used are listed in Table 4.4. The distortion measured with and without TTC is shown in Figure 4.16. Using the same specimen (geometry, material) with the same clamping gives the opportunity to compare the reduction in distortion with TTC on GMAW and GTAW welding: the best result for GMAW welding is ~25% reduction in DI whereas in case of GTAW it is 40% using TTC Setup3.

Table 4.4 Welding parameters of GTAW TTC trials

Travel Speed, m/min	0.14
Voltage, V	10.2
Current, A	85
Shielding gas	Ar, 10 l/min
Electrode material	2% Thoria
Electrode diameter	1.6
Electrode included angle, °	30
Electrode extension from cup, mm	10
Shielding cup diameter, mm	10

It should be noted, though that the nozzle was lifting significantly using TTC Setup3 as mentioned earlier. Therefore the results are affected by the loss of the cooling power during welding. When the lifting problem was solved using TTC Setup4 (shown in Figure 4.8), the reduction in distortion achieved with TTC increased to 80% as shown in Figure 4.17.

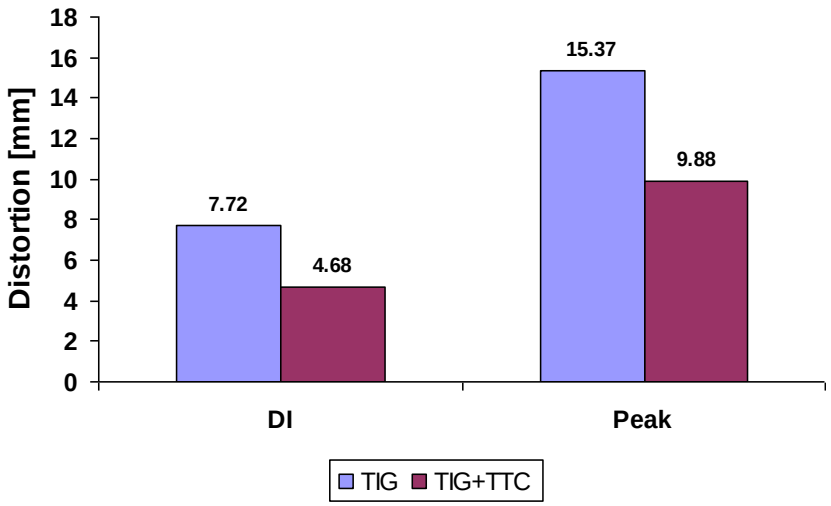

Figure 4.16 Distortion response of GTA welded plates with and without TTC

The distortion reduction achieved in with TTC Setup4 shown in Figure 4.17 suggests that bending distortion can be a problem in SE techniques. Therefore the weld profile needs to be optimised to eliminate bending distortion.

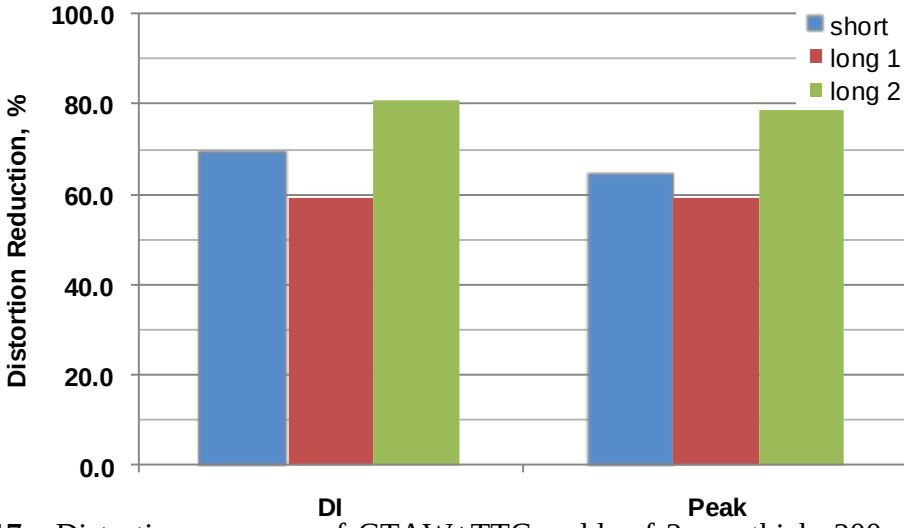

Figure 4.17 Distortion response of GTAW+TTC welds of 2 mm thick, 200 mm (short) and 500 mm (long) long plates

4.1.1.5 Issues with CO_2 delivery

Throughout the experiments with TTC pulsing was found to be a characteristic of the cryogenic CO_2 spray. Pulsing is a change of flow rate which causes a visible change of diameter of the cryogenic spray as shown in Figure 4.18. The distance between the CO_2 vessel and the delivery nozzle was approximately 25 m for these results. This figure shows how the pulsing is worse with the small (170) Amal jet. The pulsing was so severe with the 170 Amal jet that the flow was almost blocked, especially during the first minute of operation. In addition the spray contained a large amount of gas (rather than solid CO_2) which is less effective in cooling the weld zone.

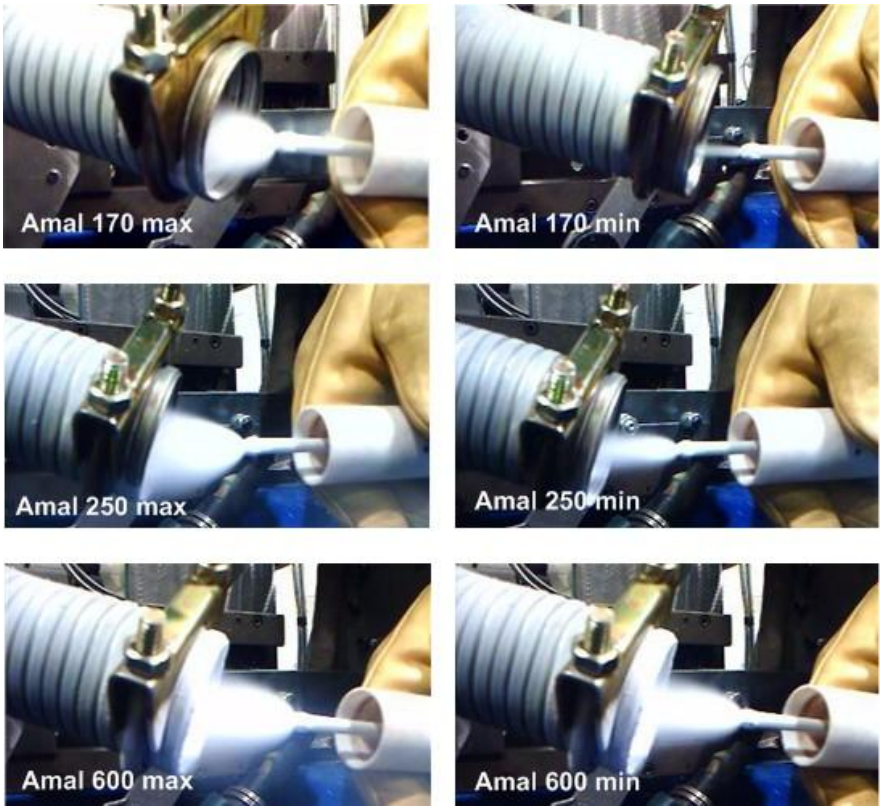

Figure 4.18 Change of the diameter of the cryogenic CO_2 spray due to pulsing (photos taken at ~1 minute of continuous spray)

To improve the spray quality (reduce pulsing, increase solid/gas ratio) of the CO_2 spray the following changes were made:

- The length of the delivery line from the CO_2 cylinder to the point of use was decreased from 25 m to 2.5 m by placing the cylinder next to the seamer.
- The un-pressurised pipe length from the last solenoid to the nozzle was reduced from 2.5 m to 600 mm.

4.1.1.6 Final TTC setup on the seamer

Considering the experience gained throughout the aforementioned trials the final setup that was used in the rest of the TTC experiments was built as shown in Figure 4.19. In this installation a new re-designed nozzle is used which is smaller and more robust (see Appendix). This new nozzle is also easier to use as it has single stage extraction as opposed to the double stage extraction of the BAE design.

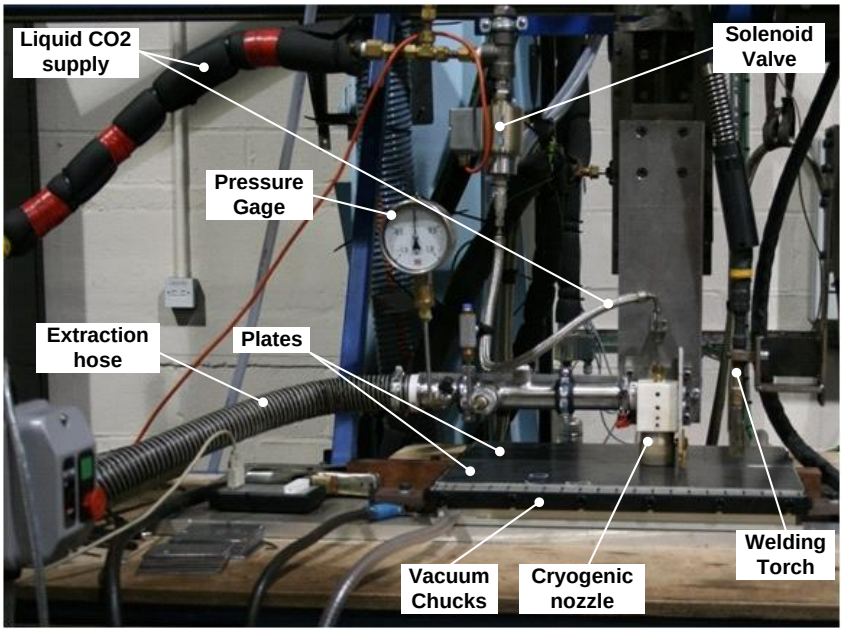

Figure 4.19 Final TTC installation on seamer (TTC Setup5)

This new setup was tested on 4 mm butt welds using the GMAW process with the parameters listed in Table 4.5.

Table 4.5 GMAW parameters of the final TTC setup testing on 4 mm butt welds

WFS [m/min]	Current [A]	Voltage [V]	Travel Speed [m/min]	CTWD [mm]	Shielding Gas Composition; Flow Rate [l/min]	Wire diameter [mm]
8.61	308	20.2	0.42	18	Ar 20 %, CO_2 20%, O_2 2%; 20	1

The separation of the cryogenic nozzle and the welding torch was 65 mm as in the previous GMAW TTC welding. The results of these experiments are shown in Figure 4.20.

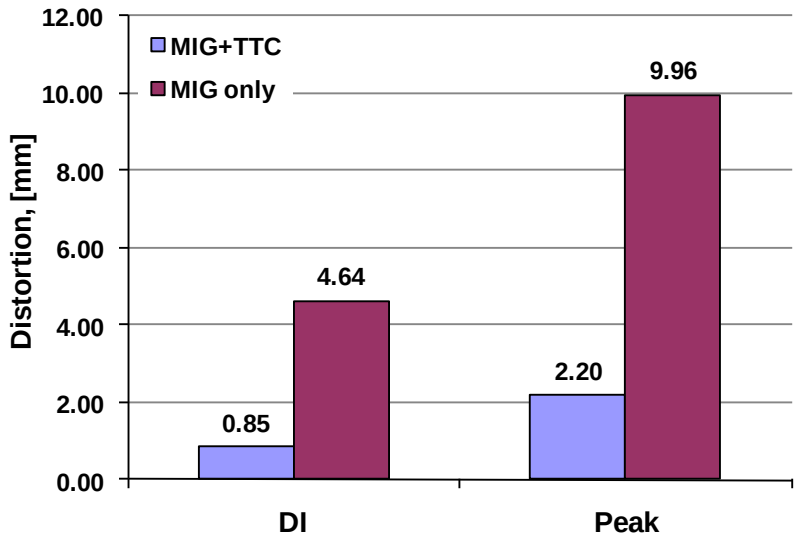

Figure 4.20 Distortion response of GMAW butt welds with and without using TTC on the final seamer installation (TTC Setup5)

4.1.1.7 Comparison of cryogenic nozzles

The cryogenic nozzle patented by Morgan [47] et al. was redesigned based on the experience gained through the technology transfer detailed above. The aim of this new design is to make the cryogenic nozzle better suited for industrial applications of TTC applied to various welding geometries. The design of the updated nozzle is detailed in Figure 4.21.

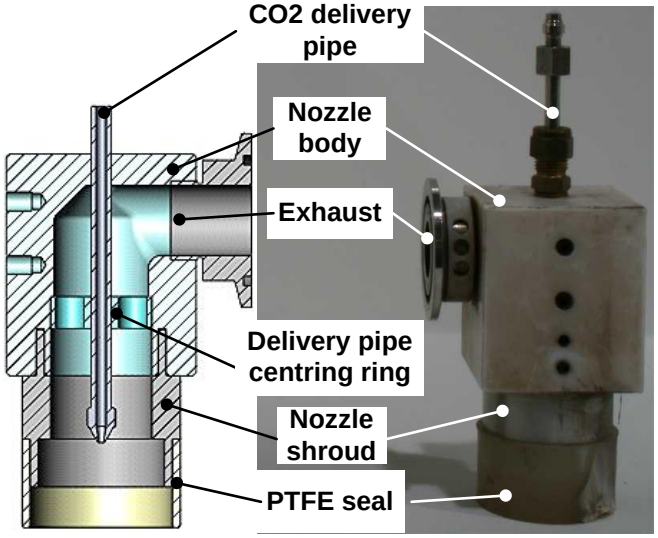

Figure 4.21 Details of the re-designed cryogenic nozzle

As Figure 4.21 shows the redesigned nozzle has single stage co-axial extraction as opposed to the dual stage co-axial extraction in the original nozzle. During previous experiments it was found that a single stage extraction is just as effective in confining the CO_2 spray within the nozzle as the dual stage extraction. Due to the single stage extraction the new nozzle became a simpler construction that can be reduced in size.

Also the extraction hose connection to the nozzle body was changed to a 90° angle from 0° to reduce the vertical footprint of the nozzle assembly as well as reducing the number of bends in the exhaust hose. Changing the orientation of the exhaust makes TTC easier to implement.

Another important feature of the updated nozzle is the vertical introduction of the CO_2 delivery pipe into the nozzle body. Through this vertical introduction, the centering of the delivery pipe within the nozzle is easier and more accurate, also the height of the liquid CO_2 delivery pipe is easily adjustable.

As the assembly of the nozzle was simplified to single piece body design with suitable shrouds the new nozzle is easily adaptable for various requirements: different nozzle diameters, nozzle heights as well as different weld geometries through the interchangeable shrouds. Adapting the re-designed nozzle to complex geometries such as fillet welds is particularly easy due to the single stage extraction.

Through all the changes in the cryogenic nozzle design detailed above the TTC process became more robust and easy to adapt to different weld geometries.

4.1.2 TTC Cooling Source Characterisation

The aims of the cooling block trials were to provide a quantitative characterisation of the cooling source of TTC and also to examine the sensitivity of the cooling source to the main parameters of the cryogenic nozzle. The purpose of these studies is to better understand the cryogenic cooling source used in this work and to help in optimising the design of the cryogenic nozzle.

To achieve this, cooling was applied on a stationary block that was pre-heated uniformly to a known temperature in a furnace. The temperature of the cooling block was recorded by both thermocouples (used to calibrate emissivity for thermal camera measurements) and thermal camera. The recorded temperature was then used in an FE model to characterise the cooling spray produced by the cryogenic nozzle.

4.1.2.1 Equipment

The cooling block trials were carried out on the seamer with the finalised CO_2 delivery system (see Figure 4.19). An overall view of the experimental setup with all the instruments and used is shown in Figure 4.22.

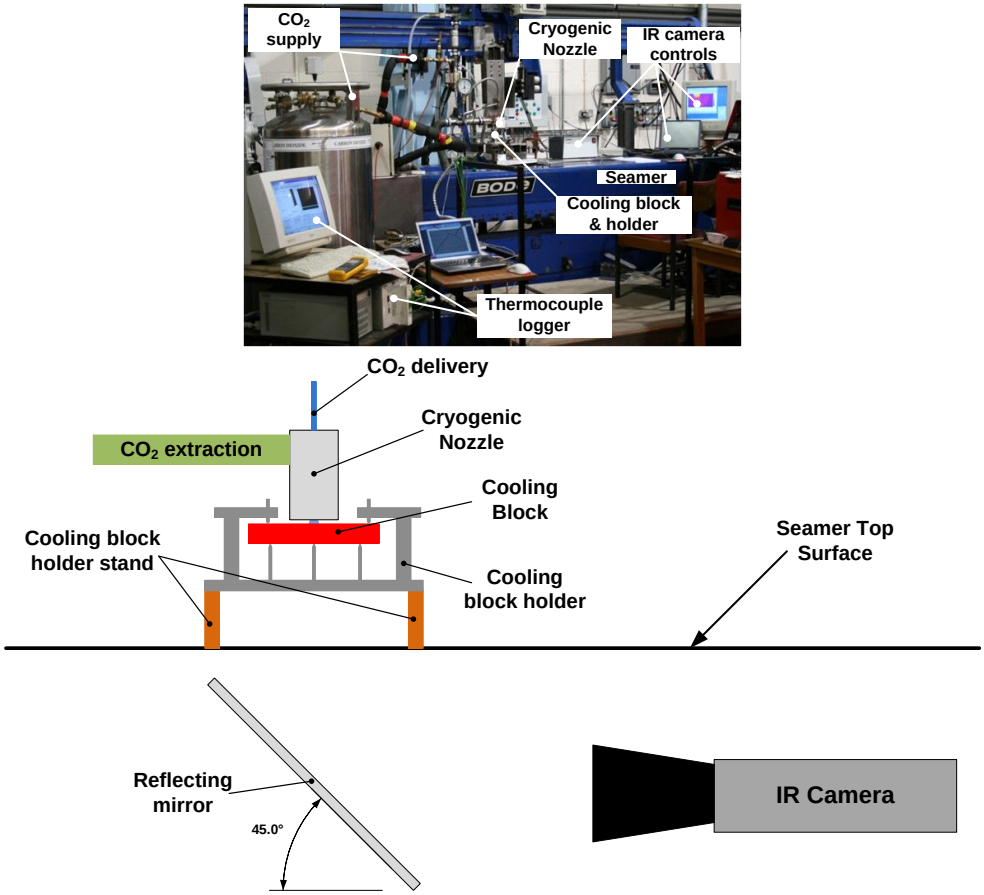

Figure 4.22 Cooling block experimental setup overview on the seamer

The setup shown in Figure 4.22 comprises of the following units:

- TTC delivery equipment
- Cooling block holder
- Thermocouple logger
- Thermal camera, reflecting mirror and their mounts
- Pre-heating oven

4.1.2.1.1 Cooling Block Holder

A holder was designed and built specifically for these trials considering the following requirements:

- Minimum thermal interaction with cooling block
- Provide firm fixture for cooling block against the high pressure/velocity CO2 spray

- Accommodate access to the bottom side of the block for thermocouples and thermal imaging
- Ease of access and use while handling pre-heated blocks
- Minimum time to mount and secure block into holder

The final design of the mount used in the cooling block trials is shown in Figure 4.23.

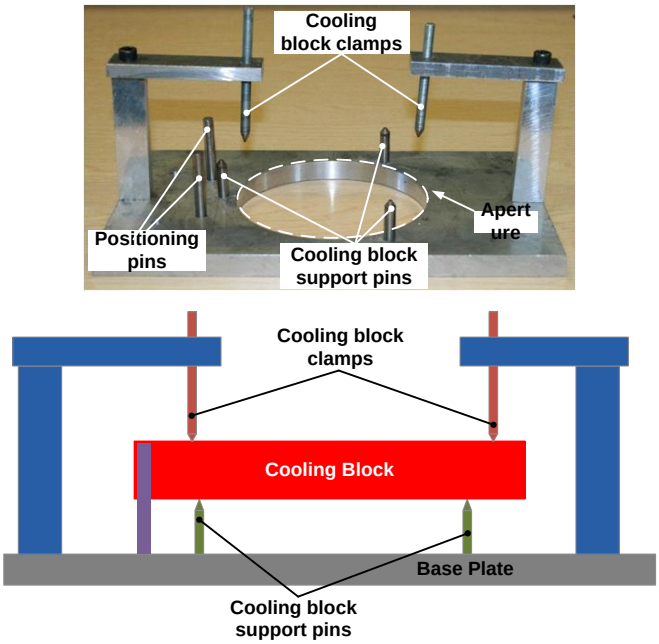

Figure 4.23 Cooling block mount used in the cooling block trials

The thermal interaction is minimised by keeping the contact area as low as possible. To achieve this, the pins supporting the blocks at the bottom side and also the pins securing it at the top side are all sharpened. Access for the thermocouples and the thermal camera is provided by a circular cut-out on the base plate of the holder.

4.1.2.1.2 Cooling Block

The blocks used in the initial experiments were borrowed from BAE ATC where the first characterisation study was carried out [14]. The geometry of this block is detailed in Figure 4.24.

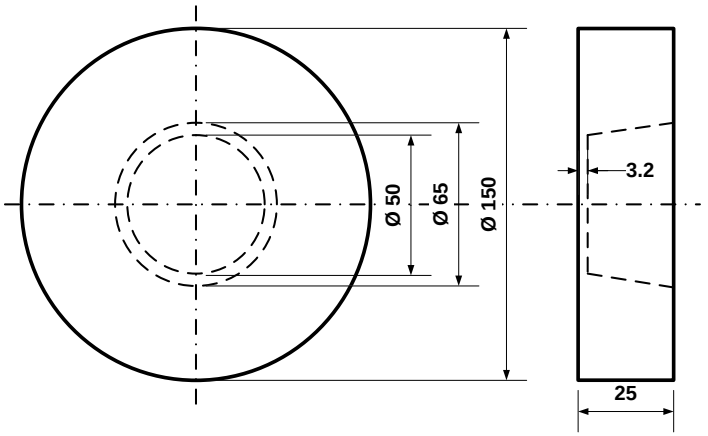

Figure 4.24 BAE cooling block used in the initial cooling block experiments

The block geometry was changed in the succeeding experiments, in which infrared thermal imaging was used to get full 2D temperature field of the same surface. The changes in the cooling block geometry were implemented due to the results in the SCAT report [14]. The cooling source characterisation results in this report shows that the diameter of the unconstrained cryogenic source is larger than the aperture diameter of the BAE block (50 mm). The modified block geometry is shown in Figure 4.25.

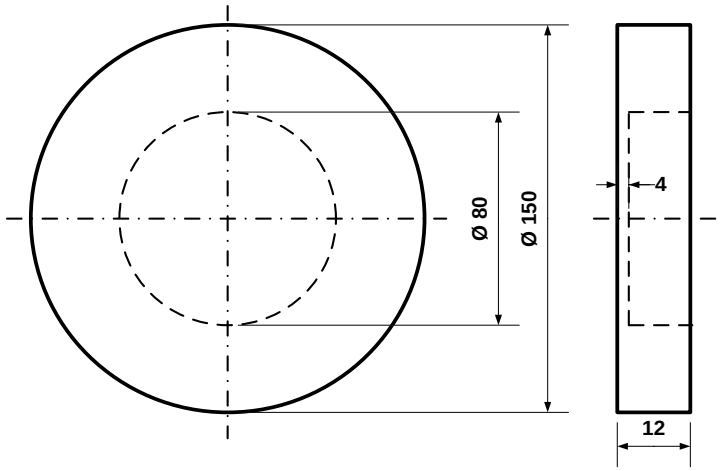

Figure 4.25 Modified cooling block used in thermal imaging cooling block trials

4.1.2.1.3 Thermocouples and thermocouple logger

Thermocouples were used to measure the temperature of the block at specific locations on the surface. The temperature range of the cooling block trials is quite wide (-60 – 400 °C), hence K-type thermocouples were used in all the cooling block experiments. The temperatures were recorded with a National Instrument NX1000 data logger.

4.1.2.1.4 Pre-Heating Oven

A Carbolite fan assisted electric oven was used to heat the cooling blocks to the required temperature before each trial. The blocks were left in the oven for an hour to ensure uniform temperature distribution.

4.1.2.1.5 Thermal Imaging Equipment

An Agema Thermovision 900 thermal camera was used in the cooling block trials. This camera was used to measure temperature via the thermal emission of the surface to be measured. The camera and its complementary accessories are shown in Figure 4.26.

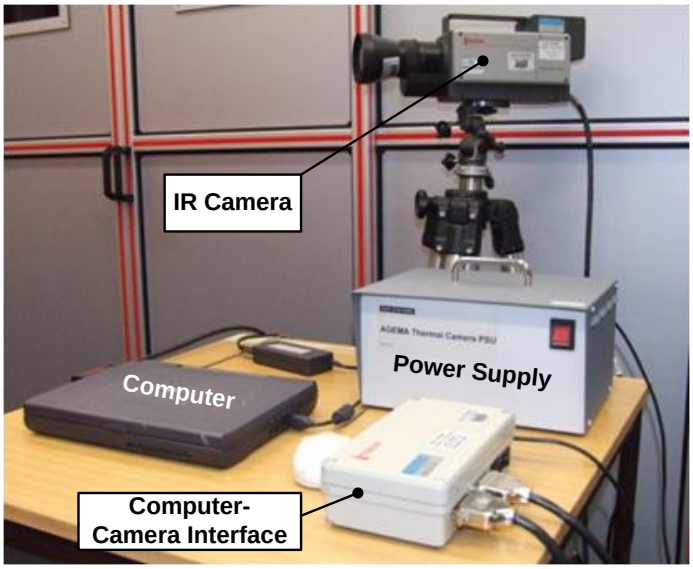

Figure 4.26 Agema Thermovision 900 thermal camera and its accessories

This thermal camera was placed in the V-shape channel of the seamer on a platform with a reflective aluminium surface acting as a mirror. The mirror was positioned at 45° angle in order to record the temperature of the bottom web surface of the cooling block. This arrangement of the thermal camera and the mirror relative to the cooling block and the cryogenic nozzle on the seamer is illustrated in Figure 4.22.

4.1.2.2 Experimental Procedure and Plan

The cooling block experiments were carried out using the following the steps:

1. Pre-heat cooling block in the oven for an hour before trial (monitor temperature using thermocouples)
2. Chill CO_2 delivery line while the block is in the oven (shortly before removing the block from the oven)
3. After one hour take block out of oven and place in the block holder
4. Connect thermocouples and start recording temperatures with both the thermocouple logger and thermal camera
5. Wait until the thermocouples indicate the required pre-heat temperature
6. Open CO_2 delivery valve and start the extraction blower approximately the same time.
7. Spray the cooling block surface for 30s
8. Close CO_2 delivery valve (stop spray)
9. After approximately 10s stop recording the temperature with both the thermocouple logger and thermal camera

During some initial cooling block trials and the technology transfer of TTC the following parameters were identified as possible main parameters, see Figure 4.27 for illustrating the parameters:

- Gap between the PTFE seal and cooled surface, Air Entrainment Gap (AEG)
- Height of Amal jet relative to the weld surface (z_A)
- Extraction, quantified as differential (relative to atmospheric pressure) pressure in the extraction pipe (p_e)
- Amal jet size
- Cryogenic nozzle shroud internal diameter (D_n)

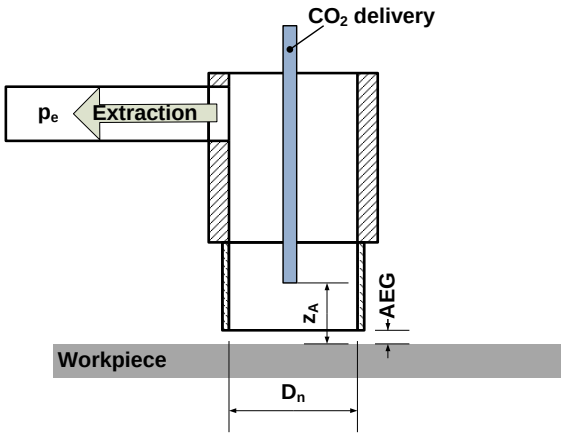

Figure 4.27 Parameters of experiments varied in the thermal camera cooling block trials

The range of variation of these parameters in the cooling block trials is listed in Table 4.6.

Table 4.6 Parameters varied in the cooling block experiments

Experiment ID	Jet size	p_e [mbar]	D_n [mm]	Z_A [mm]	AEG [mm]	T_{pre} [°C]
CB1.1	250	0...-190	45	25	1	350
CB1.2	250	-120	45	25...55	1	350
CB1.3	250	-120	35...55	25	1	350
CB1.4	170...500	-120	45	25	1	350
CB1.5	250	-120	45	25	1...2	350
CB1.6	250	-120	45	25	1	250...350

In all the heat source characterisation trials the parameters were changed relative to a baseline experiment (set of parameters). The parameters of this baseline experiment are detailed in Table 4.7.

Table 4.7 Parameters values of the TTC cooling source characterisation baseline experiment

Parameters	Value
p_e [mbar]	-150 mbar
z_A [mm]	25 mm
D_n [mm]	45 mm
Z_A [mm]	25 mm
AEG [mm]	1 mm
T_{pre} [ºC]	350 °C

4.1.2.3 Thermal camera calibration

To obtain accurate temperature recordings with the thermal camera, the correct surface emissivity needs to be determined. This is done by calibrating the surface

emissivity during measurements with the temperature recordings of a thermocouple at a known location. The thermal camera calibration in the cooling source characterisation experiments was carried out following steps below:

1. Location of thermocouples on the thermal camera image and extracting the temperature history of that location
2. Compare the extracted temperature history with the temperature recordings of the thermocouple previously located on the thermal image
3. Calculate surface emissivity at the thermocouple location

The first challenge in calibrating the thermal camera is to accurately locate the thermocouple on the thermal image and to position a virtual thermocouple onto the thermal image to extract the same temperatures as the thermocouple does. The most accurate method of doing this is to highlight a narrow temperature range that covers the location of the thermocouple and position the virtual thermocouple on the highlighted temperature band as illustrated in Figure 4.28.

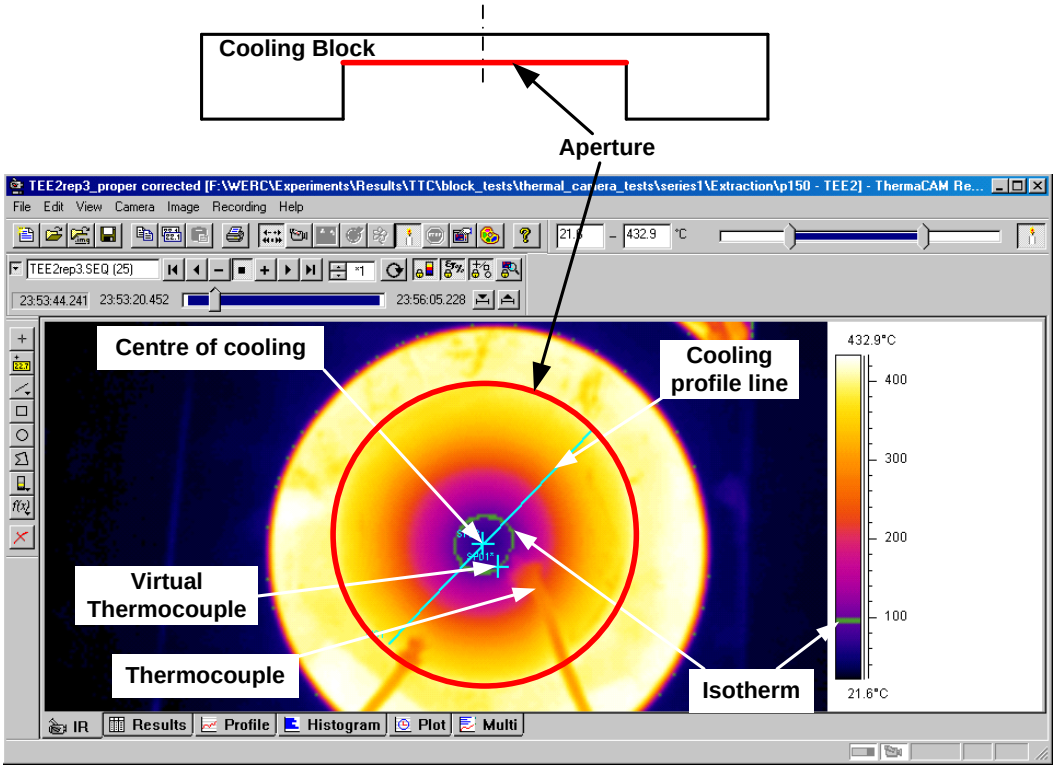

Figure 4.28 Schematics of the thermal camera calibration: positioning the virtual thermocouple with isotherm function in ThermaCAM Researcher Pro 2.9

Using the virtual thermocouple the temperature history of its location was extracted and compared to the thermocouple recordings. After aligning the time axis for each thermal history to have the CO_2 spray start at the same time, the

temperatures were compared (see Figure 4.29). In this comparison the thermocouple temperature value at a specific time was then used to calculate the surface emissivity using the thermal camera recording and analysing software ThermoCAM Researcher Pro 2.9. The calculated surface emissivity was then applied on all the frames of the thermal camera recording.

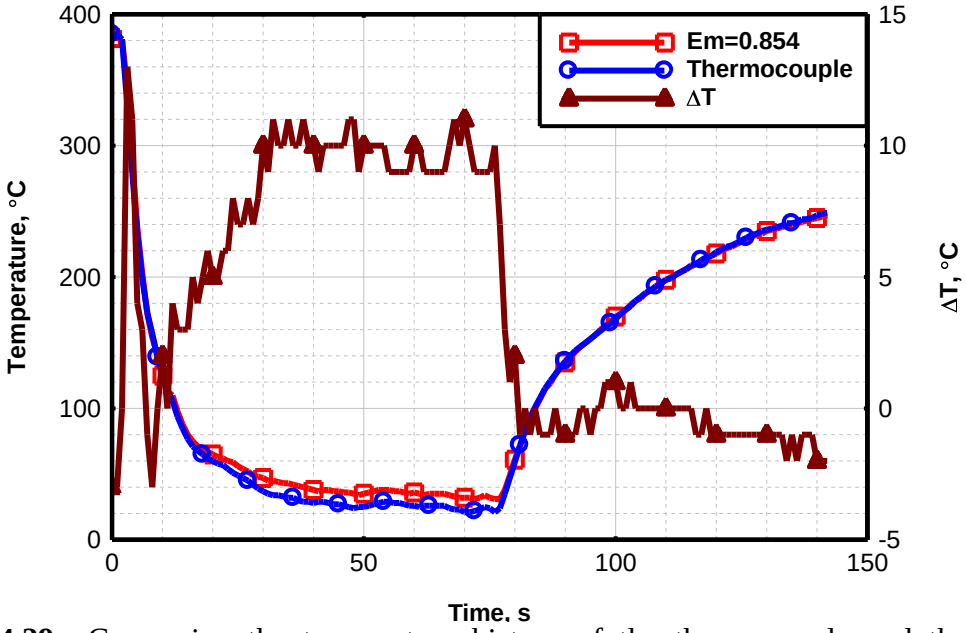

Figure 4.29 Comparing the temperature history of the thermocouple and the virtual thermocouple with the un-calibrated and calibrated values

Each cooling source experiment was calibrated individually following the method described above.

4.1.3 Application of TTC on Butt Welds

The aim of the butt weld TTC experiments was to examine the process sensitivity and limitations of TTC. These aims were achieved by applying the cryogenic CO_2 cooling on GTAW butt welds and varying the main process parameters of the cryogenic CO_2 cooling.

4.1.3.1 Specimen Material and Geometry

In the butt weld TTC experiments 2 mm thick XF350 grade steel was used the main properties of which are shown in Table 4.8 [62].

Table 4.8 Mechanical properties and chemical composition of XF350 steel

UTS, MPa	YS, MPa	Chemical Composition, [wt%]							
		C	Si	Mn	P	S	N	Al	Ti
474	368	0.59	0.21	0.61	0.017	0.008	0.006	0.047	0.0012

The geometry of the panels used in the butt weld experiments is shown in Figure 4.30. [62]

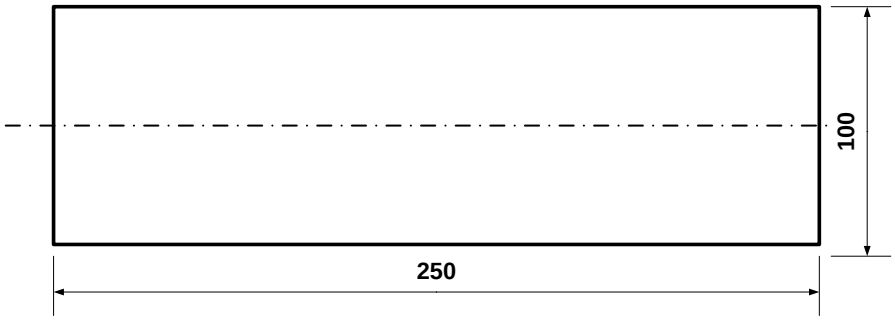

Figure 4.30 Panel geometry of the 2 mm butt welded plates

4.1.3.2 Equipment

The butt weld experiments were done on the seamer with the CO_2 delivery system described in Figure 4.19.

4.1.3.3 Experimental Plan

In the butt weld TTC trials, three sets of experiments were carried out: one examining the effect of Amal jet size (proportional to CO_2 flow rate), another the AEG and the final set investigating the effect of Travel Speed on the distortion reduction of the TTC process.

The cooling power delivered is proportional to the size of the Amal jet.. Therefore this parameter is expected to have a significant influence on the distortion reduction of TTC. The Amal jet size range and the welding parameters used in this set of experiments are listed in Table 4.9 (CW1).

The gap between the silicon seal of the nozzle and the cooled surface was previously observed to be an important parameter of the cryogenic cooling. This gap defines the air entrainment into the cryogenic nozzle during cooling, and

therefore has a major influence on the balance in the flow of CO_2 delivery and extraction.

Butt welds with TTC using different Air Entrainment Gaps (AEG) were produced in this study. The range of AEG values used along with the welding parameters used are listed in Table 4.9 (CW2).

Table 4.9 Welding and cooling parameters used in the TTC GTAW trials (S_{nt} designates the separation between the centres of the welding heat source and cooling source)

Experiment ID	Welding Conditions		Cooling Parameters					
	Current [A]	Travel Speed [m/min]	S_{nt} [mm]	Jet size	p_e [mbar]	D_n [mm]	Z_A [mm]	AEG [mm]
CW1	130	0.25	70	250-500	-120	45	25	1
CW2				340				0.5...2
CW3.1								1
CW3.2	180	0.35						
CW3.3	230	0.45						
CW3.4	250	0.5						

Travel speed is one of the main process parameters to examine when investigating the sensitivity and limitations of the TTC process. The importance of travel speed was pointed out in an earlier study as well [45]. The welding and cooling parameters of these trials are shown in Table 4.9 (CW3.1-3.4).

4.1.4 Application of TTC on Fillet Welds

The aim of the TTC fillet weld experiments was to examine the applicability of TTC on different weld geometries (other than butt weld), as it was only applied on butt welds in all previous works. Application of the TTC on fillet welds was implemented by adopting the cryogenic nozzle and the silicon seal to the shape of the joint geometry.

4.1.4.1 Specimen Material and Geometry

The geometry (particularly the thickness) was adopted from ship building application, in which buckling distortion proved to be the biggest challenge. This geometry is detailed in Figure 4.31.

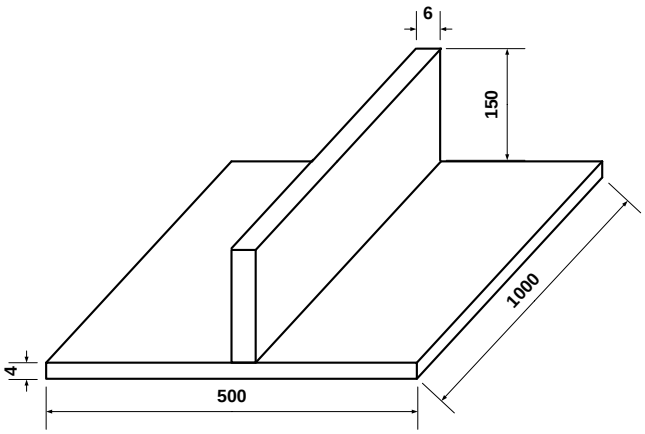

Figure 4.31 Fillet weld panel geometry used in the TTC fillet weld application

The material of fillet weld specimens was S355 grade structural steel as this grade has very similar material properties (UTS, YS) to the DH36 grade that is used in shipbuilding, but is widely available. The chemical composition and material properties of the S355 plates used are listed in Table 4.10.

Table 4.10 Chemical composition and mechanical properties of 4 and 6 mm thick S355 steel

Thickness [mm]	Chemical Composition [wt%]								UTS [N/mm^2]	YS [N/mm^2]
	C	P	S	Mn	Si	Al_{sol}	N	Cr		
4	0.179	0.023	0.02	0.998	0.003	0.056	0.00444	0.024	531	439
6	0.0127	0.012	0.034	1.071	0.0031	0.05	0.0031	0.026	556	457

4.1.4.2 Equipment

The TTC fillet weld experiments were carried out on the seamer with the CO_2 delivery and extraction system detailed in Figure 4.19 (TTC Setup5). The fillet weld components were clamped in a frame built specifically for these experiments to suit the geometry of the joint as shown in Figure 4.32

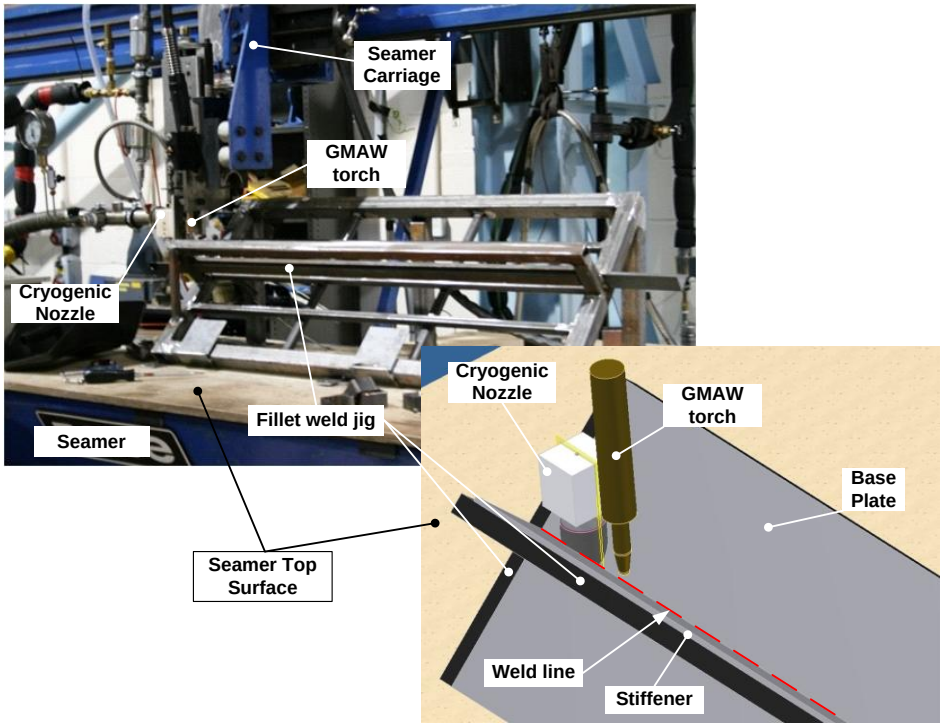

Figure 4.32 TTC fillet weld experimental setup on seamer

The nozzle shroud and the silicon seal at the end of it were modified to best fit the V-shape of the fillet weld geometry. The modification meant developing a cylindrical-to-V shape adapter (part on the top left of Figure 4.33) and matching silicon seal (top right part in Figure 4.33). The end of the seal was also trimmed to allow clearance for the weld bead as illustrated in Figure 4.33.

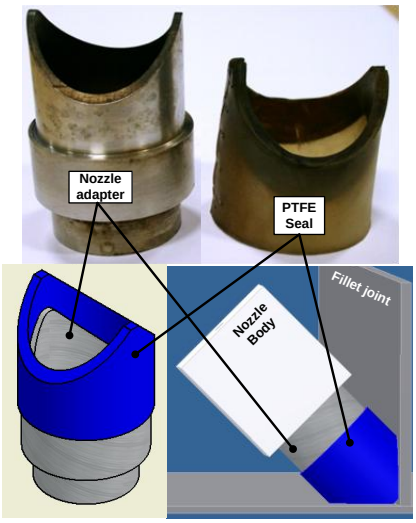

Figure 4.33 Cryogenic nozzle shroud and silicon seal adapted to fillet welds

The welding power supply used in these experiments was a Lincoln PowerWave 450 M. The welding parameters were obtained from BVT Surface Fleet and were

adapted to the above described setup. The final welding parameters are listed in Table 4.11.

Table 4.11 GMAW parameters used in the TTC fillet weld experiments

Travel Speed [m/min]	**Current** [A]	**Voltage** [V]	D_w [mm]	**CTWD** [mm]	**Shielding Gas Type / Flow Rate** [l/min]
0.42	220	19.8	1.2	15	Ar 20 %, CO2 20%, O2 2% / 18

4.1.4.3 Experimental Plan

The cooling parameters used in the TTC fillet weld experiments are listed in Table 4.12. The extraction pressure was set to -200 mbar based on the butt weld application of the TTC.

Table 4.12 Cooling parameters used in the TTC fillet welding experiments

Cooling Parameters	**Parameter Value**	**Experiment ID**
Amal Jet Size	250	CFW
z_A [mm]	25	
S_{nt} [mm]	65	
D_n [mm]	45	
AEG [mm]	0.8	
p_e [mbar]	-200	

4.1.5 Distortion measurements

Different techniques of distortion measurements were used throughout this work. The different methods are described in this section.

4.1.5.1 Measurement with Vernier

Measuring the distortion was found to be the simplest and of good accuracy using Vernier callipers with a measurement accuracy of 0.1 mm. The distorted panels were laid on a flat surface (table) with one corner of the plate clamped to prevent movement during measurement. Measuring distortion this way allows measurements around the circumference of the plate only as the flat surface (table) provides the reference for the measurement. Based on this limitation the pattern for measuring distortion with Vernier calliper is as shown in Figure 4.34.

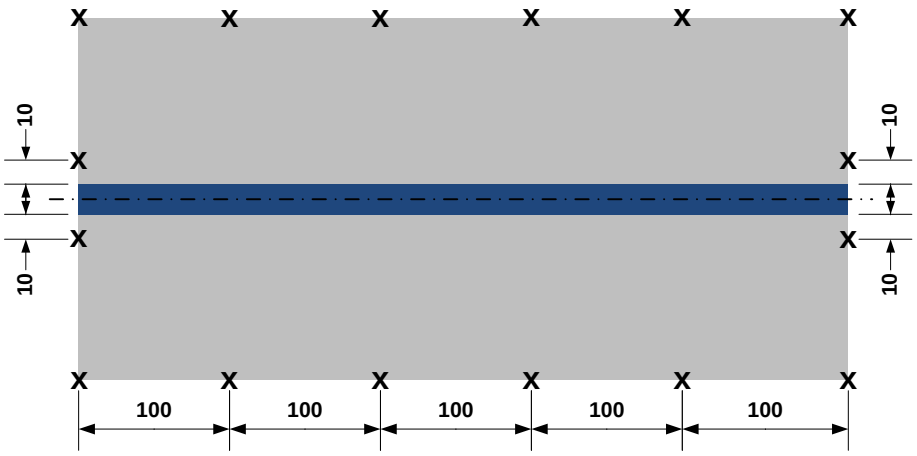

Figure 4.34 Distortion measurement pattern with Vernier calliper tool on a welded panel

The pattern for all size of plates measured with Vernier calliper is as follows: one measurement at every 100 mm along the long edge of the welded panel and one measurement at the beginning and at the end of the weld 5 mm from the weld toe.

4.1.5.2 Measurement with LVDTs

LVDTs (Linear Variable Differential Transformer) provide better accuracy (0.01 mm) as Vernier callipers with the advantage of moveable reference. This means that the measurement reference can be moved from the flat bed and the LVDTs can be mounted on a carriage moving along the plate to be measured as seen in Figure 4.35. This way distortion can be measured not only around the edges of the plate but over the whole surface of the plate.

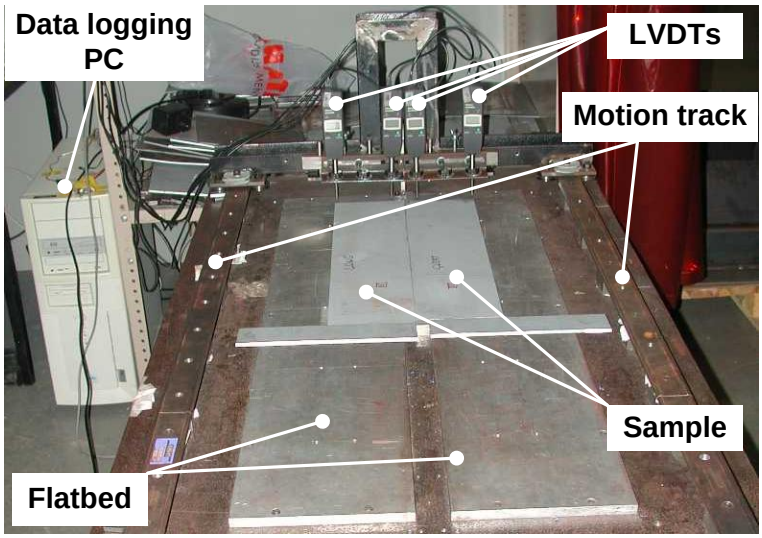

Figure 4.35 Distortion measuring bed with LVDTS on a moving carriage

With the ability of measuring distortion further away from the panel edge the measurement points can be distributed more uniformly on the whole area of the panel to be measured as shown in Figure 4.36.

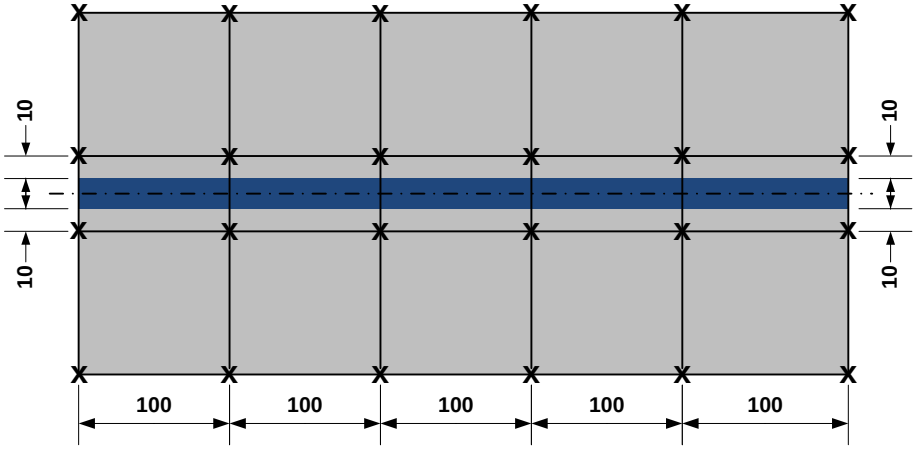

Figure 4.36 Distortion measurement pattern with LVDTs on a welded panel

4.1.5.3 Measurement with laser scanning arm

The most accurate and most sophisticated distortion measuring device used in this project was an Omega scanning arm with a laser scanning head shown in Figure 4.37. The Omega scanning arm has an accuracy of 80 µm and provides the ability to measure (scan) practically the entire surface with thousands of measured points on the surface.

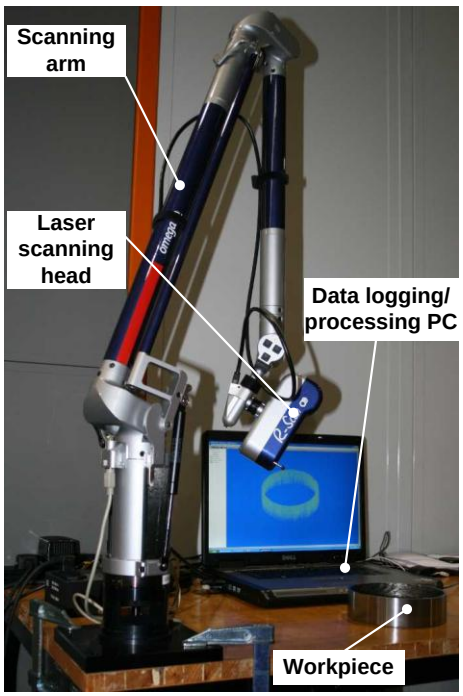

Figure 4.37 Omega scanning arm with laser scanning head

With this metronomic equipment there is no measuring pattern as the entire surface is scanned with the laser stripe giving a high resolution virtual replica of the workpiece which is then further processed to give meaningful results.

As this work is concentrating on buckling distortion, only the buckling component of the overall distortion is considered in the aforementioned measurements. A relatively small amount of out of plane distortion is generally expected to be measured even if 100 % buckling distortion reduction is achieved. The main reasons for this remnant distortion are other types of (mostly angular) distortion and a protruding weld root typical in GMAW butt joints.

Angular distortion is expected in butt welds and in fillet welds when the weld cap is significantly larger than the weld root. This type of weld cross section (see macrograph in Figure 4.38) is typical when welding closed butt joint with GMAW where the high current necessary for full penetration results in high wire feed speed. The high wire feed speed then produces a large cap at the top of the weld bead. Another typical appearance of angular distortion is fillet welded panels where the shrinkage of the weld during cooling displaces the outer edges of the base panel.

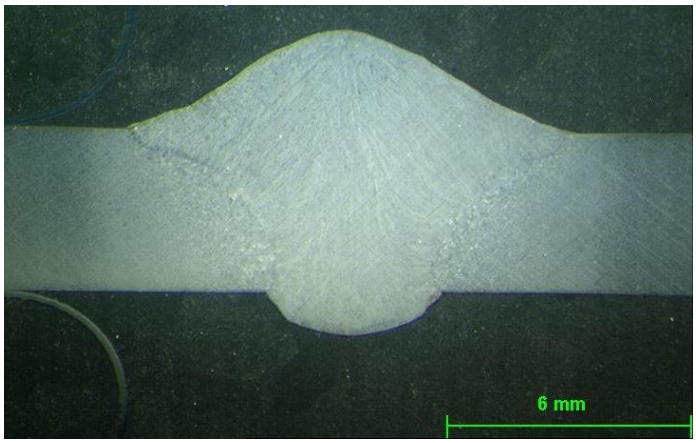

Figure 4.38 Macro section of 4 mm thick S355 mild steel GMAW butt weld with large cap and small root

The welded panels are laid on a flat surface when distortion is measured. This means that the weld root of a GMAW butt joint (such as the one shown in Figure 4.38) acts as a pivot around which the panel rotates. Due to this rotation, one edge of the welded panel is vertically displaced, which is then reflected as distortion in the distortion measurement.

Due to these reasons, the aforementioned distortion measuring techniques do not show buckling free panels as distortion free.

Two distortion values are used throughout this work to evaluate and compare the distortion of welded panels: peak distortion and Distortion Index (DI). The peak distortion is the maximum measured value, whereas the

$$DI = \frac{\sum_{i=0}^{n} D_i}{n} \tag{4.1}$$

where:

- DI: disotrion index, mm
- D_i: measured distortion values
- n: number of measurement points in measured pattern (see measurement patterns in Figure 4.34 and Figure 4.36)

4.1.6 Residual Stress measurements using neutron diffraction

Residual stress measurements were carried out on both TTC and TTH treated samples to investigate the affect of these techniques on the welding residual stress profile and to have a deeper understanding of these techniques. A number of techniques have been developed to measure residual stresses such as curvature, hole drilling and compliance mechanical methods; electron, X-ray and neutron diffraction and techniques such as magnetic, ultrasonic, thermoelastic and photoelastic methods [63].

Neutron diffraction is chosen as a measurement technique because it is relatively easy to determine the stress values within the specimen with good accuracy (±7-20 MPa) and high spacial resolution [64].

4.1.6.1 Principles of residual stress measurements using neutron diffraction

When a neutron beam (of wavelength λ) is incident on a crystalline material, a diffraction pattern is produced that is characterised by sharp peaks at different angles. The angular positions of these peaks for a family of crystallographic planes of lattice parameter *a* are given by Bragg's law:

$$2d\sin\theta = n\lambda \tag{4.2}$$

where n is an integer and 2θ is the diffraction angle as shown in Figure 4.39,a.

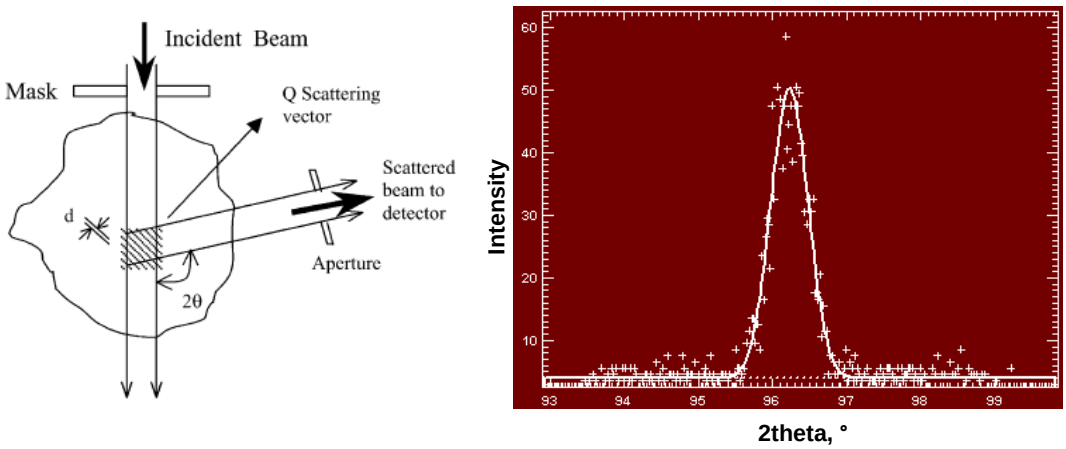

Figure 4.39 a) Principles of neutron diffraction measurements [64] b) example of a measured neutron peak profile with Gaussian fitting using LAMP

If a monochromatic beam with constant wavelength is used for the measurements (as is in this project), changes in the lattice parameter (*a)* will result in a proportional change (Δθ) in the positions of the characteristic peaks in the diffraction pattern. This means the lattice strain in the direction of the scattering vector *Q* (see Figure 4.39,a) can be calculated as:

$$\varepsilon = \frac{\Delta d}{d} = -\Delta\theta\cot\theta \tag{4.3}$$

This method examines a single diffraction peak and the angular position of the peak is determined by a Gaussian fitting routine (see Figure 4.39,b). The error of this peak fitting is provided by the fitting routine and is showed on the measured residual stress profiles.

In order to calculate absolute strains the unstrained lattice parameter (a_0) must be known. The a_0 unstrained lattice parameter is calculated by assuming bi-axial stress state where the longitudinal strain is proportional to longitudinal stress as strains in other two directions are negligible compared to that in the longitudinal sirection [21]. If the principle directions are known (and coincide with *x*, *y* and *z* coordinate directions) measurements in three orientations are sufficient to determine the principal stresses from strains using Hooke's law:

$$\sigma_x = \frac{E}{1+\nu \quad 1-2\nu}\left[\; 1-\nu \;\; \varepsilon_x + \nu \;\; \varepsilon_y + \varepsilon_z \; \right] \tag{4.4}$$

where:

- σ_x – Stress in 'x' direction
- ν – Poisson ratio
- ε_x, ε_y and ε_z – Strain in x,y and z direction
- E – Young's modulus
- σ_y and σ_z can be calculated with the corresponding equations of Equation (4.4).

4.1.6.2 Experimental setup of residual stress measurements

All the residual stress measurements were carried out in the Institut Laue-Langevin (ILL), France in the SALSA instrument. This instrument uses monochromatic neutron beam generated by a nuclear reactor.

A schematic of the instrument layout of SALSA is shown in Figure 4.40. Slits were used on both the incident and scattered beam to define the gauge volume (cross section of incident and diffracted beams) for the measurements.

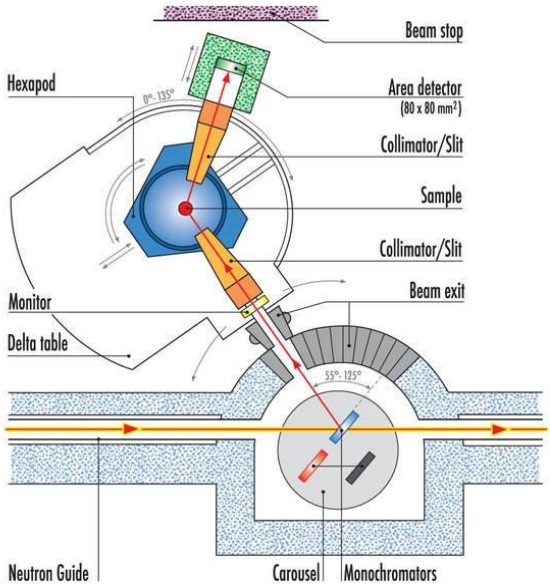

Figure 4.40 Schematics of the SALSA instrument layout used in the residual stress measurement experiments

The crystallographic plane measured is the 211 plane, and the elastic constants used are bulk constants as the 211 plane closely follows these properties. The stress free lattice parameter (a_0) is calculated through plain stress condition [65].

The samples to be measured were clamped onto and manipulated by a hexapod as shown in Figure 4.41. Care had to be taken not to impose any external local strains by the clamping. Therefore the samples were supported from both sides at the same locations.

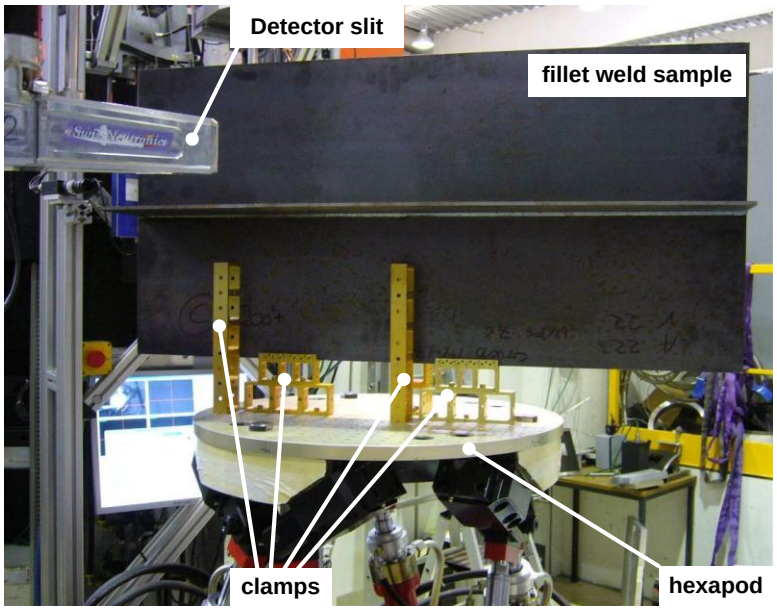

Figure 4.41 Fillet welded sample clamped onto the hexapod used to manipulate the samples

4.1.6.3 Experimental plan of residual stress measurements

In the residual stress measurements experiments six samples were measured for all three (longitudinal, transverse and normal) direction in order to be able to determine the residual stresses. The welded samples were both butt and fillet joints and with and without applying thermal tensioning as detailed in Table 4.13.

Table 4.13 List of samples used for the residual stress measurements.

Sample No.	Joint geometry	Sample description
Sample 1	Butt	TTC Setup5+GMAW
Sample 2	Fillet	CFW
Sample 3	Butt	As welded
Sample 4	Butt	TTH BW1.3
Sample 5	Fillet	As welded
Sample 6	Fillet	TTH FW 1.3

4.2 Numerical characterisation of cryogenic CO_2 cooling

The experimental characterisation of the cooling source of TTC is limited to temperature measurements and does not give direct information about the cooling power, intensity or distribution of the cooling intensity. Hence a full characterisation is only possible with the aid of numerical methods, such as Finite Element Modelling (FEM).

In this section the cooling power of the cryogenic spray is determined using both an analytical method based on jet impingement cooling theory and FEM using the thermal data obtained in the cooling source characterisation experiments detailed previously.

4.2.1 Theoretical cooling power of cryogenic CO_2 spray

The cooling power of the CO_2 spray can be determined if the flow rate and the latent heat of sublimation for solid carbon-dioxide are known. The mass flow rate of CO_2 can be calculated using Bernoulli's theory for incompressible flow:

$$\frac{p_1}{\rho}+\frac{v_1^2}{2}+g\times z_1=\frac{p_2}{\rho}+\frac{v_2^2}{2}+g\times z_2+\frac{\Delta p_{1-2}}{\rho} \tag{4.5}$$

where:

- p - pressure at the inlet and outlet
- ρ - density of liquid CO_2
- v - velocity of CO_2 spray

- g - gravitational constant
- z -: geodetic height.

Equation (4.5) can be applied to the cryogenic CO_2 spray via an Amal jet with the parameters shown in Figure 4.42.

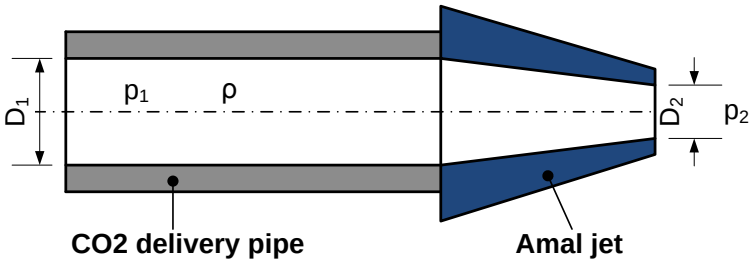

Figure 4.42 Schematic of cryogenic CO_2 spray flow conditions with the inlet and outlet parameters displayed

Δp_{1-2} pressure drop across the Amal jet in Equation (4.5) is assumed to be zero and is considered via a coefficient of discharge further below. The flow parameters shown in Figure 4.42 as well as some liquid CO_2 properties are detailed in Table 4.14.

Table 4.14 Flow rate calculation parameters

Parameter name	Parameter value
Inlet pressure, p_1, [bar]	20
Outlet pressure, p_2, [bar]	1
Inlet diameter, D_1 , [mm]	12
Outlet Diameter, D_2, [mm]	Amal jet diameter, see Figure 2.5
Density of liquid CO_2 at -18°C, [kg/m^3]	1022.7
Specific Latent heat of sublimation, [kJ/kg]	570.97

The velocities of the carbon dioxide flow in (4.5) can be substituted with volumetric flow rates:

$$v_1 = \frac{4 \times Q}{\pi \times D_1^2}, \quad v_2 = \frac{4 \times Q}{\pi \times D_2^2} \tag{4.6}$$

where:

- Q - volumetric flow rate
- D - diameter

It can be assumed that the pressure drop is negligible (this is included in coefficient of discharge, detailed further below) and $z_1=z_2$. With these assumptions

the pressure drop through the orifice, due to the velocity increase from (4.5) and (4.6) is:

$$\frac{p_1 - p_2}{\rho_{LCO_2}} = \frac{1}{2}\left(\frac{16 \times Q^2}{\pi^2 \times D_2^4} - \frac{16 \times Q^2}{\pi^2 \times D_1^4} \right) \tag{4.7}$$

From equation (4.7) the volumetric flow rate is:

$$Q = \sqrt{\frac{1}{1-\left(\frac{D_2}{D_1}\right)^4}} \frac{\pi D_2^2}{4} \sqrt{\frac{2 \ p_1 - p_2}{\rho_{LCO_2}}} \tag{4.8}$$

The first part of equation (4.8) only depends on the ratio of the inlet and outlet diameters. Introducing the diameter ratio:

$$\beta = \frac{D_2}{D_1} \tag{4.9}$$

and substituting it into Equation (4.8), the flow rate becomes:

$$Q = \frac{1}{\sqrt{1-\beta^4}} \frac{\pi D_2^2}{4} \sqrt{\frac{2 \ p_1 - p_2}{\rho_{LCO_2}}} \tag{4.10}$$

$$Q = \frac{C}{\sqrt{1-\beta^4}} \frac{\pi D_2^2}{4} \sqrt{\frac{2 \ p_1 - p_2}{\rho_{LCO_2}}} \tag{4.11}$$

where:

- C - coefficient of discharge
- β- expansion coefficient

The coefficient of discharge in (4.10) can be calculated using the following equation [66]:

$$C = 0.5961 + 0.0261 \times \beta^2 - 0.216 \times \beta^8 + 0.000521 \times \left(\frac{10^6 \times \beta}{\mathrm{Re}_D}\right)^{0.7} +$$
$$+ \ 0.0188 + 0.0063 \times A \ \times \beta^{3.5} \times \left(\frac{10^6 \times \beta}{\mathrm{Re}_D}\right)^{0.3} + \qquad (4.12)$$
$$+ \ 0.043 + 0.08 \times e^{-10 \times L_1} - 0.123 e^{-7 \times L_1} \ \times \left(1 - 0.11 \times \left(\frac{19000 \times \beta}{\mathrm{Re}_D}\right)^{0.8}\right) \times$$
$$\times \frac{\beta^4}{1-\beta^4} - 0.031 \times \left(\frac{2 \times L_2}{1-\beta} - 0.8\left(\frac{2 \times L_2}{1-\beta}\right)^{1.1}\right)\beta^{1.3}$$

where:

- Re_D - Reynolds number:

$$\mathrm{Re}_D = \frac{v_1 D}{\nu} = \frac{\rho_{LCO_2} v D}{\mu} \qquad (4.13)$$

One can notice that the coefficient of discharge is a function of the flow rate through the Reynolds number. To solve this problem Q becomes an iterative function, into which the coefficient of discharge is iterated.

Once the volumetric flow rate (Q) is known the mass flow rate (q_m) can be calculated:

$$\dot{m} = Q \times \rho_{LCO_2} \qquad (4.14)$$

The mass flow rate for some Amal jets used in this work is shown in Figure 4.43.

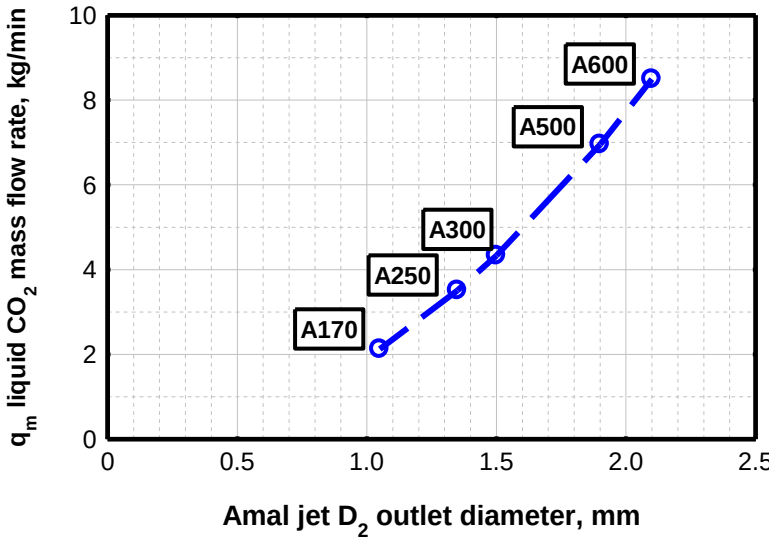

Figure 4.43 Liquid CO_2 mass flow rates of different Amal jet sizes

The cooling power of the cryogenic CO_2 spray - assuming 100 % solid CO_2 content within the spray - is then:

$$P = \dot{m} \times l_{subCO_2} \tag{4.15}$$

where l_{subCO_2} is the specific latent heat of sublimation of CO_2. The theoretical cooling powers of different Amal jet sizes are determined using Equation (4.15) with the flow rate values shown in Figure 4.43. These cooling powers are shown in Figure 4.44.

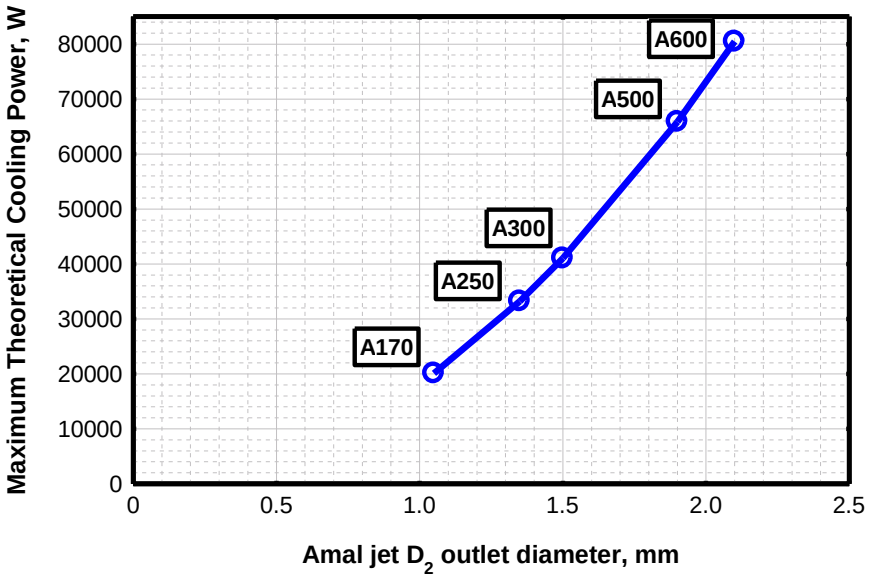

Figure 4.44 Theoretical cooling power of cryogenic CO_2 spray at different Amal jet sizes

4.2.2 Cooling Source Characterisation using FEM

As the cooling characteristics (power and intensity) of the cooling source cannot be measured directly, FE modelling was used to characterise the cryogenic spray. The aim of this FE modelling was to gain a better understanding of the cooling source behaviour as well as the TTC process itself. COMSOL Multiphysics FEM software package was utilised for the modelling work described in this section.

The temperature measurements of a cooling block experiment, shown in Figure 4.45 reveals three distinct phases. Phase I is at the start of the thermal history and is characterised by slow cooling rate (in this phase the cooling block is positioned in the cooling block holder and the only cooling present is due to natural convection and conduction). Phase II starts when the cryogenic spray is turned on at $t=t_0$. The cooling rate in this phase is significantly higher than previously. The second phase finishes and the third phase starts when the cryogenic spray stops at $t=t_1$. In phase

III the temperature increases as heat is conducted from the outer (thicker) and hotter parts into the cooler parts.

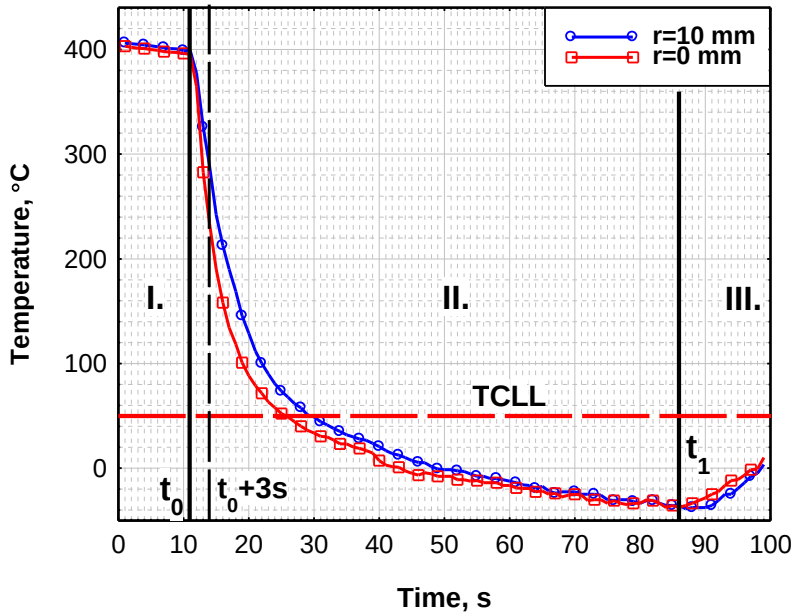

Figure 4.45 Typical temperature history of a cooling block experiment with 3 characteristic phases

The modelling of the cooling source was carried out in two steps according to the first two phases of the cooling block experiments described above. The first step in the modelling was to obtain the temperature distribution of the aperture of the cooling block immediately before the cooling is applied (Phase I – natural convection). This is necessary due to the significant amount of time (up to a minute) it took to position the cooling block in the cooling block holder, to connect the thermocouples to the thermocouple logger and to wait for the cooling block to cool down to the required pre-heat temperature.

The second step of the modelling was the actual cooling stage of the experiment when the CO_2 spray is applied on the top surface of the cooling block. The predicted temperature profiles were compared to the measured ones at 3 s from the spray start time (t_0).

4.2.2.1 Model Geometry and Mesh

The geometry of the model matches the cooling block used in the cooling source characterisation trials (Figure 4.25). As the cooling block is axi-symmetric and the

cooling source is also assumed to be axi-symmetric (CO_2 spray through cylindrical orifice), the FE model has an axi-symmetric 2D geometry.

The mesh of the FE model, shown in Figure 4.46 has 697 triangular Lagrange-Quadratic elements in total. The density near to the centre of the cooling block is increased significantly compared to the thicker, outer section of the cooling block. Hence, the mesh at the symmetry axis (centre of the cooling block) has 6 elements through the thickness. This is so, because the highest temperature gradient is expected to be in this region.

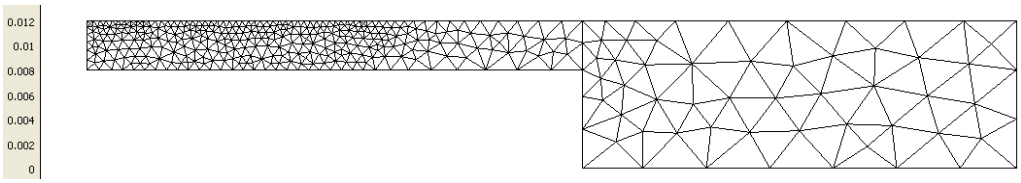

Figure 4.46 Mesh of the cooling block FE model

The elements size and density is kept the same in the region where the cooling source is applied. Further away from the cooling source the mesh size increases and density decreases in order to save calculation time for the simulation.

4.2.2.2 Material Properties

The cooling source characterisation trials were carried out on mild steel blocks, hence the material properties defined in the model are also mild steel properties. The density of the mild steel is assumed to be constant (7860 kg/m^3) whereas the thermal properties are treated as temperature dependent properties as shown in Figure 4.47 [67].

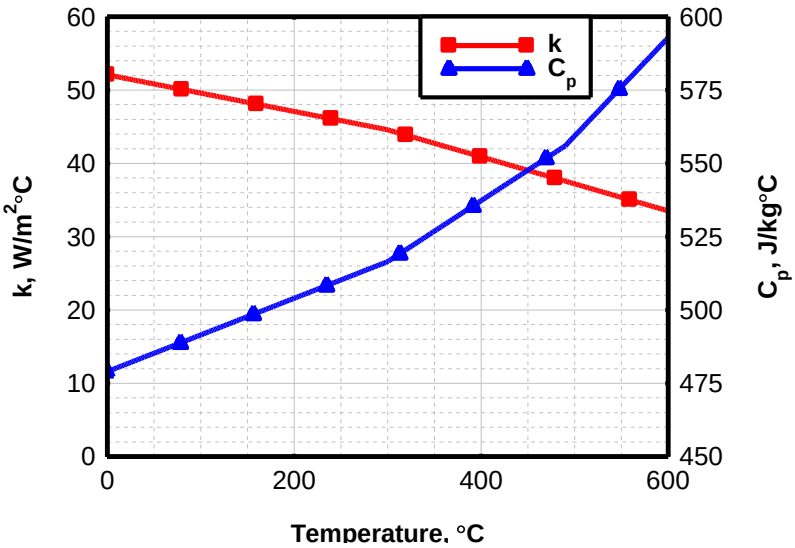

Figure 4.47 Temperature dependent heat capacity (C_p) and thermal conductivity (k) of mild steel used in the FE model of the cooling [67]

4.2.2.3 Boundary Conditions and Cooling Source Model

The thermal boundaries (shown in Figure 4.48) of the FE model are defined as convective heat losses (Equation(4.16)) according to Newton's law of cooling, with the only exception of the axial symmetry (B8 in Figure 4.48).

$$q_c = h_c(T - T_c) \tag{4.16}$$

where T_c temperature for these boundaries (B2-7) is 20°C and the heat transfer coefficients (h_c) is constant. The values of these heat transfer coefficients were obtained through simulation of experimental measurements: the cooling block was pre-heated to the required temperature (480 °C) and positioned in the cooling block holder. Temperatures were then recorded (along B7 boundary, see Figure 4.28) as the block was cooling down due to natural convection.

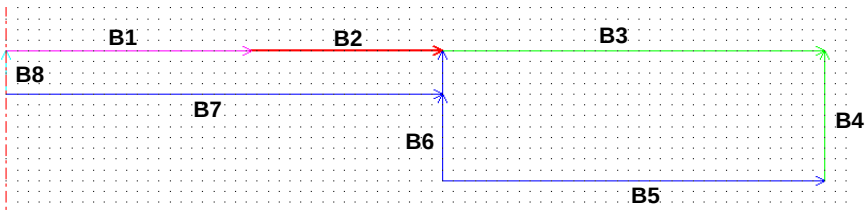

Figure 4.48 Boundary conditions labels of the cooling block thermal model

This initial natural convection cooling was then modelled by defining constant heat transfer coefficients on all boundaries (B1-7) and calculating the block temperature distribution for a period of time as it cools. The heat transfer coefficient values attained for boundaries B2-7 are shown in Table 4.15.

Table 4.15 Boundary conditions determined by (see Figure 4.48)

Boundary ID	Bounary Type	Parameters	
		h, W/m^{2}K	T_{inf}, °C
B1	Cooling Source	h_c	78.5
B2	Convective Heat Loss	35	20
B3		35	
B4			
B5		30	
B6			
B7			
B8	Axial symmetry	N/A	N/A

4.2.2.4 Cooling source model development

The cooling source in this model is represented as a convective heat loss, described in Equation(4.16)). The temperature of the cooling source (T_c in Equation(4.16)) is assumed to be the sublimation temperature (-78.5°C) of solid CO_2 at atmospheric pressure (see Figure 2.3).

As a first approach the heat transfer coefficient is represented as a top hat distribution as shown in Figure 4.49,b. As the visual best fit shows in Figure 4.49,a this heat transfer coefficient distribution did not predict the temperature distribution well. Although the temperature difference is not too large (~±20 °C within the nozzle) the curvature of the measured temperature profile – dish like dip at the core of spray is not matched well by the FE model.

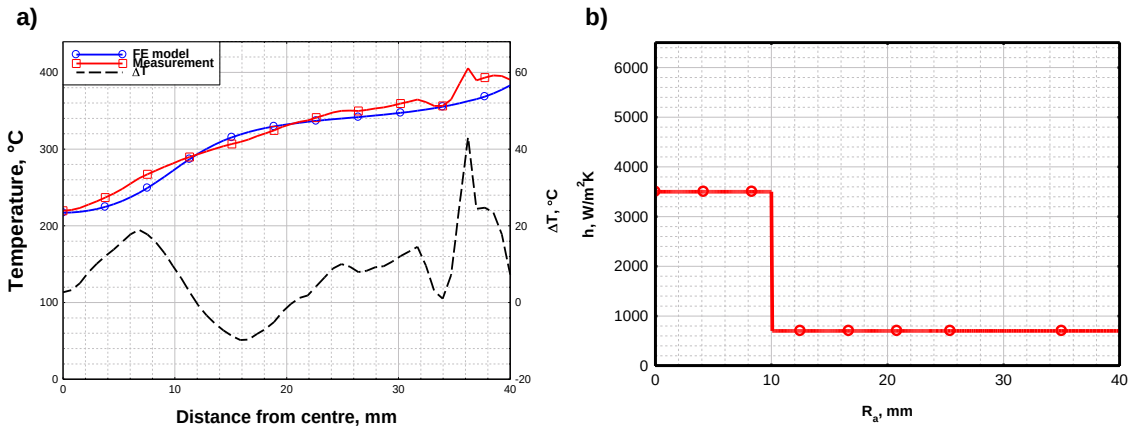

Figure 4.49 Top hat cooling source model a) temperature profile comparison along B7 boundary and b) h_c heat transfer coefficient distribution along B1 and B2 boundaries

In order to improve upon the temperature predictions of the FE model, the h_c convective heat transfer coefficient is changed to a Gaussian distribution:

$$h_c = h_p \bullet e^{-\frac{r^2}{c^2}} \tag{4.17}$$

where h_p is the peak heat transfer coefficient and c defines the width of the Gaussian distribution. The Gaussian distribution is applied to a radius corresponding to the radius of the cooling nozzle ($D_n/2$, see Figure 4.27). Variables h_p, c and h_2 (applied on B2 boundary) are varied to achieve a visual best fit of the predicted temperature profile to the one obtained experimentally.

When the cooling source described in Equation (4.17) was applied, the visual best fit shown in Figure 4.50,a was found to be inadequate: even though the difference between the measured and predicted temperatures is within a ±28°C range, the curvature of the predicted temperature does not follow the measured profile well. The r=10-r=30 mm of the calculated temperature profile over predicts the temperatures (see Figure 4.50,a). This region of over predictions is at the edge of the cooling nozzle (R_n= 22.5 mm).

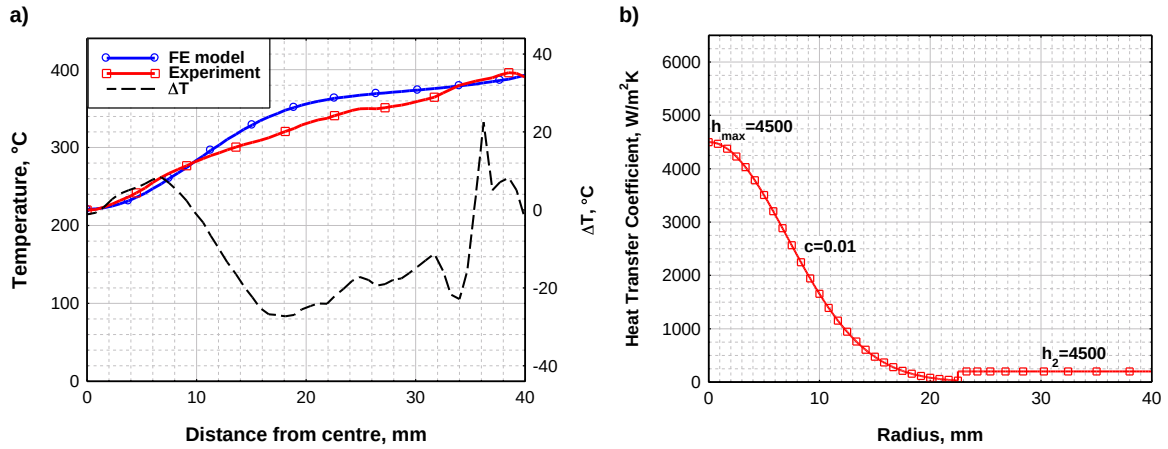

Figure 4.50 Gaussian cooling source model a) temperature profile comparison along B7 boundary and b) h_c heat transfer coefficient distribution (using Equation(4.17)) along B1 and B2 boundaries

To improve the accuracy of the temperature predictions of the model, at the edge (r=22.5 mm) of the nozzle in particular, a constant heat transfer coefficient h_b was introduced into the Gaussian distribution shown in Equation (4.17).

$$h_c = h_p \bullet e^{\frac{r^2}{c^2}} + h_b \tag{4.18}$$

This h_b additional heat transfer is due to the cooling effect of the high velocity air entrainment into the cryogenic nozzle from the atmosphere.

When the heat transfer coefficient distribution plotted in Figure 4.51,b was applied, the temperature predictions of the model improved significantly as Figure 4.51,a shows.

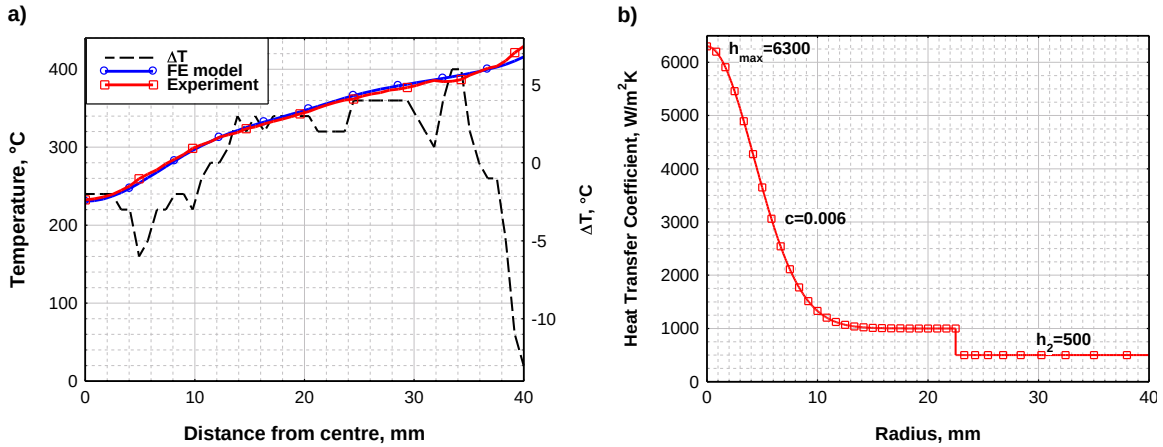

Figure 4.51 Modified Gaussian cooling source model a) temperature profile comparison along B7 boundary (visual best fir) and b) h_c heat transfer coefficient distribution (using Equation(4.17)) along B1 and B2 boundaries

The best visual fit for the model using Equation (4.18) gave temperature prediction within ±6 °C for most of the examined profile. Due to this accurate prediction the heat transfer coefficient distribution in Equation (4.18) was also used to simulate all the other cooling block experiments listed in Table 4.6. The comparisons of the predicted and measured temperature profiles for the experiments listed in Table 4.6 are detailed in Appendix 7A2

4.2.2.5 Model Outputs

Two parameters were used to compare the cooling source characteristics of the different simulations: maximum heat transfer coefficient and Total Cooling Power (TCP). On the one hand the maximum heat transfer coefficient describes the magnitude of the cooling capacity of the cooling source at the core of the cooling spray. TCP on the other hand describes the overall cooling power within the cryogenic nozzle.

TCP is the volume defined by the h_c heat transfer coefficient (in Figure 4.51,b) within the cryogenic nozzle radius (r_n):

$$TCP = \int_0^{2\pi} \int_0^{r_n} h_c(r) dr d\varphi = \overline{h_c} \bullet A \qquad (4.19)$$

This TCP is calculated by a built-in COMSOL routine. The meaning of TCP in practice is the temperature dependent cooling power:

$$Q_c = q_c \bullet A = \overline{h_c} \bullet A \bullet (T - T_c) = TCP \bullet (T - T_c) \quad (4.20)$$

This cooling power (i.e. TCP) is a sum of the cooling due to solid CO_2 sublimation, convective cooling of cold CO_2 and convective cooling of gas entrained from atmosphere.

Hence TCP and h_{cmax} are used to compare the cooling source characteristics obtained by the COMSOL model and are detailed further below.

4.3 Results

This section details the experimental and modelling results obtained throughout the TTC work. The first part of this section details the outcomes of the cooling source characterisation trials, which is then followed by the welding trials and residual stress measurement results.

4.3.1 TTC Cooling Source Characterisation

Cooling block experiments were used in conjunction with finite element modelling to characterise the cryogenic cooling used in the present work. Five sets of experiments were carried out examining the main parameters of the cooling nozzle.

The first set of trials aimed to examine the effect of extraction rate on the cooling source characteristics. A comparison of the thermal images recorded at 3s spray time is shown in Figure 4.52.

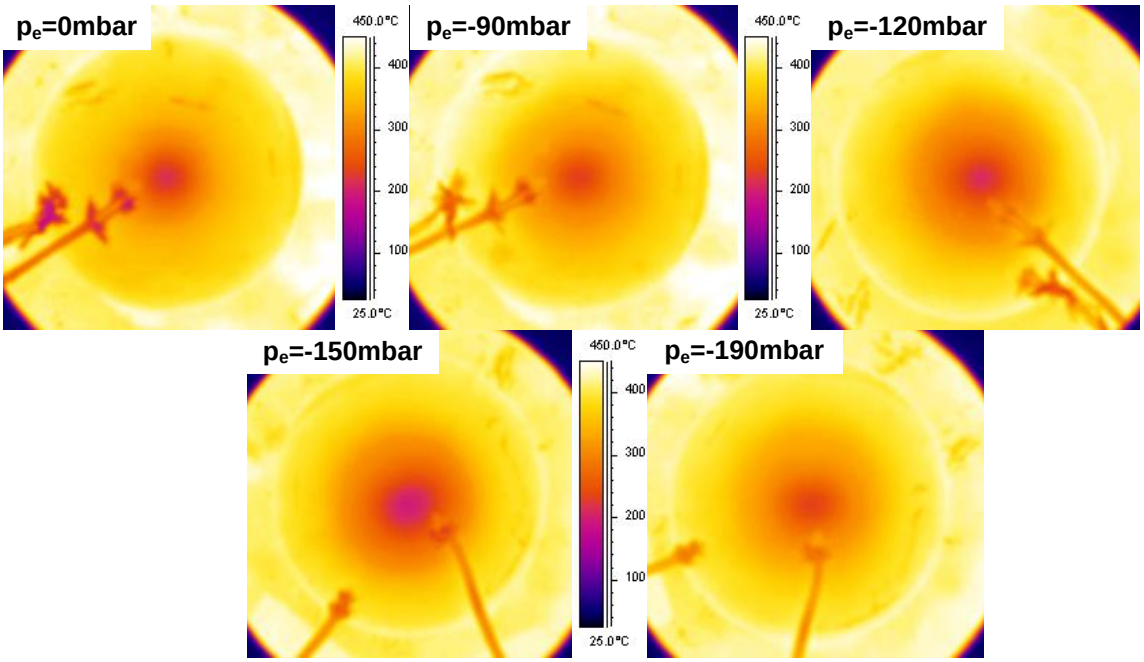

Figure 4.52 Thermal images of the cooling block after 3s cryogenic spray at different extraction pressures (p_e)

The thermal camera measurement results presented in Figure 4.52 show that increasing the extraction rate decreases the minimum temperature at the centre of the cooling block up till p_e=-150 mbar. As p_e decreases further down to -190 mbar the minimum temperature increases at the centre of the cooling block as shown in Figure 4.53. At the same time increasing the extraction reduces the cooled area as well as shown by the reducing darker areas in the IR images in Figure 4.52.

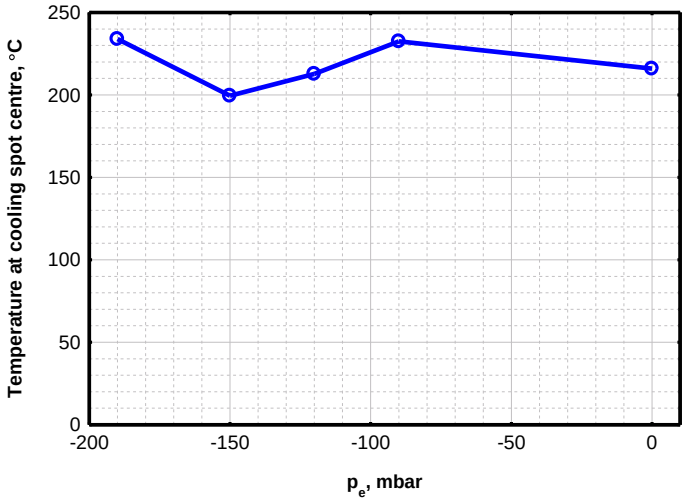

Figure 4.53 Variation of temperature with extraction at the cooling spot centre

The h_c convective heat transfer coefficient determined by the FE model using the thermal camera measurements are shown in Figure 4.54. The convective heat transfer coefficient shows a maximum peak value at p_e=0 mbar extraction level and

a minimum at p_e=-190 mbar. The h distributions for the rest of the experiments shown in Figure 4.54 (p_e=-90...-150 mbar) are very similar, although the p_e=-150 mbar h distribution (line with full circles) shows a significant increase in the R_a=10...20 mm range. The h values outside the nozzle (R_a<22.5 mm) decrease proportionally with increasing extraction.

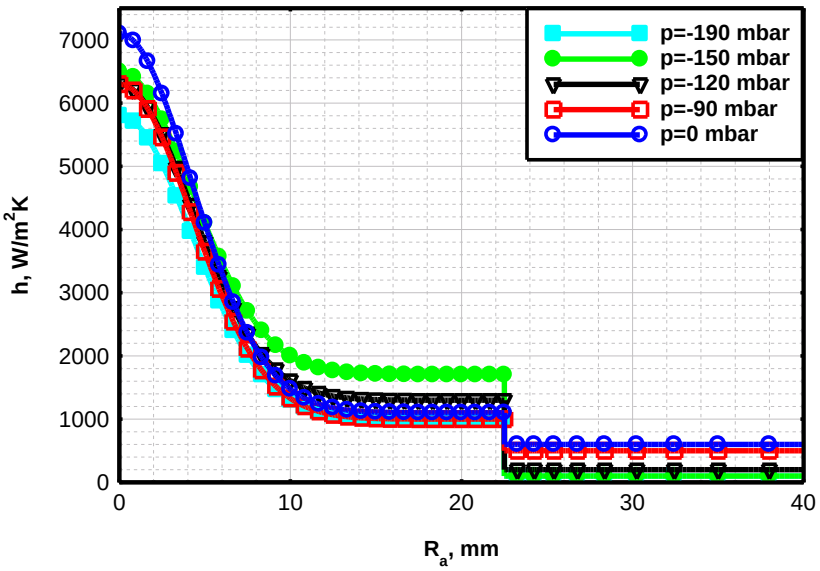

Figure 4.54 Heat transfer coefficient distribution at the bottom of the aperture versus extraction pressure

Figure 4.55 shows the peak heat transfer coefficient (h_p) and the temperature dependant cooling power in relation to the extraction levels applied. This figure clearly shows that the maximum cooling power is achieved at p_e=-150 mbar where h_p also shows a local maximum.

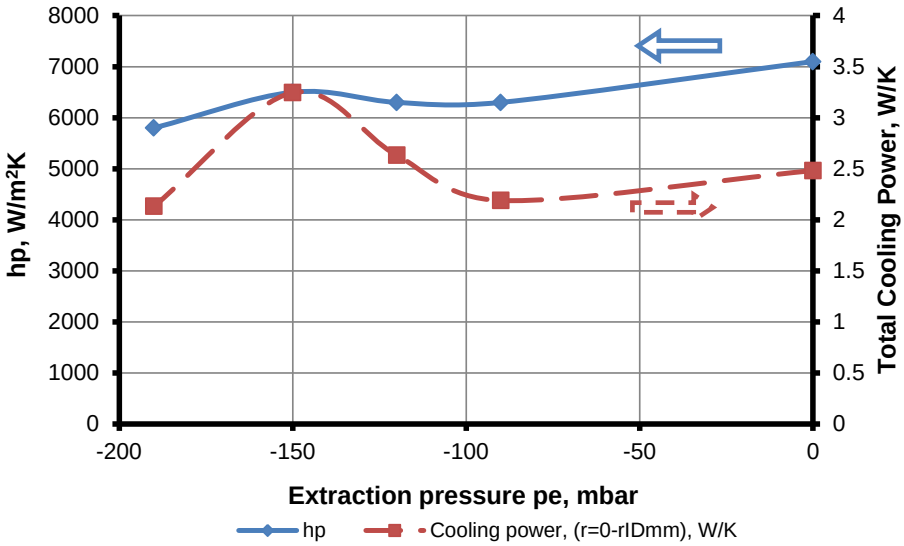

Figure 4.55 Influence of the extraction pressure on the peak convective heat transfer coefficient (h_p) and the total cooling power

The second set of cooling block experiments examined the cooling properties of the cryogenic nozzle in relation to the Amal jet height (z_A). Comparing the thermal camera images recorded at 3 s spray time shown in Figure 4.56 reveals that with increasing jet height the temperature of the cooled area increases (the darker spot at the centre of the aperture in Figure 4.56 is getting lighter with increasing z_A).

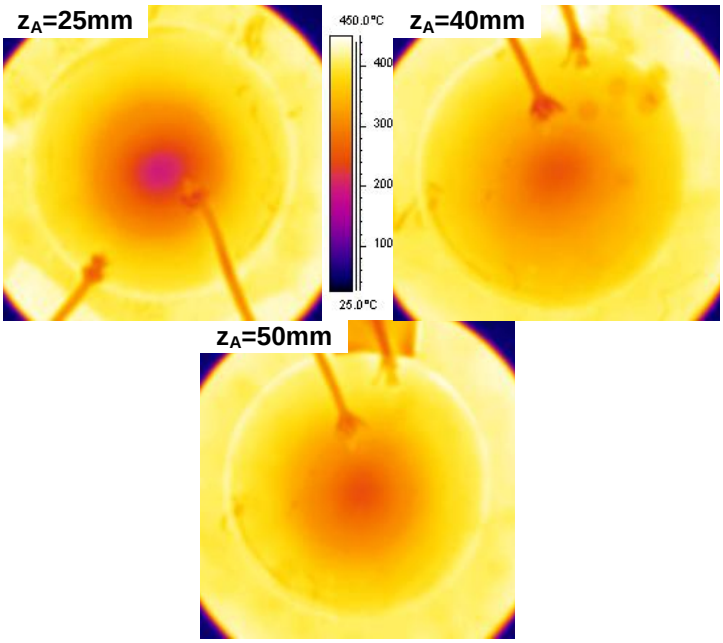

Figure 4.56 Thermal images of cooling block after 3s cryogenic spray at different Amal jet height (z_A)

It can be seen in Figure 4.56 that as z_A increases the cooling spray becomes less effective, hence the temperatures are higher at higher z_A values. The h distributions shown in Figure 4.57 confirm that when z_A is increased to 40 or 50 mm the heat transfer coefficient reduces dramatically within the nozzle (R_a<22.5 mm). At the highest Amal jet height (line with triangles) it is also clear that the extraction is not sufficient as h increased significantly outside the nozzle indicating a CO_2 leak outside the extraction system.

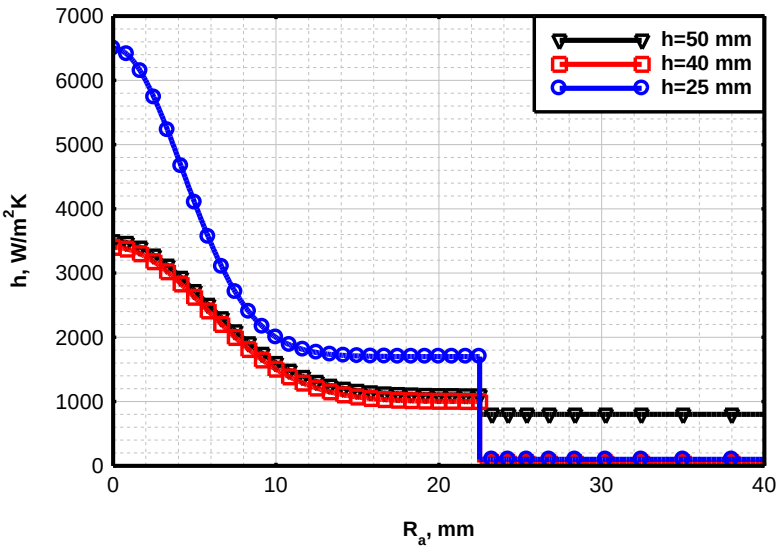

Figure 4.57 Convective heat transfer coefficient distribution along the aperture radius (R_a) versus Amal jet height

The drop in cooling effectiveness with increasing Amal jet height is apparent in Figure 4.58 as well, where h_p and temperature dependant cooling power versus Amal jet height are shown. It should be noted that the cooling power is practically the same for the higher Amal jet height settings.

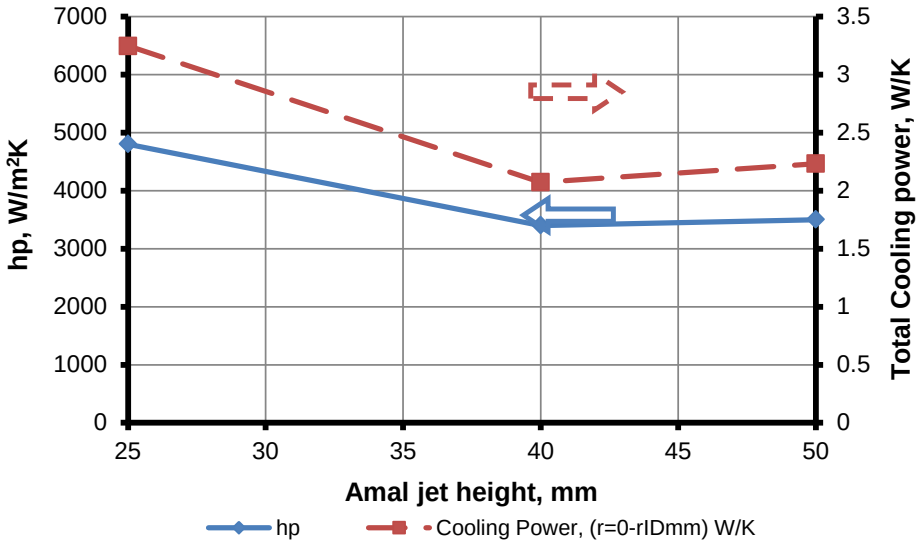

Figure 4.58 Amal jet height versus h_p peak convective heat transfer coefficient and total cooling power

The third set of experiments examined the influence of the cooling nozzle shroud diameter (D_A) on the cooling properties of the cryogenic spray. The thermal camera image comparison in Figure 4.59 shows that increasing the nozzle diameter results in a larger cooled area (larger dark area at the aperture centre).

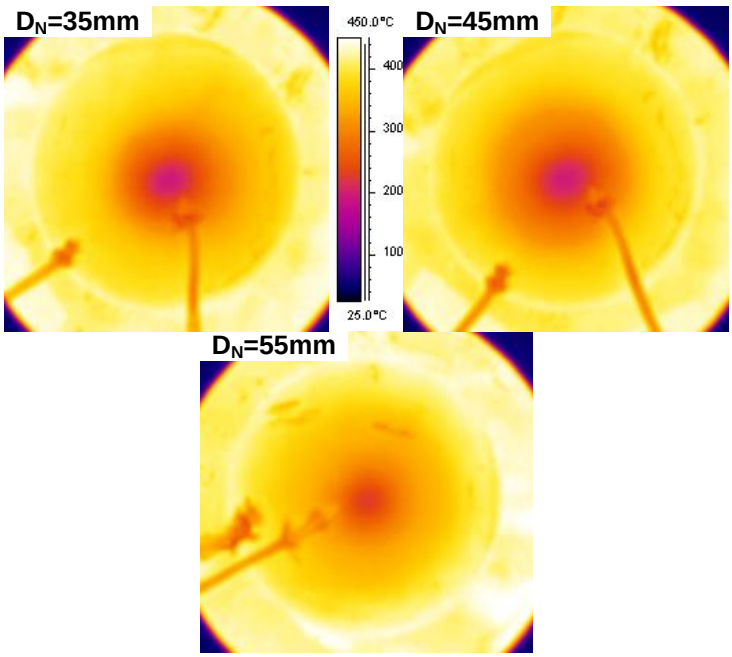

Figure 4.59 Thermal images of cooling block after 3s cryogenic spray at different cryogenic nozzle diameter height (D_N)

The heat transfer coefficient distribution for the different nozzle diameters displayed in Figure 4.60 shows that increasing the nozzle diameter expands the spray over a larger area. This shows that the cooling spot diameter in the current cryogenic cooling setup is primarily controlled by the cryogenic nozzle diameter. However, the peak heat transfer coefficient is reduced at the same time from D_n=35 to D_n=45.

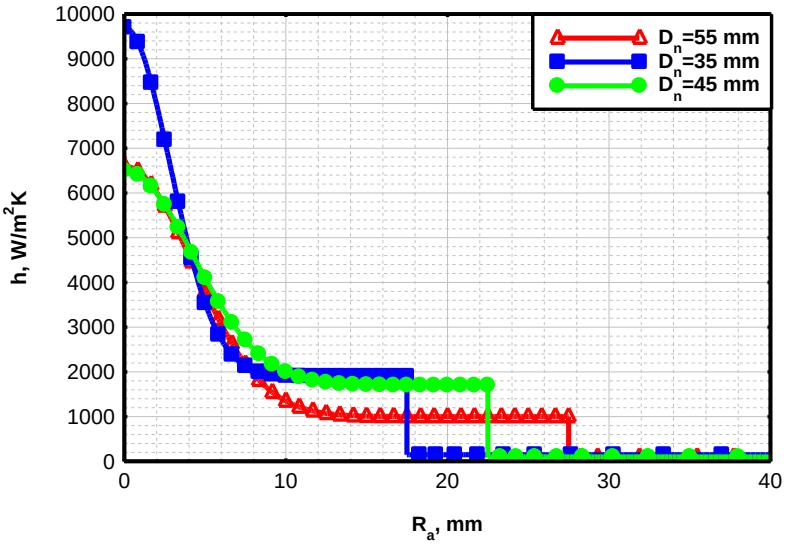

Figure 4.60 Convective heat transfer coefficient distribution along the aperture radius (R_a) versus D_n cryogenic nozzle diameter

The evident change in the heat transfer coefficient distribution does not translate into big changes in the cooling power as Figure 4.61 shows. While the h_p is nearly 50 % bigger at D_n=35 mm than at D_n=45 mm the cooling power actually drops by almost 50 %. At the same time increasing D_n from 45 to 55 mm does not change the cooling characteristic significantly.

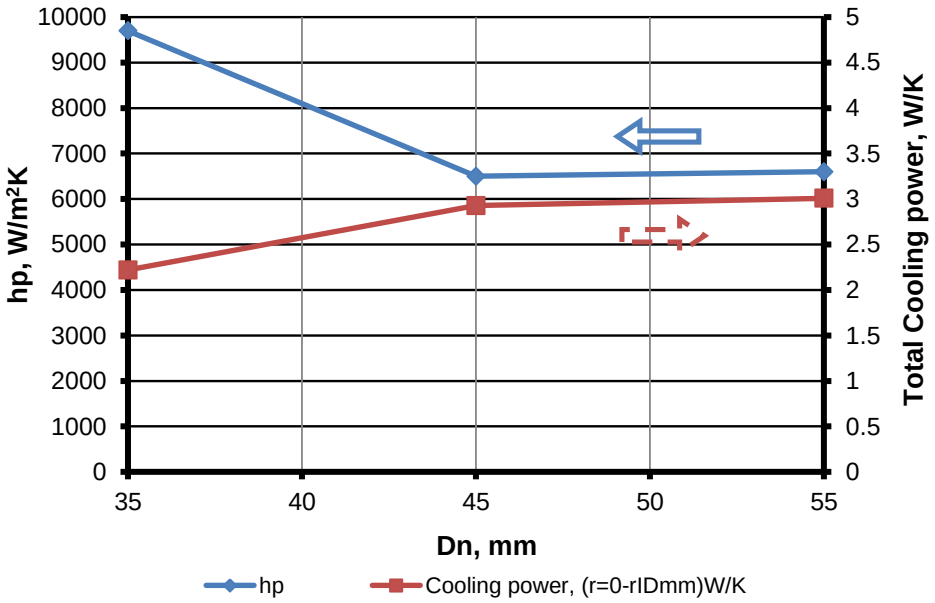

Figure 4.61 Effect of the nozzle shroud diameter (D_n) on the cooling source characteristics

The next cooling block trials were to investigate the affect of the Amal jet size on the cooling properties of the cryogenic spray. These experiments were carried out without the application of extraction allowing the CO_2 spray to expand without external restrictions..

The thermal images recorded show that larger Amal jets provide increased cooling effect of the cryogenic spray. This can be observed in Figure 4.62 as the the darker areas in the aperture increase with increasing Amal jet size. Figure 4.62 also shows that the central core area (dark spot at the centre) of the spray also increases with increasing Amal jet sizes.

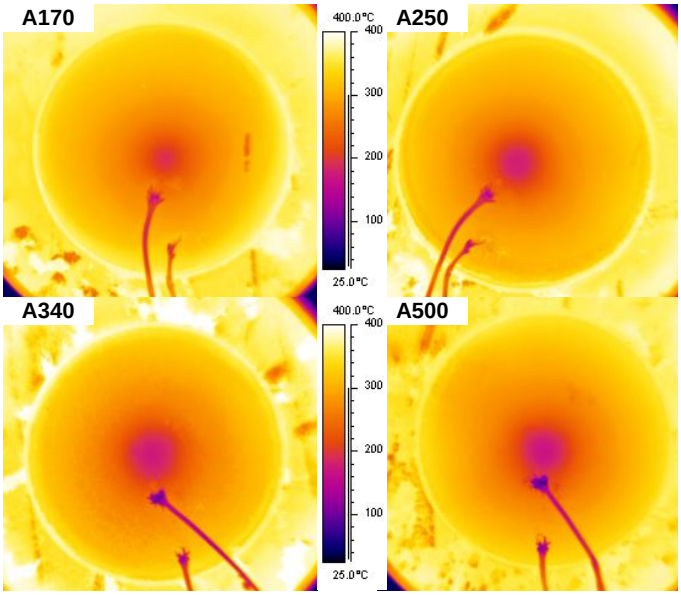

Figure 4.62 Thermal images of cooling block after 3s cryogenic spray using different Amal jet sizes

The FE modelling results in Figure 4.63 show that increasing the Amal jet size decreases the peak heat transfer coefficient and increases the cooled area at the same time.

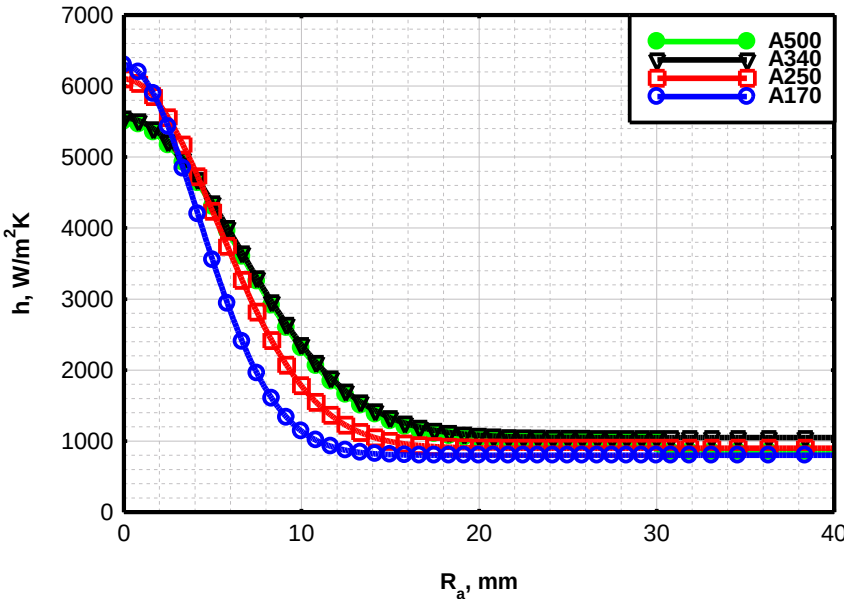

Figure 4.63 Convective heat transfer coefficient distribution along the aperture radius (R_a) versus Amal jet size

This variation in the heat transfer coefficient distribution shown in Figure 4.63, results in a quite significant change in the cooling power as Figure 4.64 illustrates.

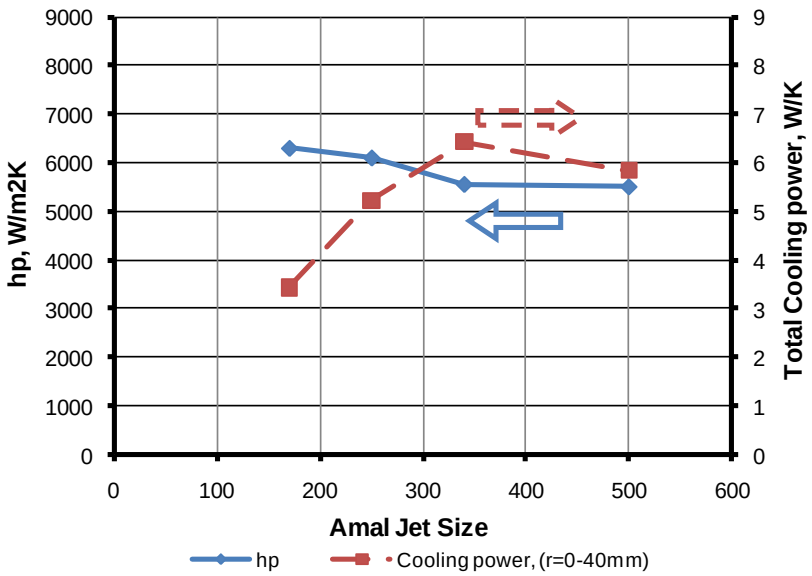

Figure 4.64 Effect of Amal jet size on the cooling characteristics of the cryogenic spray

While the h_p values slightly decrease with increasing Amal jet sizes (CO_2 flow rates) the cooling power increase with much higher gradient until the flow rate reaches 4.85 kg/min (A340).

Amal jet trials were followed by the Air Entrainment Gap (AEG) experiments in the cooling source characterisation work. In these experiments only two values of AEG were used: the default 1 mm and a much higher 2 mm to investigate the effect of AEG on the cooling source.

The comparison of the thermal camera recordings shown in Figure 4.65 reveals that increasing AEG up to 2 mm reduces the cooling effect of the cryogenic spray significantly. This is reflected in the thermal images in Figure 4.65 as smaller low temperature area (darker shade spot) at AEG=2 mm.

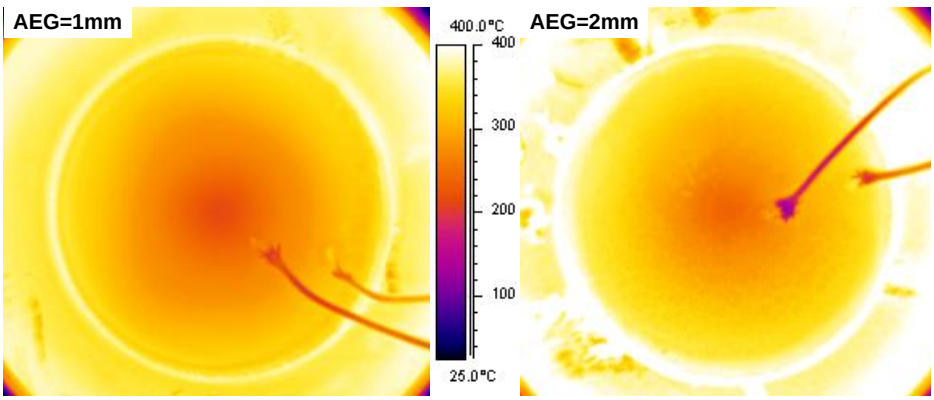

Figure 4.65 Thermal images of cooling block after 3s cryogenic spray at various Air Entrainment Gap (AEG)

The FE modelling results in Figure 4.66 shows that the heat transfer coefficient reduced across the whole area within the nozzle.

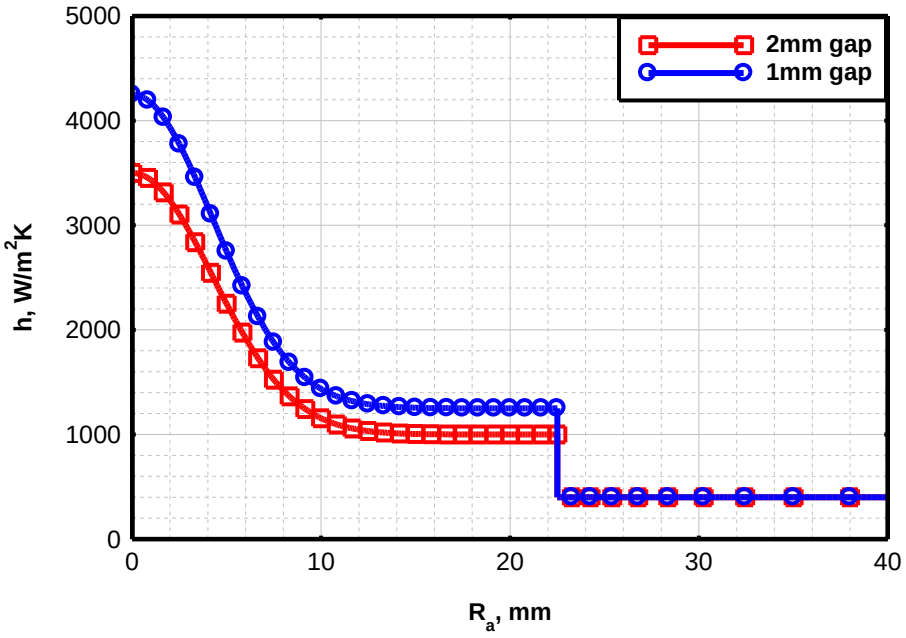

Figure 4.66 Convective heat transfer coefficient distribution along the aperture radius (R_a) versus Air Entrainment Gap (AEG)

This drop in the cooling with increasing AEG is even more evident in the cooling power as Figure 4.67 illustrates. The cooling power at AEG=2 mm is reduced by 50 % compared to AEG=1 mm. This significant change in both h_p and TCP emphasises why the effect of the nozzle lifting observed in many early experiments has such a major effect, and little distortion reduction waw observed.

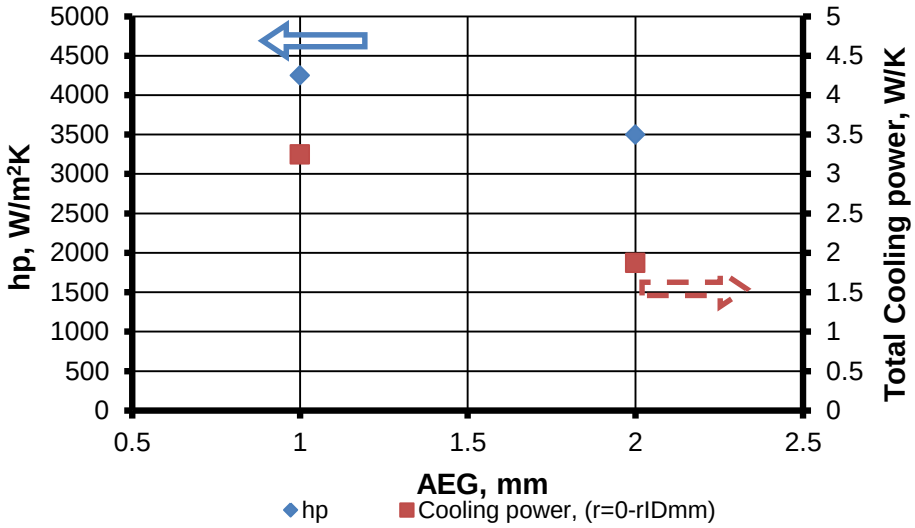

Figure 4.67 Effect of Air Entrainment Gap (AEG) on the cooling characteristic of the cryogenic spray

The last set of experiments aimed to examine the effect of the cooling block pre-heat (T_{pre}) temperature on the cooling characteristics. The comparison of the thermal images in Figure 4.68 shows smaller cooled area at lower pre-heat temperature, although on the T_{pre}=250 °C thermal camera image the cooled area is more difficult to distinguish.

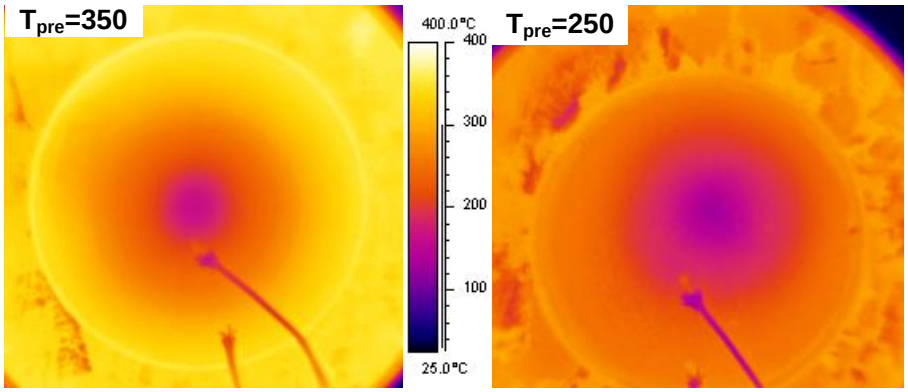

Figure 4.68 Thermal images of cooling block after 3s cryogenic spray at various cooling block pre-heat temperatures (T_{pre})

The FE modelling gives clearer results on the variation of cooling properties with varying T_{pre}. The h distributions in Figure 4.69 shows lower heat transfer coefficient at the core of the CO_2 (R_a=10 mm).

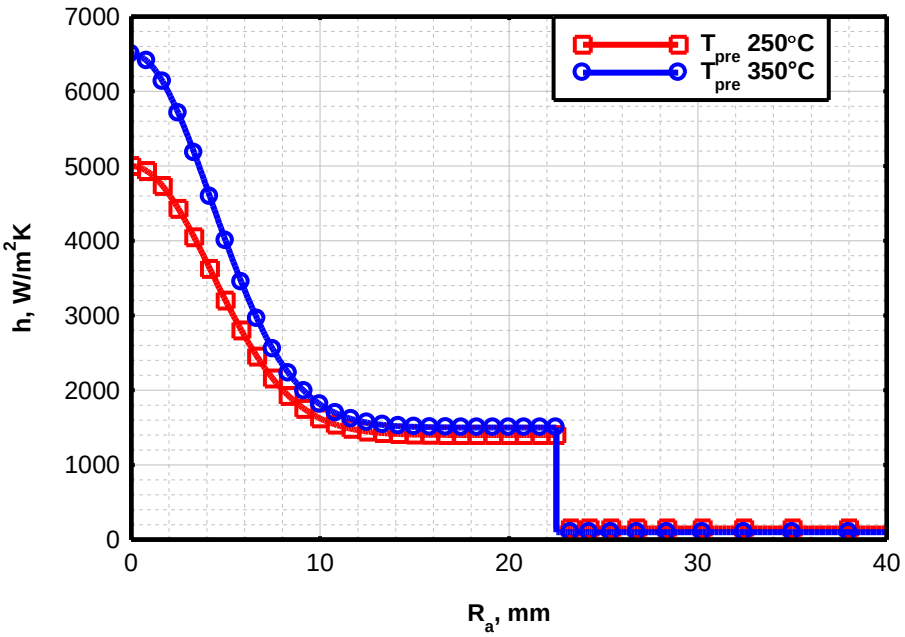

Figure 4.69 Convective heat transfer coefficient distribution along the aperture radius (R_a) versus cooling block pre-heat temperature pre heat temperature

The lower heat transfer coefficient values at the core of the spray resulted in a ~15 % drop in the cooling power over 100 °C temperature range.

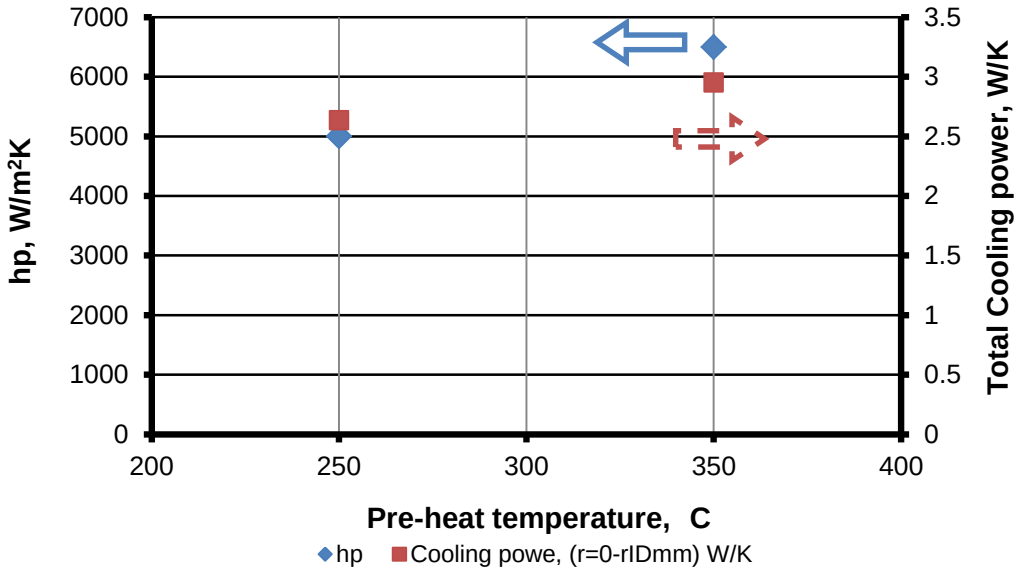

Figure 4.70 Effect of pre-heat temperature on the total cooling characteristics of the cryogenic spray

4.3.2 TTC Welding Trials

The TTC welding experiments results detailed in this chapter were carried out on small, thin plates described in Figure 4.30. The welding process used is GTAW to increase the flexibility of the welding to better suit the parameter changes implemented in this study.

The results of these experiments are detailed in this section below.

4.3.2.1 TTC Applied on Butt Welds

In the first set of trials the Amal jet size was varied to examine the influence of the delivery rate of CO_2 on the distortion of butt welded panels. The results of this set of experiments are shown in Figure 4.71.

It is clearly seen in Figure 4.71 that the bigger the Amal jet size, the higher the distortion reduction achieved by the local cooling. It is worth noting that the 250 size Amal jet did not influence the peak distortion value, only the DI.

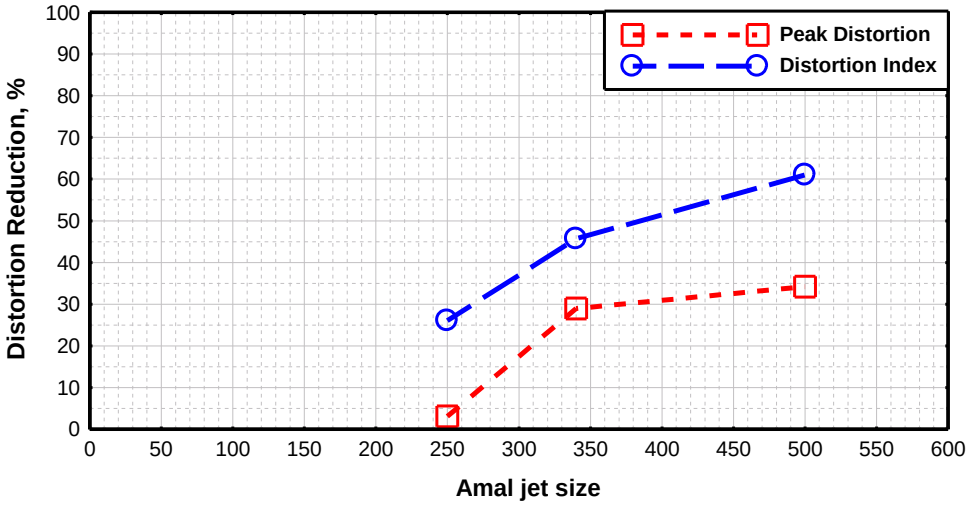

Figure 4.71 Influence of Amal jet size on the distortion response of butt welded panels, reference weld Pead Distortion: 8 mm, DI: 3.83 mm

The second set of TTC trials on butt welds was the investigation of the AEG (see Figure 4.27 schematics for definition) on the effectiveness of the cooling, hence the reduction in distortion. The results of these trials are shown in Figure 4.72.

The results presented in Figure 4.72 show that if the AEG parameter has an optimum range at 1.1-1.4 mm. If the AEG is higher than this range the effectiveness of the cooling in reducing distortion drops rapidly, reaching its minimum at AEG=2 mm. When AEG is lower than the optimum range, distortion reduction values decrease (although not as drastically as with AEG>1.4 mm).

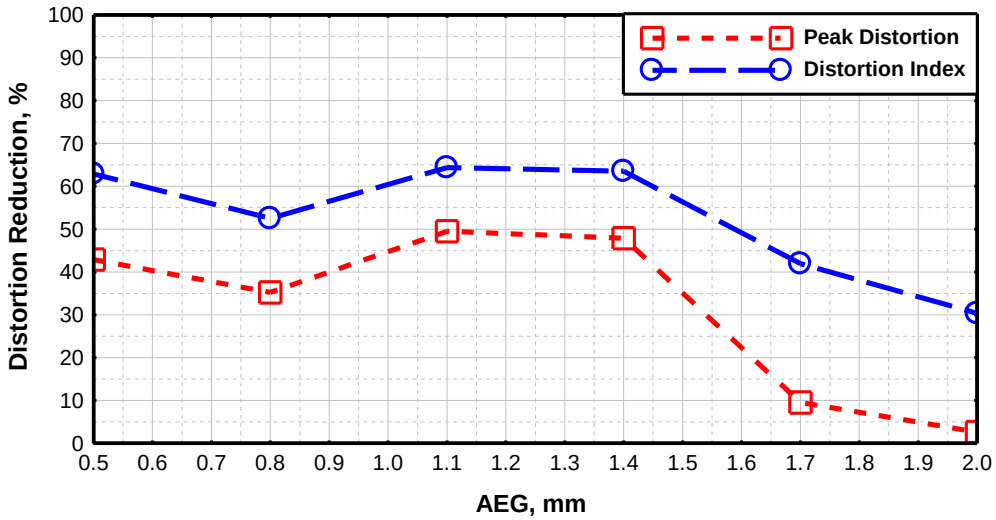

Figure 4.72 Influence of the air entrainment gap on the distortion response of butt welded panels using 340 Amal jet, reference weld Pead Distortion: 8 mm, DI: 3.83 mm

The last set of experiments in the butt weld application of TTC was aimed to examine the effect of travel speed on the distortion reduction of the TTC process. The results of these experiments are shown in Figure 4.73.

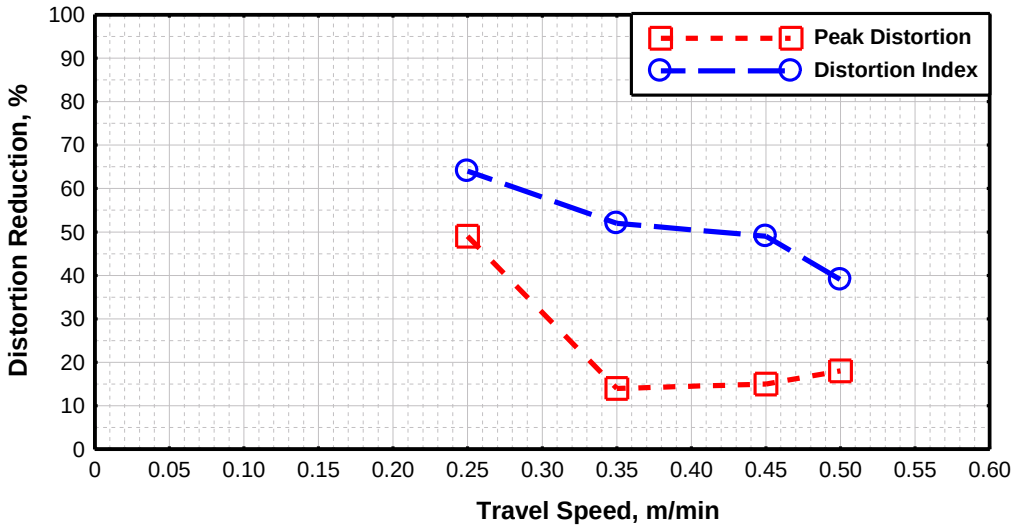

Figure 4.73 Influence of travel speed on the effectiveness of cooling in reducing distortion, reference weld Pead Distortion: 8 mm, DI: 3.83 mm

The biggest reduction in distortion is achieved at the lowest (0.25 m/min) travel speed, although at higher travel speed reduction in distortion is still significant. Interestingly, the distortion reduction values for peak distortion drop significantly (from 50 down to 15 %) when the travel speed is increased from 0.25 to 0.35 m/min and remains at this 15-20 % range when travel speed is further increased.

4.3.2.2 TTC Applied on Fillet Welds

The cryogenic cooling system with the fillet weld adapter was also applied on fillet welds. A comparison of distortion for the as welded and locally cooled weld is shown in Figure 4.74.

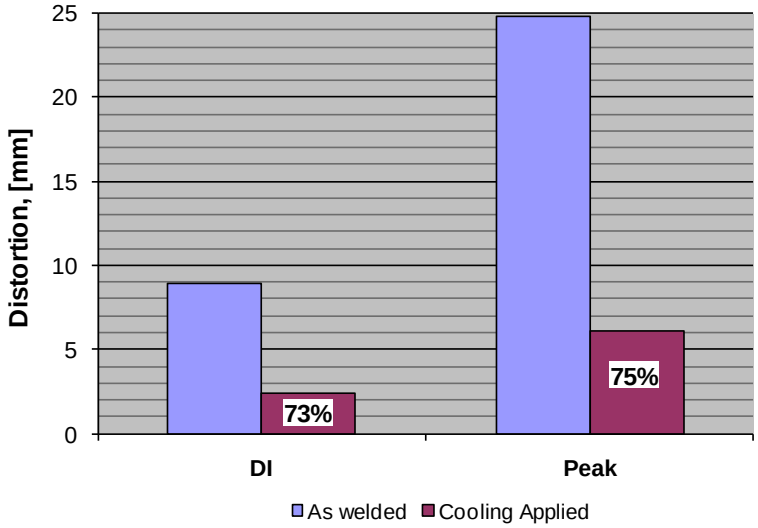

Figure 4.74 Distortion response of fillet welded panel with and without CO_2 cooling

The distortion on the fillet weld joint configuration is reduced by 75% in peak value when TTC was applied and DI values give similar figures too.

4.3.3 Data analysis and results of residual stress measurements

Residual stresses were measured on both butt and fillet welded samples to examine the effect of the cooling on the longitudinal residual stress distribution. The results of these measurements are shown below as comparisons to cooled and the as-welded samples.

The residual stress distribution comparison on butt welded samples is shown in Figure 4.75. The localised cooling changed the RS profile in two ways: the tensile region at the centre line became narrower which is particularly visible at zero stress level. At this level the cooled sample has a 20 % narrower tensile peak. Also, the compressive zone became shallower (smaller magnitude), which produces lower buckling load.

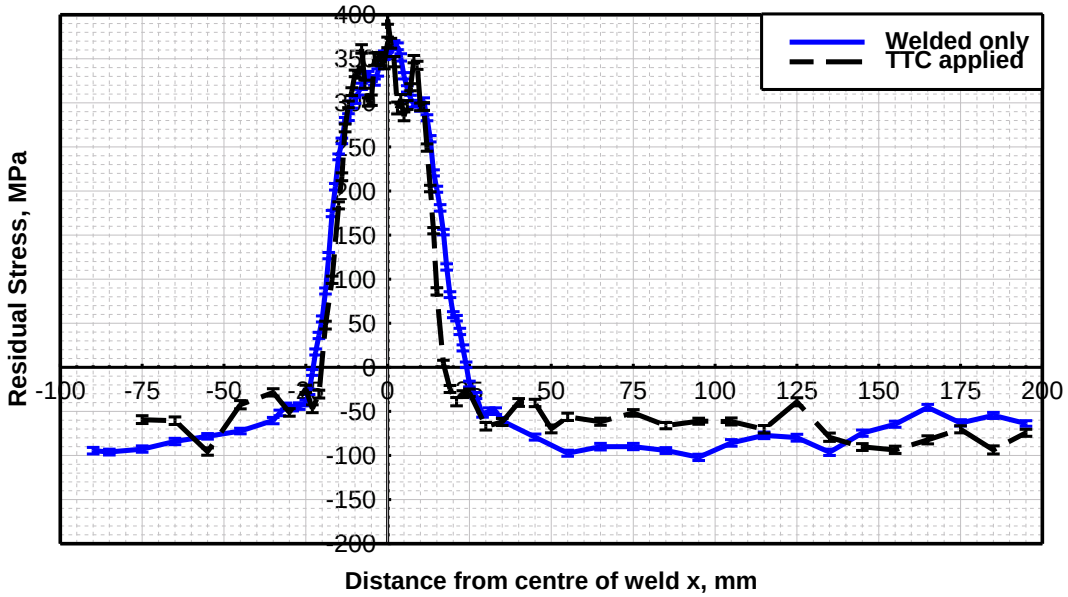

Figure 4.75 Measured residual stress profile comparison of the butt welded samples

Similar changes can be observed in the RS profile produced by cooling on fillet weld as well (see Figure 4.76). Although the change in the tensile peak at the centre line is more apparent: the magnitude of the tensile peak in the as welded sample is about 10 % larger but the width of it is reduced by approximately 40 %.

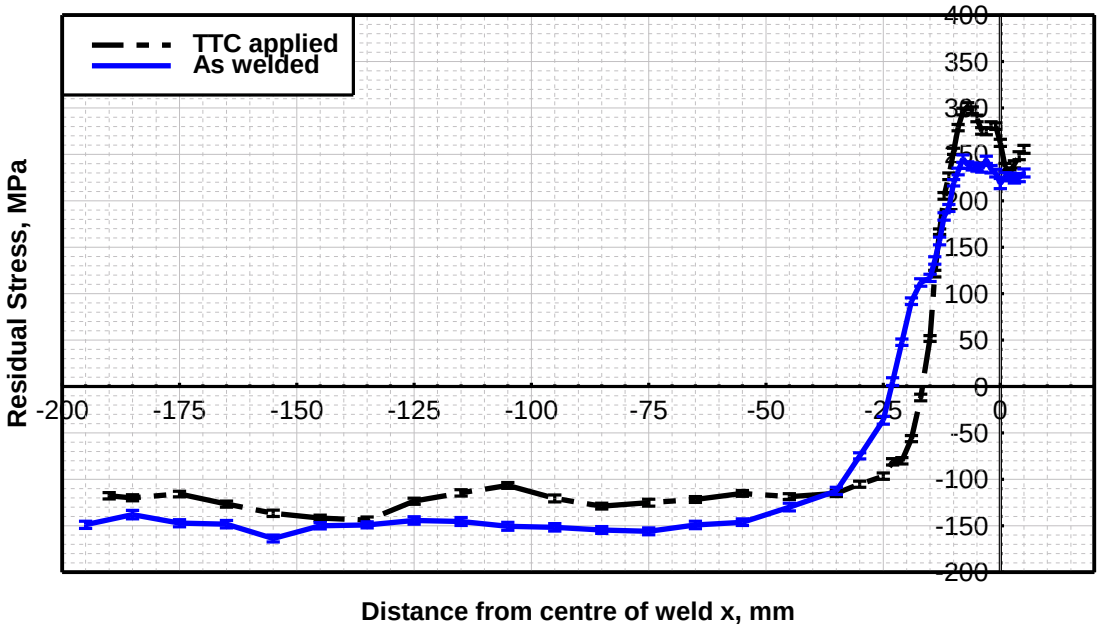

Figure 4.76 Measured residual stress profile of the TTC fillet welded sample

At the same time the compressive stresses further away from the weld centreline has not changed as dramatically as the tensile peak at the weld centre due to the cooling. The locally cooled weld exhibits 20 % lower compressive stresses

(particularly visible at x=50-100), although nearer to the edge this difference diminishes.

4.4 Discussion

Thermal Tensioning by Cooling was investigated in this work to eliminate buckling distortion in welded panels of butt and fillet weld joint configuration. The cooling source used to apply the tensioning effect was cryogenic CO_2 stored and delivered as liquid and applied on the weld surface as a mixture of solid and gas.

The TTC investigation started with a technology transfer study that encompassed the examination of the entire cooling and welding process: CO_2 delivery installation (i.e. delivery pipeline components, installation of cryogenic nozzle, design of cryogenic nozzle) welding process parameters, tooling and jigging of welding and cooling, The TTC work was then continued with cooling source characterisation. As there is little published data available on the cooling characteristics of cryogenic sprays (liquid CO_2 in particular), a significant part of the TTC experimental work coupled with FEM of the cooling source focused on the effects of the main parameters of the CO_2 delivery system on the cooling characteristics of the cryogenic spray. Based on the results of this characterisation, welding trials were also carried out to examine how the cooling process parameters influence the distortion response of plates welded with the trailing cooling source. The results of these investigations are discussed further in this chapter.

4.4.1 Process variables

As the technology transfer study revealed, the successful application of TTC depends upon a large number of factors, from the installation of the CO_2 delivery system and its components to the mounting of the cryogenic nozzle, as well as several - both cooling and welding parameters investigated in this work.

It has been observed by different authors (Guan [29-31, 33, 68, 69], Van der Aa [45, 48, 49], Camilleri [50], etc.) that a large thermal gradient behind the welding heat source is characteristic to this process and is assumed to be a requirement. This requirement then necessitates a cooling source that has high cooling power.

Equation (4.15) shows that the cooling power of liquid CO_2 spray depends on the flow rate and latent heat of sublimation (see Table 2.2 for value). As the latent heat of sublimation is constant in the current application, the cooling power of the cryogenic spray depends only on the flow rate. The theoretical maximum of the cooling power of the cryogenic spray was previously shown (Section 4.2.1). Although, this calculation is valid only if all losses of the CO_2 delivery system are neglected.

In reality, significant losses need to be considered in the cooling process: the spray exiting from the Amal jet is a mixture of solid and gas (see Figure 4.18 for illustration). Also, it is highly unlikely that all solid CO_2 sublimes upon contact with the substrate and some would always be extracted through the exhaust due to the relatively high supply pressure (~ 18 bars) of the CO_2. Hence the thermal gradient expected to be produced by the cooling source of the TTC in reality depends on the rate of sublimation of solid CO_2 at the surface of the workpiece.

The rate of sublimation at the substrate surface depends on the temperature of the substrate (T_s) at the impingement point and the rate of impingement of solid CO_2. Let us examine therefore how these two parameters are affected by the nozzle variables (illustrated in Figure 4.27) and other quantities illustrated in Figure 4.77.

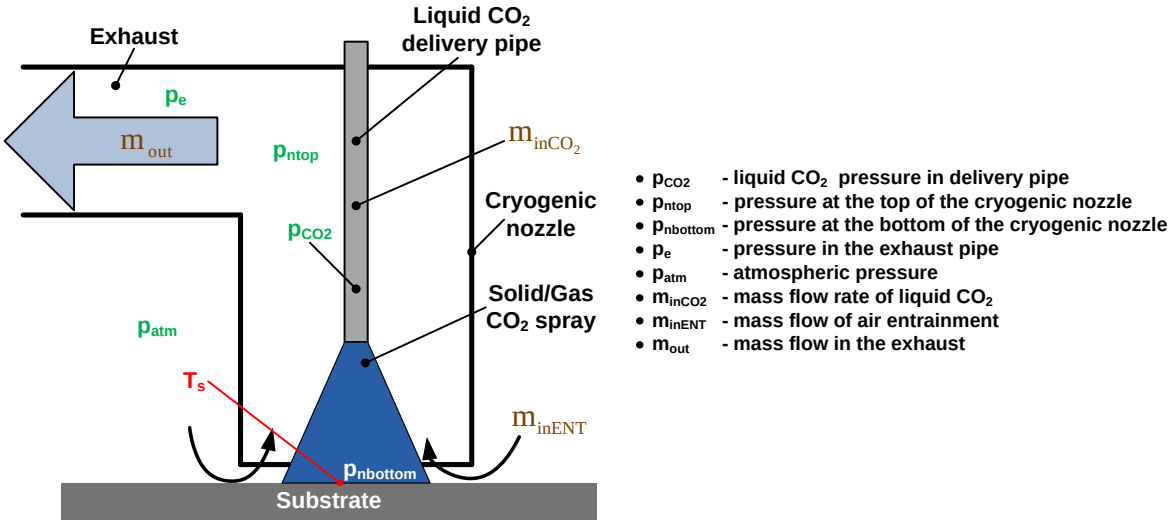

Figure 4.77 Schematics illustrating variables influencing the rate of impingement of solid CO_2 in the cryogenic nozzle used in this work

As the cooling source is located immediately behind the welding heat source, the temperature of the substrate beneath the cooling spray depends on the welding

conditions, workpiece material and geometry and weld tooling. Figure 4.68-Figure 4.70 clearly show how strongly the Total Cooling Power (TCP) depends on substrate temperature: a temperature increase of 100 °C from 250 °C to 350 °C resulted in nearly 20 % TCP and 30 % h_p increase.

The most important welding parameters affecting the substrate temperature (T_s) are Travel Speed (TS) and Heat Input (HI). The influence of the TS on the distortion reduction of TTC is shown in Figure 4.73: the lower TS the higher the distortion reduction. It is worth noting that while the peak distortion reduction shows a threshold-like relationship with TS, the Distortion Index (DI) reduction has a more linear dependency on TS. Colegrove et al. [6] showed that with increasing HI amongst other things, the peak temperature increases significantly at the same transverse position relative to the weld. Welding HI therefore is expected to have a great influence on the cooling process as well through the temperature field of the welding process.

The substrate geometry and material also has a major influence in determining the temperature of the substrate at the region of CO_2 impingement. The thermal conductivity of the substrate affects T_s greatly as well as the substrate thickness. In fact, one of the main reasons why NASA's research on this process was largely unsuccessful [15] was because they used thick (~20 mm) aluminium workpieces as substrates. The combination of aluminium (high thermal conductivity) and thick substrate results in rapid heat loss on the substrate surface making it very difficult to generate a large enough temperature gradient to produce thermal stresses.

During the technology transfer study it was observed how important the tooling and jigging are: Figure 4.13-Figure 4.14 shows that both the position and the contact conditions can have a detrimental effect on the distortion reduction of TTC. The clamps of the welding setup can extract significant amount of heat (i.e. large copper clamps on seamer) and hence can stop the cooling source producing the required thermal gradient.

The second major parameter influencing the sublimation rate at the substrate surface is the rate of impingement of solid CO_2. This depends on several variables

of the cryogenic nozzle and CO_2 delivery and exhaust system, the most significant of which are:

- Amal jet height, z_A
- Amal jet size, orifice diameter
- Air entrainment through AEG from atmosphere, m_{inENT}
- Pressure of liquid CO_2 in delivery nozzle, p_{CO2}
- CO_2 spray gas/solid ratio, $R_{s/g}$
- Extraction rate or pressure in the exhaust pipe, p_e

The z_A Amal jet height results in the cooling source characterisation study (Figure 4.56-Figure 4.58) show a significant influence on the both peak heat transfer coefficient (h_p) and Total Cooling Power (TCP). Although for these changes a relatively large variation in z_A was needed. Hence it is important to consider z_A at the design stage of the process and delivery system – the extraction nozzle in particular. At the same time z_A has little significance during the operation of the process as the change in z_A required to produce significant influence on the cooling characteristics is much larger (at least 5-10 mm) than i.e. AEG which requires only a fraction of a millimetre change for a similar effect. It should be noted though that with small z_A the contact time of solid CO_2 with the hot substrate surface might be insufficient to absorb enough heat for sublimation to take place.

The Amal jet size also has a major influence on the cooling characteristics of the CO_2 spray (see Figure 4.62-Figure 4.64). Using larger Amal jets increases both the h_p and TCP due to the increase in the flow rate (see Figure 4.43) of the cooling medium. The increased cooling effect due to the increased Amal jet size is well reflected in the distortion response of the welding trials in Figure 4.71. An important feature of Figure 4.71 is that the distortion reduction does not saturate even up to 500 Amal jet size, unlike TCP in Figure 4.43. The reason for this difference in saturation of TCP and distortion reduction is due to the difference in temperature of substrate. While in the cooling block trials the substrate temperature is 400 °C, when the cooling applied during welding the substrate temperature is expected to be significantly higher producing higher sublimation rates resulting in

higher TCP. The Amal jet size at the same time does not change (discreet increments) during operation, hence this again is a parameter that needs to be considered when the cooling process is designed rather than in the process control.

The pressure of liquid CO_2 (p_{CO2}) in the delivery pipe (at the end of the delivery line, within the nozzle) is a characteristics of the delivery system and is dependent upon the supply pressure p_s of the cryogenic cylinder and the design and installation of the delivery system. p_{CO2} can vary during operation and is observed as pulsing: periods of high and low solid/gas ratio: due to interim partial or even complete blockage of the CO_2 delivery line. The general observation during the technology transfer was that with better thermal insulation of the delivery pipes and smaller Amal jets showed more severe pulsing and larger Amal jets showed less pulsing.

The last parameter influencing the sublimation rate of CO_2 is the solid to gas ratio ($R_{s/g}$) of the cryogenic spray at the substrate surface. $R_{s/g}$ shows the proportion of solid and gas CO_2 within the cryogenic spray (and can also be used as an efficiency factor of liquid to solid CO_2 conversion) supplied through the delivery system. $R_{s/g}$ at the substrate surface ($R_{s/gs}$) primarily depends on $R_{s/g}$ at the nozzle exit ($R_{s/gn}$) and how $R_{s/gn}$ changes from the nozzle exit to the substrate surface.

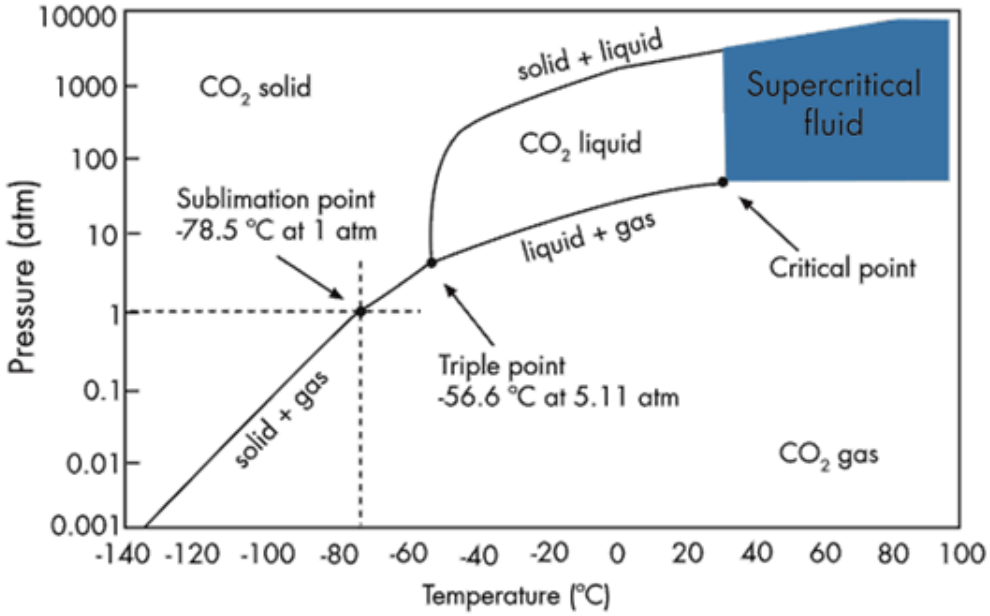

Figure 4.78 Phase diagram of CO_2 showing the sublimation point at ambient pressure [25]

Factors influencing $R_{s/gn}$ can be easier understood by examining the CO_2 phase diagram and the (pressure and temperature) conditions in the delivery system. The CO_2 in the cryogenic cylinder is stored at -21°C and 18 bar nominal (18-20 bar pressure was observed on the cylinder pressure gage). These conditions represent a point in the p-T phase diagram (see Figure 4.78) that is on the vapour-liquid saturation line. This means a small increase in temperature (as little as few °C) results in rapid vaporisation (flash) of liquid CO_2 and a relatively small pressure drop also produces the same effect.

The CO_2 delivered to the Amal jet nozzle (see schematics in Figure 4.79) should ideally be in liquid state only (at p_s and T_s) within the pipe. To ensure this, a phase separator is installed in the system as shown in Figure 4.79. As the liquid exits the Amal jet nozzle into the (near) atmospheric pressure cryogenic nozzle chamber, it vaporises rapidly as the triple point of CO_2 is at 5.11 bar (see Figure 4.78). The gas produced by the vaporisation expands adiabatically and its temperature drops rapidly due to the Joule-Thomson effect. This cooling effect lowers the gas temperature so much that it reaches the sublimation/condensation line and the vapour condenses into solid CO_2 flakes [70].

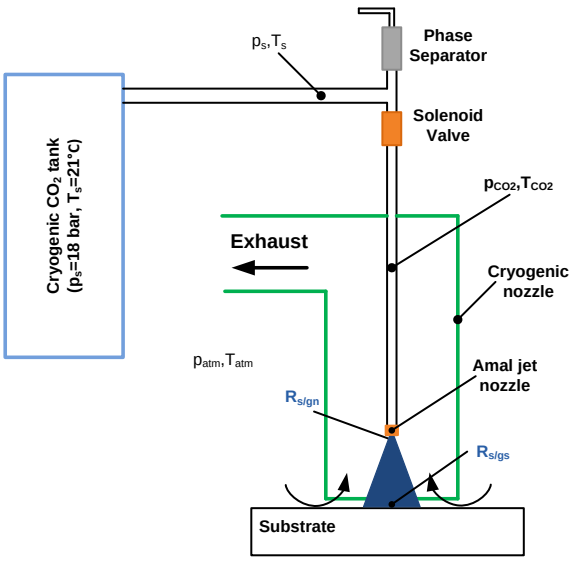

Figure 4.79 Schematics of the CO_2 delivery system used for TTC experiments

The cooling of the gas due to the pressure drop and expansion is described by the Joule-Thomson coefficient [71]:

$$\mu_{JT} = \frac{v}{c_p}\ \beta T - 1 \qquad (4.21)$$

where:

- v – specific volume
- c_p – heat capacity at constant pressure
- β – coefficient of expansion
- T – temperature of gas before expansion

The unit of μ_{JT} is Km^2N^{-1} expressing that the temperature drop of the expanding gas is proportional to the pressure drop. All the parameters in Equation (4.21) (v, c_p, β) are temperature dependant, hence the cooling effect of the gas expansion also depends on the initial temperature.

In the experimental setup used in this work the length of pipe from the phase separator to the cryogenic nozzle (300 mm long) as well as the solenoid valve and phase separator were not insulated, hence heat leaks into the pipes and the liquid CO_2 within. Also, the end piece of the delivery pipeline that is attached to the solenoid valve is initially unpressurised and is open to the nozzle chamber (pressure, p_n). Therefore during operation there is a pressure gradient in this length of pipe of which the maximum is p_s at the valve end. The minimum pressure depends on the geometry (internal diameter, length) of the pipe as well as the Amal jet size (orifice diameter at the exit).

Due to this heat in-leak and pressure gradient in the end piece of the CO_2 delivery pipe, the spray at the Amal jet orifice (within the delivery pipe) is always a mixture of solid and gas CO_2. This gas formation (called flash) within the delivery pipe is observed as pulsing (periods of high and low gas content) of the cryogenic spray (see Figure 4.18 for illustration) due to the difference of specific gravity of gas and liquid. This pulsing is detrimental to the quality and consistency of the spray and in extreme cases observed in the technology transfer it can result in complete lack of solid content of the CO_2 spray. It was observed in the technology

transfer that smaller Amal jet sizes induced more severe pulsing. This is due to the lower liquid flow rate within the delivery pipes: the liquid spends more time within the delivery pipe at lower flow rates absorbing more heat from the environment. More heat absorption results in more vaporisation of liquid within the delivery system.

The proportion of gas and liquid within the cryogenic spray in the Amal jet from the above description therefore depends on: p_s and Amal jet size which are constant as well as liquid temperature, and the delivery pipe geometry and insulation which are delivery system characteristics. These parameters through the gas/liquid ratio in the Amal jet also influence $R_{s/gn}$ as the portion of the CO_2 spray in gaseous state is less likely to expand and cool enough to form solid CO_2 than the liquid portion. This is because the vaporisation of the liquid CO_2 at the Amal jet exit has larger expansion due to the phase change (and change in density).

As the cryogenic spray approaches the substrate surface the gas within continues to expand due to the pressure drop of the CO_2 solid/gas stream. The pressure drop that would naturally occur under atmospheric condition due to the interaction (friction) with air is increased by the negative pressure superimposed via the extraction within the cryogenic nozzle. This pressure drop then continues to lower the temperature within the cryogenic spray through the Joule-Thomson effect. This means on the one hand that $R_{s/gs}$ can be higher than $R_{s/gn}$ improving the cooling capacity of the spray and on the other hand the solid CO_2 is less likely to sublime before reaching the substrate surface, although the expansion also means the spot size (area) is increased as well.

The solid CO_2 flakes completely or partially sublime when the cryogenic spray reaches the substrate surface. This sublimation also means significant volumetric expansion (1 kg solid CO_2 liberates 845 l of gas expanded at 15 °C at 1 bar [72]) that increases the pressure in the nozzle at the substrate surface ($p_{nbottom}$). $p_{nbottom}$ is then proportional to the sublimation rate of solid CO_2 at the substrate surface as well as the extraction rate (pe) and will be the highest at the centre of the cooling

spot. Higher $p_{nbottom}$ at the cooling spot centre results in an increase in the cooling spot area, although this increase is largely limited by the air flowing into the nozzle through AEG (m_{inENT}). As a result, m_{inENT} (mass flow of air entrainment) depends not only on AEG but $p_{nbottom}$ as well. As the results in Figure 4.65-Figure 4.67 and Figure 4.72 show relatively small variation in AEG results in large changes in both cooling characteristics and distortion reduction when applied to welding.

4.4.2 Control system

It became clear at a very early stage of this work that the additional CO_2 system providing the thermal tensioning during welding needs to be controlled automatically if it is to be used in industry. Also, its most likely application will be on automatic or semi-automatic production lines where the additional equipment of TTC would also need to be controlled.

In order to control the cooling process successfully, a flow balance needs to be established (see Figure 4.77):

$$\dot{m}_{out} = \dot{m}_{inCO_2} + \dot{m}_{inENT} \tag{4.22}$$

Equation (4.22) means that the extraction mass flow rate needs to be matched by the mass flow rate of the cryogenic CO_2 and the mass flow rate of the entraining air from the atmosphere. The CO_2 flow rate (as seen previously) is determined by the supply pressure (p_s) of the cryogenic tank and the Amal jet size (orifice diameter). These two parameters are both fixed, hence the CO_2 flow rate is also treated as constant. Therefore we can conclude that the purpose of the control system is to compensate for the variation in the air entrainment rate (m_{inENT}).

The air entrainment (m_{inENT}) flowing through the Air Entrainment Gap (AEG) from the atmosphere into the cryogenic nozzle is necessary to keep the CO_2 spray contained within the cryogenic nozzle. This air enters the nozzle due to the extraction (negative pressure) applied and is vented through the exhaust with the CO_2 spray (m_{out}). As discussed in the previous section, the air entrainment (m_{inENT}) depends primarily on the extraction rate (m_{out}), $p_{nbottom}$ and AEG. $p_{nbottom}$ depends strongly on the sublimation rate of solid CO_2 at the substrate surface. The

sublimation rate is also strongly influenced by the thermal field of the substrate (see details on previous section) underneath the nozzle which is outside of the CO_2 delivery system. This makes $p_{nbottom}$ difficult and complex to control.

It is clear then that AEG is the right candidate to be the parameter that m_{inENT} is controlled by. As AEG is the distance between the substrate and the cryogenic nozzle bottom (see Figure 4.27) it is relatively easy to measure as well as control. There several options in measuring height: touch probe type device (e.g. LVDT) that gives out a voltage signal proportional to the height measured. This signal can then be fed back into the control device (computer, PLC, etc.). The advantage of the touch probe type measurement is that it is simple, relatively inexpensive, easy to install and the voltage output is easy to control.

A more sophisticated way of measuring AEG is by using a laser stripe or laser pointer coupled with photodiode detectors. This system also gives a voltage output, but it needs calibration for different materials and material surfaces as the reflectivity of the laser depends strongly on substrate material as well as surface finish. Another issue with the laser based measurement is that a small amount of chilled CO_2 always escapes from the nozzle. As the colour of this escaping gas is white it would interfere with the measurement giving false readings and compromising the success of the process control.

4.4.3 TTC process mechanism

This technique as its name suggests reduces buckling distortion by applying thermal tensioning to welding using a high cooling capacity spray directly behind the weld during welding. This tensioning effect was observed by several authors (e.g. Guan [29-31, 33, 68, 69], Li [32, 34-36], Van der Aa [45, 48, 49], Camilleri [50]) in their residual stress measurements as well as FE modelling results. The sensitivity of distortion reduction to the cooling parameters (TCP and cooled area) observed in this work agrees with this tensioning mechanism.

But the residual stresses measured in both butt and fillet welds in this work (shown in Figure 4.75-Figure 4.76) does not show a decrease in the tensile peak that proves the tensioning effect of the cooling. But the measurements show a

reduction of the tensile region in width and not in height. This suggests that the cooling applied has a general cooling effect of the welding zone that also reduces the size of the plastic deformation zone in the dynamic strain field (see Figure 1.5). It should be noted though that the d_0 unstrained lattice parameters in the residual stress measurements was calculated, not measured (assuming plain stress conditions). This calculation gives a d_0 that is accurate for the parent metal but gives larger errors for the stresses measured in the weld as the microstructure and with it the actual d_0 is different. Hence the comparison of the as welded and cooled residual stress data in the weld zone is inconclusive.

At the same time the specimen used for residual stress measurements in this work were 4 mm thick (butt welds) and 4+6 mm (fillet welds). These are significantly thicker than Van der Aa's (2 mm AISI 316L) [45] and Li et al.'s samples (2.5 mm Ti6Al4V) [36]. In these authors' work not only is the thickness different but the material type as well: both stainless steel and titanium alloys have low thermal conductivity – approximately a third of that of mild steel. This significantly lower thermal conductivity makes it much easier to develop high thermal gradients probably necessary for tensile peak reduction. The thinner specimen also makes the cooling more effective in generating high thermal gradients as there is less material to cool. These differences make it difficult and impractical to compare the residual stress data of the aforementioned authors' directly to that presented in this work.

Camilleri et al. [50] applied cooling on both butt (2 mm thick) and fillet (5 mm+5 mm) welded panels in their numerical simulation. Their residual stress predictions for fillet welds (as well as the predicted peak distortion values) show practically no difference with the application of cryogenic cooling. The reason for the negligible effect of the cryogenic cooling on the residual stress and distortion values can be the significantly larger (D=90 mm compared to D_n=45 mm used in this work) cooling source area combined with relatively low cooling power (1.2 kW).

Compared to these parameters the cooling spray used in this work has a total cooling power (TCP) of 3.2 W/K over 45 mm diameter circular area. If 400 °C

(673 K) is assumed, as the surface temperature at which the cryogenic spray impacts the weld surface, the resulting cooling power will be approximately 2.15 kW. The resulting 2.15 kW is almost twice as much as the cooling power assumed by Camilleri et al. [50]. Furthermore the significantly lower cooling power is applied over an area that is four times larger than the area covered by the cryogenic nozzle (D_n=45 mm) used int his work. The required high thermal gradient behind the weld (and with it the required tensioning effect) is more difficult to achieve when the cooling is applied over a larger area as the cooling intensity drops (assuming constant cooling power) drastically by increasing area.

At the same time Camilleri et al. [50] applied the same cooling source to butt weld simulations and predicted 62.6 % (from 22.6 mm to 8.4 mm) in peak distortion. This distortion reduction value is very similar to that achieved in this work (~60-65 % distortion reduction). Unfortunately the predicted residual stress distributions of these butt welds are not published.

It should be noted, though that Camilleri et al.'s [50]simulations are not validated, hence ther accuracy of their predictions are unknown.

The application of TTC on thicker plates needs to be further investigated with the aid of FEA in order to clearly understand the process mechanism.

4.4.4 Limitations, Practical and Industrial Application Issues

As the current investigation reveals TTC can effectively reduce buckling distortion of both butt and fillet welded panels. This versatility makes TTC a potential tool in several industries, i.e. space, aerospace, automotive and even heavy industries like shipbuilding. But there are a number of application issues that need to be considered before industrial implementation.

As shown in this work TTC is very sensitive to the solid to gas ratio of the cryogenic spray which depends largely on the quality of the liquid CO_2 (gas content) delivered. Hence particular care and efforts are needed to minimise gas content of CO_2 in the delivery system both by the design and installation of the cryogenic delivery system, especially in large workshops where long delivery lines are expected. Large systems also need to be automated in pressurising and de-

pressurising as they can contain several valves, phase separators and these need to be operated in a particular sequence in order to avoid solid CO_2 (and with it blockage) formation within the delivery line. This is because solid CO_2 formation within the delivery equipment can result in pipe burst and can cause damage.

Amal jets were used in the present work to control the flow rate of the CO_2 delivered within the cryogenic spray. These jets regulate flow rate via their orifice (and pressure from the cryogenic tank) and need changing if the flow rate is to be changed. This means that with this system flow rates can only be regulated in discrete steps and they cannot be changed during operation. These characteristics of the Amal jets limits the application of TTC where the weld parameters change during welding (e.g. due to variation of thickness). Full automation of this process is also affected by the Amal jets, as their changing needs to be automated (much like tool changing in machining) and increases the complexity and with it the cost of a fully automated TTC system.

Another characteristic of regulating flow by orifice size is that the smallest usable orifice is limited by the pulsing effect (see description in previous section) as well as by the tendency to block at start-up. These make TTC difficult to implement where low cooling power or small cooling spot is required: e.g. welding of foils, micro-joining.

In practice the CO_2 is not entirely contained within the cryogenic nozzle and there is some chilled gas escaping from the cryogenic nozzle. This escaping CO_2 was observed throughout this work, even when the extraction and delivery flow rates were well balanced. This escaping chilled CO_2 did not present an issue in this work due to the low sensitivity of S355 steel welding to small changes in CO_2 content (welding gas already contains 18 %CO_2) and a barrier was installed between the cryogenic nozzle and the welding torch.

At the same time even small amounts of escaping CO_2 can present major issues when welding materials that are sensitive to oxidisation during welding (stainless steel, refractory metals). CO_2 can dissociate within the welding arc releasing

oxygen and can be an issue particularly if the welding is carried out in enclosed environment such as a welding enclosure.

5 Investigation of Thermal Tensioning by Heating

In this chapter thehe Thermal Tensioning by Heating SE technique is investigated in this chapter to reduce buckling distortion. This investigation covers heat source characterisation and weld applications using different heat sources.

5.1 Experimental Method

In the TTH experiments three different heat sources (oxy-acetylene and air-acetylene burners as well as induction coils) were used on butt, fillet and overlapped welds. Heat source calibration preceded the welding experiments for all three heat source applications.

The TTH experimental work consists of two stages, the first stage to examine the applicability of the technique on different weld geometries (butt, fillet, overlapped welds) and to establish an operating window of the main parameters of TTH using oxy-acetylene burners. The second stage is to examine and compare the applicability of two new other heat sources: air-acetylene burners and induction coils.

5.1.1 TTH Heat Source Calibration

The aim of the TTH heat source calibration trials was to characterise the oxy-acetylene burners in order to be able to achieve the temperatures that are required in the application of TTH on butt, fillet and overlapped welds.

5.1.1.1 Specimen Materials and Geometries

S355 structural steel was used for all the weld geometries of the TTH experiments, as the strength properties (YS, UTS) and the chemical composition of the S355 grade is very similar to that of DH36 commonly used in shipbuilding.

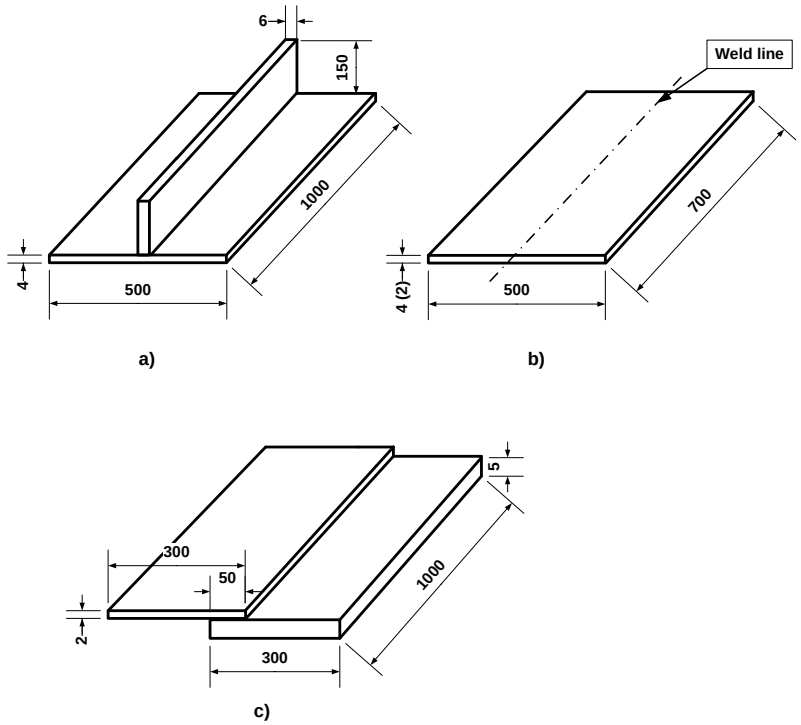

Figure 5.1 Specimen geometries used in the TTH calibration and welding experiments a) fillet welds b) 4 and 2 mm butt welds c) overlapped welds

The chemical composition and strength properties of the S355 grade steel for all the geometries shown in Figure 5.1 are detailed in Table 5.1.

Table 5.1 Material properties of different thickness S355 steel used in the TTH experiments

Chemical Composition [wt%]	**2 mm**	**4 mm**	**5 mm**	**6 mm**
C	0.163	0.164	0.119	0.139
P	0.013	0.021	0.013	0.011
S	0.015	0.03	0.009	0.014
Mn	1.115	0.955	1.094	1.091
Si	0.001	0.007	0.007	0.003
Al_{sol}	0.046	0.045	0.043	0.051
N	0.0062	0.005	0.0037	0.0033
Cr	0.019	0.021	0.023	0.027
UTS, [MPa]	570	527	439	457
YS, [MPa]	414	376	531	556

5.1.1.2 Equipment

The burner calibration tests were carried out in the same jig as the welding trials to ensure the same conditions and therefore to achieve the same temperatures with the obtained calibration parameters. The jig used for the TTH butt weld calibration is shown in Figure 5.2.

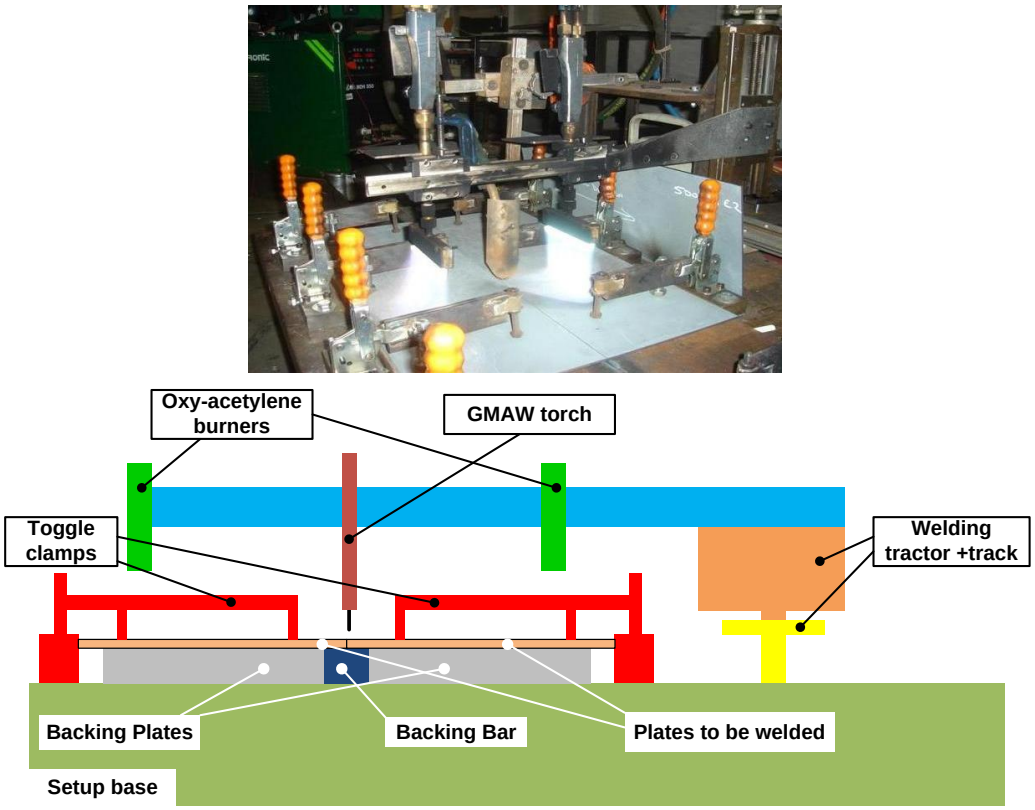

Figure 5.2 TTH oxy-acetylene burners experimental setup for butt welds a) Photo of oxy-acetylene burners in operation and b) schematic cross-section of the setup

In the butt weld experiments a clamping jig was mounted on a base that was used as a platform to accommodate the jig and the welding tractor with its track. Thick (20mm) steel plates were used as backing to ensure minimum heat build-up during and in between the calibration tests. The panels were restrained with toggle clamps which also provided minimum interruption for the oxy-acetylene flame.

A 10mm deep and 6mm wide groove was machined into each backing plate to accommodate the thermocouple wires but minimise the effect of the measurements on the thermal field generated in the plates by the burners.

A frame similar to the TTC fillet welding jig was built for the TTH (calibration and welding) fillet weld experiments. This frame was secured on the top of the backing plate used in the previous weld trials, as shown in Figure 5.3, so that the same welding and heating system can be used.

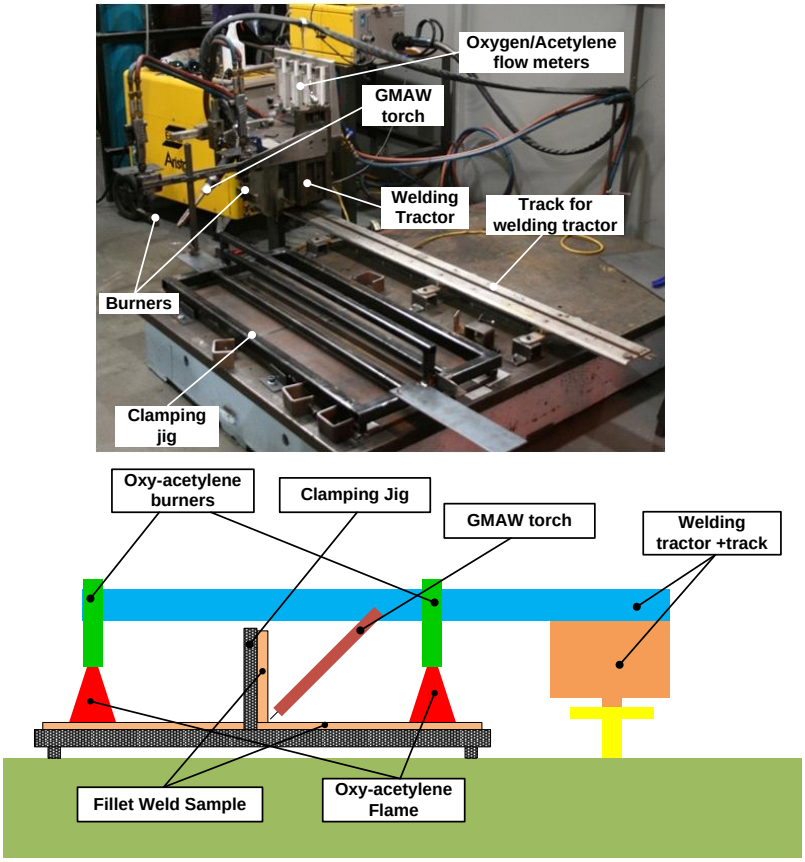

Figure 5.3 Thermal tensioning by heating fillet weld experimental setup

Variable area flow meters were used in both the oxygen and acetylene supply hoses for each burner separately. Standard bottled oxygen and acetylene were used as gas supplies for the experiments.

Temperatures were measured with K-type thermocouples attached to the bottom side of the plate at the centreline of the burners travel path.

5.1.1.3 Experimental plan

The oxy-acetylene burners were fist calibrated on 4mm panels using the welding setup shown in Figure 5.2. The parameters varied in these calibration tests are:

- Burner height from the heated surface, h_b
- Oxygen and acetylene flow rates, Q_O and Q_A
- Peak temperature measured with the thermocouples, T_p

The main parameters (constant and varied) of the TTH heat source calibration tests are listed in Table 5.2.

Table 5.2 Experimental plan of TTH heat source calibration

Weld Geometry	Travel Speed [m/min]	Burner Height (h_b) [mm]	Gas Flow Rate, [l/min]		Experiment ID
			Oxygen	Acetylene	
4 mm butt	0.63	122-172	3-7	9-12	HSC 1-3
2 mm butt	1.0	145	3-6	8-12	HSC 4-5
Fillet weld	0.55	120-140	4-9	8-16	HSC 6-8

5.1.2 Application of TTH on butt, fillet and overlapped welds

The aim of the TTH butt weld experiments were to examine the applicability of the TTH technique on butt welds and to obtain further understanding of this technique. To achieve these aims butt welds were produced with the application of TTH using a variety of burner settings.

5.1.2.1 Specimen Materials and Geometry

The materials used for the TTH application on welds are the same S355 grade and geometry as described in Table 5.1 and Figure 5.1.

5.1.2.2 Equipment

The experimental setup of TTH butt weld experiments is the same as the heat source calibration setup shown in Figure 5.3 with the addition of an ESAB welding power source.

In the 2 mm butt weld TTH experiments the clamping had to be improved as the thin plates lifted off the backing bar during welding. This issue was resolved by placing U-channels up-side-down on the plates close to the weld line and clamping these with the toggle clamps as shown in Figure 5.4.

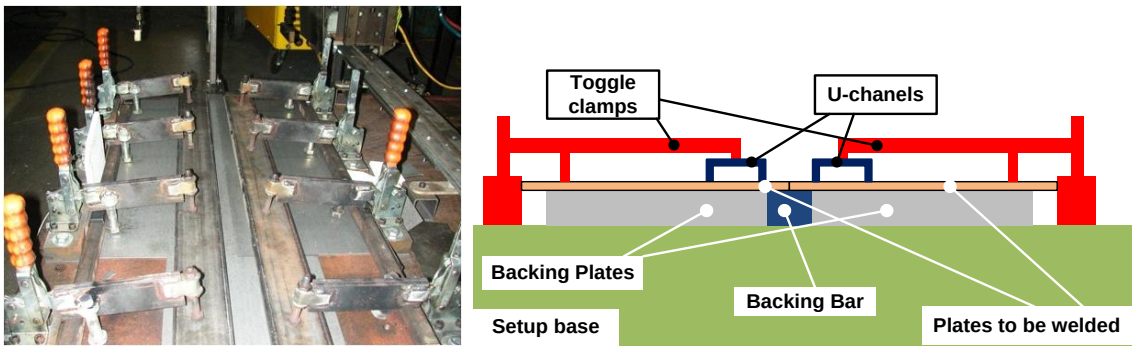

Figure 5.4 Clamping improved with U-channels on 2 mm TTH butt weld experimental setup

5.1.2.3 Experimental Plan

To investigate the applicability of TTH in butt welds and to gain further understanding of the technique the following parameters were varied:

- Burner x and y positions relative to the welding torch
- Peak temperature applied

Table 5.3 Experimental plan of TTH welding trials

Weld geometry	Burners Position [mm]		Peak Temperature [°C]	Experiment ID	Comment
	BWTD	BS			
4 mm butt	195	420	0-350	TTH BW1	
	-195 – 195	420	270	TTH BW2	
	195	420	270	TTH BW3	Heating before welding
	195	420	270	TTH BW4	Heating after welding
2 mm butt	195	420	0-280	TTH BW5	
Fillet welds	195	400	0-330	TTH FW1	
	195	250 – 400	210	TTH FW2	
	-390	400	210	TTH FW3	
Overlapped welds	195	420	280	TTH LW1	

The sequence of heating (pre- and post) and welding was also changed from simultaneous heating to examine the interaction of the welding and heating. The TTH butt weld experimental plan is summarised in Table 5.3.

The burners' positions BWTD and BS are explained in Figure 5.5. The plates in these experiments were welded using GMAW with the parameters listed in Table 5.4.

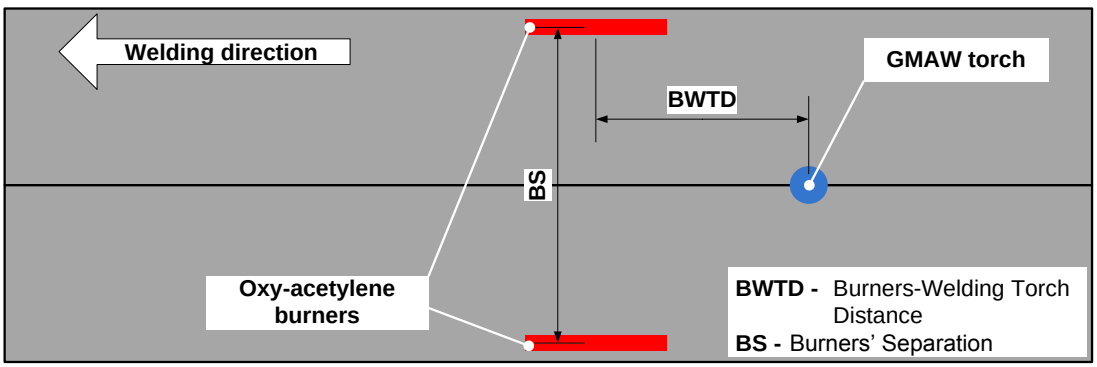

Figure 5.5 Schematics showing the torch position parameters BS and BWTD

The fillet welded panels were welded on both sides but each side was individually welded. The heating was applied the same way in each run on both sides. The plates were turned around after the first side to weld the other side as well.

Table 5.4 GMAW parameters of TTH welding trials

Welding Parameter	Joint configuration			
	4 mm butt	**2 mm butt**	**Fillet**	**Overlapped**
Travel Speed [m/min]	0.63	1	0.55	0.6
WFS [m/min]	11.5	7.5	7.6	6.8
Current[A]	235	166	225	168
Voltage [V]	38.3	33	22	20.2
CTWD [mm]	13	11	17	13
Shielding Gas Type/Flow Rate, [l/min]	Ar 20 %, CO2 20%, O2 2% /18			
D_w [mm]	1	1	1.2	1

5.1.3 TTH Using Alternative Heat Sources

The aim of using alternative heat sources for the TTH technique was to improve the heating process, gain better control and increase the repeatability of the heating. To achieve this two alternative heat sources were implemented: air-acetylene burners and induction heaters.

5.1.3.1 TTH Using Air-Acetylene Heaters

Air acetylene heaters in principal are similar to the oxy-acetylene heaters described previously with the difference that they use air instead of oxygen to mix with the acetylene. As a result, the flames produced have lower peak temperatures and lower flame velocities. Also, the air acetylene flame spread less over the heated plate (see Figure 5.6) providing a well defined and easily visible heated area.

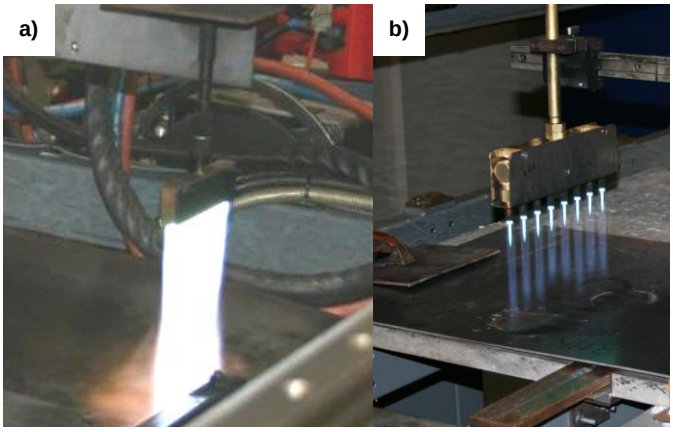

Figure 5.6 Flames produced by a) oxy-acetylene and b) air acetylene burners

5.1.3.1.1 Specimen Material and Geometry

All the air-acetylene experiments (calibration and welding) were carried out on the fillet welded panels described in Figure 5.3 (TTH) using S355 grade steel.

5.1.3.1.2 Equipment

The air-acetylene TTH setup was installed on a large gantry to make it easier to use and suitable for larger panel welding as shown in Figure 5.7.

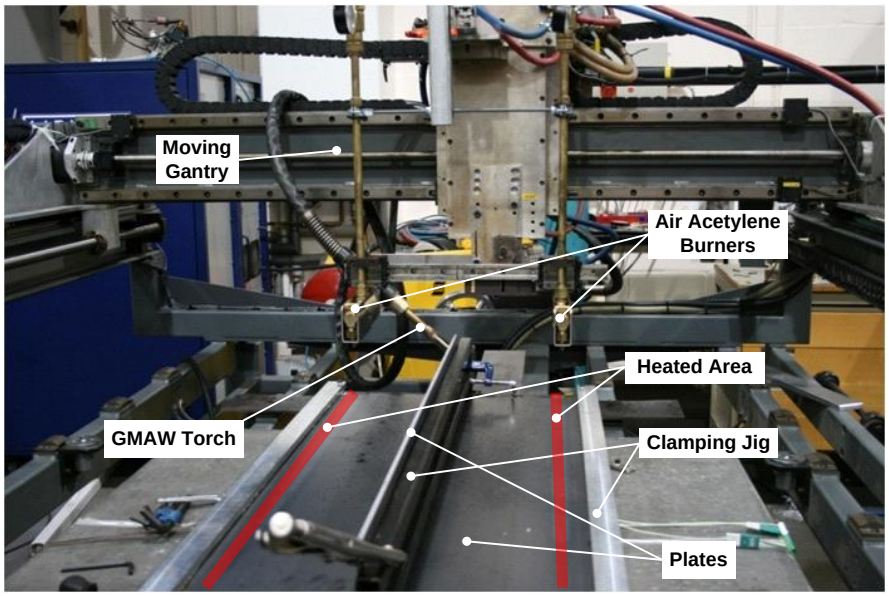

Figure 5.7 TTH experimental setup using air-acetylene burners installed on a large gantry

The air-acetylene burners use a mixture of air and acetylene at the ratio of 7:1. These burners are shown in Figure 5.8. Due to the design of the burners they operate on a higher flow rate regime than the oxy-acetylene burners.

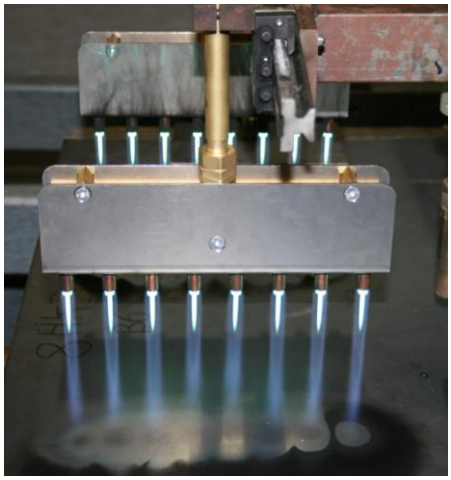

Figure 5.8 Linde Air-acetylene burners in operation

To have sufficient supply of gas a MCP (Manifold Cylinder Pack), 12 acetylene cylinders connected with a manifold, was used as the acetylene with a compressed air bottle as the gas supply.

Variable area flow meters were used in these experiments, on both the air and acetylene supply of the burners. As all the equipment was identical (gas hose diameter and length, burner dimensions) only one flow meter was used in the gas supplies. The flow valves were installed before the burners so that the gas flows were adjusted in both burners simultaneously.

5.1.3.1.3 Calibration and Welding Experimental Plan

The air -acetylene burners were calibrated using thermocouples in the same way as described in the heat source calibration chapter. The aim of the calibration experiments was to achieve the previously found optimum temperatures at different travel speeds. The work plan of these calibration experiments is summarised in Table 5.5.

Table 5.5 Air-acetylene heater calibration experiments

Travel Speed [m/min]	Burners' Height [mm]	Gas Flow Rate, [l/min]		Experiment ID
		Air	Acetylene	
0.55	50-100	35-65	5-22	HSC 9
0.775	72-100	35-60	5-17	HSC 10
1	75-100	44-60	9-17	HSC 11

After calibration the heating was applied on fillet welds. The experimental plan of these TTH fillet weld experiments is summarised to Table 5.6.

Table 5.6 TTH air-acetylene welding experimental plan

Weld geometry	Travel Speed [m/min]	Burners Position, [mm]		Peak Temperature [°C]	Experiment ID
		BWTD	BS		
Fillet welds	1	195	400	0-330	TTH FW4
	0.55	195	400	2709	TTH FW5

5.1.3.2 TTH Using Induction Heating

Induction heating on mild steel produces heating in a well defined volume of material with high thermal efficiency (see Section 2.2.2 for more details on induction heating). At the same time the lack of burning (Oxygen consuming reaction) and open flame means that induction heaters can be safely used even in a confined space. These attributes make induction heating an attractive heat source in TTH application.

The induction heating equipment used in these experiments was an EDF Minac Twin 20/40 unit shown in Figure 5.9. This induction heating power supply has two heating coils connected to it, providing the two heat sources for TTH.

Figure 5.9 EDF Minac Twin 20/40 induction heaters used in TTH induction heating experiments

The heating units were installed on the same gantry as the air-acetylene heaters as shown in Figure 5.10.

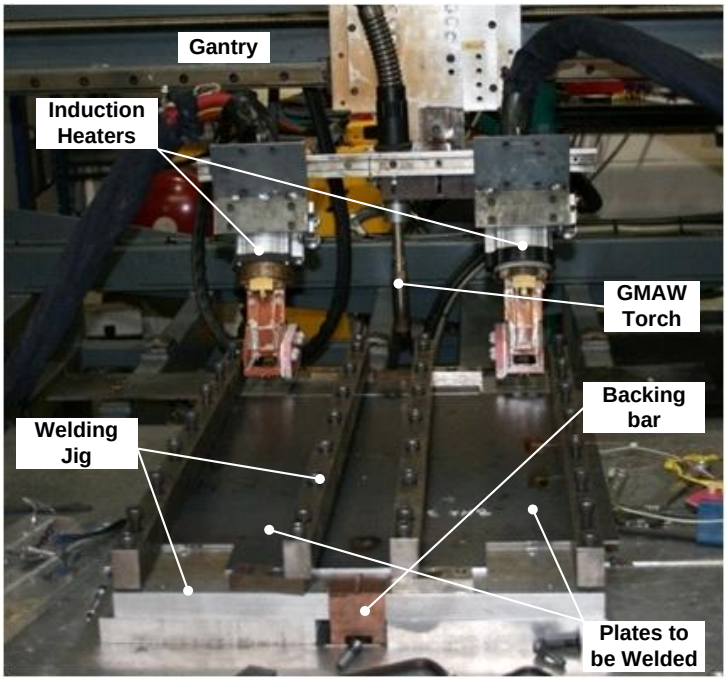

Figure 5.10 Induction heaters installed on the TTH gantry

The induction heaters were also calibrated on both butt and fillet welds to achieve a range of peak temperatures at different travel speeds. The experimental plan of the induction heaters calibration is listed in Table 5.7.

Table 5.7 TTH induction heaters calibration experiments

Weld Geometry	Travel Speed [m/min]	Power Output [%]	Experiment ID
Fillet welds	550	8-12	HSC 12
	1000	12-16	HSC 13
4 mm butt	630	12-30	HSC 14

Temperatures were measured on both sides of the plates in the calibration experiments. The thermocouples at the bottom were used to measure the peak temperatures applied whereas the thermocouples on top were used for controlling the power source of the induction heaters.

After calibration the induction heating was applied on both butt and fillet welds. The plan of the application in butt and fillet welds is detailed in Table 5.8.

Table 5.8 TTH induction heating experimental plan on butt and fillet welds

Weld Geometry	Travel Speed [m/min]	T_p, [°C]	Experiment ID
Fillet welds	550	275-330	TTH FW4
	775	330	TTH FW5
	1000	330	TTH FW6
4 mm butt	630	265-600	TTH BW6

5.2 Results

The Thermal Tensioning by Heating experimental work followed a similar structure to the TTC experiments. The first step in the TTH trials was the calibration of different heat sources which was then followed by application on different weld geometries.

5.2.1 TTH Heat Source Characterisation

The heat sources of TTH were characterised based on the peak temperature measured during the characterisation experiments as described in section 5.1.1.2. These peak temperatures were then compared when examining different parameters of the heat sources.

The results of the TTH heat source calibration experiments are presented below for all three heat sources used (i.e. oxy-acetylene, air-acetylene burners and induction coil).

5.2.1.1 Oxy-acetylene burner characterisation

The heat source calibration experiments started with the oxy-acetylene burners as these are commercially available and relatively cheap. Calibration was first carried out on butt welds (4, then 2 mm) then fillet welds.

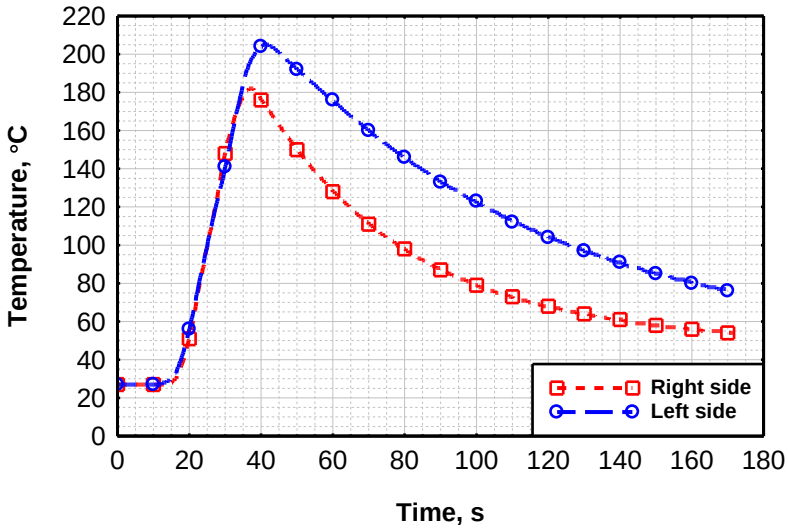

Figure 5.11 Temperature history of both plates recorded by thermocouples in the (TS: 0.63 m/min, h_b: 172 mm, acetylene flow rate: 12 l/min, oxygen flow rate: 7 l/min)

An example of the thermal history generated by the oxy-acetylene burners is shown in Figure 5.11. The temperature histories are not the same on the two sides: the peak temperature on the right side is 25 °C lower than that of the left side. This temperature difference remained consistent throughout the oxy-acetylene TTH experiment.

Initially the calibration experiments examined the relationship between the acetylene flow rate and the recorded peak temperature on 4 mm butt weld configuration. The results of these experiments are shown in Figure 5.12.

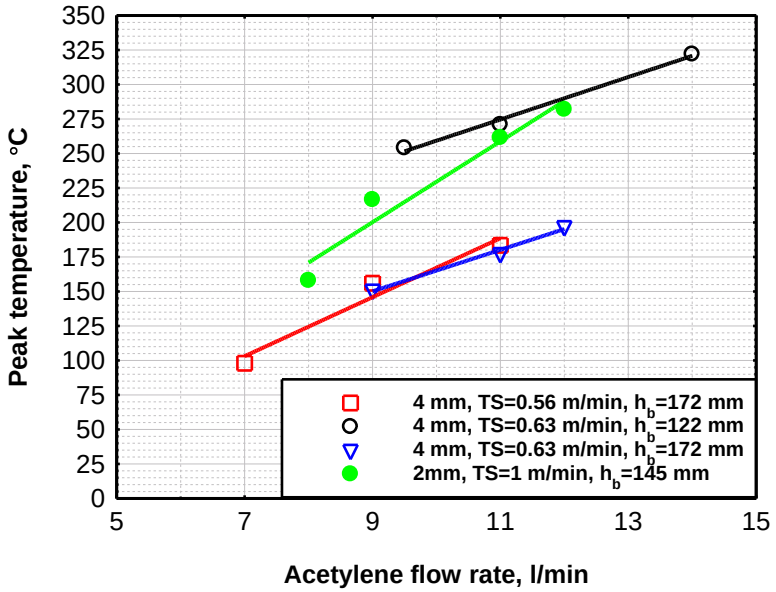

Figure 5.12 Acetylene flow rate versus measured peak temperatures on 4 and 2 mm butt welds

As Figure 5.12 shows the peak temperature is linearly dependant on the acetylene flow rates: the higher the acetylene flow rate the higher the peak temperature. Figure 5.12 indicates that the distance between the burner and the heated surface strongly affects the peak temperature. This effect is shown in more detail in Figure 5.13: as the height of the burners increases from 135 to 172 mm the peak temperature decreases also from 200 to156 °C.

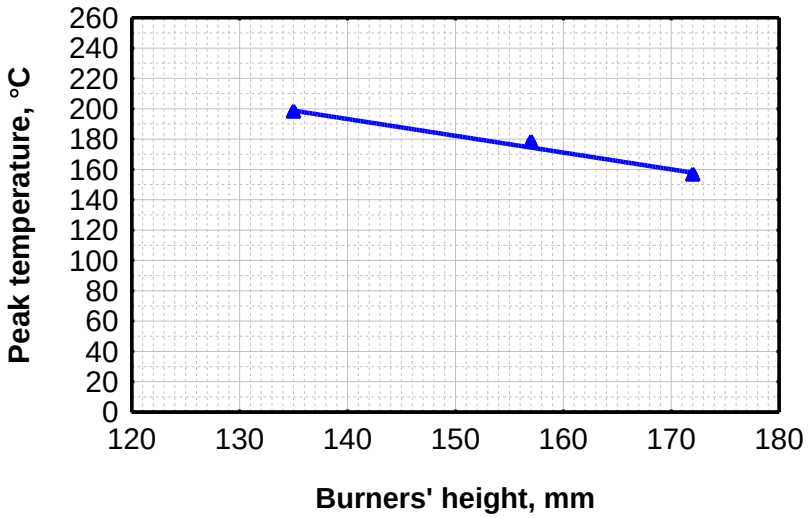

Figure 5.13 Burners height versus peak temperature in 4 mm butt weld configuration

After the butt weld configuration the oxy-acetylene burners were calibrated in the fillet weld configuration as well. The results of these calibrations are presented in Figure 5.14.

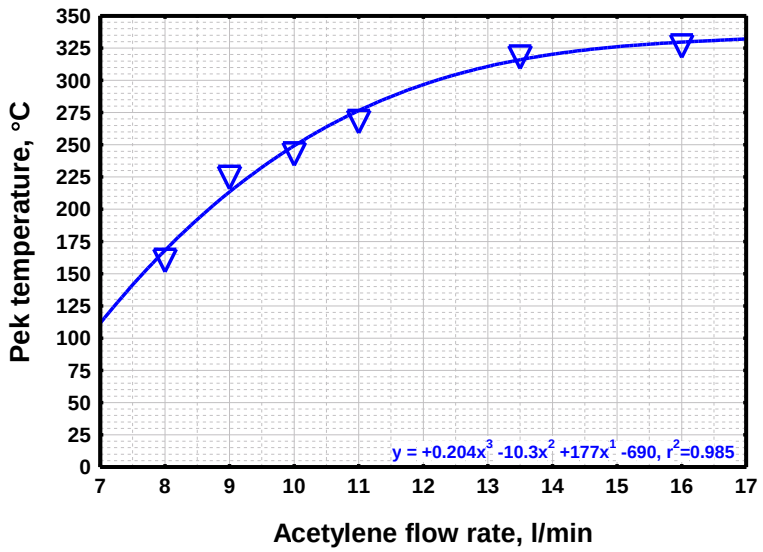

Figure 5.14 Acetylene flow rate versus peak temperature in fillet weld configuration at 0.55 m/min travel speed (oxygen flow rate adjusted to consistant flame appearance)

The temperature levels for the fillet weld calibrations are considerably higher than that of the butt weld calibrations at the same travel speed (0.55 m/min). This is due to the difference in the heat sink in the two welding setups: the butt weld setup has thick (25 mm) solid steel plate as support all across the panel, whereas the fillet welding rig is a frame made of tubular section, which provides very little heat sinking.

5.2.1.2 Air-acetylene burner characterisation

The air acetylene heat source calibration experiments aimed at achieving the optimum temperature range of 250-300 °C obtained in the butt weld TTH trials using oxy-acetylene burners. After replicating the temperatures at 0.630 m/min the travel speed was increased to 0.775 then 1 m/min as shown in Figure 5.15.

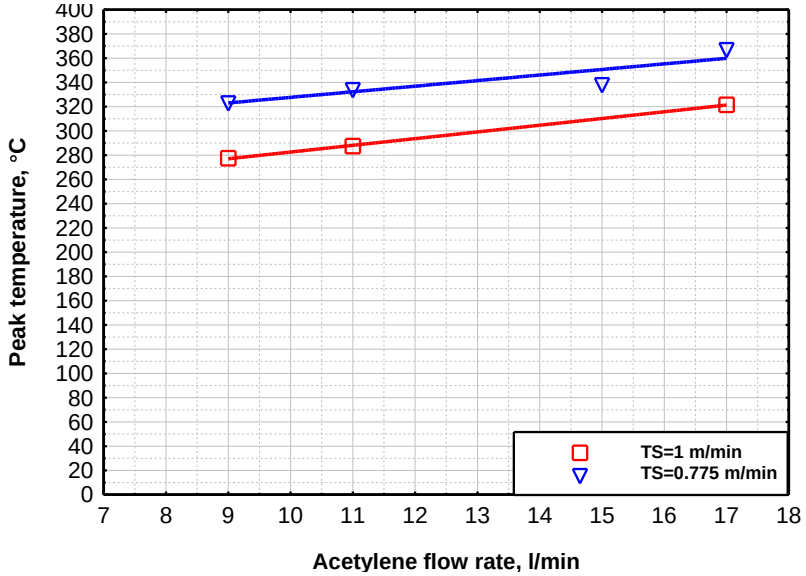

Figure 5.15 Acetylene flow rate versus peak temperature of air acetylene burners in fillet weld configuration

5.2.1.3 Induction heater characterisation

The last TTH heat source calibration experiments were those of the induction heaters. The induction coils were calibrated only for power output for the desired temperature range (250-300 °C). These calibrations were done on both butt and fillet weld configuration as shown in Figure 5.16. This figure shows that in case of induction coils 85 % travel speed increase (from 0.55 to 1 m/min) required a 34% power increase to achieve the same peak temperature (~250 °C on square and triangle series in Figure 5.16.

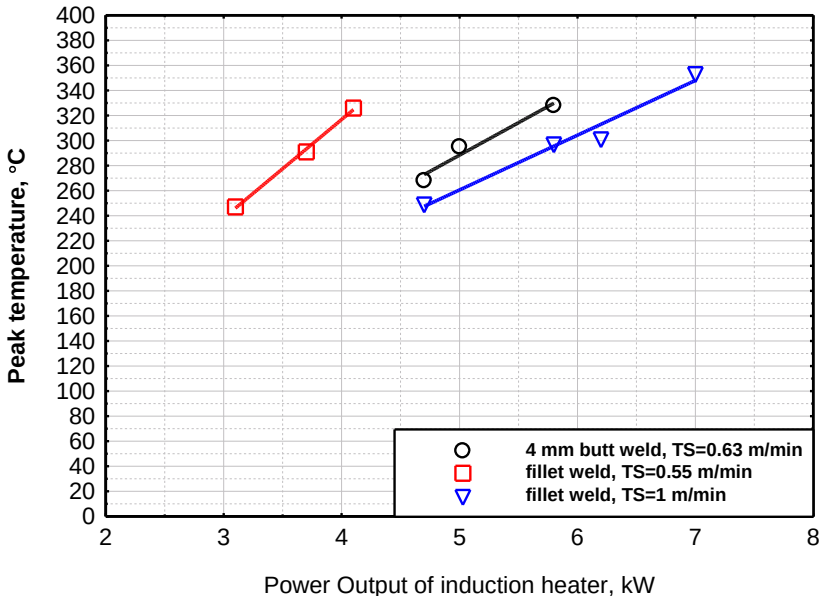

Figure 5.16 Power output versus peak temperature of induction heaters in butt and fillet weld configurations

5.2.2 TTH Welding Trials

Thermal Tensioning by Heating was applied on three different joint configurations as described in Chapter 5.1.2 (Table 5.3). The results of these experiments, focusing primarily on the distortion of the welded plates are detailed in this chapter.

5.2.2.1 TTH Applied on Butt Welds

In the first set of experiments the peak temperature applied by the burners was varied. The distortion reduction achieved by different peak temperatures is shown in Figure 5.17. The biggest distortion reduction is achieved at 240°C peak temperature, although the distortion reduction of panels in the temperature range of 200 -300°C is very similar.

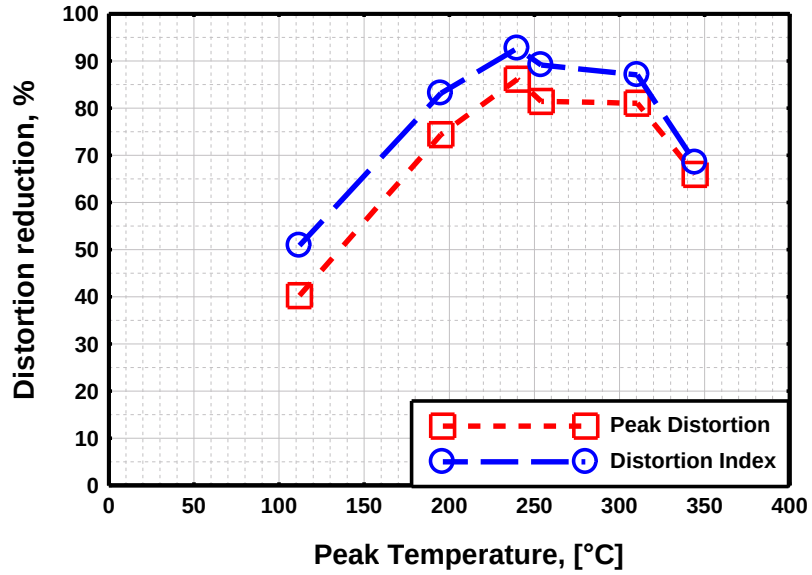

Figure 5.17 Distortion reduction achieved using different peak temperatures on 4 mm butt welded panels, reference weld Pead Distortion: 28.5 mm, DI: 10.5 mm

The second set of experiments was aimed at examining the influence of the burners position relative to the welding torch (BWTD) on the welded panels. The results of these experiments are shown in Figure 5.18.

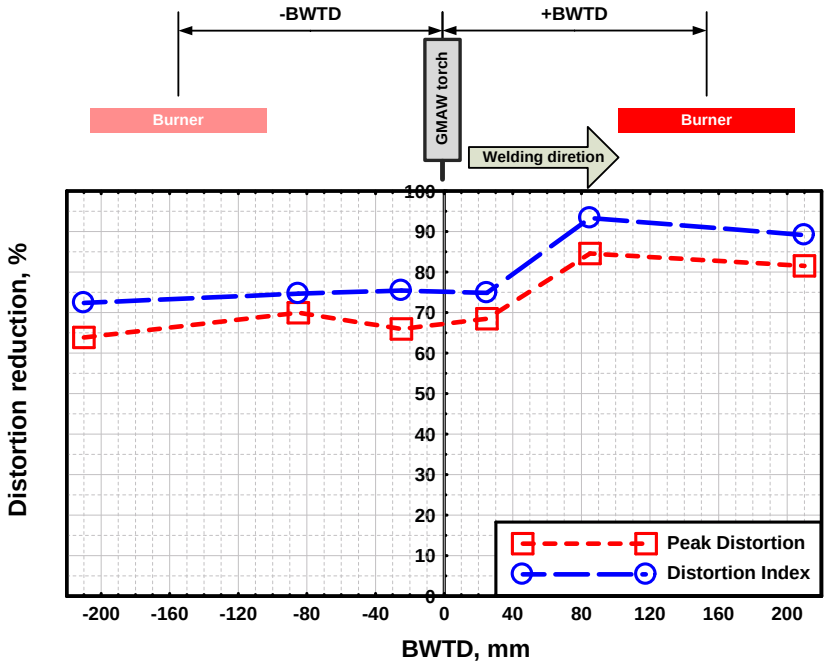

Figure 5.18 Distortion reduction achieved by TTH at different BWTDs on 4 mm butt welds, reference weld Pead Distortion: 28.5 mm, DI: 10.5 mm

The optimum BTWD was found to be +95 mm as Figure 5.18 clearly shows. Although it should be noted that the distortion was still reduced by at least 65 % (peak) and 70 % (DI) for all other positions displayed in Figure 5.18.

Further experiments were carried out to investigate the importance of the sequence of the application of TTH. The distortion response measured on the welded panels in this set of experiments is shown in Table 5.9.

Table 5.9 Distortion response of 4 mm butt welded panels using TTH applied in different sequences

Condition	Distortion Index (% change)	Peak Distortion [mm]
Pre-heating at 350 °C	11.07 (+5)	29.9 (+5)
Pre-heating at 240 °C	11.4 (+9)	35.1 (+23)
Pre-heating + Tacking	11.57 (+10)	30.69 (+8)
Post-Heating	8.34 (-21)	21.36 (-25)

The results in Table 5.9 show that TTH applied individually before welding does not reduce the distortion of the welded panels after welding. Although when TTH is applied individually post-welding there is slight improvement in distortion.

The peak temperature experiments, using the results of the heat source calibration experiments, were repeated on 2 mm thick panels to investigate the transferability of the process to different thickness panels. The distortion response of these 2 mm butt welded panels in relation to different peak temperatures of TTH is shown in Figure 5.19.

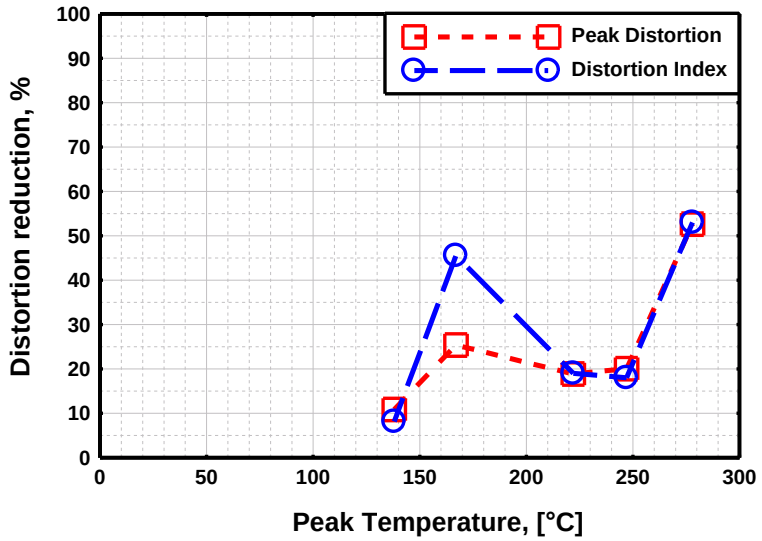

Figure 5.19 Influence of peak temperature applied by the burners on the distortion reduction of 2mm butt welded panels, reference weld Pead Distortion: 14 mm, DI: 12.04 mm

The best result in these experiments was achieved by applying 280 °C peak temperature heating with which both the peak distortion and the DI are reduced by 55 %. Although these results are not consistent with that of the 4 mm butt weld TTH trials, it is still a major improvement in distortion overall.

5.2.2.2 TTH applied on fillet welds

The fillet weld TTH experiments were carried out examining the same parameters (peak temperature and BWTD) as in the butt weld application of TTH with the addition of burners' separation (BS). Also the applicability or transferability of the TTH process onto fillet welded joint configuration was investigated.

The first set of experiments considered at the affects of the peak temperature applied by TTH on the distortion response fillet welded panels (see Figure 5.1 for geometry of panels). The results obtained in this set of experiments are illustrated in Figure 5.20.

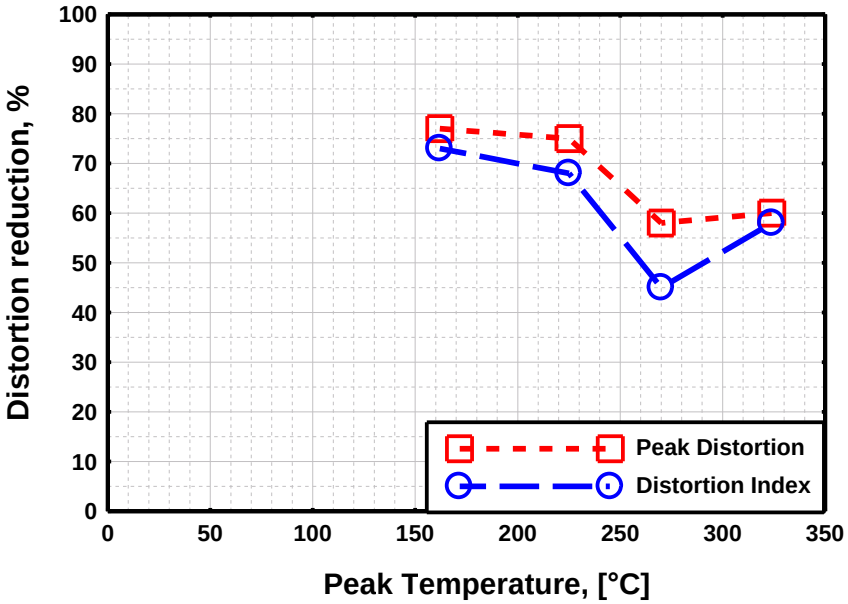

Figure 5.20 Influence of peak temperature applied by the burners on the distortion of fillet welded panels at 0.55 m/min travel speed, reference weld Pead Distortion: 21.64 mm, DI: 6.87 mm

The peak temperature with the best results in this experiment was between 160 °C and 230 ° where distortion (both peak and DI) was reduced by approximately 75 % as Figure 5.20 clearly shows.

After the peak temperature experiments the separation of the burners was examined in relation to the distortion of the fillet welded panels.

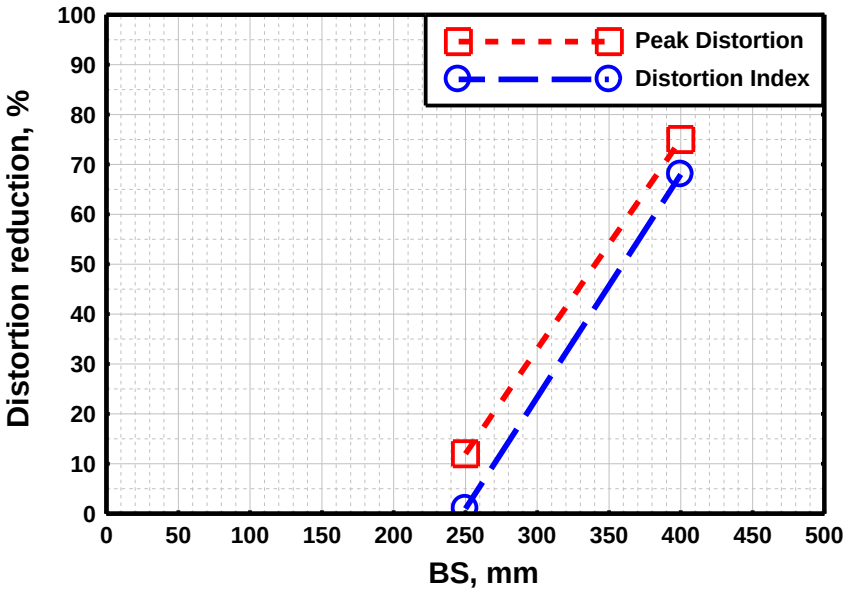

Figure 5.21 Influence of burners' separation (BS) on the distortion of fillet welded panels, reference weld Pead Distortion: 21.64 mm, DI: 6.87 mm

It is clear from Figure 5.21 that the greater the BS the higher the distortion reduction.At BS=250 mm there is no significant distortion improvement, while increasing BS to 400 mm yielded nearly 70 % improvement in the peak and somewhat more in the DI values distortion.

After the peak temperature experiments trials were carried at different BWTD positions. The distortion response measured on these panels is shown in Figure 5.22.

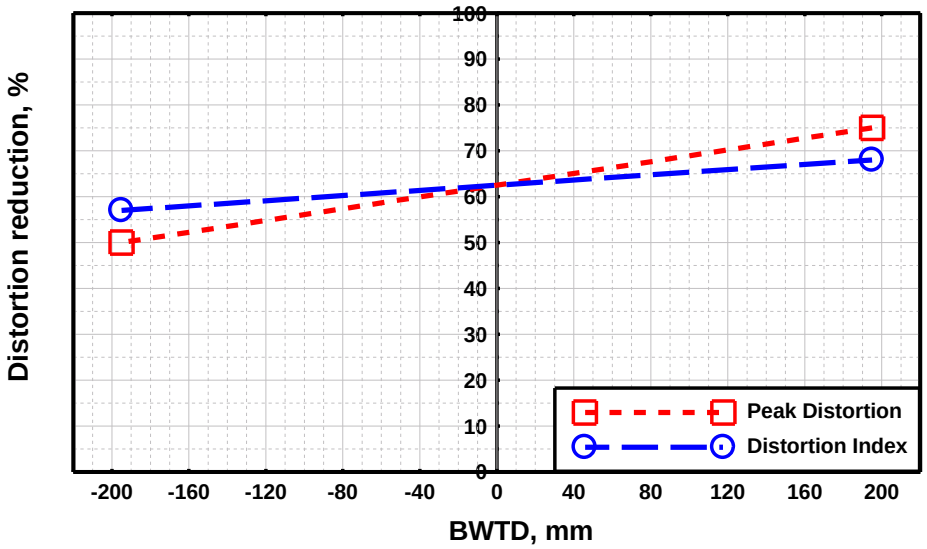

Figure 5.22 Influence of welding torch relative position (BWTD) on the distortion of fillet welded panels, reference weld Pead Distortion: 21.64 mm, DI: 6.87 mm

The results of the BWTD experiments on fillet welds show that distortion is better decreased (by 68/75 % DI/Peak distortion) when the burners are travelling ahead of the welding torch (+ve BWTD) rather than trailing behind. It is important to note though that either BWTD reduced distortion considerably.

5.2.2.3 TTH Applied on Over-lapped welds

TTH was also applied on overlapped joints to extend the applicability of this SE technique. As this experiment was only for demonstrational purpose no detailed parametric study was carried out.

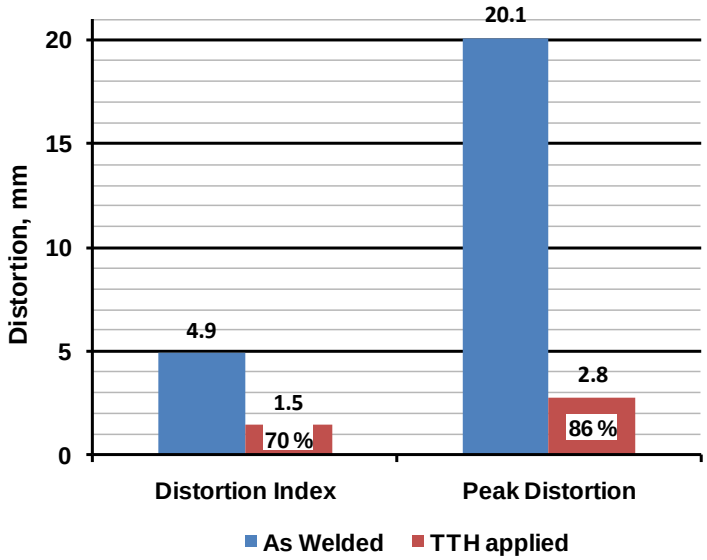

Figure 5.23 Distortion response of overlapped welds with and without TTH applied (percentage values shown within the columns are distortion reduction)

The results of the over-lapped joint experiment are shown in Figure 5.23. The application of TTH dramatically reduced both the overall (DI) and the peak distortion values.

5.2.2.4 TTH Using Alternative Heat Sources

Alternative heat sources (i.e. air-acetylene burners and induction heaters) were primarily applied on fillet welds as temperature measurements were easier and more reliable in this setup.

Air-acetylene burners were applied first to examine the optimum peak temperature of TTH with a different heat source. The results of these experiments are shown in Figure 5.24.

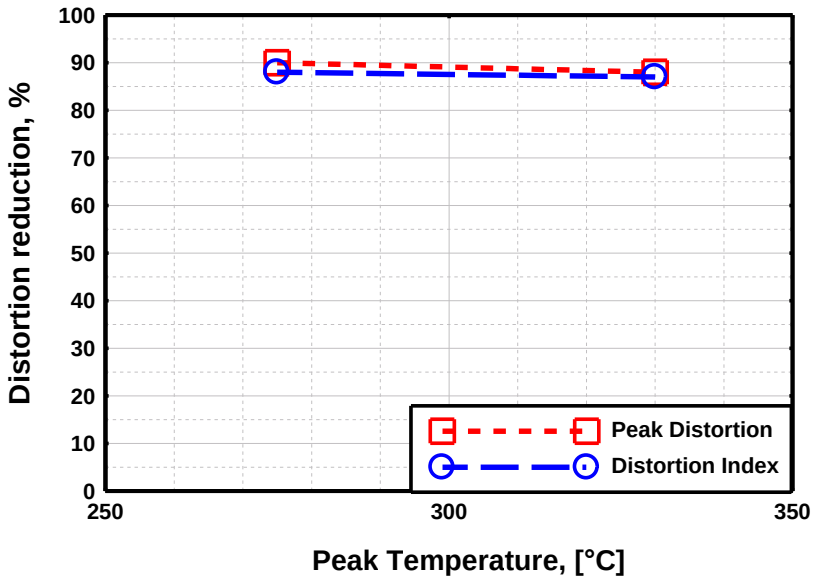

Figure 5.24 Distortion reduction of TTH using air-acetylene burners on fillet welded panels at different peak temperatures, reference weld Pead Distortion: 19.7 mm, DI: 6.57 mm

As Figure 5.24 shows, distortion is nearly completely eliminated at both 275 and 330 °C peak temperatures. Also the difference in distortion reduction at the two temperature levels is negligibly small (~2 %) using air-acetylene burners.

Induction heaters were also used as alternative heat sources for the TTH process. The first set of experiments was carried out on fillet welds at 0.55 m/min travel speed and the results of these experiments are shown in Figure 5.25.

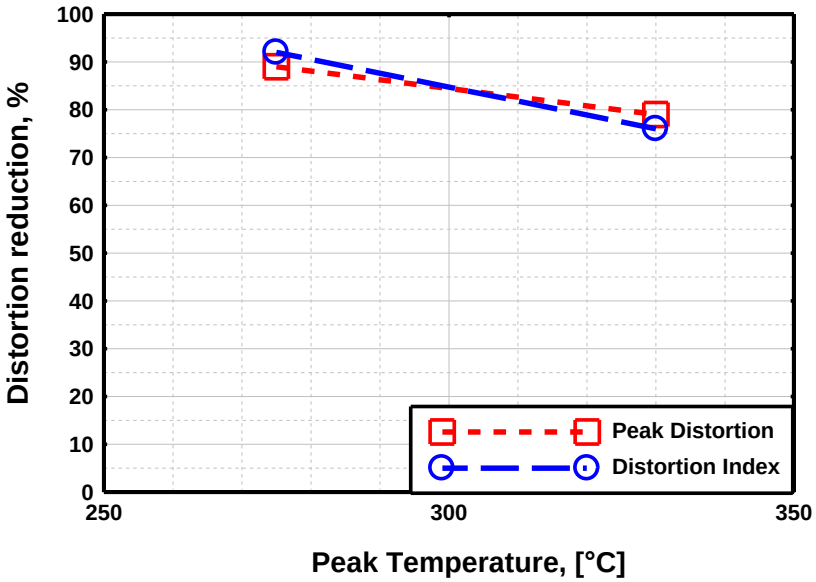

Figure 5.25 Distortion response of fillet welded panels with TTH using induction heaters at 0.55 m/min travel speed, reference weld Pead Distortion: 19.7 mm, DI: 6.57 mm

Distortion reduction is higher when using the induction heaters at 275 °C peak temperature. The reverse travel experiment refers to the induction heaters trailing the welding torch as opposed to leading.

In the second set of trials the travel speed was increased to 1 m/min. The distortion response of these panels is shown in Figure 5.26. The extent of distortion reduction is quite remarkable at nearly 80 % in both DI and peak values.

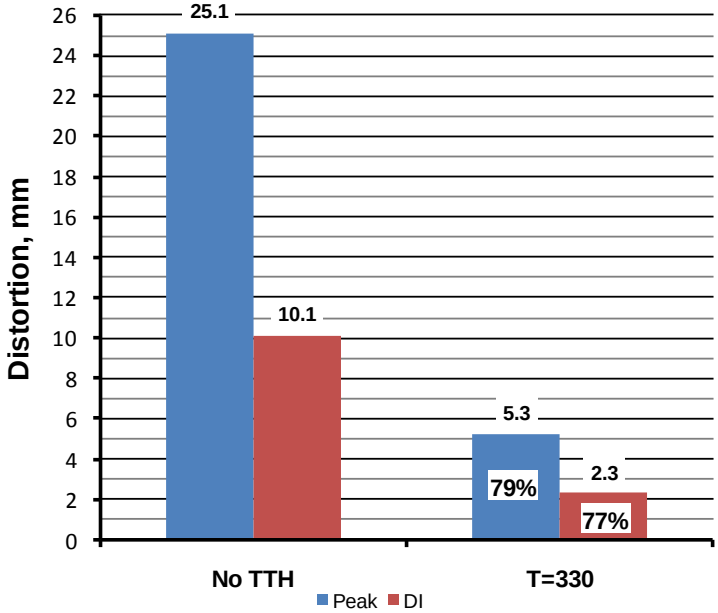

Figure 5.26 Distortion response of fillet welded panels with TTH using induction heaters at 1 m/min travel speed

Induction heating was also applied on butt welds to compare with the initial set of results obtained with oxy-acetylene burners. These experiments were carried out at the same travel speed as the earlier ones (0.63 m/min) for better comparison. The results of these butt weld induction heating TTH trials are summarised in Figure 5.27. The best results are achieved at T_p=330°C and both higher or lower temperatures result in smaller distortion reduction.

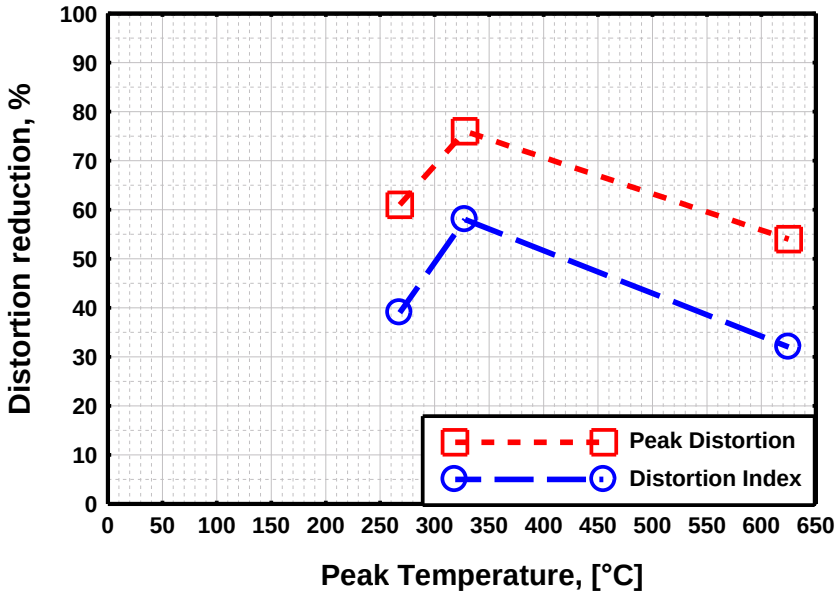

Figure 5.27 Distortion reduction achieved by induction heaters on butt welds at 0.63 m/min travel speed, reference weld Pead Distortion: 9.6 mm, DI: 2.75 mm

5.2.3 Data analysis and results of residual stress measurement

Residual stresses were measured on both butt and fillet welded sample with and without the application of TTH. The results of these measurements are presented below as comparisons of residual stress distribution with and without the application of TTH on both the butt and fillet weld joint configurations.

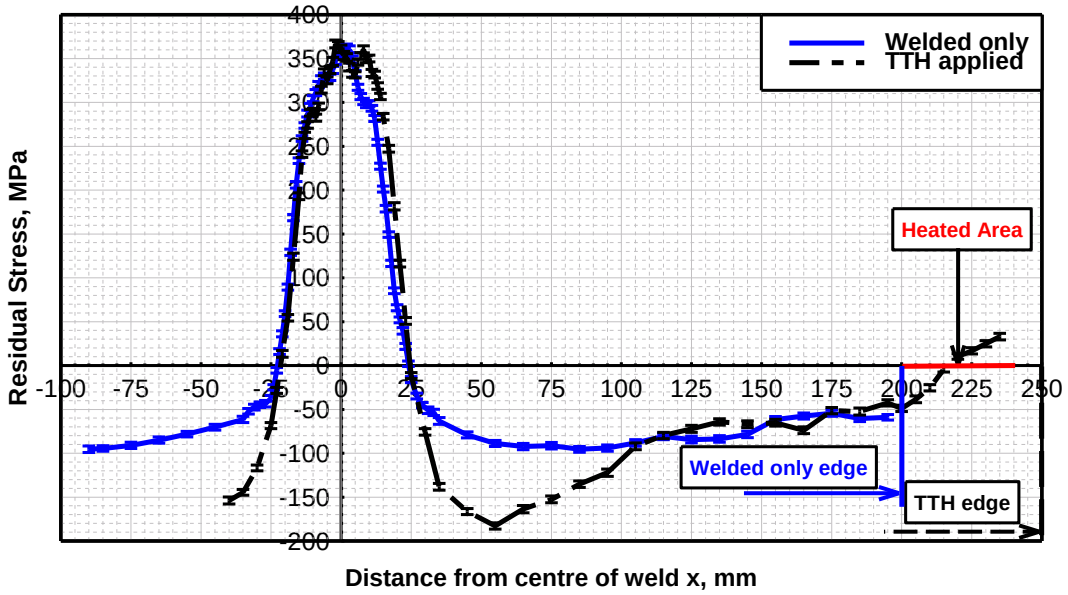

Figure 5.28 Comparison of the residual stresses measured in as welded and TTH butt weld samples

The difference in the residual stress profiles on the butt welds can be seen in Figure 5.28. The weld panel sizes for the welded only and TTH treated samples are different (400 mm and 500 mm wide respectively). Although the tensile peak does not show any significant change when TTH is applied the compressive residual stress distribution changed significantly due to the heating applied in TTH.

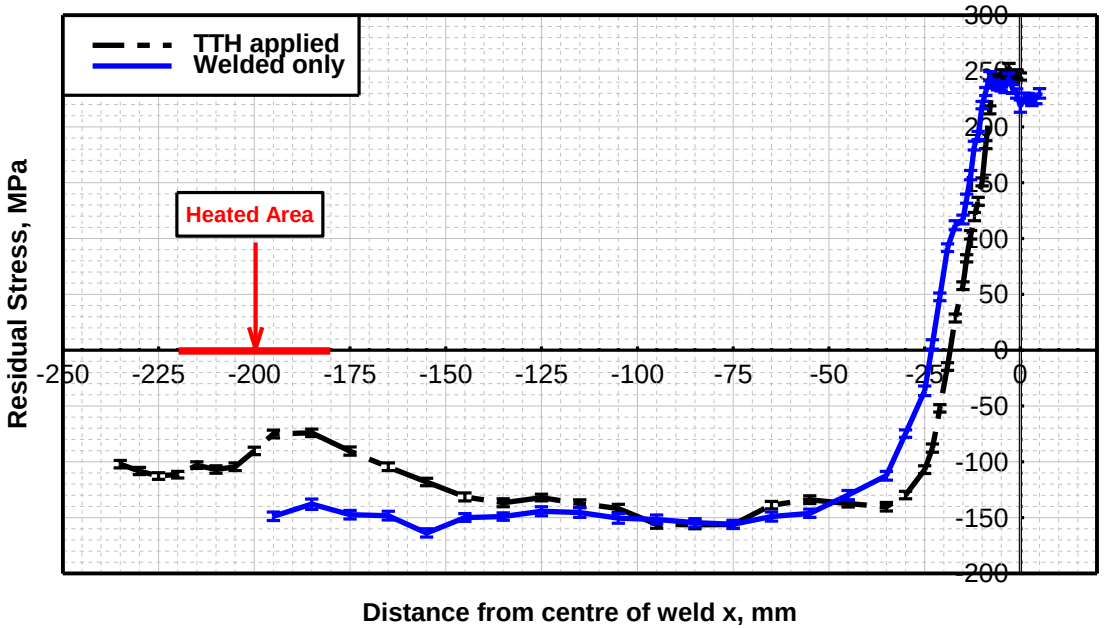

Figure 5.29 Comparison of the residual stresses measured in as welded and TTH fillet weld samples

The fillet weld RS measurement results illustrated in Figure 5.29 shows that in this joint configuration both the tensile and compressive region changed in the heated sample. The tensile peak at the centre line increased and there is a dip in the compressive region where the heating was applied on top of an upward (increasing) trend. At the same time the as welded sample shows neither this hump nor the upward trend in the compressive stress region.

5.3 Discussion

The Thermal Tensioning by Heating experiments, similarly to the Thermal Tensioning by Cooling, started with characterisation of the heat source of the process. After characterising the thermal source of TTH the research commenced with the application of TTH on first butt, then fillet and finally overlapped weld joint geometries. The results of these experiments are discussed below.

5.3.1 TTH Process Mechanism

As the TTH welding trial results show, this technique is highly effective in reducing buckling distortion (up to 80-90 % distortion reduction achieved) in butt, fillet as well as overlap joint configuration welded panels. The achieved distortion reduction values are higher than that of the TTC process (maximum ~65 %). Examining the residual stress profile of the butt welded panels (Figure 5.28) it can be seen though that the is reduced by the heating while the Applied Weld Load (AWL) remains unchanged. The unaffected tensile peak suggests that the heating does not generate a tensioning effect as does TTC. Instead, the heating applied changes the distribution of the residual stresses, particularly further away from the weld in the compressive stress region, where the heating is applied. Hence, TTH controls the Critical Buckling Load (CBL) in such a way that the compressive stresses in the residual stress profile do not a generate high enough buckling load to exceed CBL therefore reducing or eliminating buckling.

CBL for a beam subject to compressive load can be determined by Euler's equation:

$$\sigma_{cr} = \frac{F_{cr}}{bh}, \quad F_{cr} = -\frac{Ebh^3\pi^2}{12a^2}$$
$$\sigma_{cr} = -\frac{Eh^2\pi^2}{12a^2} \tag{5.1}$$

where:

- E – Young's modulus
- b – width, a – length, h – thickness of column

It can be seen in Equation (5.1) that the thinner and the longer the plate the lower CBL becomes. Euler's equation can only determine CBL (or σ_{cr}) for a uniformly loaded column or plate. The residual stress profile generated by welding forms a non-uniform load on the plate. Hence Euler's equation is not suitable for calculating CBL for welded plates.

Van der Aa [45] and Masubuchi [3] both analysed the buckling phenomena of a welded plate with non-uniform load and obtained similar results for CBL [45]:

$$\sigma_{cr} = \left[\frac{E\pi^2}{12\ 1-\nu^2}\right]\left[\frac{h}{b}\right]^2\left[\frac{a}{b}+\frac{b}{a}\right]^2\left[\frac{\pi c/b}{\sin\ \pi c/b}\right] \tag{5.2}$$

where:

- ν - Poisson ratio
- c - width of tensile region in the residual stress distribution

Equation (5.2) refers to a boundary condition where all sides are simply supported (SSSS). In this equation it can be seen that the larger c (width of tensile region) the larger σ_{cr} becomes as with increasing c, the proportion of the cross section under compressive load is decreasing.

Similarly, if additional tensile regions are added to the residual stress profile (as Figure 5.28 shows) the cross section under compressive load decreases even if the tensile peak (or Applied Weld Load) at the welding centre line is unchanged, as is the case for butt welded panels with TTH applied.

The residual stress measurement results for both butt (Figure 5.28) and fillet welded panels (Figure 5.29) show that relatively small changes in the residual stress distribution can cause significant reduction in buckling distortion. This is due to the threshold behaviour of the buckling phenomena: if AWL is below CBL, no buckling distortion occurs, but as soon as AWL exceeds CBL buckling does occur. This threshold behaviour also means that the change in residual stresses is not necessarily proportional to the change in buckling distortion. For instance reducing DI by 50 % does not necessitate 50 % change in AWL or CBL.This can also explain why the application of TTH in the current work produces buckling free welds at much lower temperatures (200-300 °C) compared to Dull et al.'s [58-60] higher (500-600 °C) temperatures. The higher temperature heating also produces higher tensile stress peaks at the location of heating (see Figure 3.41) which are comparable (approcimately half of the welding tensile peak) in magnitude. These large peaks increase CBL even more than the smaller stress peaks produced in the current work at lower temperatures, hence the successful application of this technique by Dull. Unfortunately Dull et al. did not present any residual stress data at lower heating temperatures, therefore direct comparison of their work to the current work is impractical.

The residual stress measurements of the fillet welded TTH panels in Figure 5.29 show different results than the butt welded panels. The residual stress distribution of the TTH treated panel shows a higher magnitude tensile peak at the weld centre line and also shows less increase in the residual stress where heating is applied. The higher tensile peak can be explained by looking at the macro section of a fillet weld in Figure 5.30.

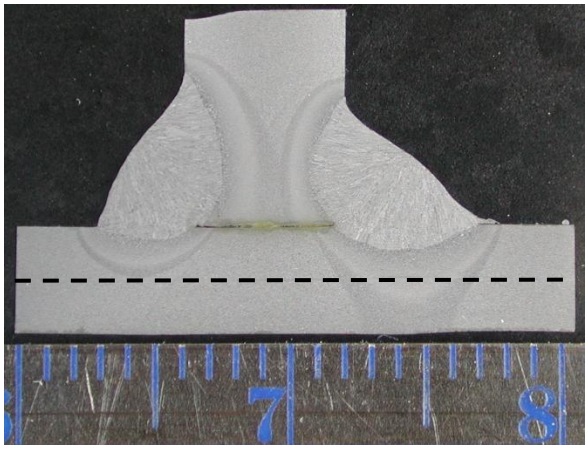

Figure 5.30 Macrograph of a fillet weld produced in the TTH experiments (non-TTH treated sample), dashed line marks the scanning line of residual stress measurement

As the macrograph in Figure 5.30 shows the fillet welds on either side of the vertical member of the joint is not aligned symmetrically. The reason for this misalignment is the difference in the landing of the welding wire for the two sides as the fillet welds on either side of the vertical member were not welded simultaneously but consecutively and the welding wire was aligned by eye.

Due to this difference in weld orientation the Heat Affected Zones (HAZ) of the welds in the base plate on either side are also different as Figure 5.30 shows, the weld on the right has a HAZ extending to the bottom of the base plate (dashed line goes through this HAZ) while the HAZ on the right only extends to mid-thickness of the base plate. Hence the residual strain measurements were carried out in different locations relative to the welds giving different widths of the tensile peak measured.

The tensile peak observed in the residual stress profile (Figure 5.28 and Figure 5.29) at the heaters location is a result of a mechanical interaction of the welding and heating zone produced by the combined thermal field of welding and heating. The welding thermal field, particularly in long, narrow plates, results in the expansion of the metal in the weld zone. This expansion at the same time is limited by the adjacent colder material and the clamping. Hence the weld centre line expands and “rotates” due to these constraints and the clamping of the panels. When the heating is applied on the outer edge of the panel individually, similar

expansion and rotation occurs but in the opposite direction. The closer the heating to the outer edge of the plate, the more expansion and rotation occur.

When the heating and the welding are applied simultaneously these opposite "rotations" of the plate interact and produce a tensile peak (or positive stress gradient, Figure 5.28 and Figure 5.29) at the location of the heating even at relatively low temperatures. The temperature of the heating applied alone is not sufficient to generate a tensile residual stress peak in the plate. This is confirmed with the distortion response of the butt welded panels that were first welded then TTH treated subsequently (see results in Table 5.9): the panels that were subsequently treated with TTH exhibit no significant distortion reduction.

The profound difference in the positive stress gradient generated by the heating is on the one hand likely to be the result of the different mechanical constraints produced by the different joint configuration, the vertical member of the fillet weld (stiffener) provides additional mechanical constraints during welding. On the other hand the difference in stress gradient generated by the heating is also a product of the significant difference in the clamping conditions, while the fillet weld members were attached to the welding frame by clips providing simple support and allowing material movement (expansion and contraction) in the (vertical or horizontal) panel plane.

At the same time the butt welded panels were not only clamped vertically onto the welding bed but were also supported on either side by adjustable screws. This means that the thermal expansion and contraction of the butt welded panels during welding were restricted in the panel plane resulting in higher residual stresses generated by the same thermal tensioning than that of the fillet welded panels.

All the TTH samples produced in this work were relatively small (maximum 1 m long and 0.5 m wide) panels. An important factor of this technique (being developed for ship building) is the scalability. Large panel trials were carried out in Cranfield (using the experimental setup shown in Figure 5.7) as part of the sponsoring SEALS project by Kazanas [73] using the same oxy-acetylene burners as used in this work. The results presented in Figure 5.31 show that the TTH

characterised in this work scales well and reduces distortion on a 4 m wide butt welded panels.

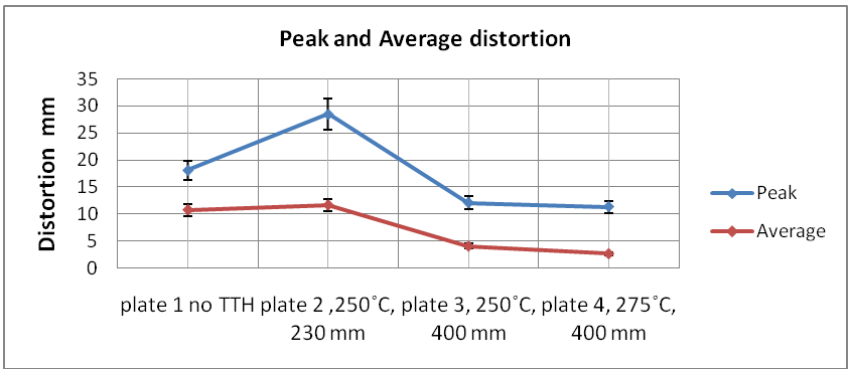

Figure 5.31 TTH applied to large (4 m x 1 m) plates using oxy-acetylene burners by Kazanas [73] as part of the sponsoring SEALS project in Cranfield University

Unfortunately the optimum conditions of heating (temperature and position) are difficult to compare with other authors' work as not all of them include these parameters in their work. Masubuchi et al. [52] only refer to an analytical study to optimise side heating conditions. In this analytical study they obtained an optimum temperature of 93°C, though there is no evidence of experimental verification and no mention of optimum positioning either.

Michaleris et al. [53-57] described their experiments in more detail: their optimum temperatures were 270 °C for the static and 200 °C for the transient thermal tensioning process. These temperatures are significantly higher than the optimum temperature obtained on fillet welds in this work (160 °C) even though the specimen geometry, and the plate thickness specifically is similar (4.7 mm) to the specimen used for the fillet welds here. The reason behind this difference between optimum temperatures could be the different positioning of heating in both the static and transient thermal tensioning. In the static thermal tensioning process the centre of the heating elements is 97 mm from the weld centreline on a 600 mm wide panel.

On the other hand the transient thermal tensioning in Michaleris et al.'s research applies side heating in a different way than that used in this work (see Figure 3.33-Figure 3.34). They optimised the side heater design for minimum residual stress at the plate edge and minimum sum of squares of stress. In these two optimum heater

designs the heaters are relatively close to the weld centre line and extend across most of the width of the plate, providing a wide heated area. In both cases the dimension of the heaters in the transverse direction is significantly larger than in the longitudinal or travel direction.Using induction heaters Bagshaw et al. [61] stated an optimum temperature range for side heating of 300-400 °C for Inconel 22 and 400-500 °C for C-Mn steel welded using Reduced Pressure Electron Beam (RPEB) welding as well as 200-300 °C for Inconel 22 when welded using GTAW. It should be noted though, that the plates welded in this work were 20 mm thick.

5.3.2 Limitations, Practical and Industrial Application Issues

Even though TTH is applied successfully in this work to eliminate buckling distortion, this process is not without its limitations. A major drawback of TTH is that is does not reduce the welding residual stresses, but adds more stresses in different locations. These additional stresses can cause issues in further manufacturing processes (e.g. machining) and can also influence the structural integrity of a welded structure (e.g. impact resistance of a ship).

The heating in TTH needs to be a localised heating, hence applying TTH can prove difficult for high thermal conductivity materials such as Al alloys. Also, even though the heating temperatures used in this work are low, possible microstructural changes need to be considered as a relatively large area of the panels are heated. Free access also needs to be ensured to the areas to be heated.

In some applications it might be difficult or expensive to achieve heating of a large area at relatively low temperatures even though there are many heat sources available for this process. Such an application could be Ti alloy or austenitic stainless steel welding in Ar environmental chamber, where oxy-fuel burners would contaminate the Ar atmosphere and induction heating is impractical as these alloys are non-magnetic. In this case some type of laser heat source is needed to apply TTH which makes the application expensive.

Automation of the heating process is not a necessity, although highly recommended. This automation should not be difficult as there are many automatic oxy-fuel heating systems already in use in industry.

6 Conclusion

The conclusions drawn in this research work are detailed in the following paragraphs.

Both TTH and TTC techniques were applied successfully on different weld configurations: butt (TTH and TTC), fillet (TTH and TTC) and overlapped (TTH) welds. Amongst these joint configurations the application of TTC to fillet weld and the application of TTH to overlapped joint configurations are new welding configurations.

Both TTH and TTC techniques were quantitatively characterised and as a result of the quantitative characterisation the main parameters of both techniques were identified. The main parameters of TTC identified in this work are:

- AEG – Air Entrainment Gap,
- z_A – distance of Amal jet from the substrate surface,
- p_e – extraction, quantified as differential pressure in the extraction pipe,
- Amal jet size,
- D_n – cryogenic nozzle shroud internal diameter.

The main parameters of TTH identified in this work are:

- T_p – peak temperature of plate at the location of heating
- BWTD – distance between the burners and the welding torch in the direction of travel
- BS – distance of TTH heat sources from each other

The main differences of TTH and TTC in mechanism were resolved: TTC reduces the Applied Weld Load of the welding residual stress profile by reducing the width/height of the tensile stress peak in the weld area. In contrast TTH does not affect the tensile stress peak in the weld zone in the residual stress profile but changes the Critical Buckling Load of the welded panel by adding tensile stresses in the compressive region further away from the weld where heating is applied.

In this work both TTH and TTC were moved forward in maturity, where now they can be applied in industry. Main application issues were identified for both tensioning techniques. The detailed technology transfer study of TTC resulted in significant improvements in the quality of the cryogenic spray, issues of weld tooling and weld process parameters as key factors were also identified and resolved. A cooling process control system was proposed to aid the automation and with it the industrial application of TTC.

7 Recommendations for Future Work

The work presented in this thesis shows that TTH and TTC can be applied to welding successfully to eliminate buckling distortion. Based on the knowledge and experience gained through this work the following actions are recommended to further extend the understanding and the applicability of these processes:

- Development of cooling system control based on the method detailed in the discussion to enable automation of TTC applied to welding to ease the applicability in industry.
- Investigation of CO_2 delivery system in order to optimise liquid to solid CO_2 conversion.
- Investigate the influence of cryogenic nozzle diameter (D_n) on the effectiveness of distortion reduction of TTC.
- Application of TTC and TTH to other materials than mild steel (S355 and DH36).
- Application of TTC to thicker plates, multi-pass welds, pipes and pressure vessels.
- Investigation of other benefits such as fatigue and Stress Corrosion Cracking properties of materials as well as elimination of hot cracking phenomena in different materials.
- Investigation of cooling applied to other processes such as thermal spraying, surface hardening processes to reduce residual stresses
- Modelling of TTC applied to welding.
- Modelling of TTH applied to welding.
- Numerical modelling of flow process within the cryogenic nozzle to improve and optimise cryogenic nozzle design.

References

1. T. Man, (2012), *World Affairs Board*, http://www.worldaffairsboard.com/naval-warfare/39675-type-45-leaves-begin-sea-trials.html, access date 2012
2. J. Blackburn, (1997), The Navy-Wide Weld Residual Stress and Distortion Program, www.dt.navy.mil, accessed 2009
3. K. Masubuchi, (1980), *Analyses of Welded Structures:residual stresses, distortion, and their consequences*, Pergamon Press Ltd., Oxford
4. D. Radaj, (1992), *Heat effects of welding: temperature field, residual stress, distortion*, Springer-Verlag, Berlin
5. S. Williams and A. Steuwer, (2009), Residual Stresses in Friction Stir Welding, in Lohwasser and Chen, *Friction Stir Welding: From Basics to Applications*, Woodhead Publishing Limited
6. P. A. Colegrove, C. Ikeagu, A. Thistlethwaite, S. Williams, T. Nagy, W. Suder, A. Steuwer and T. Pirling, (2009), The welding process impact on residual stress and distortion *Science and Technology of Welding & Joining*, 14(8), pp. 717-725
7. J.S. Rossmann and C.L. Dym, (2008), *Introduction to engineering mechanics: a continuum approach*, Taylor & Francis
8. B. Lucas, (2003), *Controlling distortion in welding - a guide to best practice*, www.twi.co.uk, accessed 2008
9. T. Schenk, M. Doig, G. Esser and I. M. Richardson, (2010), Influence of clamping support distance on distortion of welded T joints, *Science and Technology of Welding and Joining*, 15(7), pp. 575-582
10. T. Schenk, I. M. Richardson, M. Kraska and S. Ohnimus, (2009), A study on the influence of clamping on welding distortion, *Computational Materials Science*, 45(4), pp. 999-1005
11. T. Schenk, I. M. Richardson, M. Kraska and S. Ohnimus, (2009), Influence of clamping on distortion of welded S355 T-joints, *Science and Technology of Welding and Joining*, 14(4), pp. 369-375
12. G. E. Turner, J. E. Jones, V. L. Rhoades, T. E. Clem, P. L. Sarnow, S. K. Madden, A. Cuneo and J. Mcmahon, (2006), Portable automated plate straightener, *Journal of Ship Production*, 22(2), pp. 72-86
13. G. E. Turner, J. E. Jones, V. L. Rhoades, T. E. Clem, P. L. Sarnow, S. K. Madden, A. Cuneo, J. Mcmahon and R. Arner, (2007), Portable Automated Plate Straightener (PAPS): Flexible automation for ship production-integration into the shipyard, *Journal of Ship Production*, 23(4), pp. 185-196
14. D. Price, C. Harrison, S. Williams, A. Wescott, A. Johnson, J. Gabzdyl, M. Smith and M. Rahim, (2004), *The Performance of Active Tensioning Techniques for Stress Control in Welding*,BAE Systems, Report No. JS15232

15. D. Q. Cole, (1968), *Development of Techniques for Controlling Warpage and Residual Stresses in Welded Structures*, NASA, Report No. NASA CR-61235, Huntsville
16. V. I. Pavlovsky and K. Masubuchi, (1994), Research in the U.S.S.R. on residual stresses and distortion in welded structures, *Welding Research Council Bulletin*, 388, pp. 1-62
17. D. A. Price, S. W. Williams, A. Wescott, C. J. C. Harrison, A. Rezai, A. Steuwer, M. Peel, P. Staron and M. Kocak, (2007), Distortion control in welding by mechanical tensioning, *Science and Technology of Welding and Joining*, 12(7), pp. 620-633
18. D. G. Richards, P. B. Prangnell, S. W. Williams and P. J. Withers, (2008), Global mechanical tensioning for the management of residual stresses in welds, *Materials Science and Engineering: A*, 489(1-2), pp. 351-362
19. W. Liu, X. Tian and X. Zhang, (1996), Preventing weld hot cracking by synchronous rolling during welding, *Welding Journal*, 75(9), pp. 297-s
20. S. W. Wen, P. A. Colegrove, S. W. Williams, S. A. Morgan, A. Wescott and M. Poad, (2010), Rolling to control residual stress and distortion in friction stir welds, *Science and Technology of Welding and Joining*, 15(6), pp. 440-447
21. J. Altenkirch, A. Steuwer, P. J. Withers, S. W. Williams, M. Poad and S. W. Wen, (2009), Residual stress engineering in friction stir welds by roller tensioning, *Science and Technology of Welding and Joining*, 14(2), pp. 185-192
22. S. Morgan, P.A. Colegrove and T. Nagy, (2008), *Industrial Requirements, SE Tool Scaling Studies and Matching of SE Tools to Naval Applications*,BAE Systems, Report No. TES102344
23. R. V. Preston, (2001), *Modelling of Residual Stresses in Welded Aerospace Alloys*,PhD thesis, University of Cambridge, Cambridge
24. R.W. Serth, (2007), *Process heat transfer: principles and applications*, Elsevier Academic Press
25. Lynn Hunter, (2010), *CO2 flow measurement key in CCS schemes*, http://www.powerengineeringint.com/articles/print/volume-18/issue-4/features/co2-flow-measurement-key-in-ccs-schemes.html, access date 2012
26. A. N. Johnson and C. P. Rand, (2008), *Nozzle for emitting solid carbon dioxide particles with an axially displaceable valve member; Apparatus for cooling a heated weld zone with such a nozzle; Welding apparatus with such cooling apparatus*, International Patent No. WO 2007/052071 A1
27. Acetylene…there is no better fuel gas for oxy-fuel gas processes (2010), Linde marketing brochure
28. Facts About. Fundamentals of flame straightening, Linde marketing brochure

29. Q. Guan, C. X. Zhang and D. Guo, (1993), *Dynamically Controlled Low Stress No Distortion Welding Method and its Facility*, Patent No. CN 93101690.8, China

30. Q. Guan, C. X. Zhang and D. L. Guo, (1994), Dynamic control of welding distortion by moving spot heat sink, *Welding in the World*, 33(4), pp. 308-312

31. Q. Guan and J. Li, (2005), Mechanism of localized thermal tensioning effect in preventing budding distortions of thin-walled weldments, *Materials Science and Technology*, 25-28 September 2005, Pittsburgh, PA, USA, pp. 3-14

32. J. Li, Q. Guan, D. Guo, Y. Du, Y. Sun and Y. Shi, (2007), Effects of distance between arc and heat sink on stress and distortion in DC-LSND welding technology, *China Welding (English Edition)*, 16(3), pp. 6-9

33. Q. Guan, K. W. Brown, D. Guo, Y. Cao, C. Li and Y. Shao, (1988), *Improvements Relating to Welding*, International Patent No. WO8806505

34. J. Li, Q. Guan, Y. Shi, D. Guo, Y. Du and Y. Sun, (2004), Studies on characteristics of temperature field during GTAW with a trailing heat sink for titanium sheet, *Journal of Materials Processing Technology*, 147(3), pp. 328-335

35. J. Li, Q. Guan, Y. W. Shi and D. L. Guo, (2004), Stress and distortion mitigation technique for welding titanium alloy thin sheet, *Science and Technology of Welding and Joining*, 9(5), pp. 451-458

36. J. Li, (2005), Localized thermal tensioning technique to prevent buckling distortion, *Welding in the World*, 49(11-12), pp. 4-14

37. Y. P. Yang, P. Dong, J. Zhang and X. Tian, (2000), A hot-cracking mitigation technique for welding high-strength aluminum alloy, *Welding Journal*, 79(1), pp.

38. G. Luan, G. Li, C. Li, and C. Dong, DC-LSND Friction Stir Welding, *17th International Conference, Computer Technology in Welding and Manufacturing, 18-19 June 2008, Cranfield, UK*

39. J. Gabzdyl, M. Cole, S. W. Williams and D. Price, (2002), Cryogenic Weld Cooling, *Industrial Laser Solution for Manufacturing*, 17(5), accessible www.industrial-lasers.com

40. J. Gabzdyl, A Johnson, S. Williams, D. Price, I. Miyamoto K. F. Kobayashi K. Sugioka R. Poprawe and H. Helvajian, (2002), Laser weld distortion control by cryogenic cooling, *High-Power Laser Macroprocessing*, First International Symposium, Osaka, Japan, 27-31 May 2002., Bellingham, International Society for Optical Engineering; 2003., pp. 269-274

41. P. Staron, M. Koçak, S. Williams and A. Wescott, (2004), Residual stress in friction stir-welded A1 sheets, *Physica B: Condensed Matter*, 350(1-3 Suppl. 1), pp. 491-493

42. P. Staron, M. Koçak and S. Williams, (2002), Residual stresses in friction stir welded Al sheets, *Applied Physics A: Materials Science and Processing*, 74(SUPPL.II), pp. 1161-1162

43. S. Williams, Personal Communication, (2009), Cranfield University

44. D. Bertaso, G. B. Melton, R. L. Jones and C. C. Hardy, (2003), Advanced manufacturing using low stress no distortion (LSND) techniques, *Metal Fabrication and Welding Technology 2003*, Nottingham, 16-18 September 2003. University of Nottingham, pp.87-94

45. E. M. Van Der Aa, (2007), *Local Cooling during Welding: Prediction and Control of Residual Stresses nad Buckling Distortion*, PhD thesis, Delft University of Technology, Netherlands

46. S. Morgan and J. Mawella, Reducing Welding Distortion Using Cryogenic Sprays, (2007), *Proceedings of 2007 International Defence Applications of Materials Meeting*, Halifax

47. S. Morgan, A. Wescott, P. Devall and S. Williams, (2007), *Improvements Relating to Coolant Delivery*, Internationsl Patent No. WO 2007/080372 A1, BAE Systems

48. E. M. Van Der Aa, M. J. M. Hermans and I. M. Richardson, (2006), Conceptual model for stress and strain development during welding with trailing heat sink, *Science and Technology of Welding and Joining*, 11(4), pp. 488-495

49. E. M. Van Der Aa, M. J. M. Hermans and I. M. Richardson, (2005), Welding with a trailing heat sink: How to optimise the cooling parameters?, *ASM Proceedings of the International Conference: Trends in Welding Research*, Pine Mountain, GA, USA, pp577-582

50. D. Camilleri, G. F. G. Thomas, D. Nash, (2008), Mitigation of Welding Distortion and Residual Stresses via Cryogenic Cooling – A Numerical Investigation, *17th International Conference, Computer Technology in Welding and Manufacturing, 18-19 June 2008, Cranfield, UK*

51. I. E. Hernandez and T. H. North, (1984), Influence of External Local Heating in Preventing Cracking During Welding of Aluminum Alloy Sheet, *Welding Journal*, 63(3), pp. 84-s

52. K. Masubuchi, (1991), In-process control and reduction of residual stresses and distortion in weldments, *Proceedings of 3rd International Conference on Practical Applications of Residual Stress Technology,* Indianapolis, IN; USA, 15-17 May 1991, pp. 95-101

53. M. V. Deo and P. Michaleris, (2003), Mitigation of welding induced buckling distortion using transient thermal tensioning, *Science and Technology of Welding & Joining*, 8(1), pp. 49-54

54. P. Michaleris, J. Dantzig and D. Tortorelli, (1999), Minimization of welding residual stress and distortion in large structures, *Welding Journal*, 78(11), pp. 361-s

55. P. Michaleris and X. Sun, (1996), Finite element analysis of thermal tensioning techniques mitigating weld buckling distortion, *American Society of Mechanical Engineers, Pressure Vessels and Piping Division (Publication) PVP*, 327, pp. 77-87

56. P. Michaleris and X. Sun, (1997), Finite element analysis of thermal tensioning techniques mitigating weld buckling distortion, *Welding Journal*, 76(11), pp. 451s-457s

57. J. Song, J. Y. Shanghvi and P. Michaleris, (2004), Sensitivity analysis and optimization of thermo-elasto-plastic processes with applications to welding side heater design, *Computer Methods in Applied Mechanics and Engineering*, 193(42-44), pp. 4541-4566

58. R. Dull, (2004), Controlling Buckling Distortion with Transient Thermal Tensioning, *Shiptech*, 27 January 2004, Biloxi, MS., USA

59. R. Dull, (2007), Transient Thermal Tensioning to Control Buckling Distortion, *5th Charting the Course in Welding: US Shipyards*, 19 October 2007, Newport News, VA, USA

60. R. Dull, J. R. Dydo, J. J. Rusell and J. Shanghvi, (2005), *Method of Reducing Distortion by Transient Thermal Tensioning*, Patent No. US 6861617 B2

61. I. O. Fafiolu, (2007), *Evaluating the Heating Methods to Reduce the Distortion of 4mm Thick DH36 Ship Panels,* MSc thesis, Cranfield University, Cranfield

62. N.M. Bagshaw and C.S. Punshon, (2008), *Method of Relieving Residual Stress in a Welded Structure*, International Patent No. WO2008107660A1

63. J. A. Marsden, (2009), *Measurement of source plate distortion for weld distortion evaluation - Part 2,* Corus Research, Development & Technology, Report No. 145399

64. P. J. Withers and H. K. D. H. Bhadeshia, (2001), Residual stress part 1 - Measurement techniques, *Materials Science and Technology*, 17(4), pp. 355-365

65. G. A. Webster and R. C. Wimpory, (2001), Non-destructive measurement of residual stress by neutron diffraction, *Journal of Materials Processing Technology*, 117(3), pp. 395-399

66. M. E. Fitzpatrick and Alain Lodini, (2003), *Analysis of Residual Stress by Diffraction using Neutron and Synchrotron Radiation*, Taylor & Francis Inc,

67. *BS EN ISO 5167-2:2003,* (2003), Measurement of fluid flow by menas of pressure differential devices inserted in circular cross-section conduits running full. Part 2: Orifice Plates,2003, BSI

68. P. Michaleris and A. Debiccari, (1997), Prediction of welding distortion, *Welding Journal*, 76(12), pp. 172-s

69. Q. Guan, D. L. Guo, C. Q. Li and R. H. Leggatt, (1994), Low stress non-distortion (LSND) welding - a new technique for thin materials, *Welding in the World, Le Soudage Dans Le Monde*, 33(3), pp. 160-167

70. Q. Guan, R. H. Leggatt and K. W. Brown, (1998), *Low stress, non-distortion (LSND) TIG welding of thin-walled structural elements,* report number: 374/1988,

71. J. McHardy, S. P. Sawan, (1998), *Supercritical Fluid Cleaning – Fundamentals, Technology, and Applications,* William Andrew Publishing/Noyes
72. D. E. Winterbone, (1997), Advanced Thermodynamics for Engineers, Elsevier
73. Air Liquide, Gas Encyclopedia - Carbon dioxide, accessed at http://encyclopedia.airliquide.com, accessed 2010
74. Panagiotis Kazanas, (2008), *Evaluation of Heating Methods for Distortion Reduction of 4 mm S355 ship plates*, MSc thesis, Cranfield University

Appendixes

A1 S355 mild steel plates test certificates

corus

A04 A01

Port Talbot,
West Glamorgan, SA13 2NG
United Kingdom.
Telephone: 01639 871111
Fax: 01639 872067

INSPECTION CERTIFICATE

A02 Our Order No. 6/68310/1/1 A08 Customer Order No. 173258-1 A07

Works Order No 6/68310/1/1 A08 Despatch/Invoice No. and Date 20181416 28/04/08 A10

Certificate No. 20639885 A03 Certificate Date 28/04/08 202 Page 1 of 1 Part No. A09

Customer Name & Address A06

CD&BS DUDLEY
HR COIL PROCESSING CENTRE
BRIDGNORTH ROAD
WOMBOURNE WOLVERHAMPTON
WEST MIDLANDS WV5 8AT

Ordered dimensions mm B09-B11

GAUGE = 4.0000 WIDTH = 1000.000 LENGTH = COIL

Product Description B01

STRUCTURAL STEEL HOT ROLLED COIL NON SKIN PASSED MILL EDGES,NOT CUT BACK TO GAUGE

Specification B02 BSEN10025-2:2004

Grade B02 S355JR+AR

Certificate Specification A02 BSEN10204:2004 TYPE 3.1

MATERIAL IDENTITY B07	CAST / HEAT No. B07	YIELD STRESS T MPa C11	TENSILE STRENGTH T MPa C12	ELONG % A80 T C13	C	P	S	Mn	Si	S.Al	N	Cr	Mo	Ni	Al	As	B	Co	Cu	Nb	Sn	Ti	V	W	Ca	CEV
1426410	83112PT	376	527	20																						

PROCESS C70 BASIC OXYGEN STEEL CONTINUOUS CAST SLAB

ANALYSIS B07 C71-C92	C	P	S	Mn	Si	S.Al	N	Cr	Mo	Ni	Al	As	B	Co	Cu	Nb	Sn	Ti	V	W	Ca	CEV
CAST/HEAT No Min																						
Max																						
83112PT	0.1440	0.0110	0.0150	1.1530	0.0120	0.0390	0.0050	0.0170	0.0010	0.0130	0.0420	0.0020	0.0001	0.0010	0.0140	0.0010	0.0050	0.0020	0.0010	0.0010	0.0001	0.3420

A10-A99 204

SUPPLEMENTARY INFORMATION

IT IS CERTIFIED THAT UNLESS OTHERWISE STATED THE SUPPLIES DETAILED HEREON HAVE BEEN MANUFACTURED INSPECTED AND TESTED IN ACCORDANCE WITH OUR QUALITY MANAGEMENT SYSTEM APPROVAL TO BS EN ISO/TS16949 AND CONFORM TO THE TERMS OF OUR ORDER ACKNOWLEDGEMENT

0038/CPD/200E0004/A

On behalf of Corus UK Limited PORT TALBOT Works.
These results are certified by Corus UK Limited and comply with the requirements of the Product Description Z02

MIKE PASKINS
TECHNICAL MANAGER - LABORATORIES A05

Corus UK Limited Registered Office: 30 Millbank, London, SW1P 4WY. Registered in England No. 2280000.

corus
Port Talbot,
West Glamorgan, SA13 2NG
United Kingdom.
Telephone: 01639 871111
Fax: 01639 872067

INSPECTION CERTIFICATE

Our Order No.	Customer Order No.
6/09883/1/1	116707

Works Order No	Despatch/Invoice No. and Date
6/09883/1/1	20095791 11/09/07

Certificate No.	Certificate Date	Page	Part No.
20618762	11/09/07	1 of 1	

Customer Name & Address

CD&BS DUDLEY
HR COIL PROCESSING CENTRE
BRIDGNORTH ROAD
WOMBOURNE WOLVERHAMPTON
WEST MIDLANDS WV5 8AT

Ordered dimensions mm: GAUGE = 4.0000 WIDTH = 1500.000 LENGTH = COIL

Product Description: STRUCTURAL STEEL HOT ROLLED COIL NON SKIN PASSED MILL EDGES,NOT CUT BACK TO GAUGE

Specification	Grade	Certificate Specification
BSEN10025-2:2004	S355JR+AR	BSEN10204:2004 TYPE 2.2

MATERIAL IDENTITY	CAST / HEAT No.
1487210	72242PT

PROCESS: BASIC OXYGEN STEEL — CONTINUOUS CAST SLAB

ANALYSIS CAST/HEAT No.		C	P	S	Mn	Si	S.Al	N	Cr	Mo	Ni	Al	As	B	Co	Cu	Nb	Sn	Ti	V	Ca	CEV
	Min																					
	Max																					
72242PT		0.1880	0.0150	0.0140	0.9960	0.0020	0.0420	0.0052	0.0370	0.0010	0.0210	0.0460	0.0020	0.0001	0.0010	0.0270	0.0010	0.0040	0.0010	0.0010	0.0001	0.3650

SUPPLEMENTARY INFORMATION

IT IS CERTIFIED THAT UNLESS OTHERWISE STATED THE SUPPLIES DETAILED HEREON HAVE BEEN MANUFACTURED INSPECTED AND TESTED IN ACCORDANCE WITH OUR QUALITY MANAGEMENT SYSTEM APPROVAL TO BS EN ISO/TS16949 AND CONFORM TO THE TERMS OF OUR ORDER ACKNOWLEDGEMENT

CE
0038/CPD/20060004/A

On behalf of Corus UK Limited PORT TALBOT Works.
These results are certified by Corus UK Limited and comply with the requirements of the Product Description

MIKE PASKINS
TECHNICAL MANAGER - LABORATORIES

corus

Port Talbot,
West Glamorgan, SA13 2NG
United Kingdom.
Telephone: 01639 871111
Fax: 01639 872067

INSPECTION CERTIFICATE

Certificate No.	Certificate Date	Page of	Our Order No.	Customer Order No.	Works Order No	Despatch/Invoice No. and Date	Part No.
20618510	7/09/07	1 1	6/25502/1/1	137374	6/25502/1/1	20094500 7/09/07	

Customer Name & Address

CD&BS DUDLEY
HR COIL PROCESSING CENTRE
BRIDGNORTH ROAD
WOMBOURNE WOLVERHAMPTON
WEST MIDLANDS WV5 8AT

Ordered dimensions mm: GAUGE = 6.0000 WIDTH = 1250.000 LENGTH = COIL

Product Description: STRUCTURAL STEEL HOT ROLLED COIL NON SKIN PASSED MILL EDGES,NOT CUT BACK TO GAUGE

Specification	Grade	Certificate Specification
BSEN10025-2:2004	S355JR+AR	BSEN10204:2004 TYPE 3.1

MATERIAL IDENTITY	CAST / HEAT No.	YIELD STRESS T MPa C11	TENSILE STRNGTH T MPa C12	ELONG % A80 T C13
3045030	74187PT	422	530	21

PROCESS BASIC OXYGEN STEEL CONTINUOUS CAST SLAB

ANALYSIS CAST/HEAT No.		C	P	S	Mn	Si	S.Al	N	Cr	Mo	Ni	Al	As	B	Co	Cu	Nb	Sn	Ti	V	Ca	CEV
	Min																					
	Max																					
74187PT		0.1510	0.0190	0.0048	1.0800	0.0040	0.0420	0.0066	0.0310	0.0010	0.0170	0.0460	0.0020	0.0001	0.0020	0.0170	0.0210	0.0030	0.0020	0.0010	0.0002	0.3400

SUPPLEMENTARY INFORMATION

IT IS CERTIFIED THAT UNLESS OTHERWISE STATED THE SUPPLIES DETAILED HEREON HAVE BEEN MANUFACTURED INSPECTED AND TESTED IN ACCORDANCE WITH OUR QUALITY MANAGEMENT SYSTEM APPROVAL TO BS EN ISO/TS16949 AND CONFORM TO THE TERMS OF OUR ORDER ACKNOWLEDGEMENT

CE
0038/CPD/20060004/A

On behalf of Corus UK Limited PORT TALBOT Works.
These results are certified by Corus UK Limited and comply with the requirements of the Product Description

MIKE PASKINS
TECHNICAL MANAGER - LABORATORIES

A2 Cooling Block FE Model Temperature Fits

The visual best fit of the temperature profiles of the FE model and the experimental measurements are detailed in this appendix in the order listed in **Table 4.6**.

Experiments CB1.1, variable: p_e

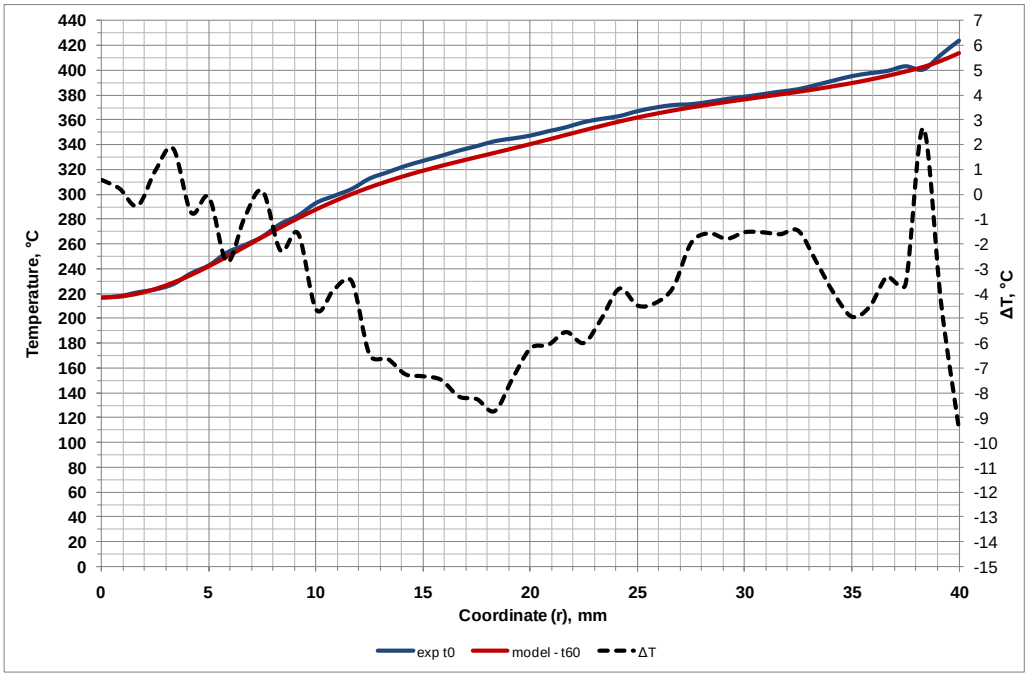

Figure A2.1 Visual best fit of the temperatures predicted by the FE model to the measured thermal profile. Experiment CB1.1, p_e=0 mbar

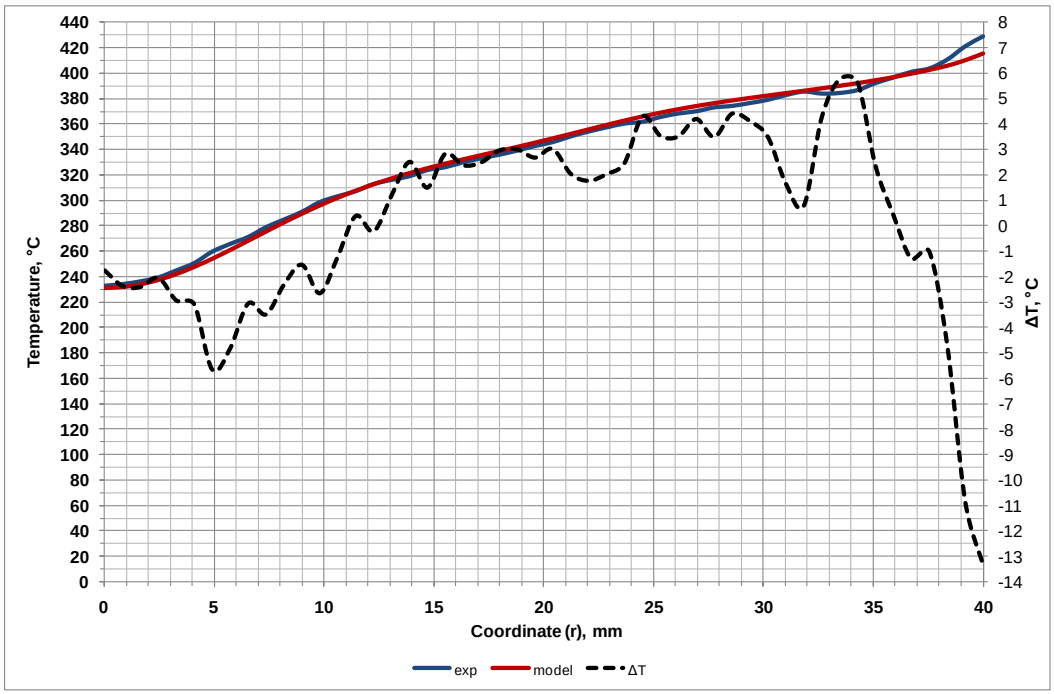

Figure A2.2 Visual best fit of the temperatures predicted by the FE model to the measured thermal profile. Experiment CB1.1, p_e=-90 mbar

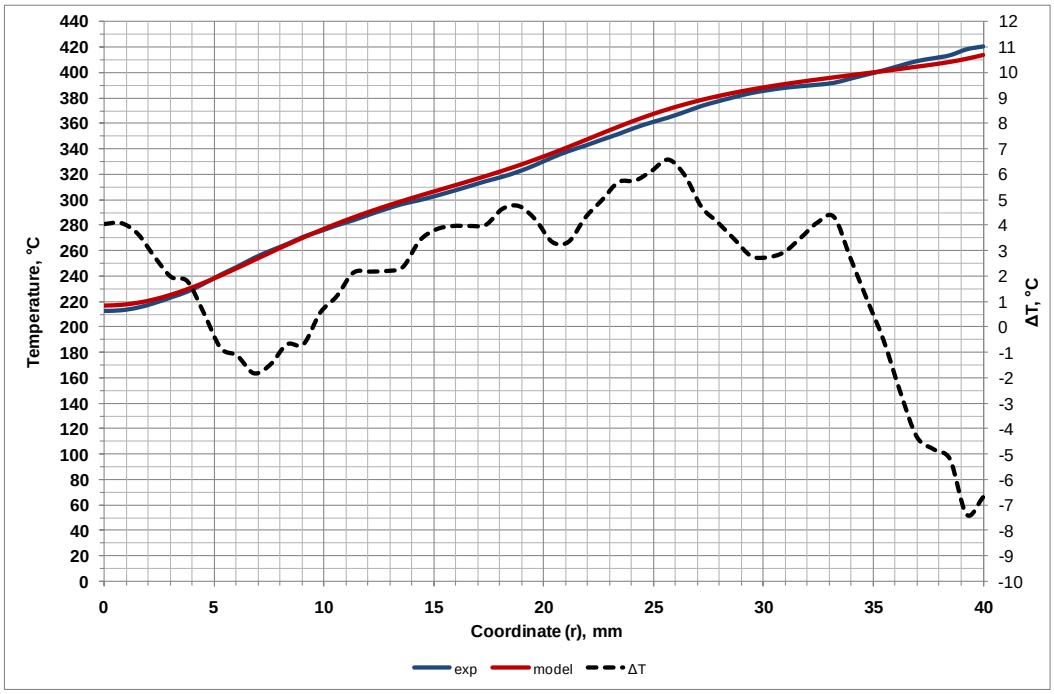

Figure A2.3 Visual best fit of the temperatures predicted by the FE model to the measured thermal profile. Experiment CB1.1, p_e=-120 mbar

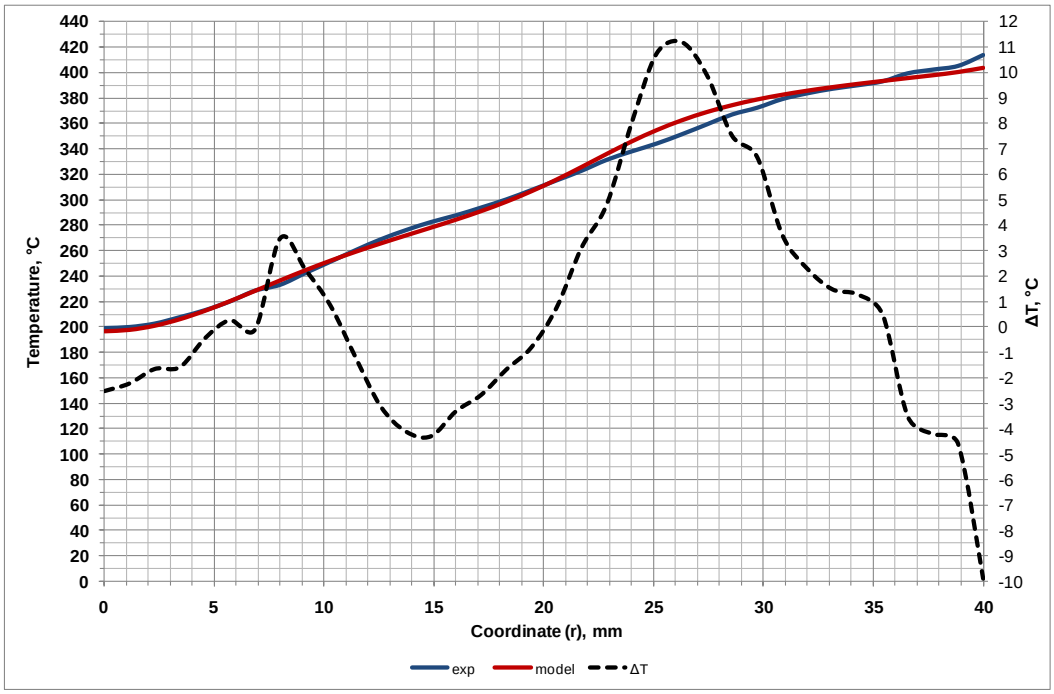

Figure A2.4 Visual best fit of the temperatures predicted by the FE model to the measured thermal profile. Experiment CB1.1, p_e=-150 mbar

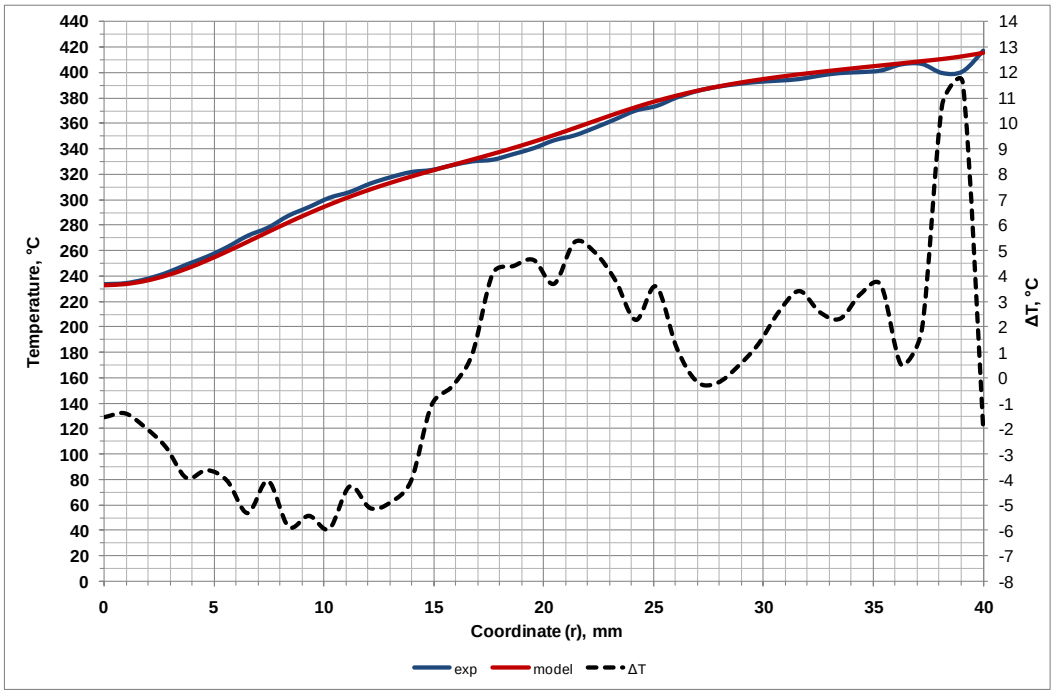

Figure A2.5 Visual best fit of the temperatures predicted by the FE model to the measured thermal profile. Experiment CB1.1, p_e=-190 mbar

Experiments CB1.2, variable: z_A

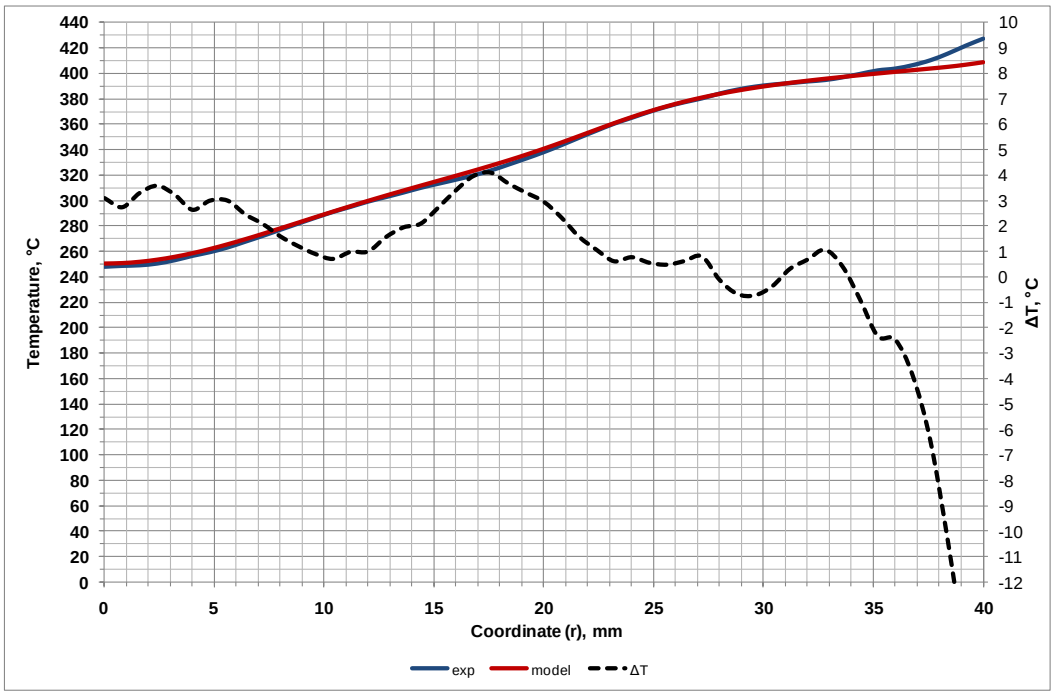

Figure A2.6 Visual best fit of the temperatures predicted by the FE model to the measured thermal profile. Experiment CB1.2, z_A=40 mm

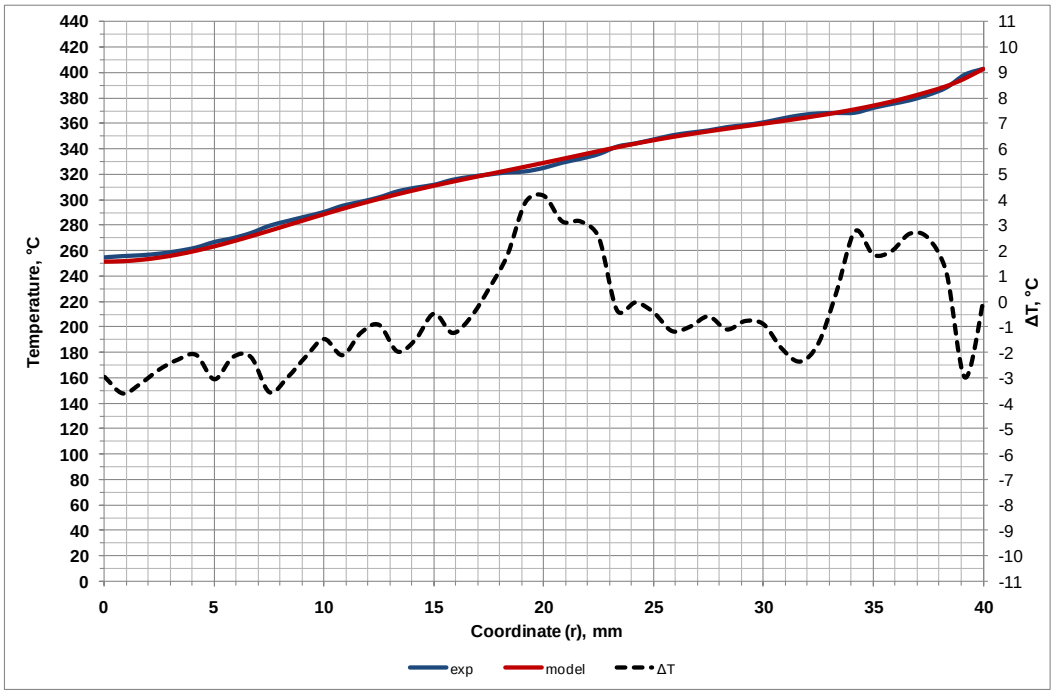

Figure A2.7 Visual best fit of the temperatures predicted by the FE model to the measured thermal profile. Experiment CB1.2, z_A=50 mm

Experiments CB1.3, variable: D_n

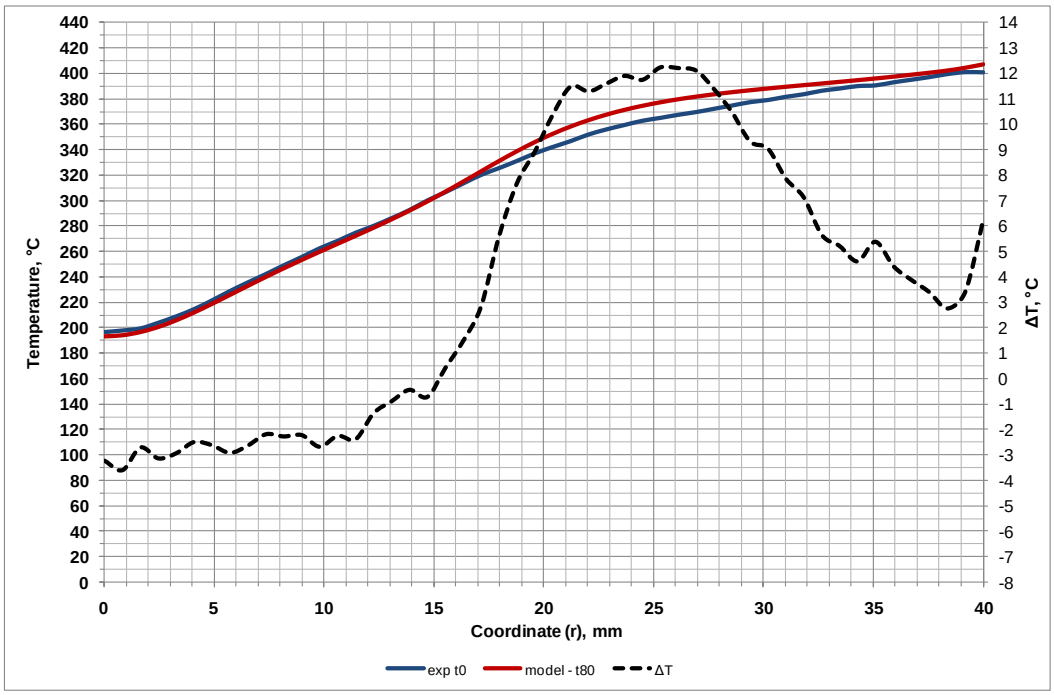

Figure A2.8 Visual best fit of the temperatures predicted by the FE model to the measured thermal profile. Experiment CB1.3, D_n=35 mm

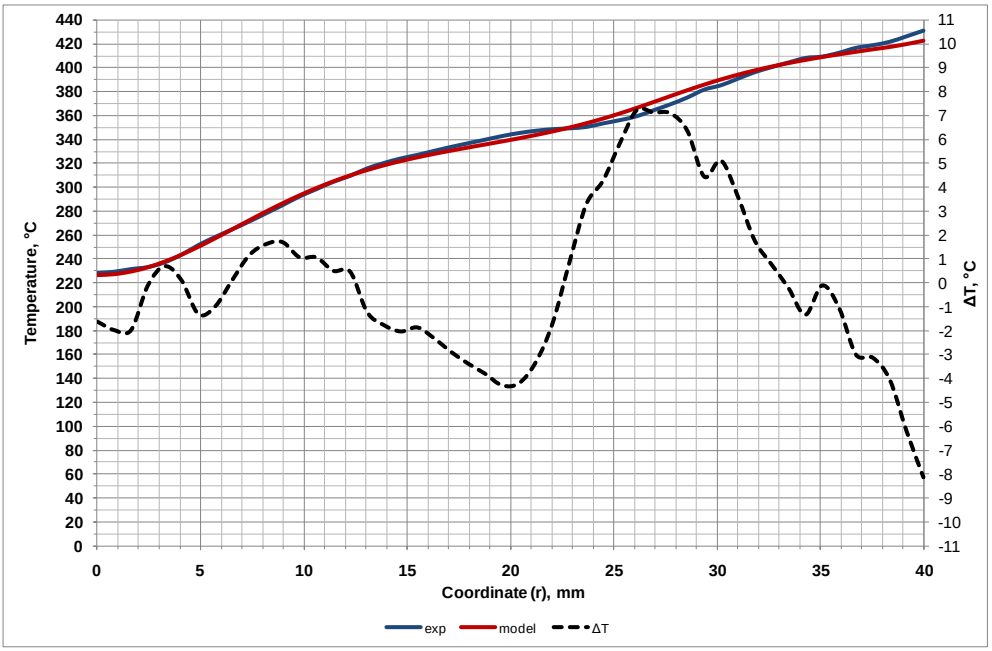

Figure A2.9 Visual best fit of the temperatures predicted by the FE model to the measured thermal profile. Experiment CB1.3, D_n=55 mm

Experiments CB1.4, variable: Amal jet size

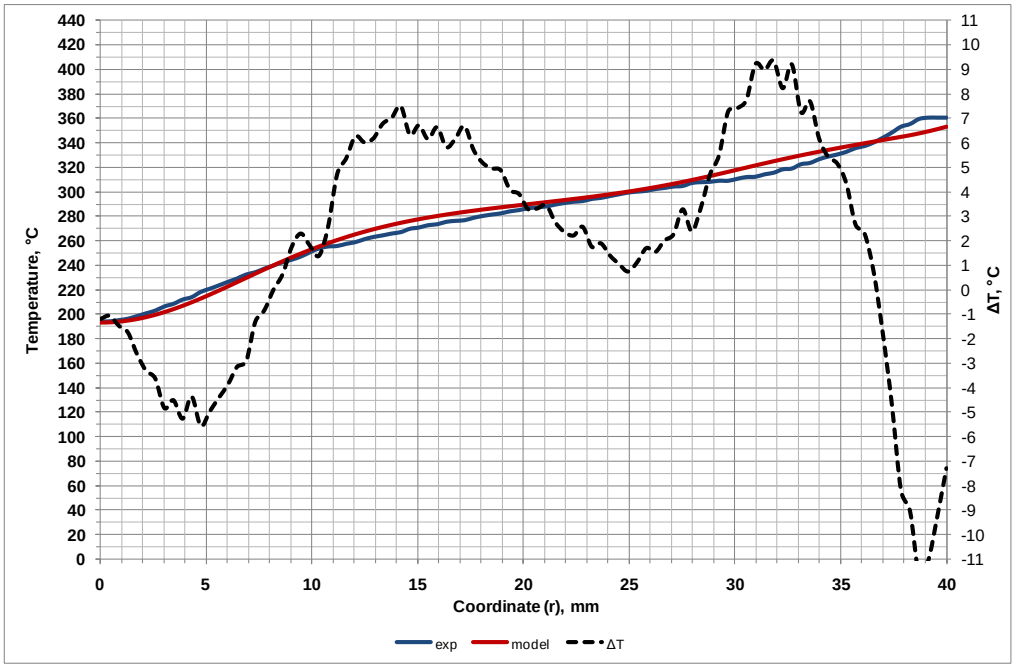

Figure A2.10 Visual best fit of the temperatures predicted by the FE model to the measured thermal profile. Experiment CB1.4, Amal jet: 170

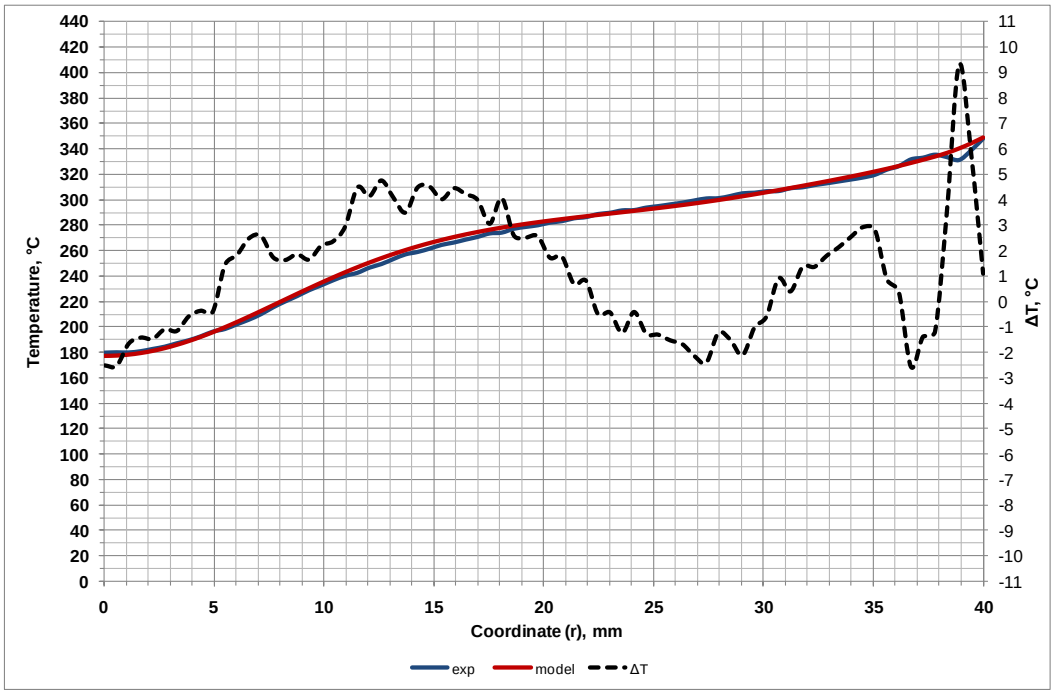

Figure A2.11 Visual best fit of the temperatures predicted by the FE model to the measured thermal profile. Experiment CB1.4, Amal jet: 250

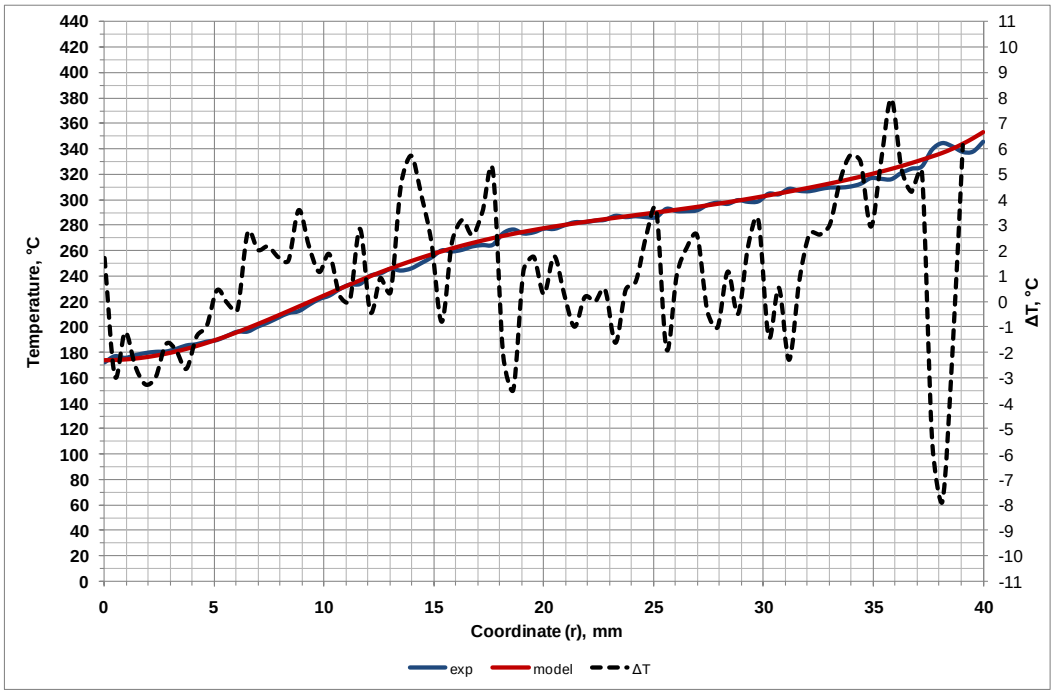

Figure A2.12 Visual best fit of the temperatures predicted by the FE model to the measured thermal profile. Experiment CB1.4, Amal jet: 340

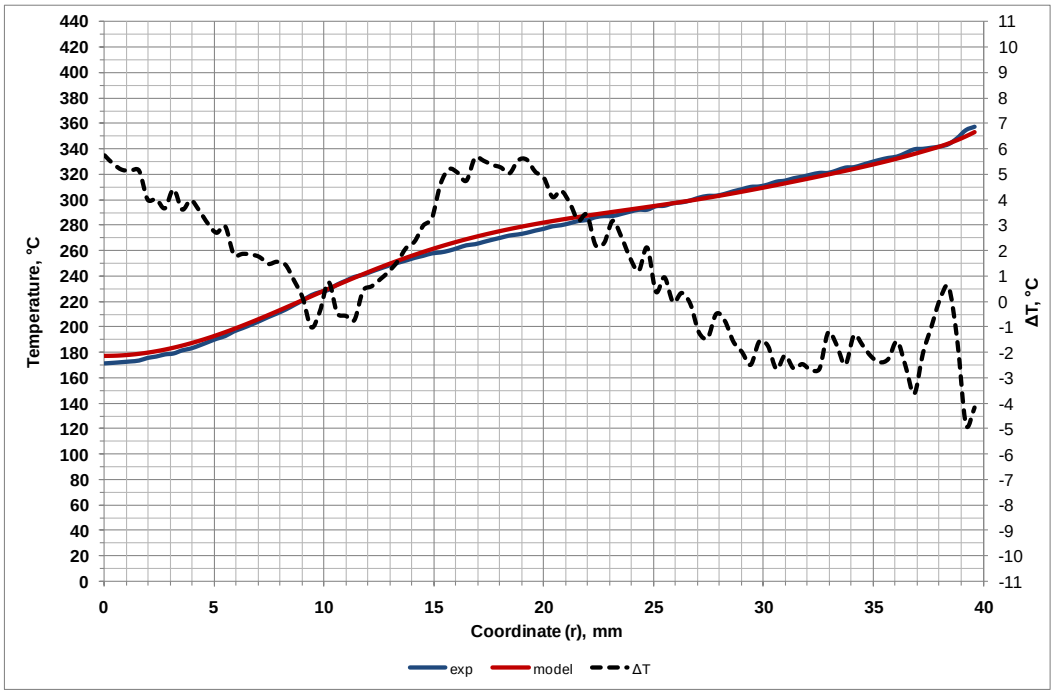

Figure A2.13 Visual best fit of the temperatures predicted by the FE model to the measured thermal profile. Experiment CB1.4, Amal jet: 500

Experiments CB1.5, variable: AEG

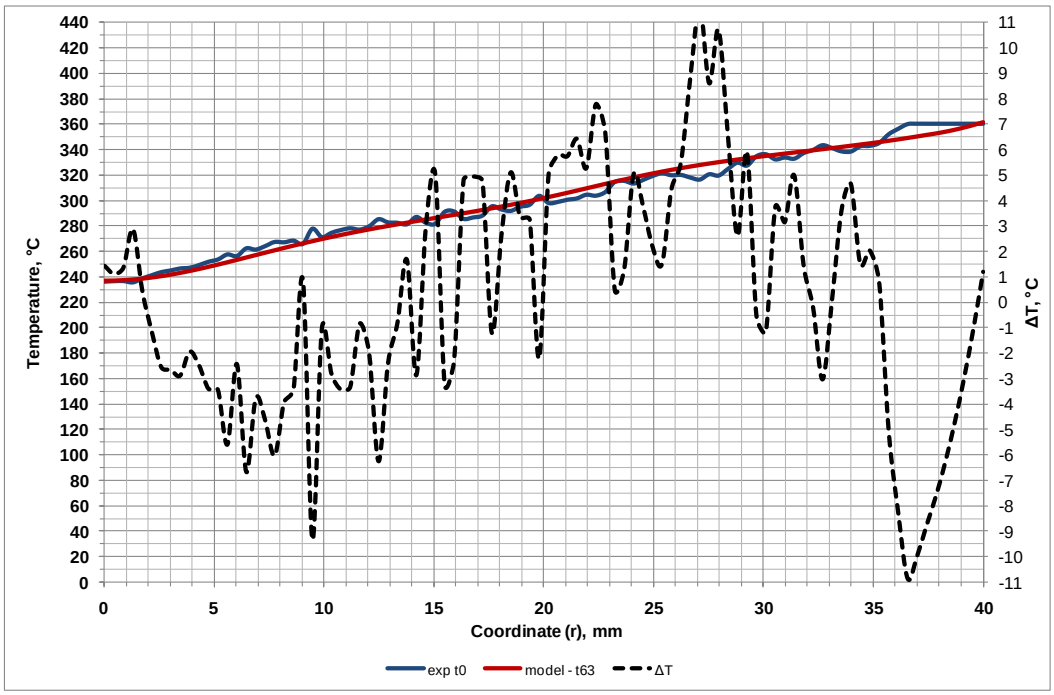

Figure A2.14 Visual best fit of the temperatures predicted by the FE model to the measured thermal profile. Experiment CB1.5, AEG: 2 mm

Experiments CB1.6, variable: T_{pre}

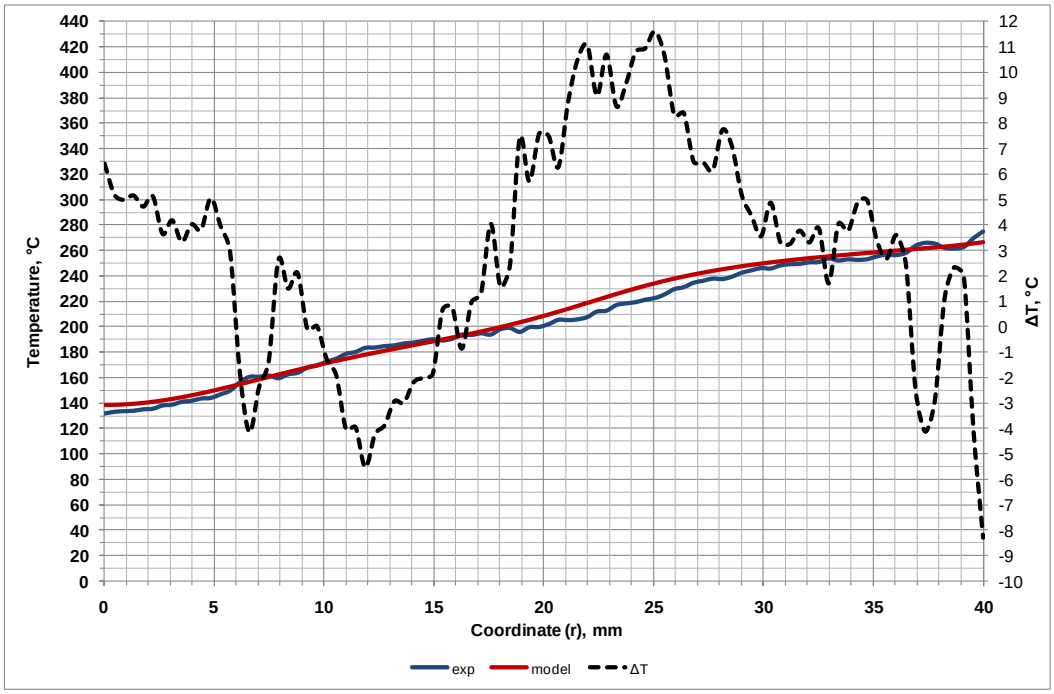

Figure A2.15 Visual best fit of the temperatures predicted by the FE model to the measured thermal profile. Experiment CB1.6, T_{pre} : 250 °C